N72-20847-55

NASA TECHNICAL MEMORANDUM

NASA TM X-2506

NASA TM X-2506

CASE FILE COPY

SPACE SHUTTLE AEROTHERMODYNAMICS TECHNOLOGY CONFERENCE

Volume I - Flow Fields

Held at
Ames Research Center
Moffett Field, California
December 15-16, 1971

NATIONAL AERONAUTICS AND SPACE ADMINISTRATION • WASHINGTON, D. C. • FEBRUARY 1972

1. Report No.	2. Government Accession No.	3. Recipient's Catalog No.
NASA TM X-2506		

4. Title and Subtitle	5. Report Date
SPACE SHUTTLE AEROTHERMODYNAMICS TECHNOLOGY CONFERENCE VOLUME I - FLOW FIELDS	February 1972
	6. Performing Organization Code
7. Author(s)	8. Performing Organization Report No. L-8136
	10. Work Unit No.
9. Performing Organization Name and Address NASA Langley Research Center Hampton, Va. 23365	11. Contract or Grant No.
	13. Type of Report and Period Covered Technical Memorandum
12. Sponsoring Agency Name and Address National Aeronautics and Space Administration Washington, D.C. 20546	14. Sponsoring Agency Code

15. Supplementary Notes

Held at NASA Ames Research Center, December 15-16, 1971.

16. Abstract

The conference encompasses four technology efforts, each published as a separate volume.

Volume I - Flow Fields (NASA TM X-2506)

Volume II - Heating (NASA TM X-2507)

Volume III - Aerodynamics (NASA TM X-2508)

Volume IV - Operational Flight Mechanics (NASA TM X-2509)

17. Key Words (Suggested by Author(s))	18. Distribution Statement
Flow fields Heating Aerodynamics Operational flight mechanics Space shuttle Aerothermodynamics	Unclassified - Unlimited

19. Security Classif. (of this report)	20. Security Classif. (of this page)	21. No. of Pages	22. Price*
Unclassified	Unclassified	270	$3.00

*For sale by the National Technical Information Service, Springfield, Virginia 22151

Page intentionally left blank

PREFACE

A Space Shuttle Technology Conference on Flow Fields, Heat Transfer, Aerodynamics, and Operational Flight Mechanics was held at the NASA Ames Research Center on December 15 and 16, 1971. The objective of this conference was to review the broad base of aerothermodynamics technology developed for the space shuttle during the period of the Phase B studies and, thereby, help focus attention on the technology required for further space shuttle development. This publication is a compilation of the conference papers. It has been divided into four volumes, one for each of the sessions. Five papers which were omitted from the oral presentation at the conference are included in this publication. Contributing organizations include U.S. Aerospace Contractors, Universities, Canadian and European Space Agencies, in addition to NASA Research Centers.

Page intentionally left blank

CONTENTS

GLOSSARY ix

OPENING REMARKS

1. SHUTTLE PROGRAM STATUS 1
Edward P. Andrews, NASA Headquarters

2. SHUTTLE TECHNOLOGY - INTRODUCTORY REMARKS 41
A. O. Tischler, NASA Headquarters

VOLUME I.- FLOW FIELDS

3. INTRODUCTION 45
Joseph G. Marvin, ARC

4. DETERMINATION OF SPACE SHUTTLE FLOW FIELD BY THE THREE-DIMENSIONAL METHOD OF CHARACTERISTICS 47
Chong-Wei Chu and S. A. Powers, Northrop

5. APPLICATION OF SHOCK CAPTURING AND CHARACTERISTICS METHODS TO SHUTTLE FLOW FIELDS 65
P. Kutler, J. V. Rakich, and G. G. Mateer, ARC

6. FLOW FIELD PREDICTIONS FOR A SLAB DELTA WING AT INCIDENCE 93
R. J. Conti, P. D. Thomas, and Y. S. Chou, Lockheed

7. SPACE SHUTTLE ORBITER REENTRY FLOW FIELD AND HEATING ANALYSIS 115
W. C. Rochelle, TRACOR; B. B. Roberts, MSC; F. W. Vogenitz, and L. d'Attorre, TRW Systems

8. A VISCOUS STARTER SOLUTION FOR SHUTTLE FLOW FIELD COMPUTATIONS 157
C. P. Li, Lockheed Electronics Co.; and W. D. Goodrich, MSC

9. CHEMICAL NONEQUILIBRIUM EFFECTS ON THE FLOW IN THE WINDWARD PLANE OF SYMMETRY OF A BLUNTED DELTA ORBITER 185
J. A. Lordi, R. J. Vidal, Cornell Aeronautical Laboratory; and C. B. Johnson, LRC

10. INVISCID-SURFACE-STREAMLINE PROGRAM FOR USE IN PREDICTING SHUTTLE HEATING RATES 239
H. Harris Hamilton, LRC; and Fred R. DeJarnette, North Carolina State University

11. SUMMARY 255
Joseph G. Marvin, ARC

VOLUME II.- HEATING

12. INTRODUCTION 257
James C. Dunavant, LRC

13. EXPERIMENTAL AND THEORETICAL AERODYNAMIC HEATING AND FLOW FIELD ANALYSIS OF A SPACE SHUTTLE ORBITER 261
R. K. Matthews, T. D. Buchanan, W. R. Martindale, ARO, Inc.; and J. D. Warmbrod, MSFC

14. A REVIEW OF THE GRUMMAN ORBITER WIND TUNNEL HEAT TRANSFER TESTS . . . 297
A: R. Mendelsohn, M. Bourbin, M. Jew, and C. W. Osonitsch, Grumman

15. HIGH REYNOLDS NUMBER TURBULENT HEATING TO TWO SIMPLIFIED SHUTTLE CONFIGURATIONS 347
Charles B. Johnson, LRC

16. EFFECTS OF ROUGHNESS ON HEATING AND BOUNDARY-LAYER TRANSITION
I. EFFECTS OF SIMULATED PANEL JOINTS ON BOUNDARY-LAYER TRANSITION 375
H. Lee Seegmiller, ARC
II. EFFECTS OF DISCRETE ROUGHNESS ON HEATING 395
George G. Mateer, ARC

17. LEE-SIDE FLOW PHENOMENA ON SPACE SHUTTLE CONFIGURATIONS AT HYPERSONIC SPEEDS
I. FLOW SEPARATION AND FLOW FIELD VISCOUS PHENOMENA OF A DELTA-WING SHUTTLE ORBITER CONFIGURATION 413
J. W. Cleary, ARC
II. STUDIES OF LEE-SURFACE HEATING AT HYPERSONIC MACH NUMBERS . . . 451
Jerry N. Hefner and Allen H. Whitehead, Jr., LRC

18. AEROTHERMODYNAMIC MEASUREMENTS FOR SPACE SHUTTLE CONFIGURATIONS IN HYPERSONIC WIND TUNNELS 469
John J. Bertin, Frank E. Williams, Robert C. Baker, University of Texas; Winston D. Goodrich, MSC; and William C. Kessler, McDonnell Douglas

19. DETERMINATION OF AEROTHERMODYNAMIC ENVIRONMENT UNCERTAINTIES WITH APPLICATION TO SPACE SHUTTLE VEHICLES 503
C. A. Scottoline, North American Rockwell

20. SPACE SHUTTLE BOOSTER MULTI-ENGINE BASE FLOW ANALYSIS 519
Homer H. Tang, Charles P. Gardiner, William A. Anderson, and John Navickas, McDonnell Douglas

21. AN ANALYSIS OF THE BOOSTER PLUME IMPINGEMENT ENVIRONMENT DURING THE SPACE SHUTTLE NOMINAL STAGING MANEUVER 607
C. J. Wojciechowski, M. M. Penny, Lockheed - Huntsville; T. F. Greenwood, MSFC; and I. H. Fossler, MSC

22. CONVECTIVE HEATING MEASUREMENT BY MEANS OF AN INFRARED CAMERA 645
Dale L. Compton, ARC

23. HEAT-TRANSFER TESTING PROCEDURES IN PHASE B SHUTTLE STUDIES WITH EMPHASIS ON PHASE-CHANGE-DATA IMPROVEMENT 661
David A. Throckmorton, LRC

24. EVALUATION OF BOUNDARY-LAYER-TRANSITION CRITERIA FOR SPACE SHUTTLE ORBITER ENTRY 683
Vernon T. Helms III, LRC

VOLUME III.- AERODYNAMICS

25. INTRODUCTORY REMARKS OF SESSION CHAIRMAN 705
Beverly Z. Henry, LRC

26. STATUS OF LANGLEY STUDIES OF AERODYNAMICS AND INTERFERENCE EFFECTS OF TANDEM LAUNCH VEHICLES 707
William I. Scallion and Kermit G. Pratt, LRC

27. IMPACT OF SUBSONIC AERODYNAMIC CONSIDERATIONS ON A SPACE SHUTTLE BOOSTER CONFIGURATION 737
R. L. Roensch, Douglas Aircraft Co.; and R. L. Odenbaugh, McDonnell Douglas Astronautics Co. - West

28. AERODYNAMIC STUDIES OF DELTA-WING SHUTTLE ORBITERS
I. LOW SPEED 785
Delma C. Freeman, Jr., and James C. Ellison, LRC
II. HYPERSONICS 803
Howard W. Stone and James P. Arrington, LRC

29. WING OPTIMIZATION FOR SPACE SHUTTLE ORBITER VEHICLES 831
T. E. Surber, W. E. Bornemann, and W. D. Miller, North American Rockwell

30. REVIEW OF DELTA WING SPACE SHUTTLE VEHICLE DYNAMICS 861
J. Peter Reding and Lars E. Ericsson, Lockheed

31. EXPERIMENTS ON THE DYNAMIC STABILITY OF THE SPACE SHUTTLE 933
K. J. Orlik-Rückemann, J. G. LaBerge, and E. S. Hanff, National Research Council of Canada

32. AEROSPACE TRANSPORTER AND LIFTING BODY ACTIVITIES IN EUROPE AND POTENTIAL PARTICIPATION IN THE DEVELOPMENT OF THE SPACE SHUTTLE ORBITER 969
M. Fuchs, J. Haseloff, and G. Peters, ERNO

33. SUMMARY REMARKS OF SESSION CHAIRMAN 993
Beverly Z. Henry, LRC

VOLUME IV.- OPERATIONAL FLIGHT MECHANICS

34. INTRODUCTION 997
Victor L. Peterson, ARC

35. VEHICLE PERFORMANCE IMPACT ON SPACE SHUTTLE DESIGN AND CONCEPT EVALUATION 999
Mark K. Craig, MSC

36. SPACE SHUTTLE ATMOSPHERIC ASCENT FLIGHT DYNAMICS 1041
J. T. Patha, K. A. Noess, and M. V. Lines, Boeing

37. OPTIMAL LIFTING ASCENT TRAJECTORIES FOR THE SPACE SHUTTLE 1063
T. R. Rau and J. R. Elliott, LRC

38. OPTIMAL ASCENT TRAJECTORIES OF A TWO STAGE SPACE SHUTTLE VEHICLE . . . 1089
R. A. Wilson, North American Rockwell

39. ABORT SEPARATION OF THE SHUTTLE 1105
John P. Decker, LRC; Kenneth L. Blackwell, Joseph L. Sims, MSFC; R. H. Burt, W. T. Strike, Jr., ARO; C. Donald Andrews, L. Ray Baker, Jr., LMSC - Huntsville; and John M. Rampy, Northrop - Huntsville

40. BOOSTER RECOVERY FOLLOWING PREMATURE SPACE SHUTTLE STAGE SEPARATION 1165
M. J. Hurley, General Dynamics/Convair

41. EFFECT OF COMMERCIAL AND MILITARY PERFORMANCE REQUIREMENTS FOR TRANSPORT CATEGORY AIRCRAFT ON SPACE SHUTTLE BOOSTER DESIGN AND OPERATION 1191
R. A. Bithell and W. A. Pence, Jr., General Dynamics/Convair

42. SPACE SHUTTLE ORBITER HANDLING QUALITY CRITERIA APPLICABLE TO TERMINAL AREA, APPROACH, AND LANDING 1239
Gordon H. Hardy, ARC

43. ORBITER ENTRY TRAJECTORY CONSIDERATIONS 1265
John J. Rehder and Paul F. Holloway, LRC

44. STAGE SEPARATION OF PARALLEL-STAGED SHUTTLE VEHICLES, A CAPABILITY ASSESSMENT 1301
M. J. Hurley and G. W. Carrie, General Dynamics/Convair

45. SPACE SHUTTLE BOOSTER FLYBACK SYSTEM SYNTHESIS 1397
D. W. Jones, W. J. Moran, and V. A. Lee, General Dynamics/Convair

46. OPTIMIZED SPACE SHUTTLE TRAJECTORY SIMULATION 1439
Louis Tramonti and Richard G. Brusch, General Dynamics/Convair

GLOSSARY

ABES	air breathing engines
ACPS	attitude control propulsion system
AEDC	Arnold Engineering Development Center
AFB	air force base
AFFDL	Air Force Flight Dynamics Laboratory
ALT	altitude
APS	auxiliary propulsion system
AR	aspect ratio
ARC	Ames Research Center
ARDC	Air Research and Development Command
BECO	booster engine cutoff
BLOW	booster lift-off weight
BV	body-vertical tail
BW	body-wing
BWV	body-wing-vertical tail
CAL	Cornell Aeronautical Laboratory
CALCS	calculations
CAL HST	Cornell Aeronautical Laboratory hypersonic shock tunnel
CFHT	continuous-flow hypersonic tunnel
CG; C.G.; c.g.	center of gravity
CONFIG	configuration
CRT	cathode ray tube
Cyl	cylinder
2-D	two-dimensional
3-D	three-dimensional

DAC	Douglas Aircraft Company
DCM	data control management
DEX	exit diameter
DIA	diameter
DIAT	diatomic
DIF. REFL.	differential deflection
3DMoC	three-dimensional method of characteristics
DOD	Department of Defense
DOF	degrees of freedom
DWO	delta-wing orbiter
EHT	external hydrogen tank
EOHT	external oxygen-hydrogen tank
EPL	emergency power level
EST	estimated
ETR	eastern test range
F&M	force and moment
FAR; F.A.R.	Federal Aircraft Regulation
FBS	flyback system
F.D.	finite difference
F/O	fuel-oxygen ratio
FO/FS	fail operational/fail safe
FPR	flight performance reserve
FPRE	flat-plate reference enthalpy
FR	fully reusable
FREQ	frequency
GAC	Grumman Aerospace Corporation

GD	General Dynamics
GDC	General Dynamics Corporation
GD/C	General Dynamics/Convair
G.E.	General Electric Company
GLOW	vehicle gross lift-off weight
GTOP	general trajectory optimization program
GW	gross weight
H	hydrogen
HCF	highly compacted fibers
HCR	high cross range
HeT	Mach 20 helium tunnel
HO	hydrogen-oxygen system
H.W.T.	hypersonic wind tunnel
IAC	industrial air center
IBFF	impulse base flow facility
ICD	interface control drawing
IFR	instrument flight rules
ILRV	integral launch and reentry vehicle
ILS	instrument landing system
IND	industrial
IR	infrared
IRAD	Independent Research and Development
KSC	Kennedy Space Center
L.E.	leading edge
LEE	leeward
LH_2	liquid hydrogen

LMSC	Lockheed Missiles & Space Company
LO_2; LOX	liquid oxygen
LRC; LaRC	Langley Research Center
LRU	link retraction unit
MAC	mean aerodynamic chord
MAC Exp	exposed mean aerodynamic chord
MARK I, MARK II	shuttle configurations
MAX	maximum
MC	Monte Carlo
MCAIR	a low-speed wind tunnel
MCAS	Marine Corps Air Station
MDAC	McDonnell Douglas Astronautics Company
MDC	McDonnell Douglas Corporation
MIL SPEC	military specification
MIN	minimum
MM HWT	Martin Marietta Corporation hotshot wind tunnel
MOC	method of characteristics
MPL	minimum power level
MSC	Manned Spacecraft Center
MSFC	Marshall Space Flight Center
MT.	mountain
NA	North American
NAE; N.A.E.	National Aeronautical Establishment
NAR; NARC; NR	North American Rockwell Corporation
NAS	Naval Air Station
NASA	National Aeronautics and Space Administration

NO.; No.	number
NOZ	nozzle
NPL	normal power level
O/F	oxygen-fuel ratio
OLOW	orbiter lift-off weight
OMS	orbiting maneuvering system
P/L	payload
PM	pitching moment
RCC	reinforced carbon carbon
RCS	reaction control system
Ref	reference
REQD	required
RFP	request for porposals
RGAS	real gas
R.H.	right hand engine
RSI	reusable surface insulation
RTV	room-temperature vulcanizing rubber
S&C	stability and control
SCT	shock capturing technique
SF	stick force
S.L.; SL	sea level
SM	service module
SPEC	specification
SRM	solid rocket motors
SS	stainless steel
SSV	space shuttle vehicle
ST	straight

STAR	strings and array computer; self-testing and repair computer
STD	standard
STI	Systems Technology, Incorporated
STOL	short take-off and landing
SW	southwest
SYM	symbol
T/C	thermocouple
T.E.	trailing edge
T.E.D.	trailing edge down
TEMP	temperature
T.E.U.	trailing edge up
THEO	theoretical
TPS	thermal protection system
TRAJ	trajectory
TVC	thrust vector control
Typ	typical
UPWT	Unitary Plan wind tunnel
USAF	U.S. Air Force
VAC HVWT	Vought Aeronautics Company hypervelocity wind tunnel
VAFB	Vandenburg Air Force Base
VDT	variable density tunnel
VFR	visual flight rules
V/STOL	vertical and short take-off and landing
w/o	without
WT	weight
WWD	windward
YM	yawing moment

SHUTTLE PROGRAM STATUS

By Edward P. Andrews

OMSF Space Shuttle Program Office
NASA Headquarters

FIGURE 1

The Space Transportation System consists of an earth-to-earth orbit Space Shuttle (a concept of the orbiter stage of the two stage system is depicted) and an orbit-to-orbit shuttle (a concept of the space tug is depicted). This status report today will be limited to the earth-to-earth orbit system.

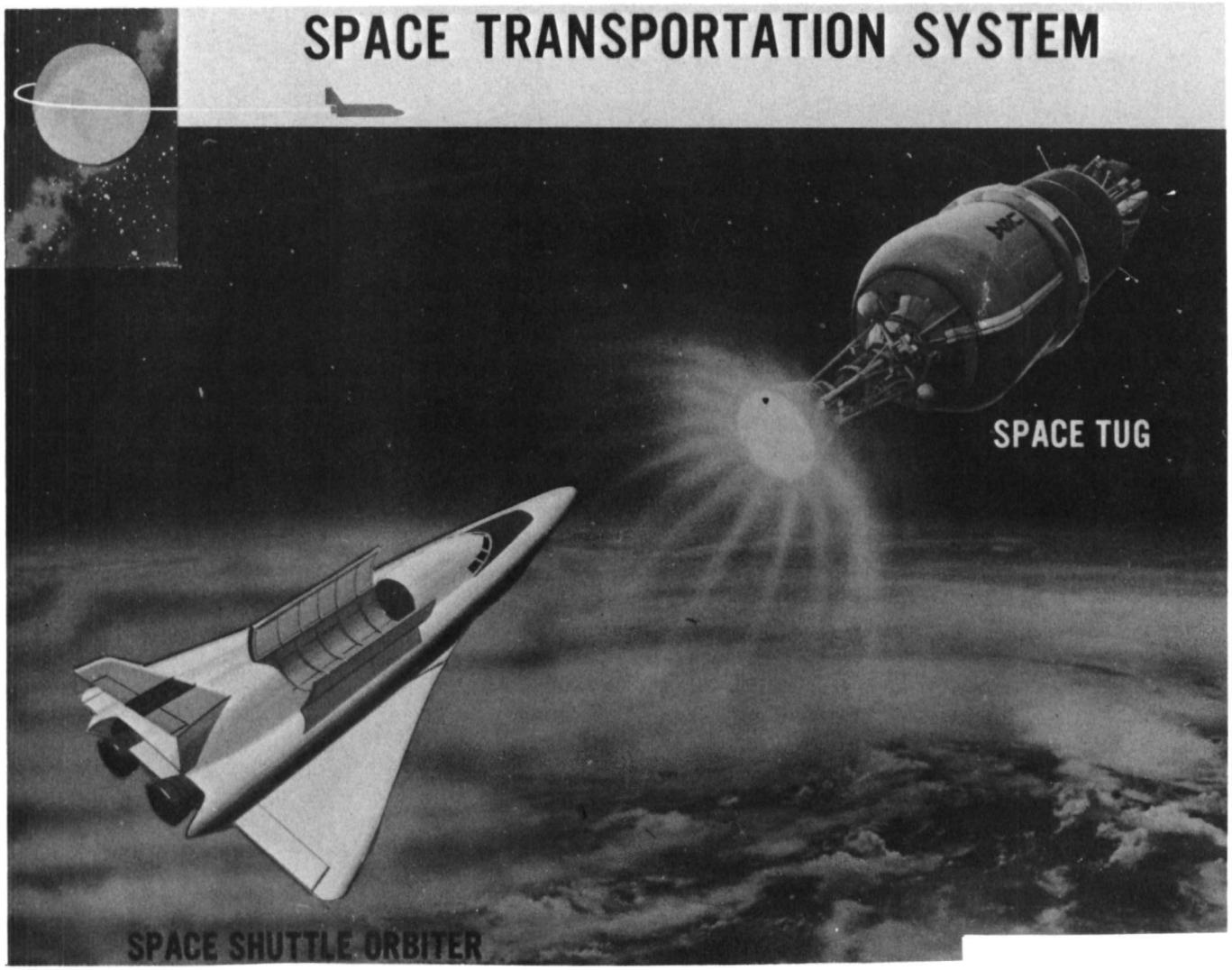
SPACE TRANSPORTATION SYSTEM
SPACE TUG
SPACE SHUTTLE ORBITER

Figure 1

FIGURE 2

The principal objectives of the Space Shuttle Program are listed on this figure.

SPACE SHUTTLE

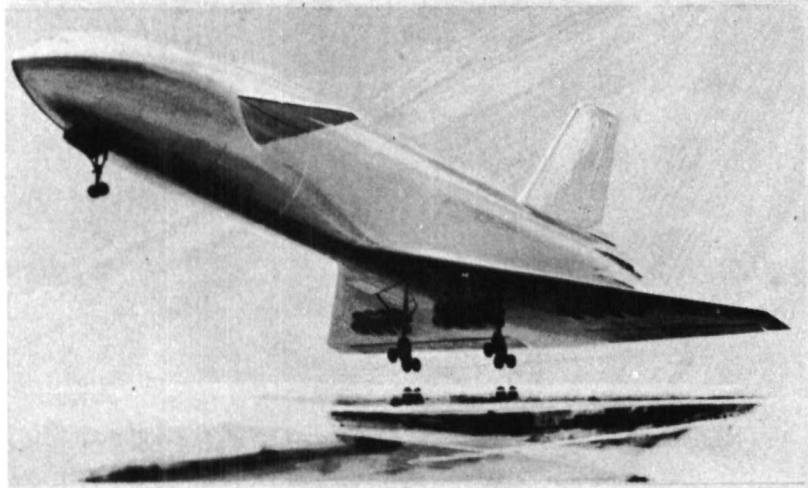

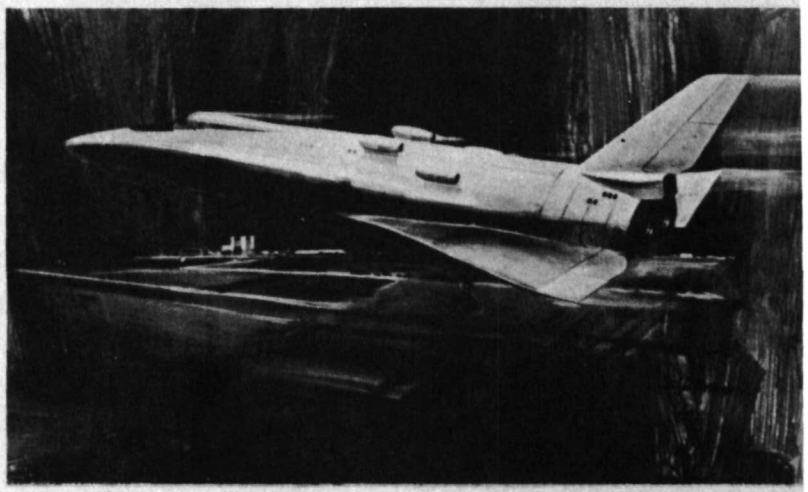

- REDUCE SUBSTANTIALLY COST OF SPACE OPERATIONS
- PROVIDE FUTURE CAPABILITY DESIGNED TO SUPPORT WIDE RANGE OF SCIENTIFIC, DEFENSE & COMMERCIAL USES

Figure 2

FIGURE 3

The earth-to-earth orbit Space Shuttle capabilities being utilized as a basis for system design are summarized on this figure. Of particular importance to payload designers is the ability to retrieve and to return satellites (or other payloads) from orbit to the earth's surface for refurbishment.

SPACE SHUTTLE CAPABILITIES

- SATELLITE PLACEMENT AND RETURN
- REPAIR AND SERVICE SATELLITES
- DELIVERY OF PROPULSIVE STAGE AND SATELLITE TO LOW EARTH ORBIT FOR TRANSFER TO SYNCHRONOUS ORBIT OR ESCAPE
- SHORT DURATION SCIENCE AND APPLICATIONS MISSIONS
- RESEARCH LABORATORY
- SPACE RESCUE
- PROPELLANT DELIVERY
- SPACE STATION SUPPORT

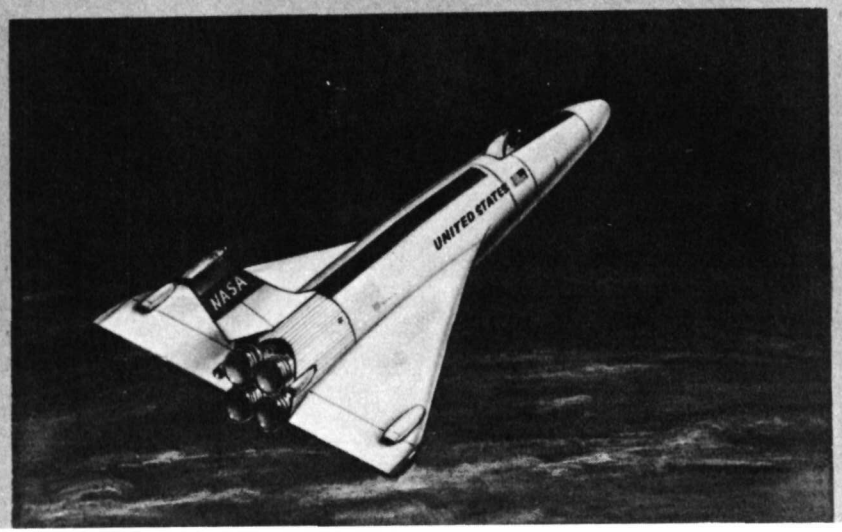

Figure 3

FIGURE 4

The classes of launch vehicles which are envisioned at this time to be replaced by the Space Shuttle are displayed in the shaded portion of this figure. The small Scout and the giant Saturn V are examples of launch vehicle payload and/or operational cost characteristics falling outside the competitive range of the Space Shuttle.

LAUNCH VEHICLE REPLACEMENT

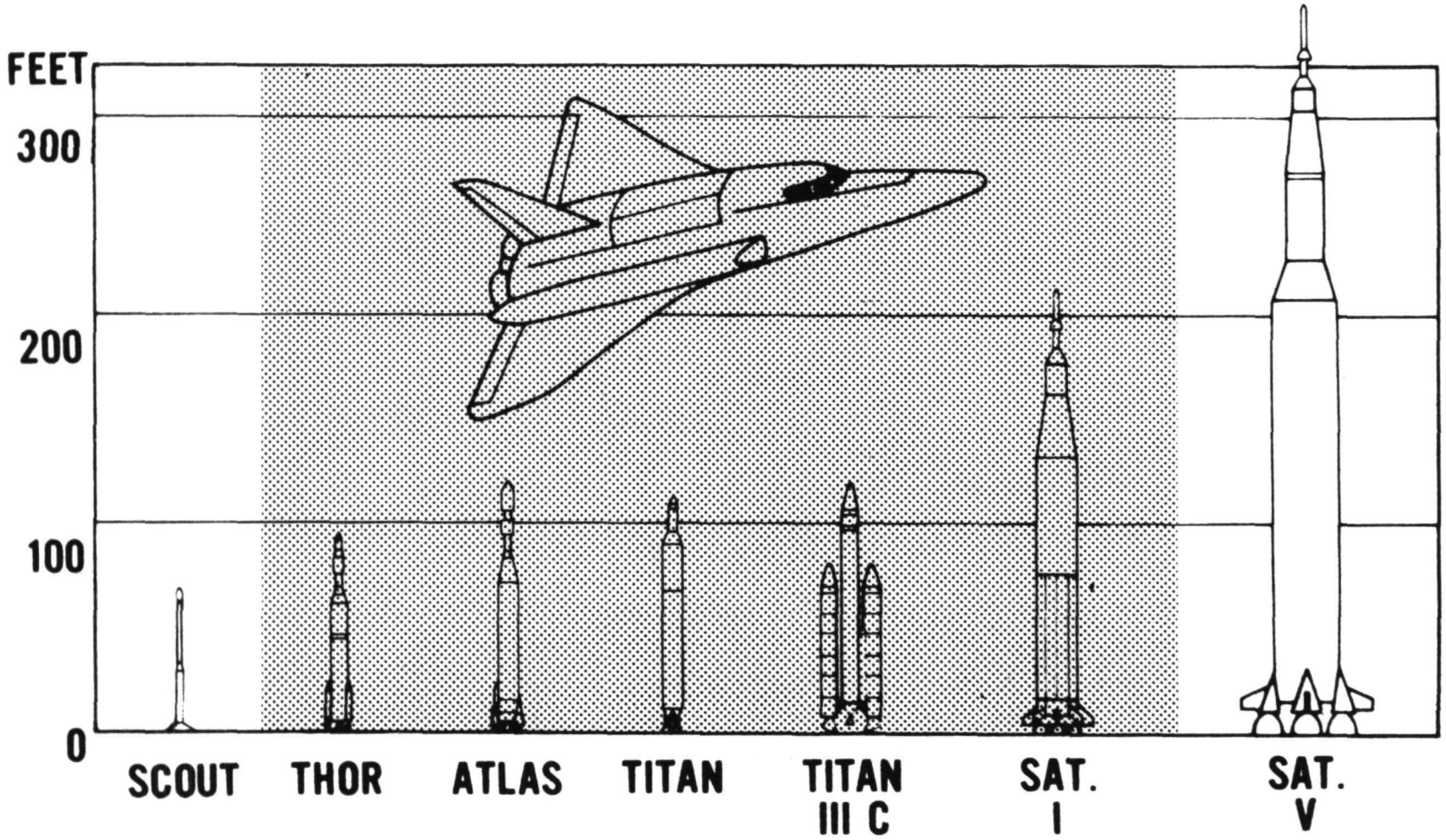

Figure 4

FIGURE 5

Space Shuttle studies have considered a wide variety of system configurations which are represented by the six comparative size outline drawings displayed on this figure. Chronologically, the figure should be read from right to left in that the system studies initiated in 1969 were based on "fully reusable" configurations with liquid oxygen and liquid hydrogen propellant tanks inside the orbiter. Later studies developed the advantage of reduced orbiter and booster size by tanking the hydrogen propellant external to the orbiter (the H_2 tank baseline configuration).

The concept of external tanking of propellants was extended to consider both hydrogen and oxygen (the HO tank concept) outside the orbiter. Concepts illustrating this configuration are shown in the two center drawings. The change in HO tank length (152' to 184') with change in booster configuration from the Reusable F-1 Flyback to Twin Pressure Fed for the same orbiter size is also shown.

Other concepts studied to develop data on smaller expendable systems are illustrated in the two drawings on the left (the Titan III L Glider and the Ballistic/Titan III M). The glider concept has no integral main propulsion system; orbital insertion is obtained through use of expendable booster and insertion stages. On the Titan III L the glider cargo bay would be 12' diameter by 40' long compared to 15' diameter by 60' long for the configurations shown to the right of the glider. The Ballistic/III M is a manned spacecraft of the "big" Gemini concept having limited capability compared to the other concepts illustrated. The Ballistic/T III M was studied to develop its characteristics for comparison with the larger systems.

Four space shuttle system configurations characterized by the two center illustrations (Twin Pressure Fed and Reusable F-1 Flyback) are under active study today. The following illustrations provide more detail on the orbiter and the four system configurations:

(1) Reusable F-1 Flyback Booster (series burn)
(2) Pressure Fed Recoverable Booster (series burn)
(3) Twin Pressure Fed Booster (parallel burn)
(4) Twin Solid Rocket Motors (parallel burn).

REPRESENTATIVE ALTERNATE TRANSPORTATION SYSTEMS

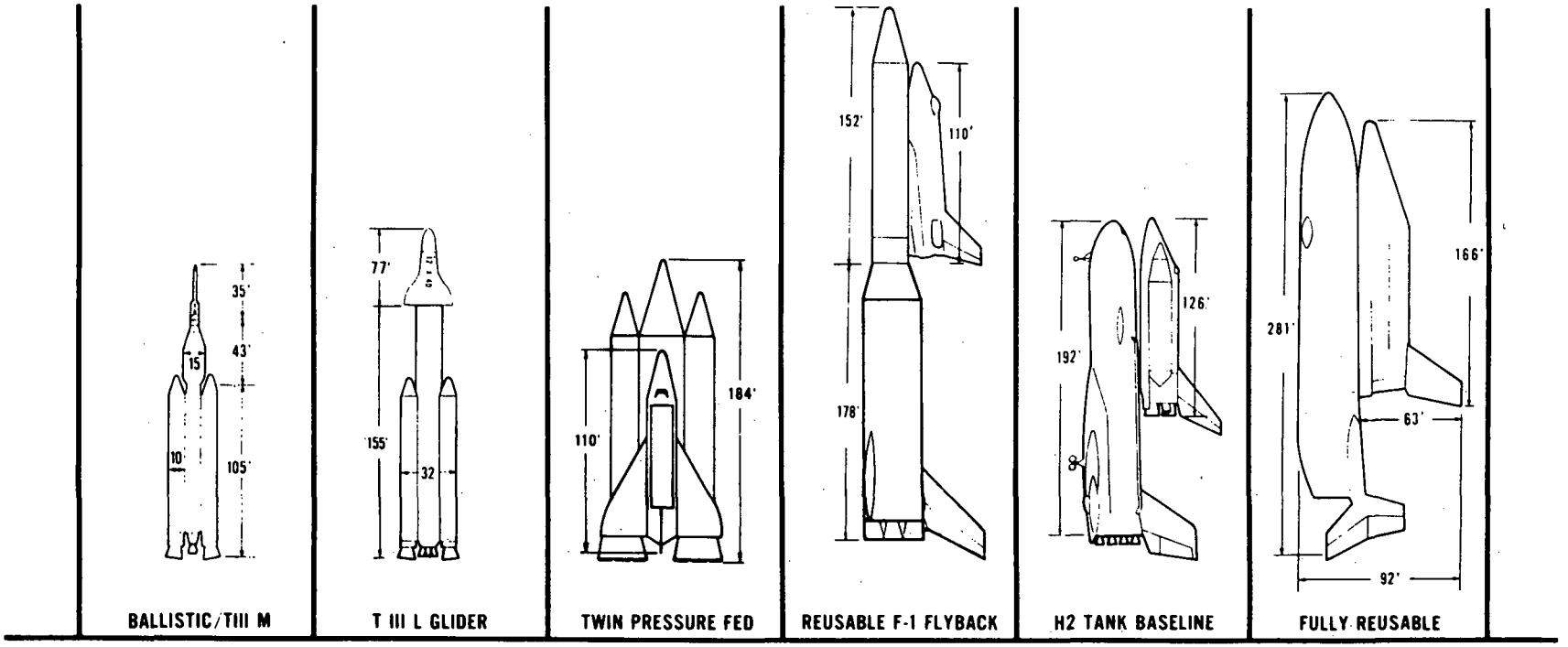

Figure 5

FIGURE 6

Reduction in Space Shuttle orbiter length, body surface area, dry weight, and rocket engine thrust level with change in system configuration from fully reusable to external liquid hydrogen (LH_2) tanks to external liquid oxygen/liquid hydrogen tank (LO_2/LH_2) is shown in this illustration. The advantages of the LO_2/LH_2 configuration compared to the other concepts are summarized in the elliptical box in the left center. It appears at this time that the orbiter configuration is settling on the LO_2/LH_2 concept.

ORBITER COMPARISON

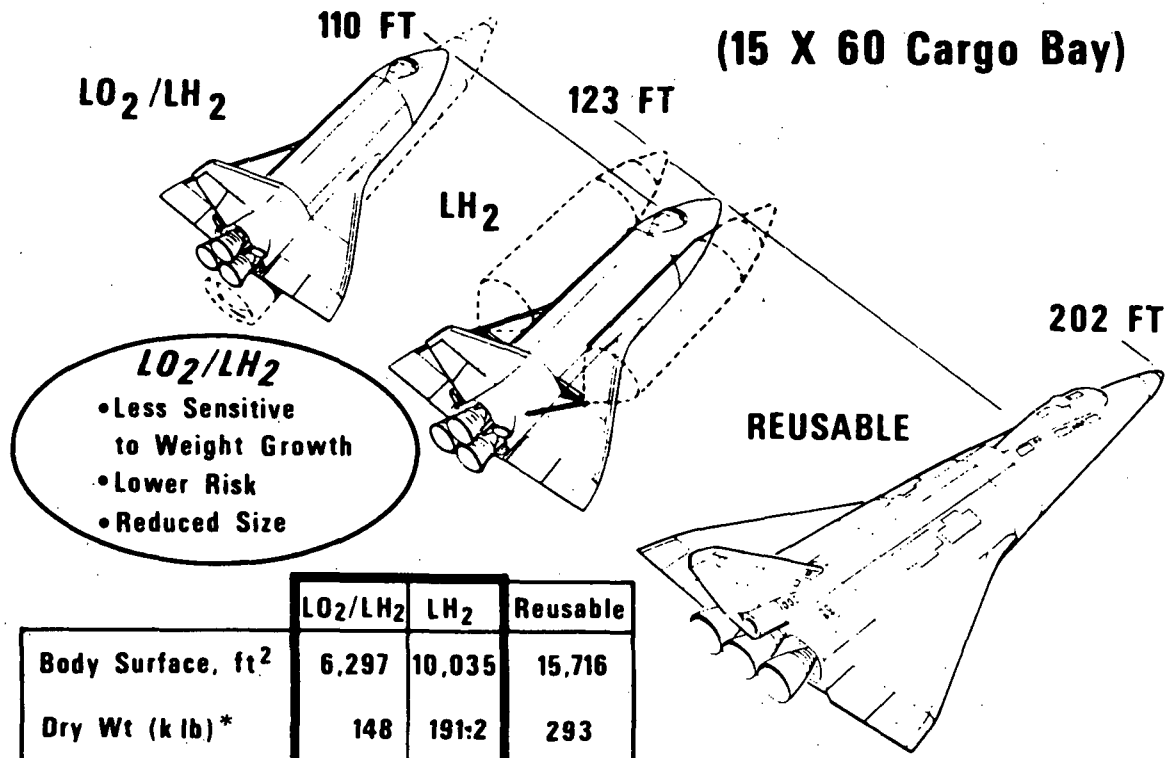

	LO_2/LH_2	LH_2	Reusable
Body Surface, ft^2	6,297	10,035	15,716
Dry Wt (k lb)*	148	191.2	293
3 Hi-Pc-F_{vac} Eng (k lb)	420	447.5	551

*Less Tanks & Payload

Figure 6

SPACE SHUTTLE ORBITER

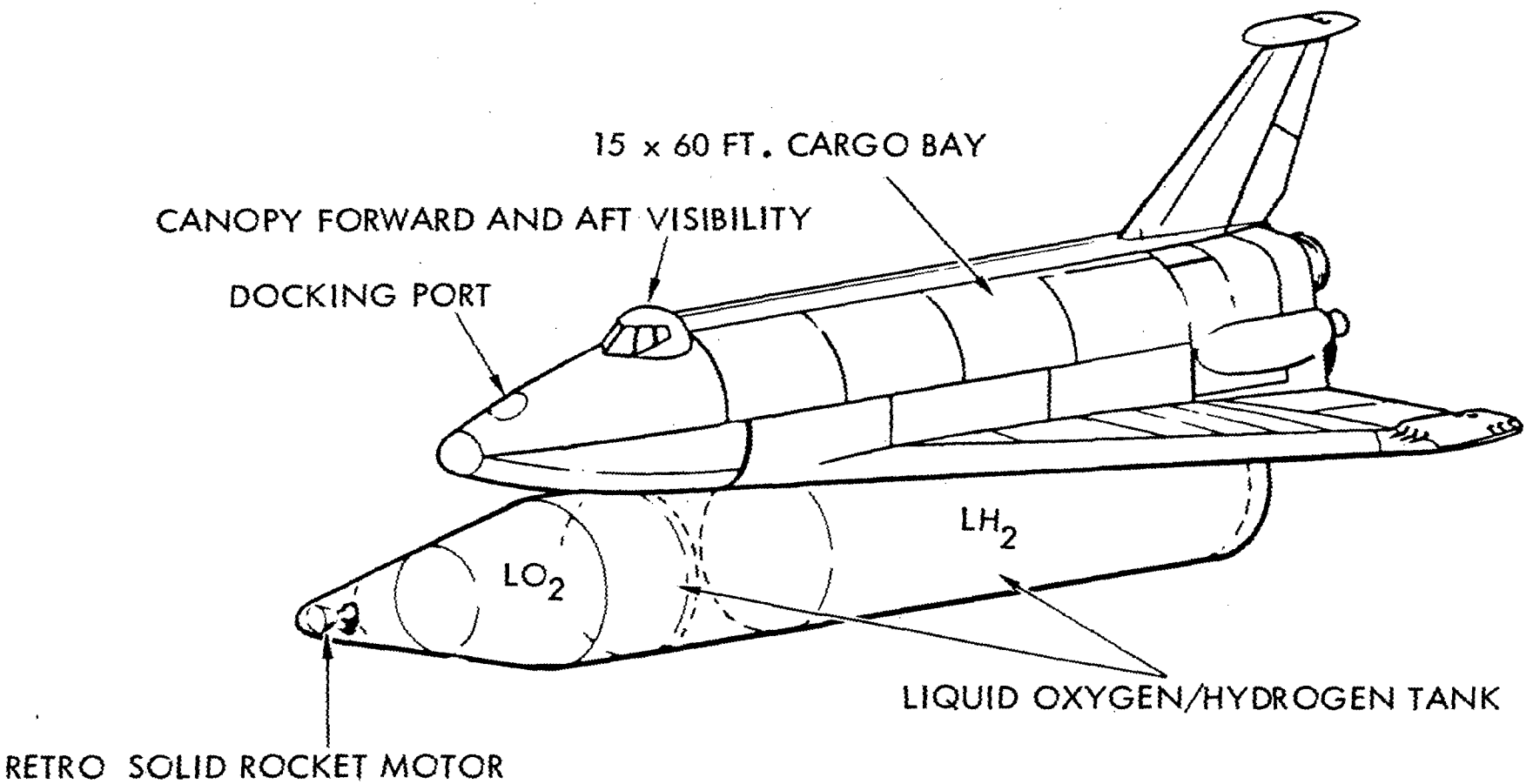

Figure 7

FIGURE 8

Highlights of system configuration of the Reusable F-1 Flyback Booster based on the Saturn V S-IC stage are shown. The crew cabin, canard, and ballast tanks are forward and a "stretched" intertank section accommodates wing attachment and air breathing jet engines for flyback.

SHUTTLE WITH REUSABLE F-1 FLYBACK BOOSTER

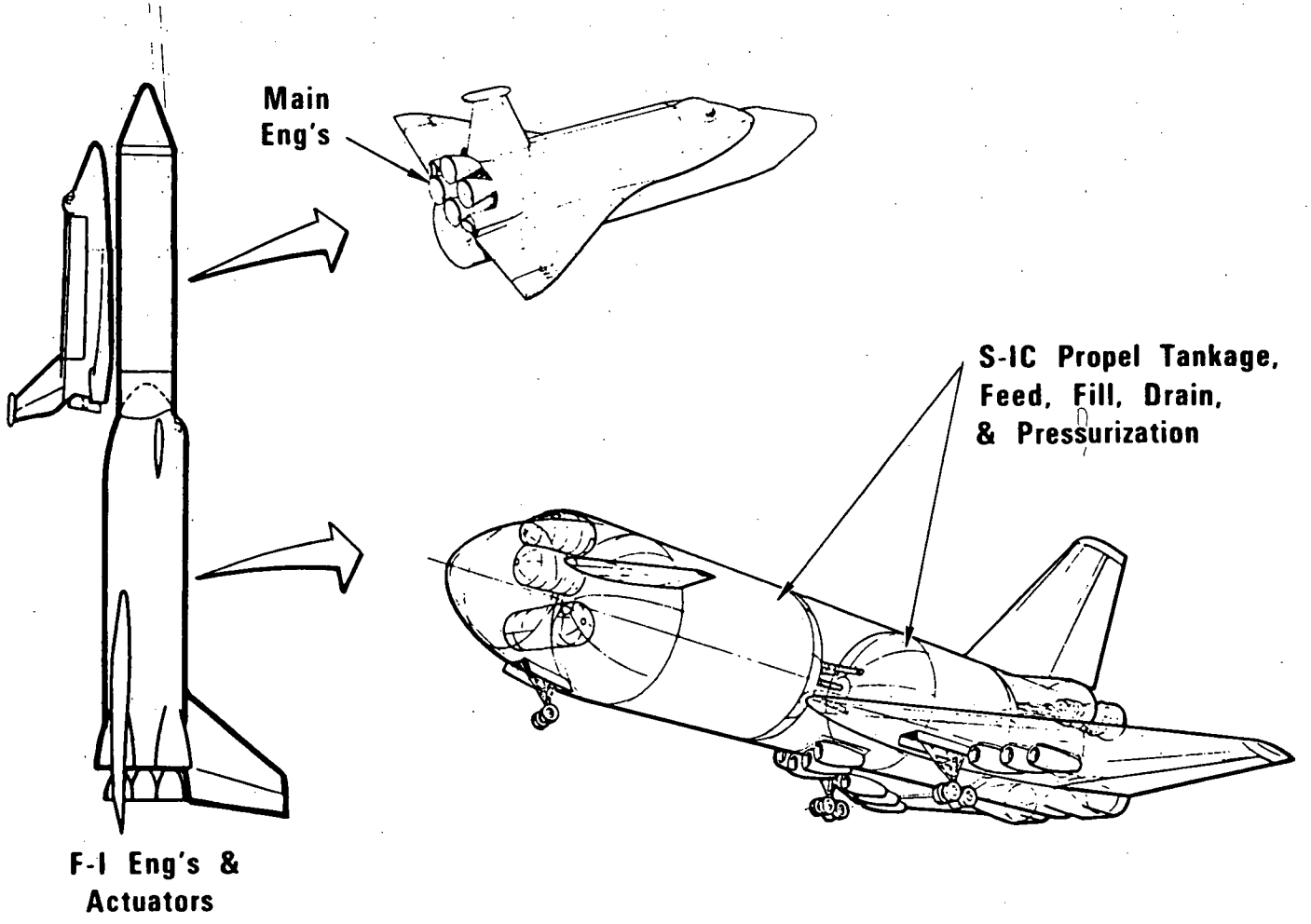

Figure 8

FIGURE 9

A summary mission profile of the F-1 Flyback Space Shuttle indicates LO_2/LH_2 tank disposal following orbital insertion. Deorbit of the tank is planned for all missions for the middle of the Indian Ocean.

SPACE SHUTTLE MISSION PROFILE

(F-1 FLYBACK)

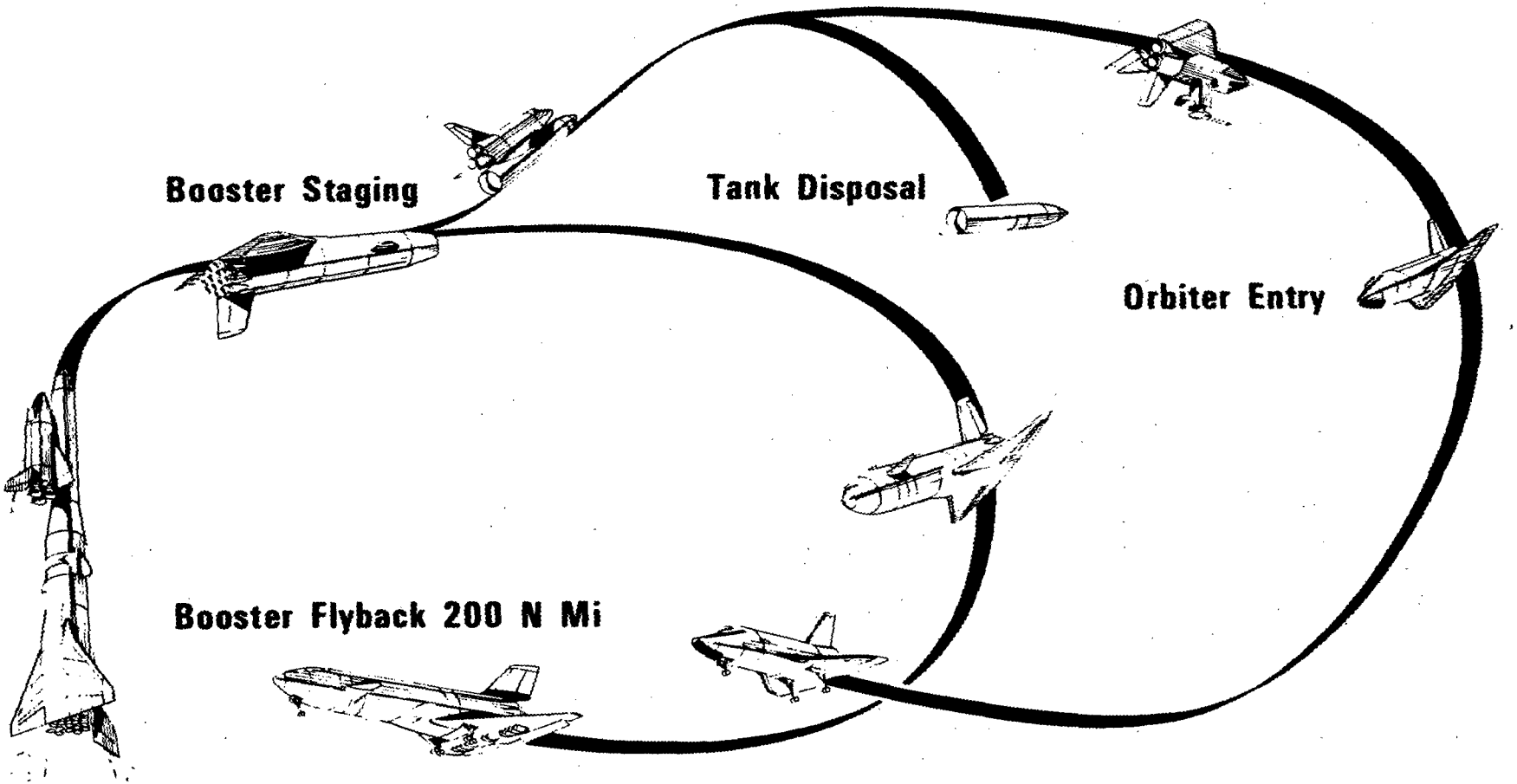

Figure 9

FIGURE 10

Highlights of systems configuration of the Pressure Fed Recoverable Booster based on use of Inconel 718 for corrosion resistance is shown. Aluminium is also being considered as the main structural material. This concept, like the Reusable F-1 Flyback, is burned in a series manner, i.e., only the booster engines are started at liftoff and burned to shutdown and staging when the orbiter engines are started.

SHUTTLE WITH PRESSURE FED RECOVERABLE BOOSTER

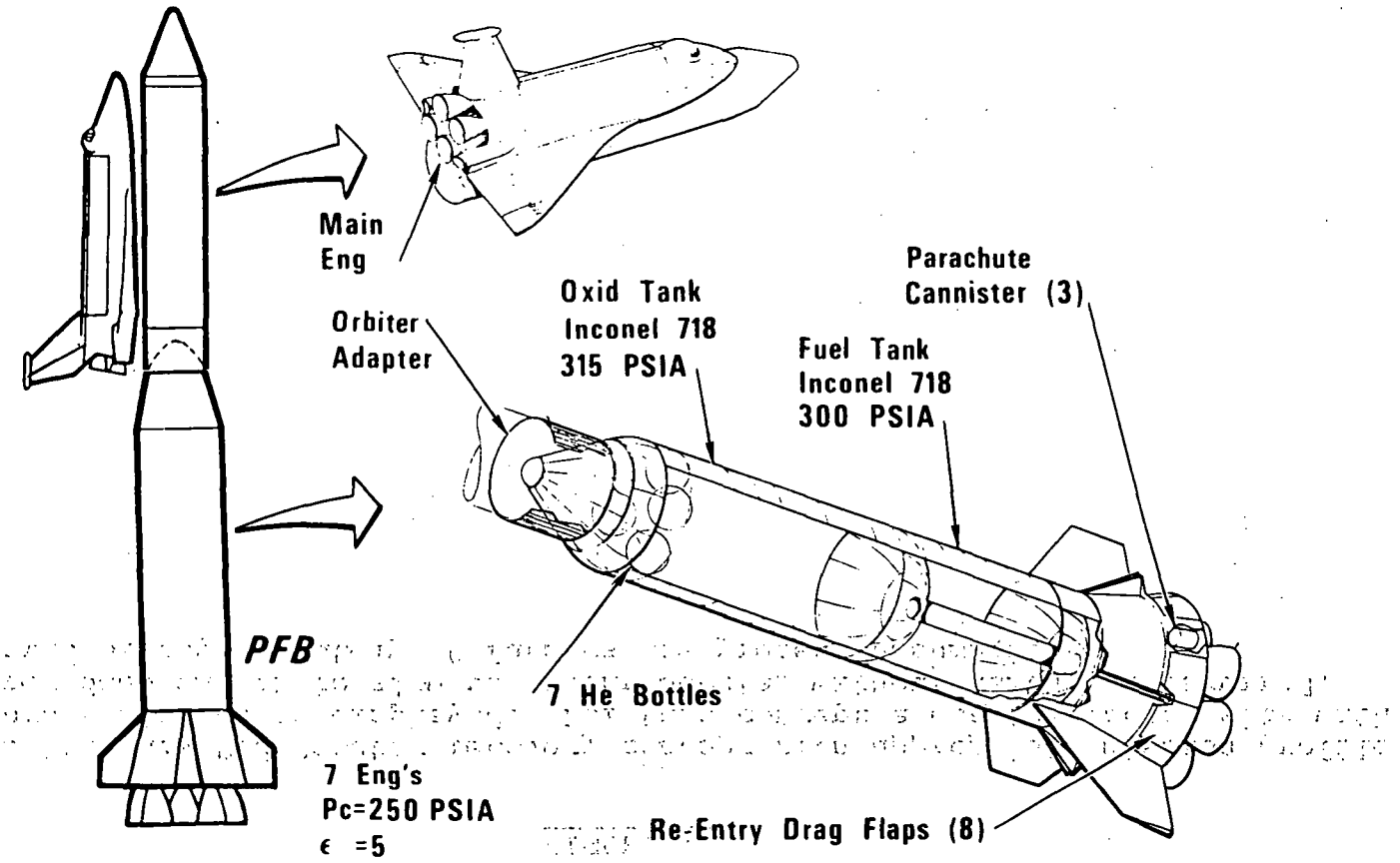

Figure 10

FIGURE 11

The Pressure Fed Booster recovery concept with appropriate mission profile characteristics is displayed. For this concept a coastal launch site with water deep enough to slow the spent booster without damage is required. Depths of approximately 20 fathoms are present assumptions.

PRESSURE FED BOOSTER RECOVERY CONCEPT

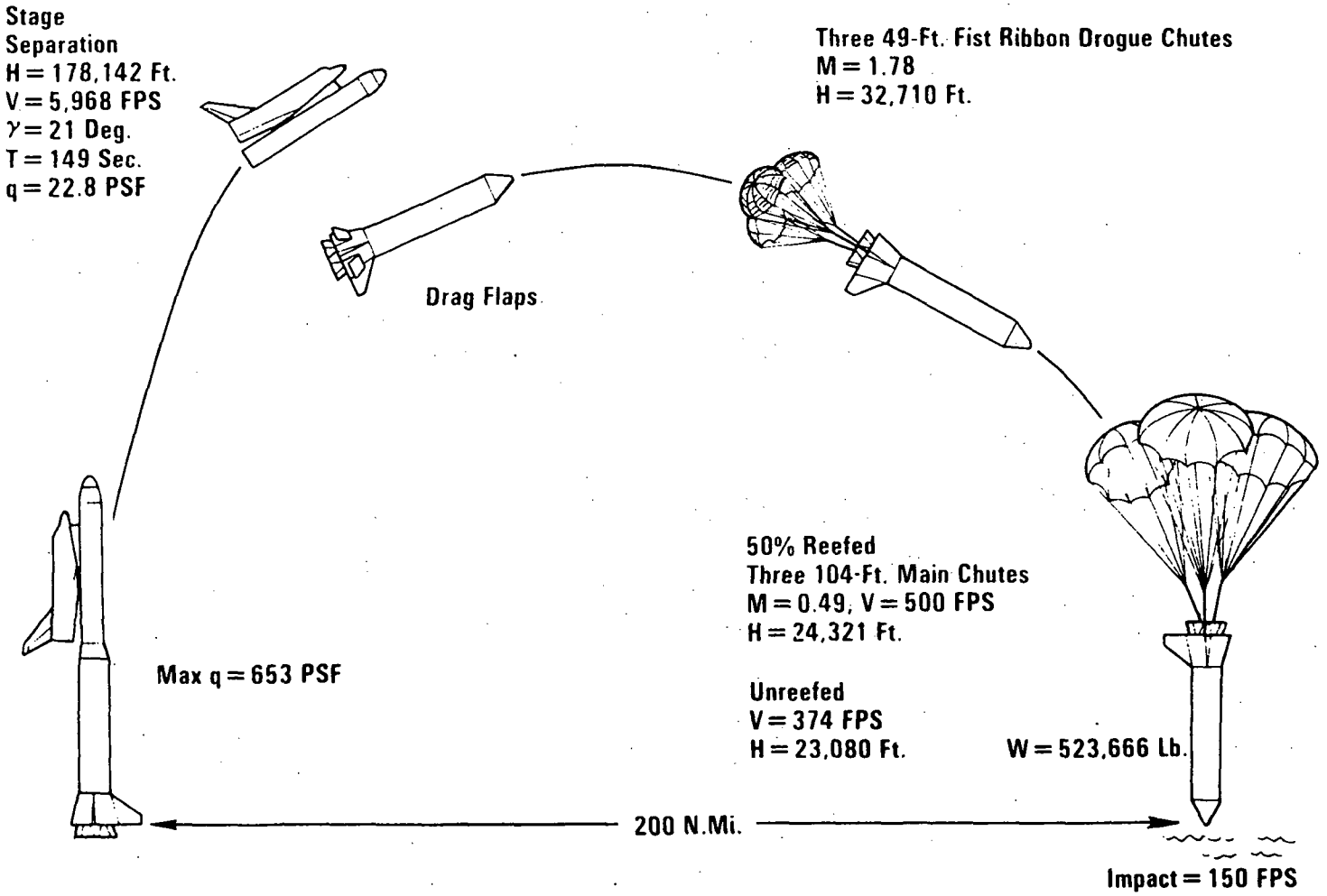

Figure 11

FIGURE 12

The third configuration presently being studied, Shuttle with Twin Pressure Fed Booster, is shown in an artist's concept. The orbiter and booster engines are started for liftoff for a parallel burn to approximately 6000 feet per second staging velocity. Each twin booster element would be recovered in a manner similar to that of the single pressure-fed booster stage.

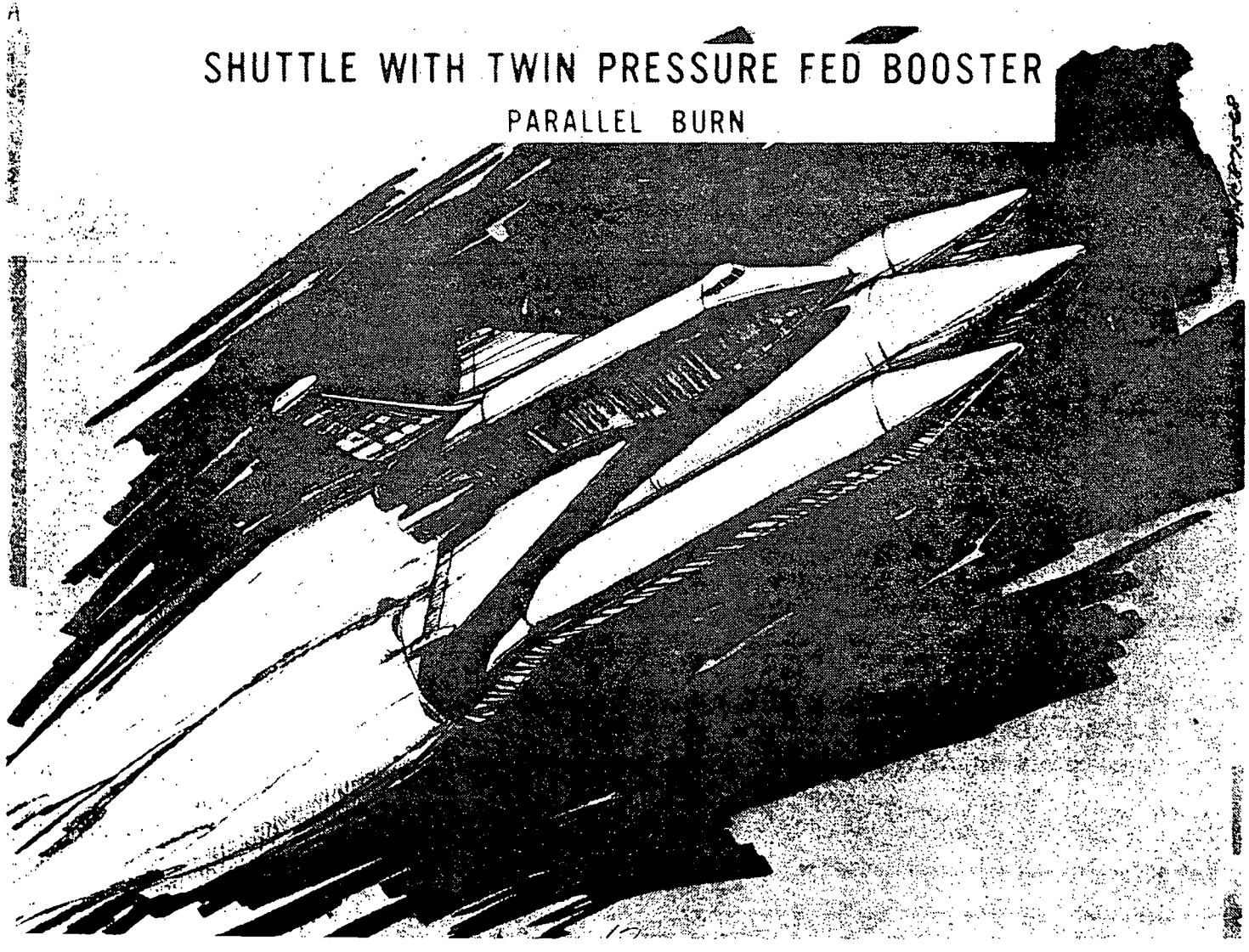

Figure 12

FIGURE 13

The fourth concept is similar to the twin pressure fed concept except the twin booster stages are solid rocket motors (SRM's). In this illustration twin 156 in SRM's are shown.

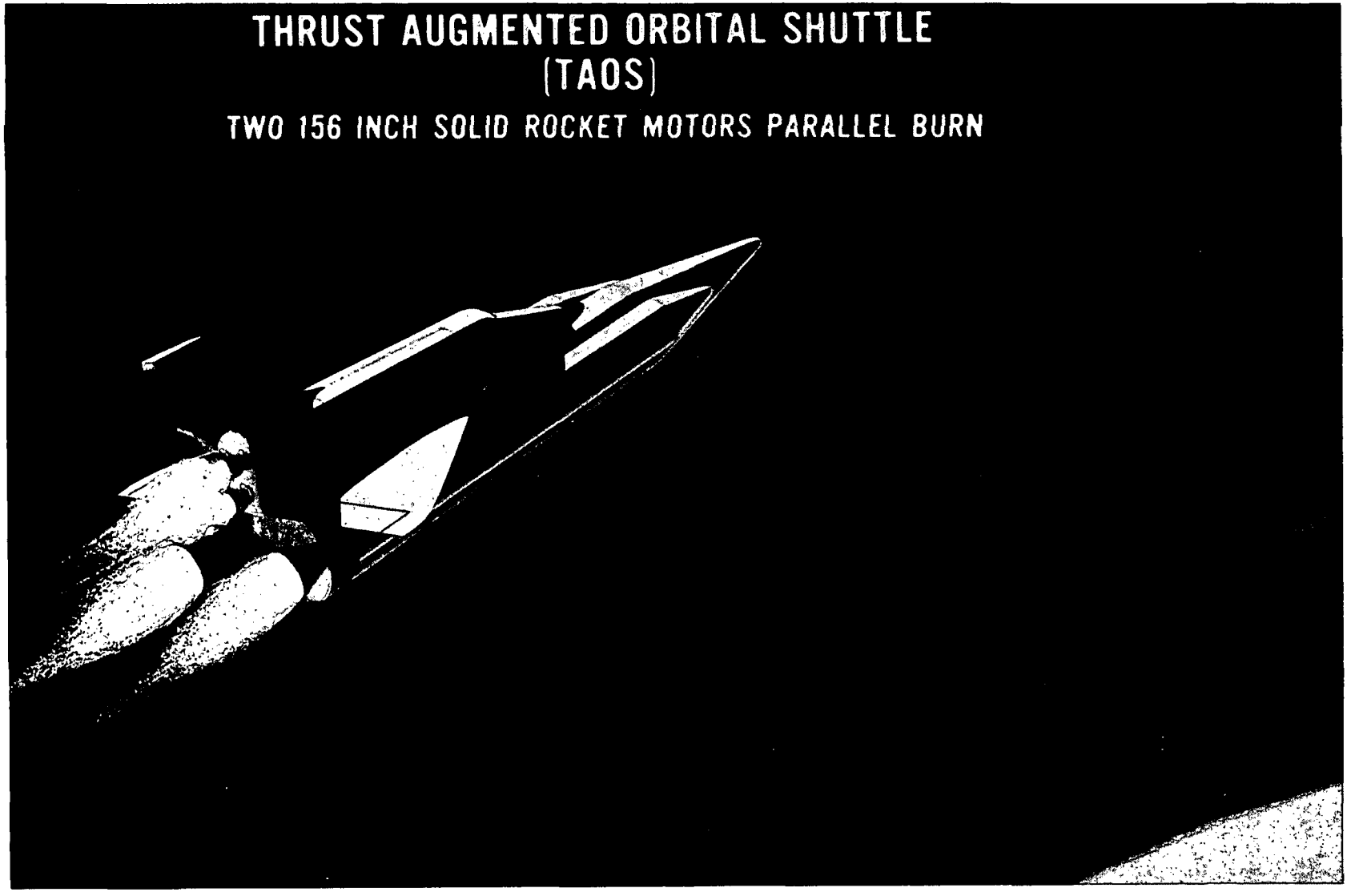
THRUST AUGMENTED ORBITAL SHUTTLE
(TAOS)
TWO 156 INCH SOLID ROCKET MOTORS PARALLEL BURN

Figure 13

FIGURE 14

The mission profile of the twin solid rocket motor (SRM) shuttle indicates that recovery and reuse of the spent SRM's is not contemplated. Water or land impact of the SRM's in areas where injury or property damage is highly unlikely would be acceptable. LO_2/LH_2 tank disposal in the Indian Ocean is the same as in other concepts.

THRUST AUGMENTED ORBITAL SHUTTLE (TAOS) MISSION PROFILE

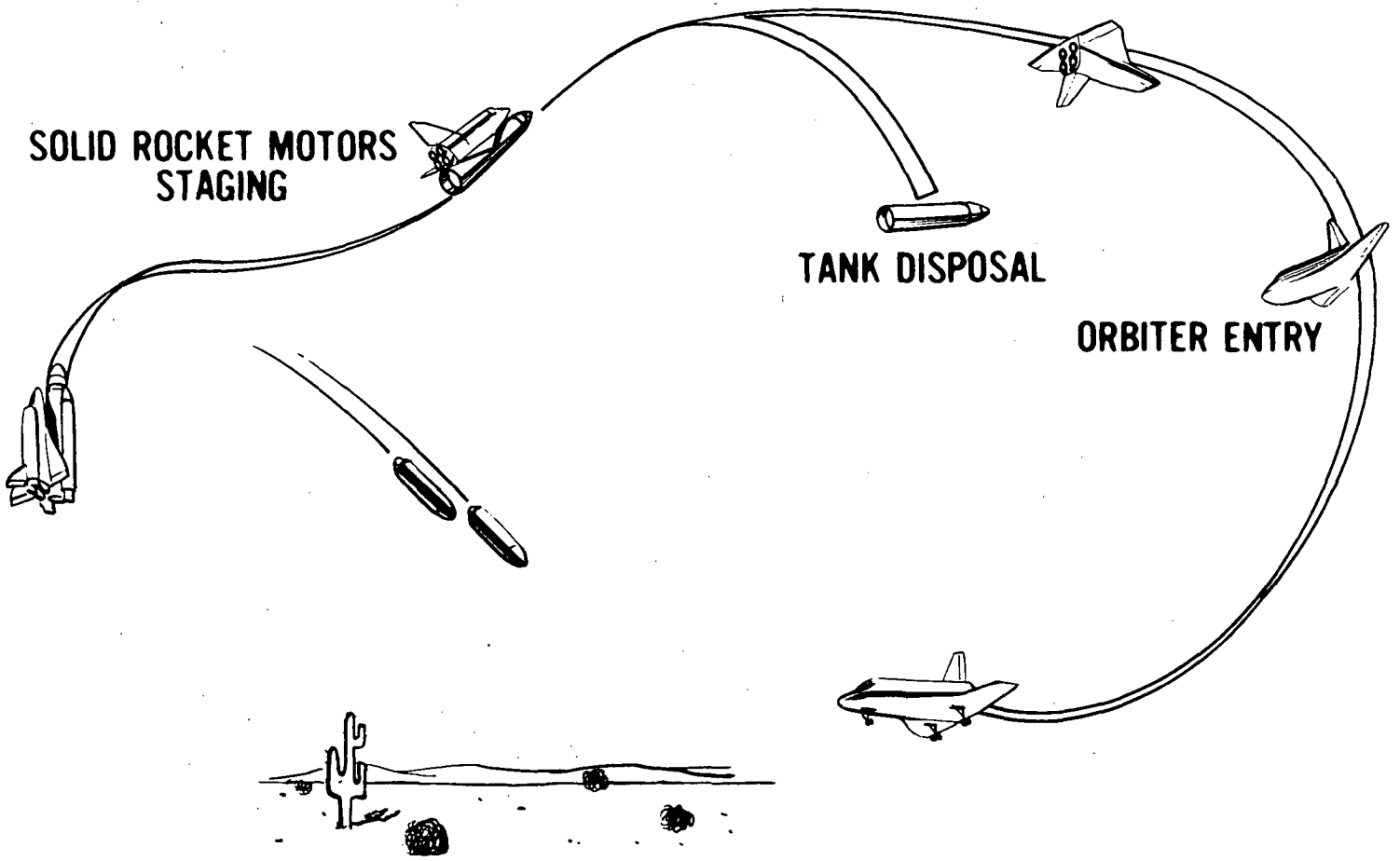

Figure 14

FIGURE 15

Comparison of the current design study concepts with the fully reusable and the H_2 tank baseline designs is made for equal payload into a 100 X 100 nautical mile polar orbit.

SPACE SHUTTLE COMPARISON

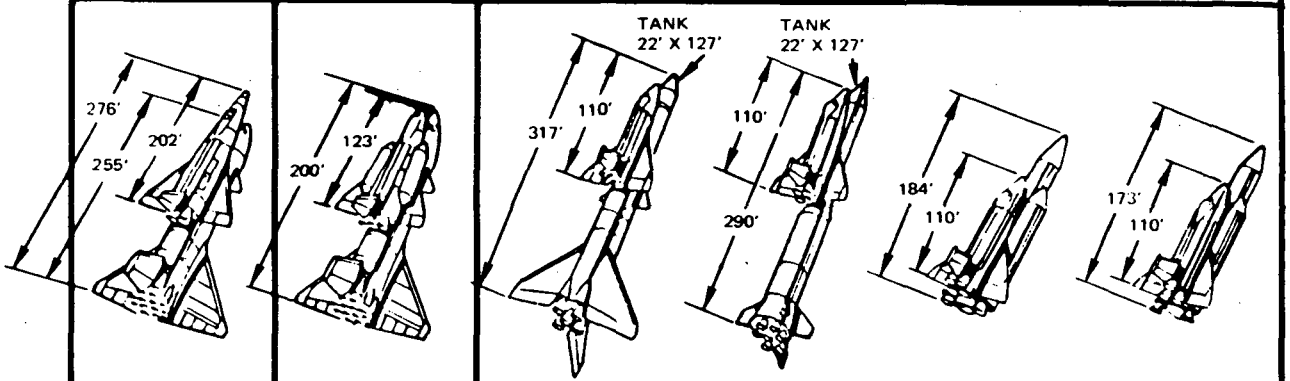

	FULLY REUSABLE	H_2 TANK BASELINE	CURRENT DESIGN STUDIES			
BOOSTER	REUSABLE	REUSABLE	F-1 REUSABLE	PF RECOVERABLE	TWIN PRESS.FED	156 IN. DIA SRM (AUGM)
BURN MODE	SERIES	SERIES	SERIES	SERIES	PARALLEL	PARALLEL
STAGING VELOCITY (FPS)	10,832	6838	6000	5968	6,216	4,369
SYSTEM GLOW (KLB)	5,047	3593	5090	5253	5,830	4,560
SYSTEM DRY WT (KLB)	850	604	790	691	686	607
ORBITER/BOOSTER DRY (KLB)	223/627	191/393	148/584	148/487	130/482	127/372
TANK DRY WT (KLB)	–	20	58	56	74	108
POLAR PAYLOAD (KLB)	40.0	40.0	40.8	40.0	40.0	40.0

Figure 15

FIGURE 16

A comparison of Space Shuttle estimated development costs in billions of 1970 dollars with the estimated cost per flight in millions of 1970 dollars is shown, except for the Ballistic/T III M, for the concepts illustrated in Figure 5 and the four current design studies.

SPACE SHUTTLE COST COMPARISON

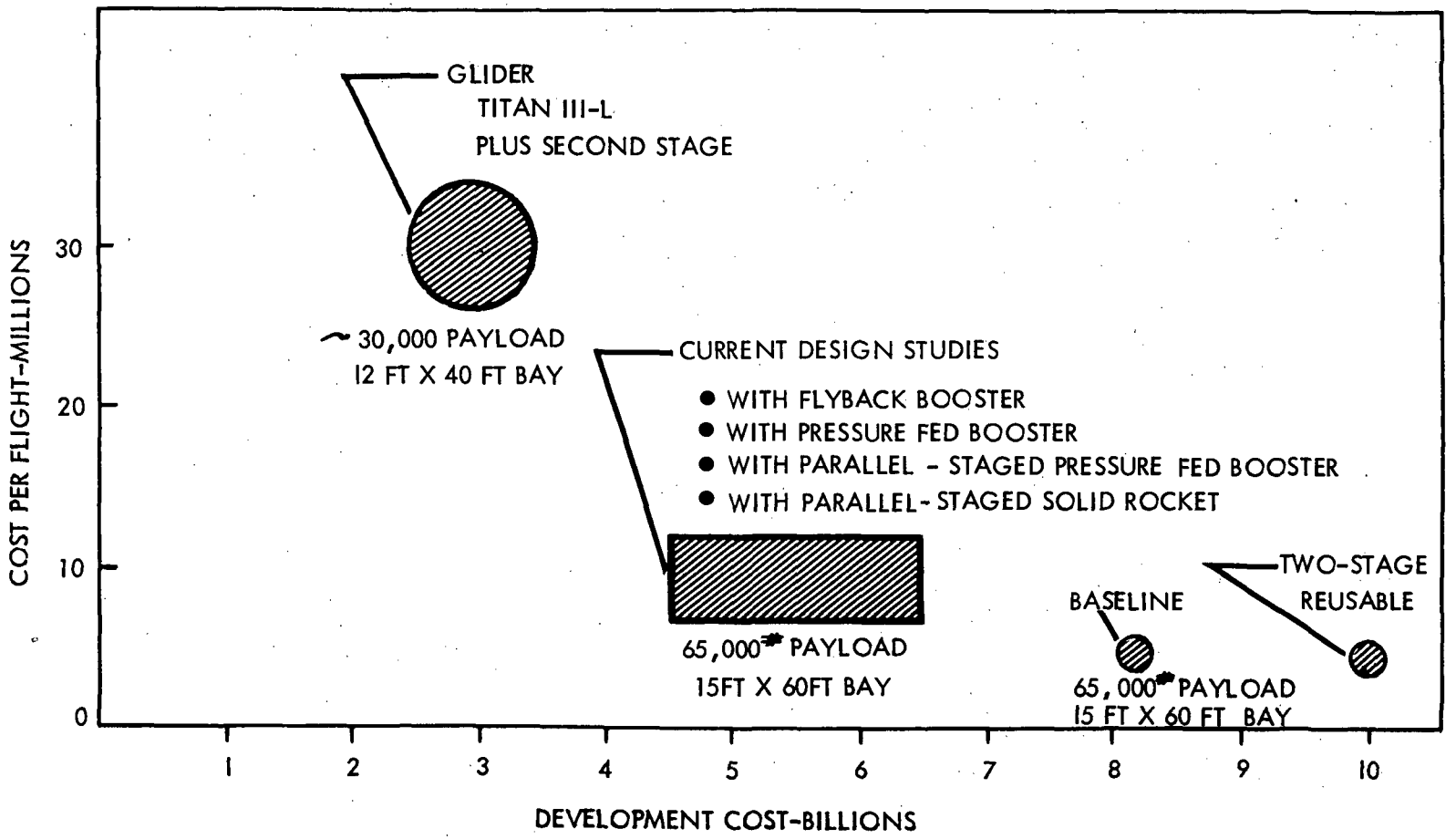

Figure 16

FIGURE 17

The Space Shuttle Program study schedule depicts the activities leading to the data reviews being held in Washington, D.C. today and tomorrow. Based on decisions made in late December 1971 and January 1972, the RFP for systems preliminary design and development (Phases C/D) could be released as early as March 1, 1972, with design/development to start as early as July 1, 1972.

SPACE SHUTTLE PROGRAM
(1970–1972)

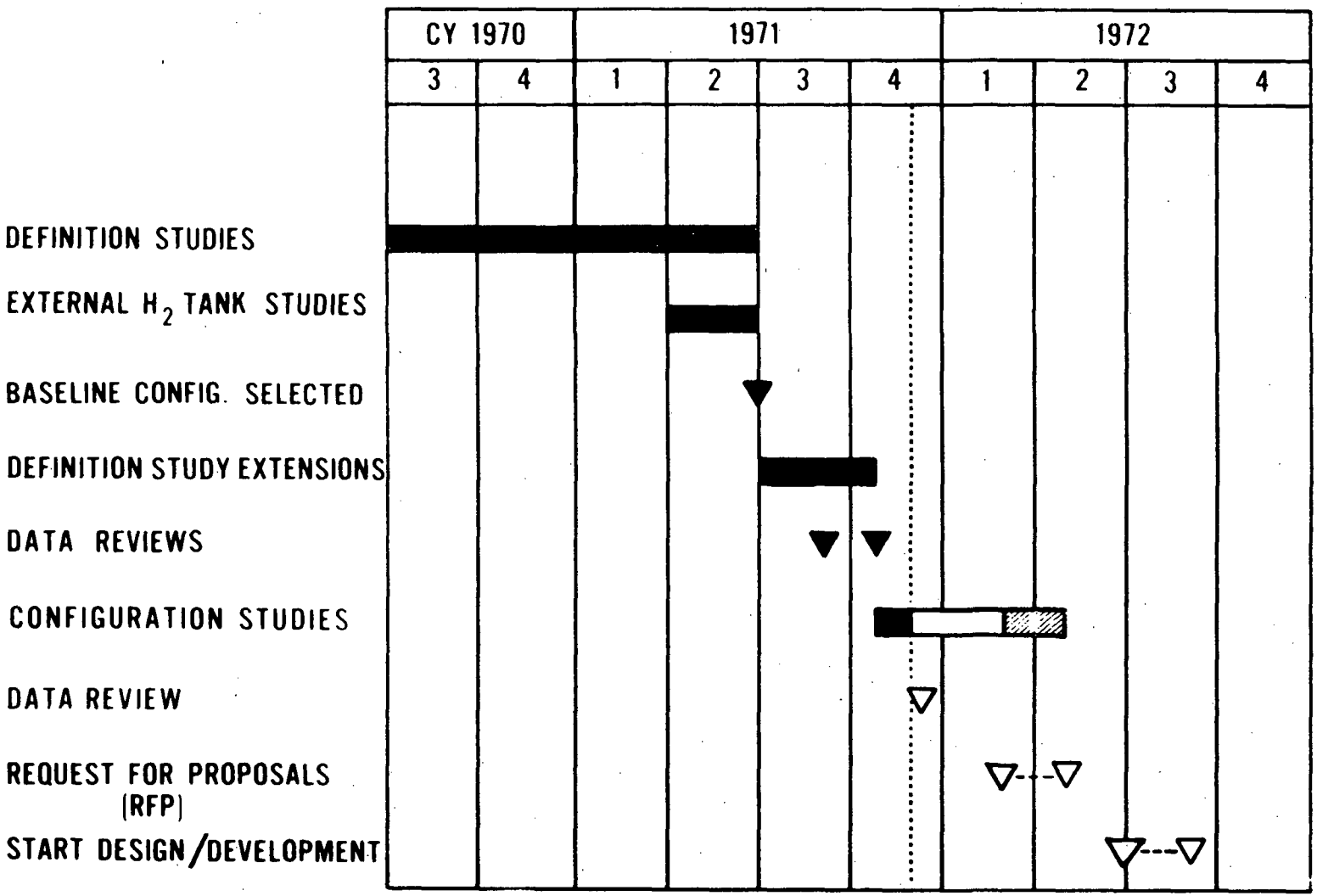

Figure 17

FIGURE 18

The major Space Shuttle development milestones indicate that start of design and development in 1972 will support beginning of the horizontal flight test program in 1976 and the first manned orbital flight in 1978.

SPACE SHUTTLE DEVELOPMENT SCHEDULE

MILESTONES	CY 72	73	74	75	76	77	78	79	80
CONFIGURATION STUDIES COMPLETE	△								
PLANNED START VEHICLE DESIGN & DEVELOPMENT	△								
START HORIZONTAL TEST PROGRAM					△				
FIRST MANNED ORBITAL FLIGHT							△		

Figure 18

FIGURE 19

As a summation of present status, the benefits of a reusable space transportation system which the current design studies encompass are listed.

BENEFITS OF REUSABLE SPACE TRANSPORTATION

- DIRECT COST REDUCTIONS
- EASY ACCESS TO SPACE
- SCIENTIFIC PROGRESS
- NATIONAL SECURITY
- TECHNOLOGICAL PROGRESS
- INDUSTRY CAPABILITY
- MERGER OF MANNED AND UNMANNED SPACE FLIGHT
- CONTINUATION OF MANNED SPACE FLIGHT
- FOREIGN SALES -- IMPACT ON BALANCE OF OF PAYMENTS
- RAPID INTRODUCTION OF NEW SPACE USES
- STIMULATION OF SPACE USES NOW UNFORESEEN
- CAPABILITY TO RESPOND TO INTERNATIONAL COMPETITION
- POTENTIAL FOR INTERNATIONAL COOPERATION

Figure 19

Page intentionally left blank

SHUTTLE TECHNOLOGY – INTRODUCTORY REMARKS

By A. O. Tischler

Director of Shuttle Technologies Office, OART
NASA Headquarters, Washington, D.C.

This conference is the third large conference covering the general subject of aerothermodynamics for the reusable earth-to-orbit transportation system, commonly called the "shuttle," and the first to be devoted exclusively to the aerothermodynamic problems and issues. The first of these conferences, held at the Lewis Research Center in the summer of 1970, told everyone what the approach to shuttle technology work would be. The second, held at the Langley Research Center in the late winter of 1971, made the overall plan more substantive and provided some results. This conference, hopefully, will disclose much data and correlations on the shuttle-related aerothermodynamic technology.

Aerodynamics has played an important role in shaping the shuttle concept. Even before the formation of NASA in 1958, serious thought was being given to the idea of an aerodynamically controllable entry and return space vehicle. It was only a matter of technological state of the art that led to the use of blunt conical semiballistic reentry bodies for Mercury, Gemini, and Apollo. The work that sprang out of these early deliberations, which led NASA to the lifting-body programs, and more importantly, led the U.S. Air Force to sponsor the DynaSoar project, on which some $400M were spent, along with continuing technology work by the Flight Dynamics Laboratory at the Wright Patterson Air Force Base, gave a considerable background for flyable reentry vehicles. This work, the improved high-performance propulsion systems being developed by both NASA and Air Force, and the improvements in refractory materials resulting from a broad frontal research

attack, laid alongside the high present cost of injecting payloads into space, paved the way for accepting the idea that the time to start developing a reusable space vehicle was at hand.

The shuttle vehicle has, however, encountered severe constraints in its fiscal diet for the early development years. Consequently, a series of vehicle design and configuration studies have been made to determine a vehicle design approach which, for a prescribed mission model, will have least cost in terms of the present value of money. The systems that are the front runners at this moment have been described by Edward Andrews (paper no. 1.)

It is probably unnecessary to remind anyone here that the changing configurational picture has kept the aerodynamics and aerothermodynamics personnel busy. The importance of understanding the aerodynamic and aerothermal effects on the flight mechanics and structural integrity of this three-piece vehicle during a flight spectrum which ranges from Mach 0 to Mach 25 and back to Mach 0 under continually varying pressure and density cannot be minimized. In spite of the obvious difficulties one advantage is the fact that the shuttle does not have to be a superior airplane. As long as it can be adequately controlled through the flight regime without scorching its skin it would appear to meet the mandatory requirements.

Back in the summer of 1969 OMSF and OART began a precedent-setting joint effort to examine and prepare a technological base to support the shuttle. As most of you know this program has pulled together the talents of the research and space flight centers of NASA, has vastly improved communications at the problem-solving level, and tied in not only the contractors, but also the European technologists who are interested in participating in the post-Apollo endeavors.

The management approach to this program is to solicit and to use the advice of seven Working Groups. These Working Groups, of which the Group on Aerothermodynamics chaired by Arthur Henderson of Langley Research Center is one, comprise representatives of all NASA Centers engaged in the work activity. They recommend the program content; they are also actively engaged in monitoring it. This conference represents one of the Working Group information dissemination functions. I would like here to express my appreciation to Dr. Hans Mark and his entire team for organizing and hosting this symposium.

Funding for the technology effort, which will total $130M by the end of FY 1972, is derived from both OART and OMSF fund sources. The Aerothermodynamics total effort during this period will be $16M, a sum which does not include the salary expenses of NASA personnel engaged in the work, nor any contractors' efforts paid under vehicle configuration studies, nor any of the independent research and development funds which various companies have been persuaded to invest in the shuttle prospect. 925 NASA personnel are directly involved in this technology work; the aerothermodynamics effort accounts for nearly one-fourth of these personnel.

Some of the results of this work have been noteworthy. New test methods for studying heat-transfer rates and shock flow and impingement have been invented out of necessity to handle the large volume of work. The program has now used about 20 000 wind-tunnel hours. This technical progress will be covered here in much detail in the next 2 days.

With the coming fiscal year, NASA anticipates moving the shuttle program into the design and development phase. This change will require a transition of many of our technology investigations into development support. Because of the

intrinsic need to support closely the shuttle configurational design selections, it seems likely that this aerodynamic work effort will continue at a high level. In fact, it is expected that test facilities located in Europe will be used to relieve the load of work imposed on the U.S. facilities if satisfactory working relationships can be worked out and it is believed that they will be.

I look forward, along with you, to the development and operation of this system so vital to a healthy and aggressive space program. I expect that this conference will be seen in retrospect as a significant contribution to the development of economical access to the space arena.

FLOW FIELDS SESSION

INTRODUCTION

by

Joseph G. Marvin
NASA Ames Research Center

3

Vehicle aerodynamics, heating, thermal protection system response, chemical effects on surface materials, and chemical effects within the shock layer are a few of the many variables that depend on the flow field around the Space Shuttle vehicle during its flight through the atmosphere. A need for flow field calculations arises mainly from the inability to completely simulate the flight environment in ground-based facilities. For example, tests performed to simulate the high enthalpies associated with entry often have the incorrect flow chemistry because of model scale effects. Therefore, the designer must extrapolate test data by using the best information about the real flow field. Exact three-dimensional flow field calculations are now at the threshold of providing the necessary rationale upon which to base this important extrapolation.

At the last Space Shuttle Technology Conference held at Langley Field in March 1971, there was only one paper devoted to exact flow field calculations. In this session there are seven papers, five of which contain exact methods for computing three-dimensional flow fields. The remaining two papers treat in an approximate way chemical nonequilibrium effects and streamline calculations used as input for heating estimates. The emphasis on flow fields at this conference developed mainly from recent technology advances made in exact calculation methods and in computer storage and speed that is necessary in the practical application of these methods. The papers were selected in order that the progress made on shuttle flow field calculations can be judged and so that future needs can be determined.

Page intentionally left blank

DETERMINATION OF SPACE SHUTTLE FLOW FIELD BY THE THREE-DIMENSIONAL METHOD OF CHARACTERISTICS

By Chong-Wei Chu and S.A. Powers

Northrop Corporation, Hawthorne, California

INTRODUCTION

Northrop's approach to the three-dimensional method of characteristics (3DMoC) has evolved over the last ten years (Refs. 1 to 7). Its fundamentals and initial formulation are discussed in References 1 to 3. Recently, the first author (CWC) has extensively revised and improved the numerical method and the computer program. The result is a new 3DMoC program that is accurate, efficient, and versatile, as verified by the excellent agreement between computed results and experimental data for a variety of bodies. This paper discusses the application of this method to space shuttle flow fields including wing-body interactions.

Basically, the Northrop approach follows streamlines from one data surface to the next and uses the redundant method to solve the compatibility relations (Ref. 3). All data surfaces are normal to a selected axis, usually the longitudinal body axis. The data rings on each data surface and the data points along each data ring are automatically respaced whenever their distribution becomes appreciably uneven. Provisions are made for automatic addition of data rings and for changing the number of data points per data ring at prescribed intervals. In addition, grid size variation can be related to the body geometry and flow-property gradients; for instance, smaller grid sizes can be specified near the wing tip and the wing-body junction. The step size (distance between two adjacent data surfaces) is automatically regulated by applying the Courant-Friedrichs-Lewy stability condition. The program also uses newly developed shock-point and body-point procedures, which eliminate most of the troublesome iterations. Very importantly, a shock stabilization technique has been developed to control shock point drift and thus maintain numerical stability even under adverse conditions. Realistic configurations can be easily treated by this program which uses a body description technique based on aircraft lofting practice.

The new program has been applied successfully to the calculation of flow fields over a variety of bodies including slab delta wings and shuttle orbiters. Flow fields over fuselage shapes for Mach numbers as low as 1.5 have been calculated. Some typical results are presented here.

CENTERLINE PRESSURE DISTRIBUTION ON SLAB DELTA WINGS
(Figure 1)

We have selected the computed pressure distribution on two slab delta wings as examples of the program's capabilities. Figure 1 shows the centerline pressure distribution on the windward side. At the left is a plot of local static pressure (non-dimensionalized by total pressure) against the distance along the windward surface centerline for a 70° slab delta wing at a free stream Mach number of 9.6 and at angles of attack of 0°, 4.5° and 15°. The computed pressure distributions are compared with experimental data of Bertram (Ref. 8). The comparison is excellent except for one point on each curve. At the right side of Figure 1 is a plot of the centerline pressure distribution on the windward side of an 80° sweep slab delta wing at 30° angle of attack, compared with experimental data of Whitehead (Ref. 9). Again, there is only slight difference between the computed pressure and the measured pressure. The curvature discontinuity at the junction of the spherical nose and the flat surface causes the wiggles which become more pronounced as the angle of attack increases. The computing time for 0 and 4.5° angle of attack cases was about 3 minutes on the CDC 6600 (including input and output), while for the 15° and 30° cases it was approximately 8 minutes.

CENTERLINE PRESSURE DISTRIBUTION ON SLAB DELTA WINGS

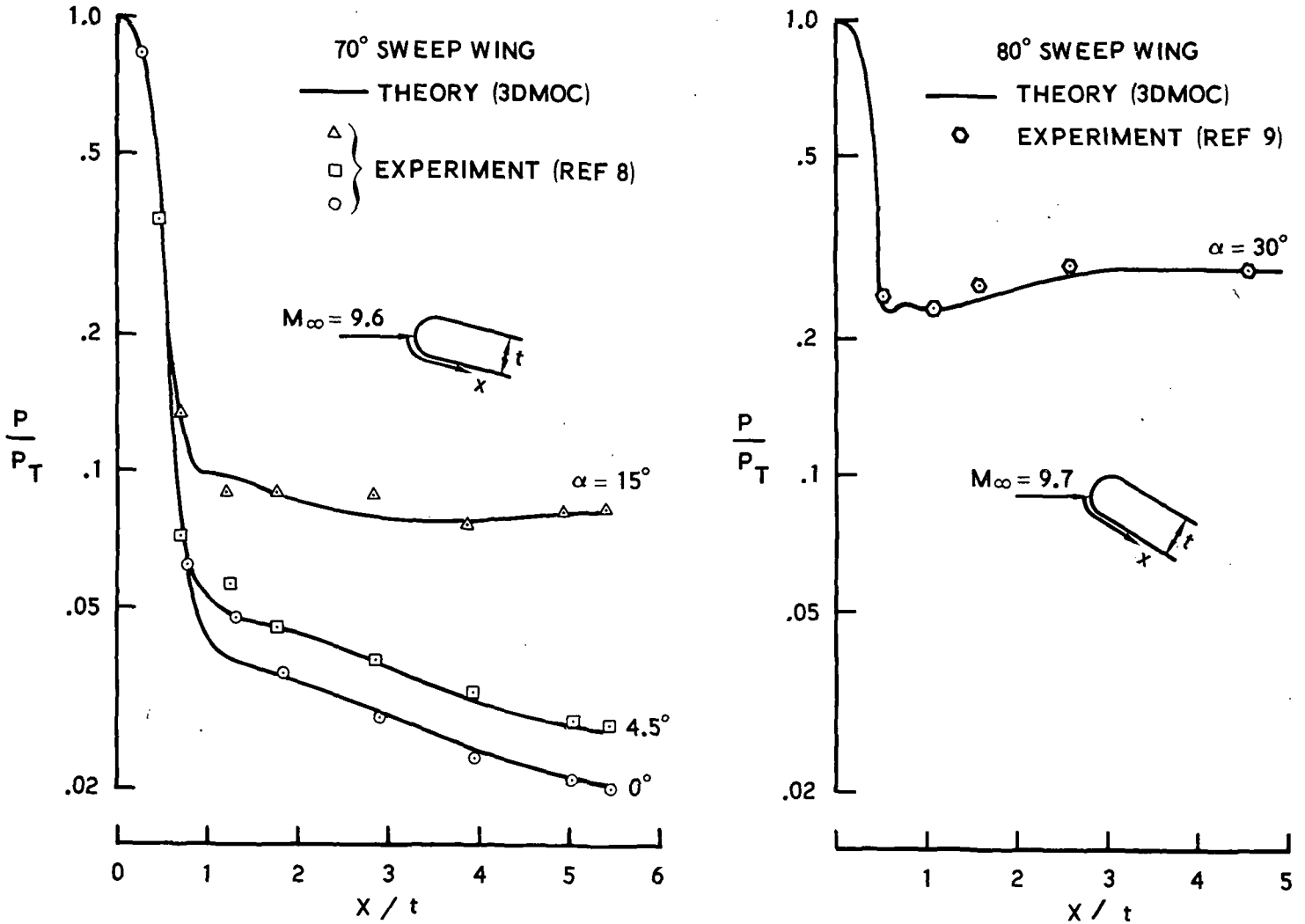

Figure 1

TRANSVERSE PRESSURE DISTRIBUTION ON SLAB DELTA WINGS
(Figure 2)

Typical transverse pressure distributions for the same two delta wings are shown in Figure 2. At the left is a plot of the local pressure (non-dimensionalized by the free stream pressure) at station L/t = 5 versus surface distance for the 70° sweep wing at 15° angle of attack. Positive S/t is the distance from the leading edge along the windward surface; negative S/t, along the leeward surface. Note that the maximum pressure occurs on the windward surface near the leading edge. The experimental data of Ref. 8 are again used for comparison. The agreement is excellent on the windward side. On the leeward side the agreement is surprisingly good except in the region near the leading edge. This indicates that the viscous effects play a secondary role in determining the surface pressure distribution even on the leeside at this angle of attack. At the right is a similar plot for the 80° sweep wing at 30° angle of attack, as compared with experimental data of Ref. 9. The agreement is again quite good except near the leading edge. It is possible that the discrepancy near the leading edge could be reduced by using a finer mesh size in the region of the leading edge.

TRANSVERSE PRESSURE DISTRIBUTION ON SLAB DELTA WINGS

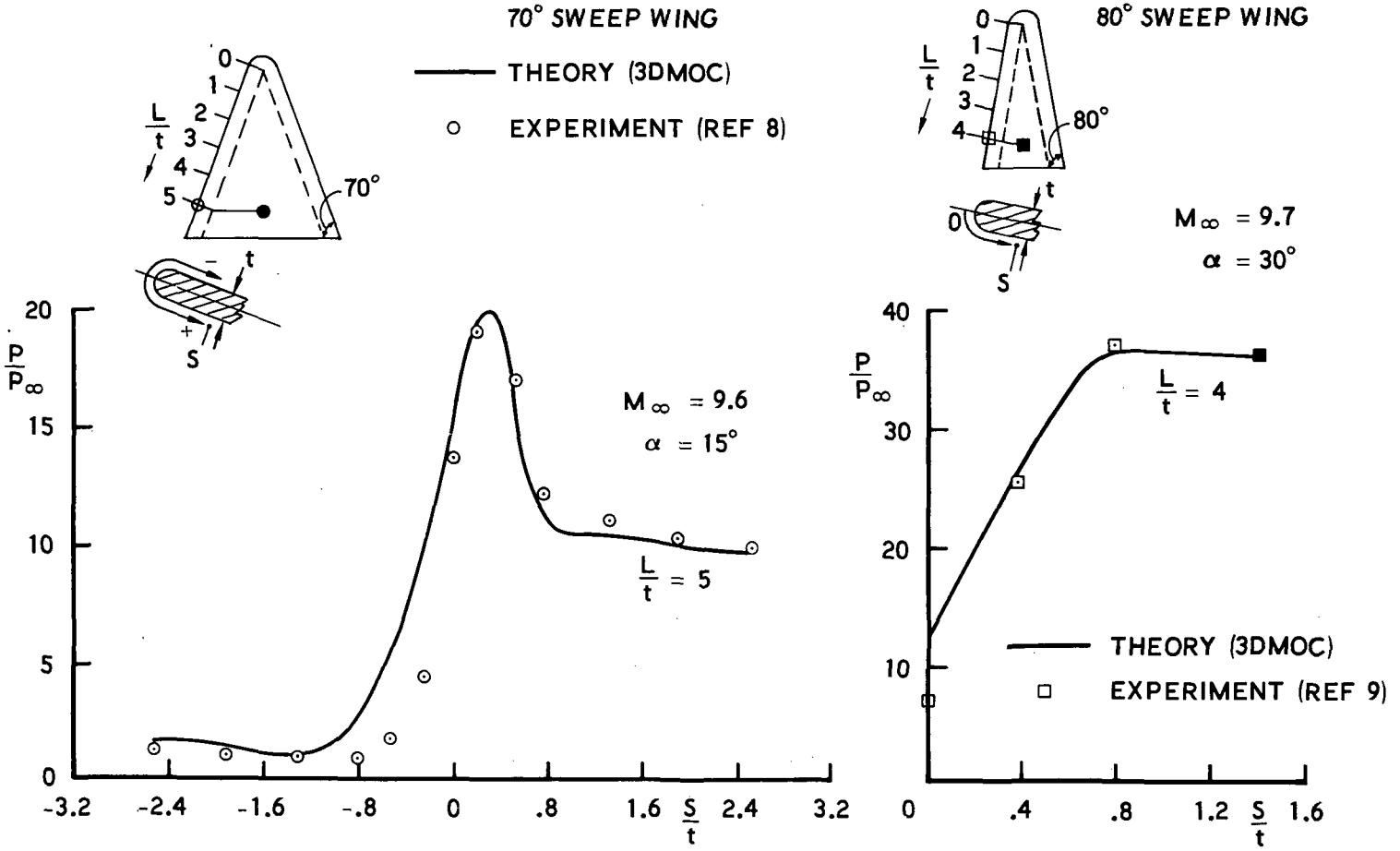

Figure 2

A SHUTTLE ORBITER AND COMPUTED SHOCK SHAPES
(Figure 3)

Our present method can handle very general smooth shuttle bodies. Figure 3 shows a shuttle orbiter and the computed shock shapes at Mach 5 and angles of attack of 5° and 20°. The body is described analytically. The upper profile, the lower profile, the maximum half breadth line and the wing leading edge are described by general conic equations in segments. The cross-section is described by an ellipse from a to b, a straight line from b to c, a cubic from c to d, and finally another ellipse from d to e. A realistic shuttle configuration can be described analytically in a similar way. Two cross-sections are noted for later use. Section C-C is located where the wing begins to emerge from the body and section D-D is located at the inflection point of the wing leading edge, which at that point makes a maximum angle of 32° with the body axis. Flow properties at these two sections will be discussed later.

At 5° angle of attack the bow shock, shown by dashed line, is well-behaved. At 20° angle of attack the bow shock, shown by the solid line, develops a kinked cross-section at the last station. However, as will be shown later, no such kink is observed at section D-D, even though the maximum local pressure, the maximum cross flow and the strongest embedded shock occur near section D-D. Nor was any kinked shock cross-section evident in the case of slab delta wings at high angles of attack. Thus, we believe that the kink is due to the added expansion caused by the curving back of the wing leading edge.

The location of the embedded shock is estimated by noting rapid changes of pressure gradients in the flow field. Even at 20° angle of attack, the embedded shock was weak and no provision for entropy change was made in the computation. The 5° angle of attack case took approximately 9 minutes of CDC 6600 time, while the 20° angle of attack case required approximately 35 minutes.

A SHUTTLE ORBITER AND COMPUTED SHOCK SHAPES

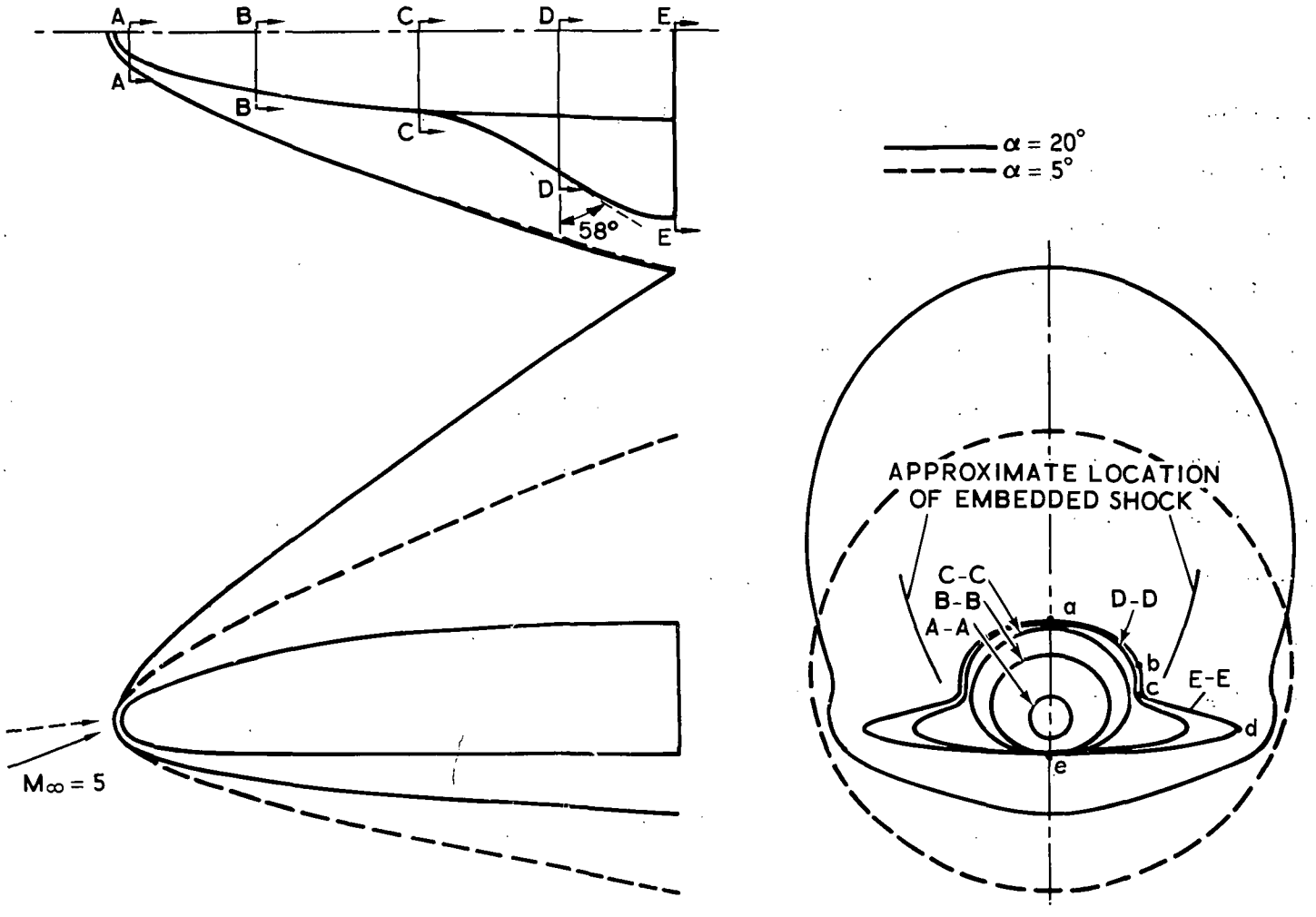

Figure 3

COMPUTED PRESSURE DISTRIBUTION ON WINDWARD SURFACE
(Figure 4)

Figure 4 shows the pressure distribution on the windward surface and the associated cross-sections of the orbiter at $M_\infty = 5$ and $\alpha = 20°$. On the left are 5 cross-sections of the orbiter, and on the right is the plan view of the orbiter along with pressure plots corresponding to each cross-section. Along the centerline the pressure first decreases from the nose and then recovers somewhat. This recovery is apparently due to the widening of the windward surface in the winged portion of the orbiter. Along the wing leading edge the pressure attains a maximum near the 4th section (Section D-D in Figure 3), at which the leading edge makes a maximum angle of 32° with the body axis. At each station in the winged portion of the orbiter, the pressure attains a maximum near the wing leading edge, just as in the case of the slab delta wing at 15° angle of attack. As the wing leading edge curves back, the maximum pressure drops rapidly. It is worth noting that the local Mach number attained a minimum of 1.25 at the maximum-pressure point and the computation went through without any problem.

COMPUTED PRESSURE DISTRIBUTION ON WINDWARD SURFACE

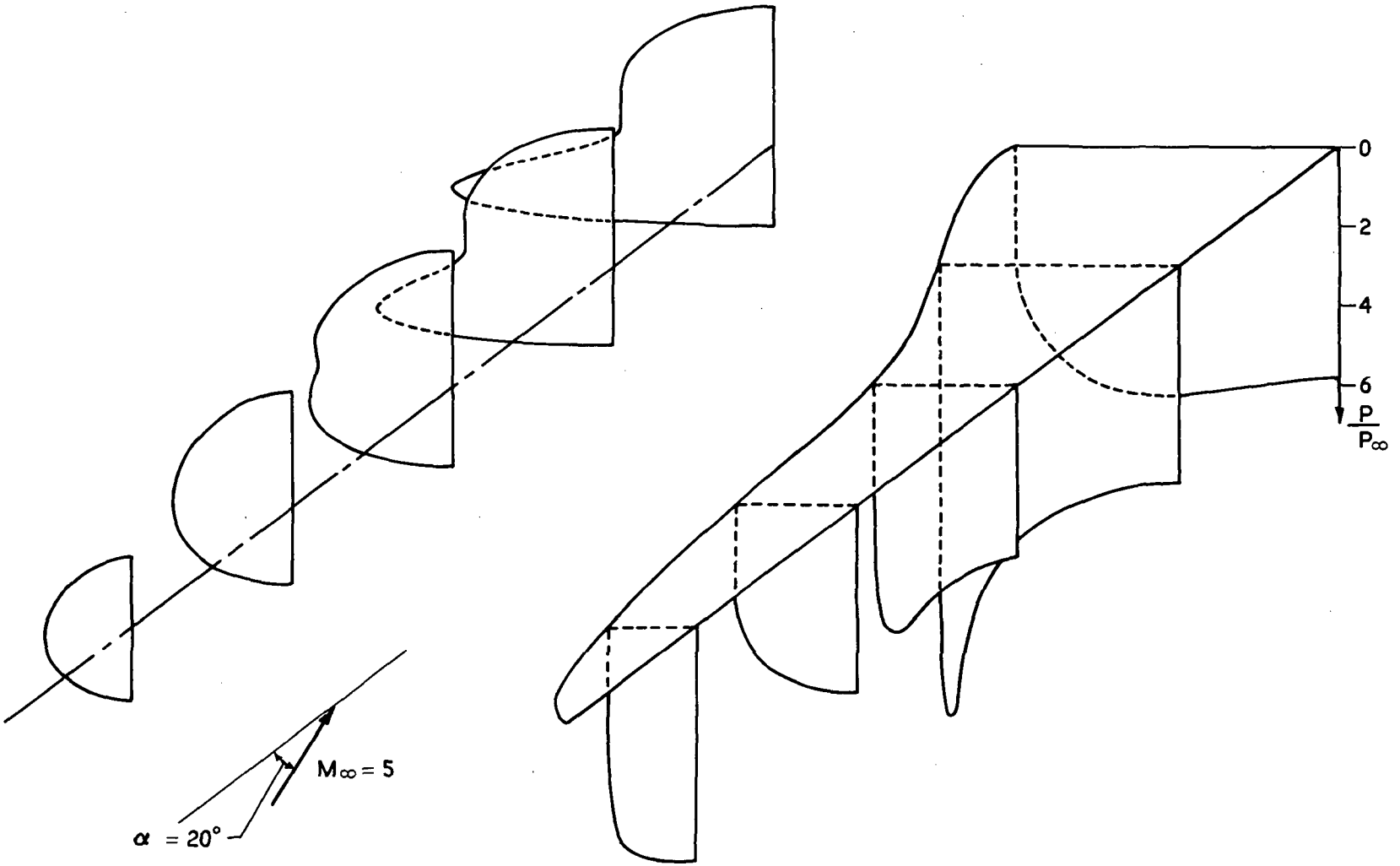

Figure 4

COMPUTED PRESSURE DISTRIBUTION ON LEEWARD SURFACE
(Figure 5)

Figure 5 shows the leeward surface pressure distributions, which are continuations of those shown in Figure 4. Along the centerline the pressure first drops because of the continued expansion from the nose; the pressure then rises owing to the recompression created by the converging flow toward the plane of symmetry on the leeside. Since the flow is continually expanding from the windward side, the highest pressure on the leeward surface occurs along the leading edge. At 20° angle of attack considerable cross flow exists on the leeside. At the wing-body junction the cross flow generates a series of compression waves as shown by the pressure peak of the pressure curve. Actually the pressure spike is due to the method of plotting; there exists only a pressure bump as can be seen from the next figure.

COMPUTED PRESSURE DISTRIBUTION ON LEEWARD SURFACE

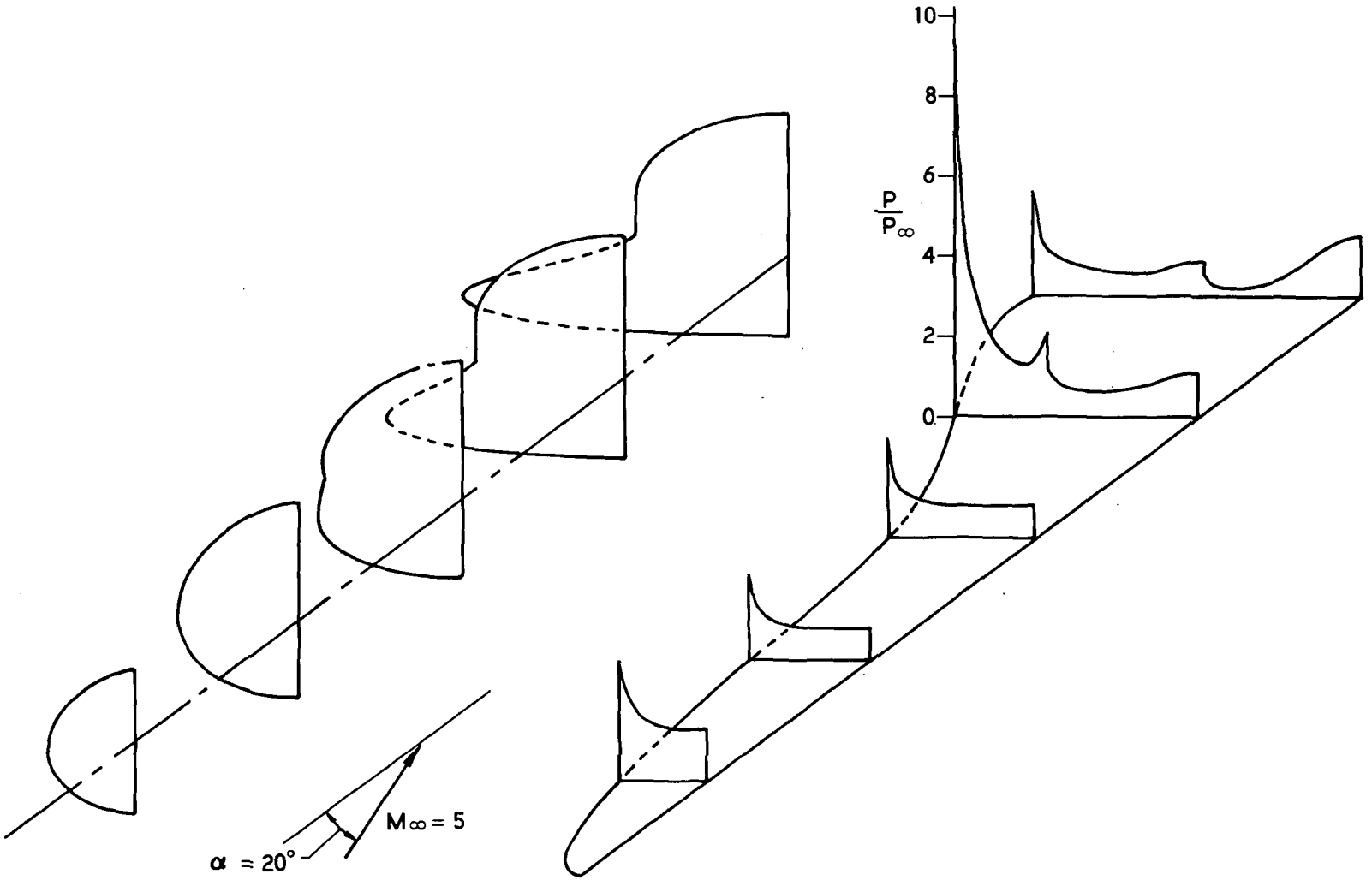

Figure 5

POLAR GRAPH OF PRESSURE DISTRIBUTION
(Figure 6)

Figure 6 is a polar plot of pressure distribution at section C-C and D-D. Section C-C is located where the wing is about to emerge from the body and section D-D is located where the wing leading edge makes a maximum angle with the body axis. At section C-C the pressure drops smoothly from the windside to the leeside, as might be expected. At section D-D, however, the pressure curve exhibits three peaks between the windward and leeward centerlines. The first peak occurs just below the wing tip where the combined effect of increasing wing span and high angle of attack causes the pressure to rise. The second peak at the wing-body junction is generated by the cross flow impinging on the upper body. The third peak at the leeside centerline of the orbiter is created by the flow converging toward the plane of symmetry. The second peak, which consists of a series of compression waves, is responsible for generating a weak embedded shock in the flow field. This pressure peak is the spike shown in the previous figure. It is interesting to note that the shape of the pressure distribution bears some resemblance to the body contour at both sections.

In order to define the local gradients in this complex flow field accurately, it was necessary to halve the grid size from the wing tip to the wing-body junction, and to halve it again in the region of the wing-body juncture.

POLAR GRAPH OF PRESSURE DISTRIBUTION

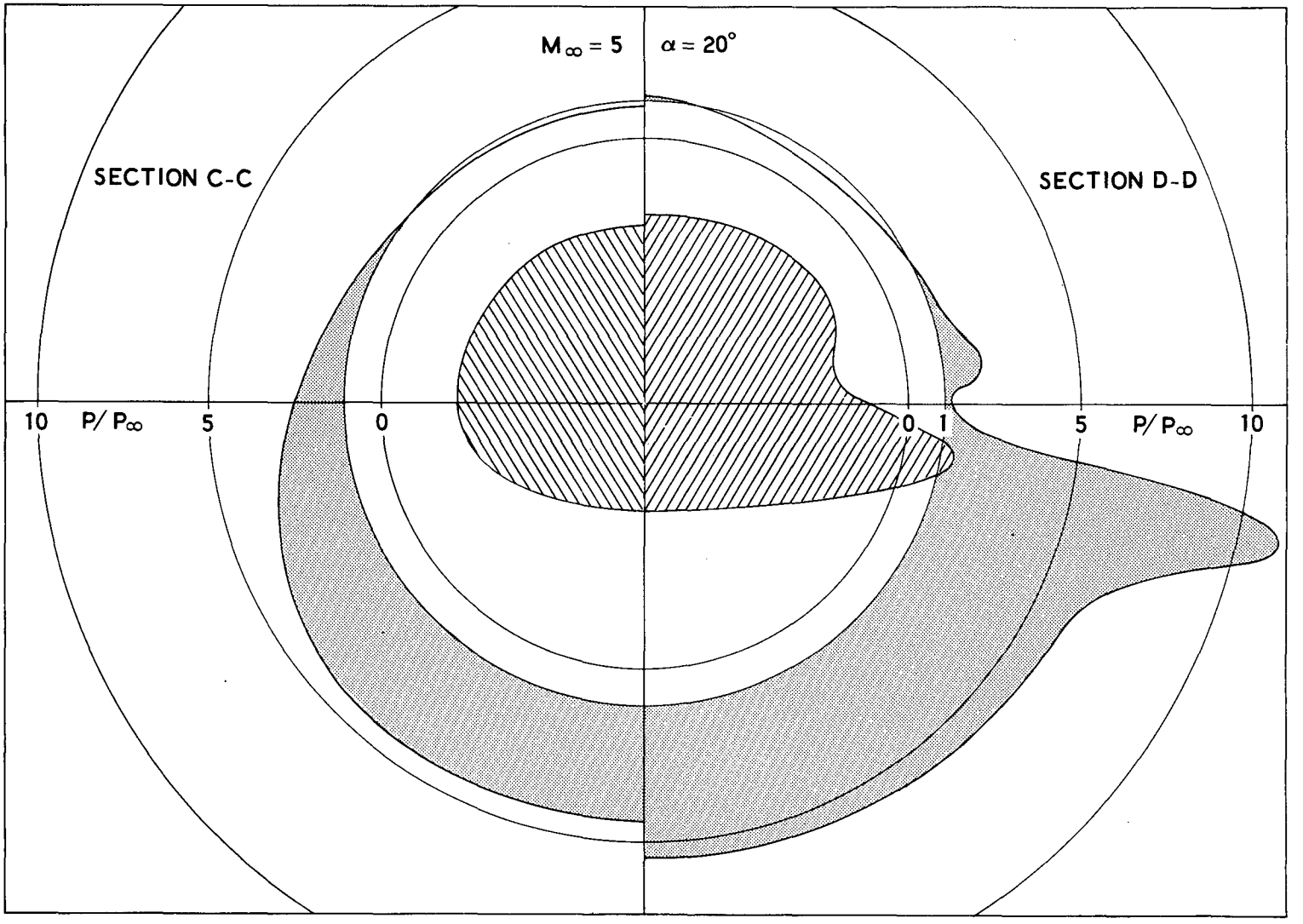

Figure 6

LOCAL FLOW DIRECTIONS
(Figure 7)

The local flow directions are shown in Figure 7, which is a plot of the projections of local unit velocity vectors on sections C-C and D-D. These arrows can be interpreted as velocity components normalized by the local speed.

The cross flow patterns are similar in both sections except in the region of the wing where the flow is greatly disturbed. As expected, large changes in the flow direction occur near the wing tip and considerable cross flow occurs near the wing root. It is this cross flow that generated the recompression observed as the second pressure peak in the preceding figure. The arrows are in general not tangent to the cross-sections because the axial velocity components are absent; the velocity is tangent to the body in three dimensions. For the same reason, the flow appears to move out of the shock on the leeside.

PROJECTIONS OF LOCAL UNIT VELOCITY VECTORS

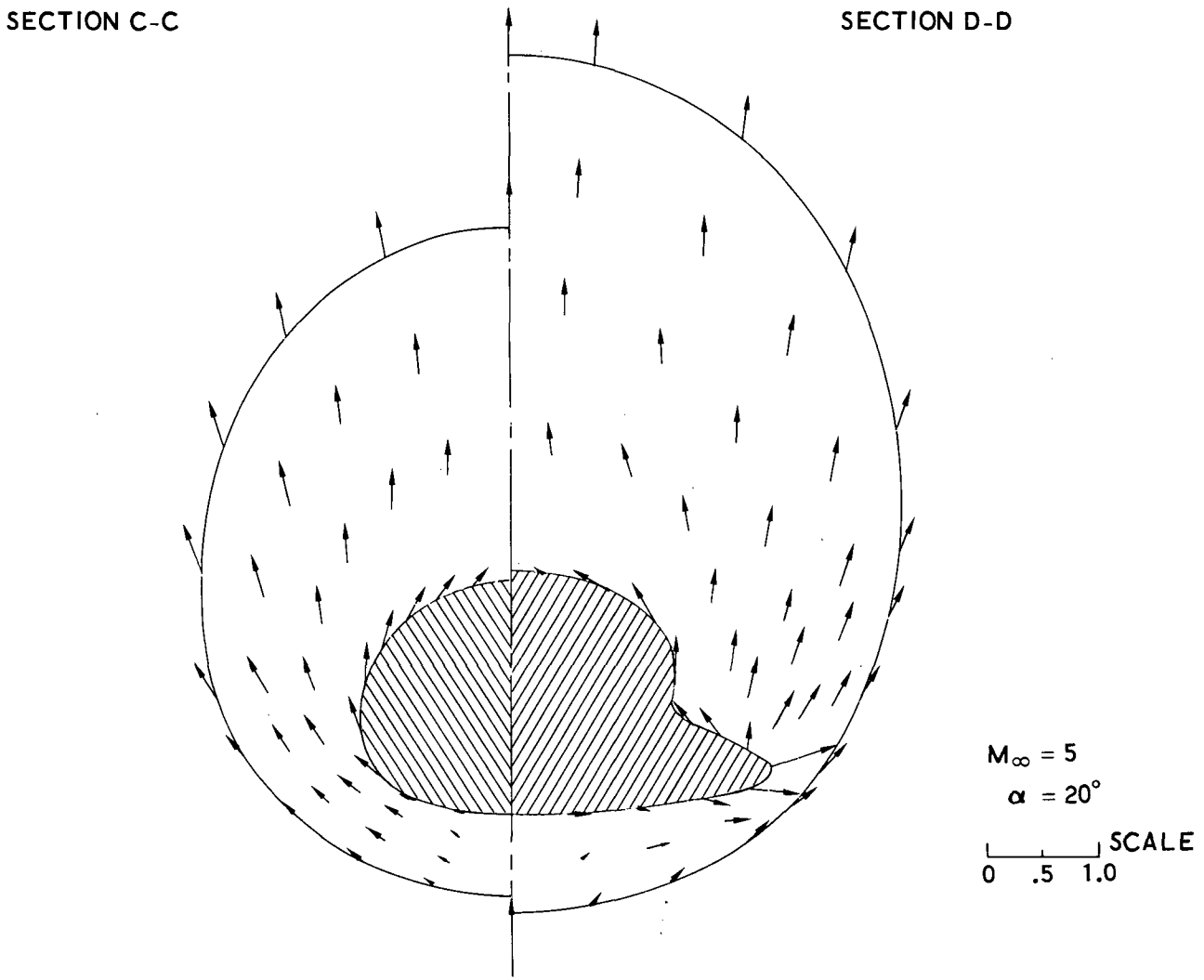

Figure 7

CONCLUSION

We have shown that Northrop's Three-Dimensional Method of Characteristics program is suitable for determining flow fields over space shuttle vehicles. Realistic configurations can be handled by this program if slope discontinuities on the body surfaces are smoothed out. However, this restriction will be removed in future developments. Configurations with thinner wings than those of the computed example will need more data points and correspondingly longer computer time, but they cause no fundamental difficulties. As long as the flow is supersonic and suitable initial value surfaces are obtained, this program can be used to determine the flow fields over realistic shuttle configurations even at high angles of attack.

REFERENCES

1. Fowell, L. R., "Solution of the starting region for the method of characteristics in general three-dimensional flow and solution of conical flows without symmetry," Northrop Report NOR 61-62 (1961).

2. Fowell, L. R., "The calculation of flow properties in a general three-dimensional field, a method of characteristics," Northrop Report NOR 61-65 (1961).

3. Chu, C. W., "Compatibility Relations and a Generalized Finite Difference Approximation for Three-Dimensional Steady Supersonic Flow," AIAA J. 5, 493-501 (1967).

4. Powers, S. A., Niemann, A. F. Jr. and Der, J. Jr., "A numerical procedure for determining the combined viscid-inviscid flow fields over generalized three-dimensional bodies," Air Force Flight Dynamics Laboratory Rept. AFFDL-TR-67-124 (1967).

5. Pridmore Brown, B. N. and Franks, W. J., "A method of characteristics solution in three independent variables," Aerospace Research Laboratories Report ARL 65-124 (1965).

6. Chu, C. W. and Ziegler, H., "Calculation of multiple rocket engine exhaust plumes by the method of characteristics," Northrop Report NOR 69-71 (1969).

7. Powers, S. A. and Beeman, E. R., Jr., "Flow fields over sharp-edge delta wings with attached shock," NASA CR-1738, (1971).

8. Bertram, M. H. and Everhart, P. E., "An experimental study of the pressure and heat transfer distribution on a 70° sweep slab delta wing in hypersonic flow," NASA TR-153 (1963).

9. Whitehead, A. H., "A study of the pressure and heat transfer distribution on a highly swept slab delta wing in hypersonic flow," Master Thesis, University of Virginia (1966).

Page Intentionally Left Blank

APPLICATION OF SHOCK CAPTURING AND CHARACTERISTICS METHODS TO SHUTTLE FLOW FIELDS

By P. Kutler, J. V. Rakich, and G. G. Mateer

NASA Ames Research Center
Moffett Field, California

INTRODUCTION

The ultimate objective of the work described herein is to calculate real gas flows, including rate chemistry, around the space shuttle vehicle. This would permit the prediction of the heating and heat-shield erosion for actual flight conditions, something that no present wind tunnel can do completely. A limiting factor in the simulation of real gas flows is the speed of present computers. Fortunately, advanced computers such as STAR and ILLIAC will soon be available and they have the potential for such computations. In fact, ILLIAC is scheduled for installation here at Ames Research Center this summer. With this goal in mind, and in anticipation of ILLIAC, advanced techniques are now being developed which can exploit the unique capabilities of ILLIAC.

Methods for computing complicated inviscid supersonic flows in three space dimensions have been under development at Ames Research Center for several years. Two fundamentally different approaches are being used and are discussed in this paper. The first and oldest is based on the method of characteristics[1] (referred to as MOC in the following discussion). The particular technique used in this program is referred to in the literature as a "reference-plane" or "semicharacteristic" method, since finite difference relations are used to treat certain cross derivatives. The second and newest method[2] utilizes the gas-dynamic equations in conservation-law form and automatically allows for the existence and formation of shock waves without special application of the Rankine-Hugoniot conditions (referred to as a shock capturing technique, or SCT in the following discussion). An explicit second or third order noncentered, finite-difference scheme is used to solve the governing equations.

This paper will show some recent results obtained with these methods for an early orbiter shape proposed by the North American Rockwell Corporation and also for the more recent 040A configuration suggested by NASA-MSC. Results obtained with the SCT code demonstrate its three-dimensional, multiple shock capturing capability while results obtained with the MOC code demonstrate the calculation of equilibrium real gas flows and the determination of flow variables required for a heating analysis.

SHOCK SHAPES FOR SIMULATED NARC SHUTTLE ORBITER

(Figure 1)

Initial efforts to calculate the flow field for the NARC space shuttle orbiter included a pointed nose to simplify determination of the initial conditions. For this case, the SCT code generated its own starting solution, however, subsequent calculations, which utilized blunted noses, relied on the use of the inverse blunt body method[3] and the MOC code[1] to generate the required starting data. A typical body cross section for the NARC orbiter was approximated by two ellipses whose semi-major and minor axes varied as cubic polynomials between a discrete number of longitudinal stations (see ref. 4). Simulation of the wing on the NARC orbiter was included by varying the semi-major axes of the ellipses according to the wing planform. The canopy for this example was excluded, but has been included in subsequent calculations.

The shock pattern predicted for this configuration by the SCT code is shown in Figure 1 for both the planform and profile views. At an x/L of .6, a shock appears off the leading edge of the wing as a result of the compressive turning of the flow in that vicinity. As the calculations proceed downstream, the shock wave starts to move further from the wing. This is a result of the thick wing approximated by the top ellipse. The wing leading-edge shock eventually intersects the bow shock at an x/L of about .78 and extends beyond it at stations further downstream of this point. The main point of this calculation was to demonstrate that the SCT code is capable of predicting the formation of secondary shock waves and, also, shock-shock intersections. For this calculation the computational plane was discretized into 30 points in the radial direction and 19 points in the meridional direction The integration procedure required 1×10^{-4} minutes per point and the entire calculation consumed approximately 19 minutes on an IBM 360/67 with interactive graphics.

As indicated in the figure, the MOC code gave virtually identical shock shapes up to about x/L = 0.6. The MOC code had difficulty in proceeding beyond that point because of the secondary shock.

SHOCK SHAPES FOR SIMULATED NARC SHUTTLE ORBITER

M = 5 α = 5°

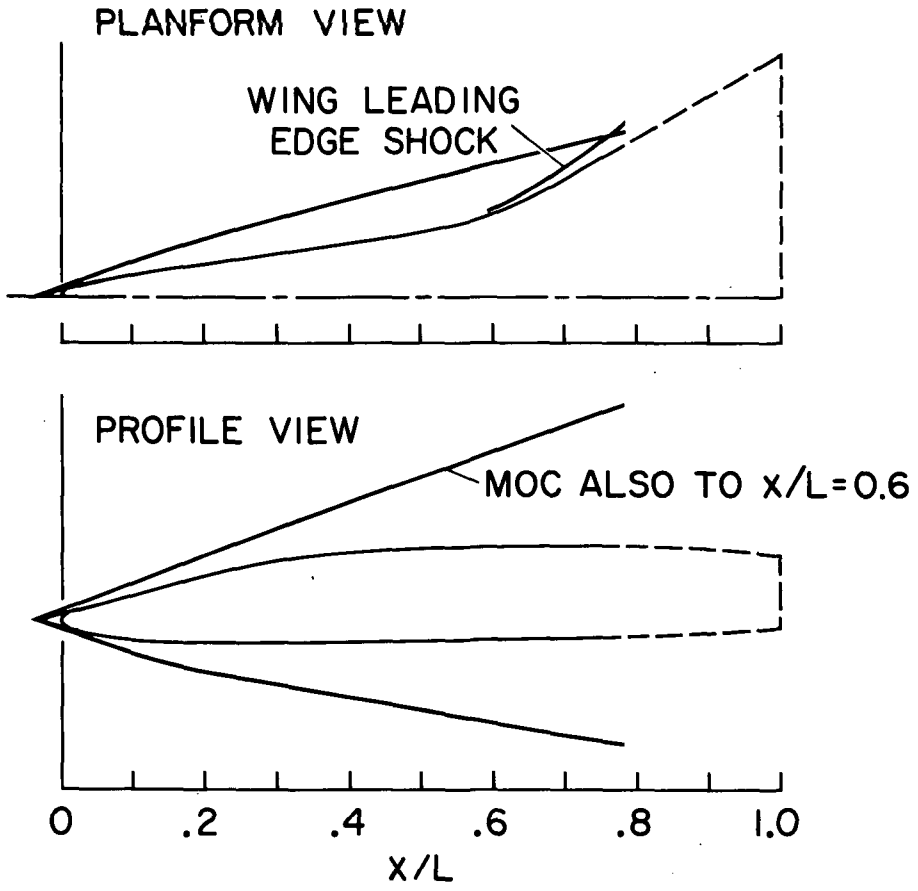

Figure 1

CROSS SECTIONAL SHOCK SHAPES FOR NARC SHUTTLE ORBITER

(Figure 2)

The cross sectional shock shapes and simulated body shapes are shown in Figure 2 for three longitudinal stations. At an x/L of .66 there is a clearly defined leading edge shock which just stands off the body. Further downstream at an x/L of .785 the leading edge shock intersects and extends beyond the main bow shock. This complicated three-dimensional shock pattern presented no problems for the SCT code. In the future the analytical description of the body will be improved, especially in the vicinity of the wing leading edge. It is believed that such changes will have only a minor effect on the windward portion of the flow, but a noticeable effect on the standoff distance of the wing leading edge shock wave.

The limiting factor in these calculations is the computer and not the method. More mesh points are needed in the vicinity of the wing leading edge to properly resolve the rapid variation of the flow there. Utilization of a finer mesh will become possible with advanced computers such as ILLIAC.

In principle, complicated shock intersections, such as shown in Figure 2 can be treated by the method of characteristics also. However, the programming for intersecting shocks is extremely difficult. With the SCT code, the programming is simple and the calculations routine.

CROSS SECTIONAL SHOCK SHAPES FOR NARC SHUTTLE ORBITER

$M = 5 \qquad \alpha = 5°$

——— SIMULATED CONFIGURATION

– – – ACTUAL CONFIGURATION

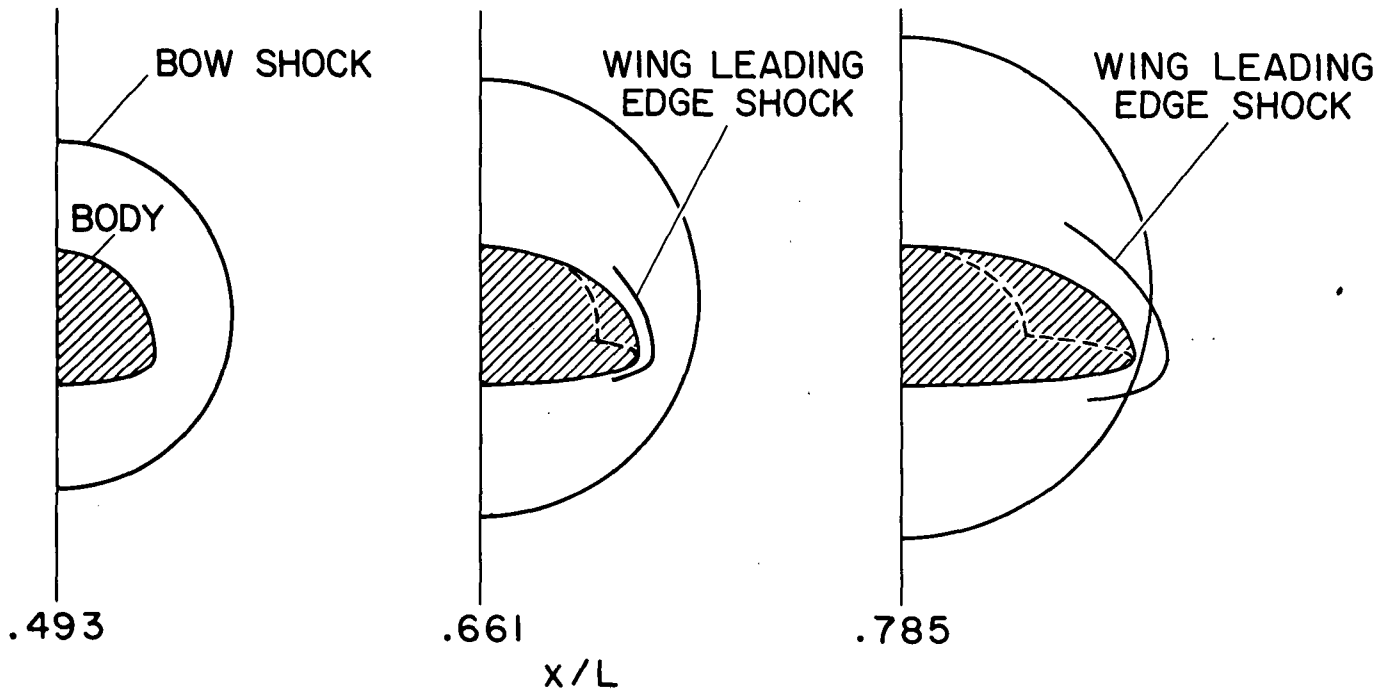

Figure 2

LONGITUDINAL SURFACE PRESSURE DISTRIBUTION FOR NARC SHUTTLE ORBITER

(Figure 3)

The variation of surface pressure coefficient with longitudinal distance for the 0°, 90°, and 180° meridians is shown in Figure 3. The constant pressure coefficient near the nose is a result of the cone solution. The 90° meridian contains the simulated wing leading edge, and as the flow is turned due to the presence of the wing the pressure rises rapidly. It begins to decrease as the leading edge reaches its final swept position and the secondary shock moves away from the surface. Of course, a sharp peak in heating is expected to accompany the pressure rise.

The irregularities in the pressure distribution arise from the body description which matched slopes but allowed curvatures to be discontinuous. Similar pressure variations were obtained from the MOC code and agreement is excellent; numerous comparisons of the two methods are given in reference 4.

LONGITUDINAL SURFACE PRESSURE DISTRIBUTION FOR NARC SHUTTLE ORBITER

M = 5 $\alpha = 5°$

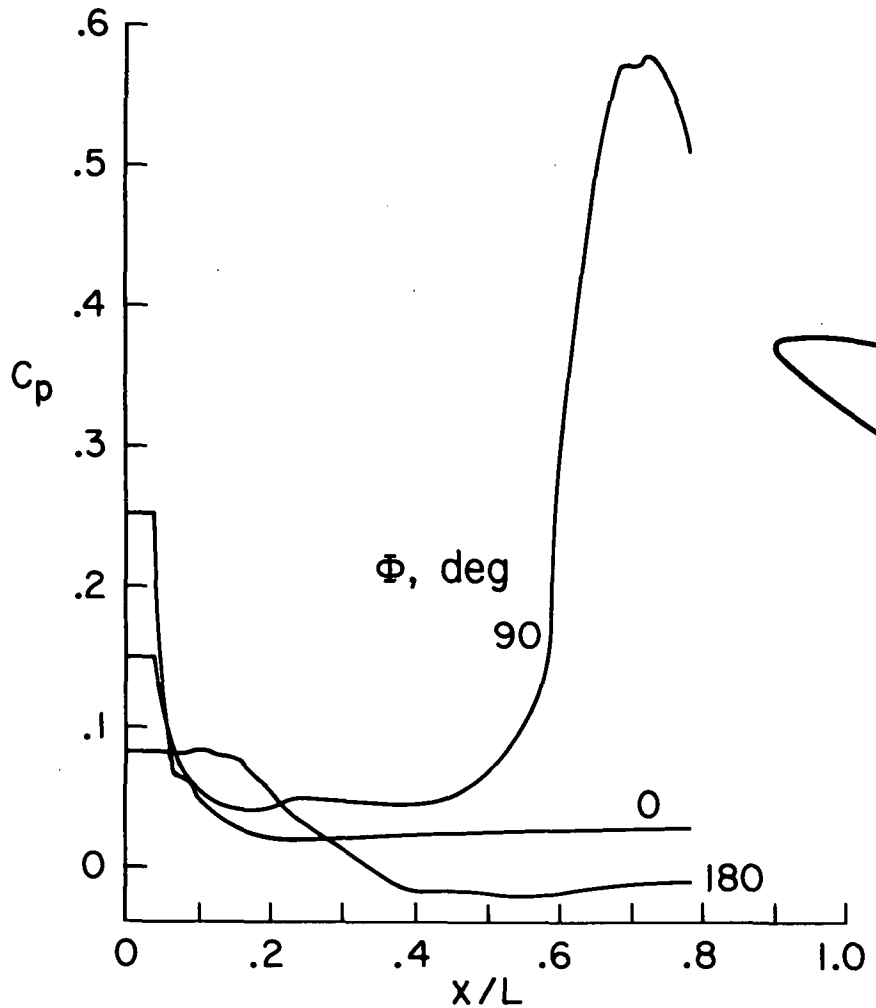

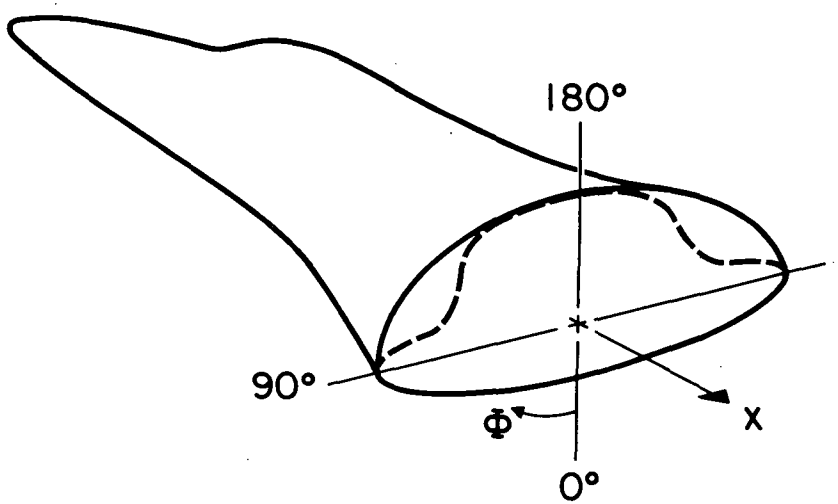

Figure 3

SHOCK LOCATION FOR BLUNTED SHUTTLE ORBITER

(Figure 4)

Figure 4 shows the shock shape for a blunt nosed version of the same body. Also, a more realistic approximation for the canopy has been made here. The angle of attack is 15.3° and $M = 7.4$. Comparison is made with experiment (shadowgraph) obtained by J.W. Cleary[5] in the Ames 3.5-foot Hypersonic Wind Tunnel. Agreement between theory and experiment is excellent for the bow wave. The small differences for the canopy wave are believed due to an inexact modeling of the canopy shape.

The good agreement with experiment provides confidence in the shock capturing method. In addition, the method is able to resolve a weak recompression shock behind the canopy shock, although the recompression shock was too weak to show in the shadowgraph.

Results of the MOC code are in reasonable agreement with SCT code (and experiment) for the bow shock. However, the MOC code does not resolve the canopy shock very well.

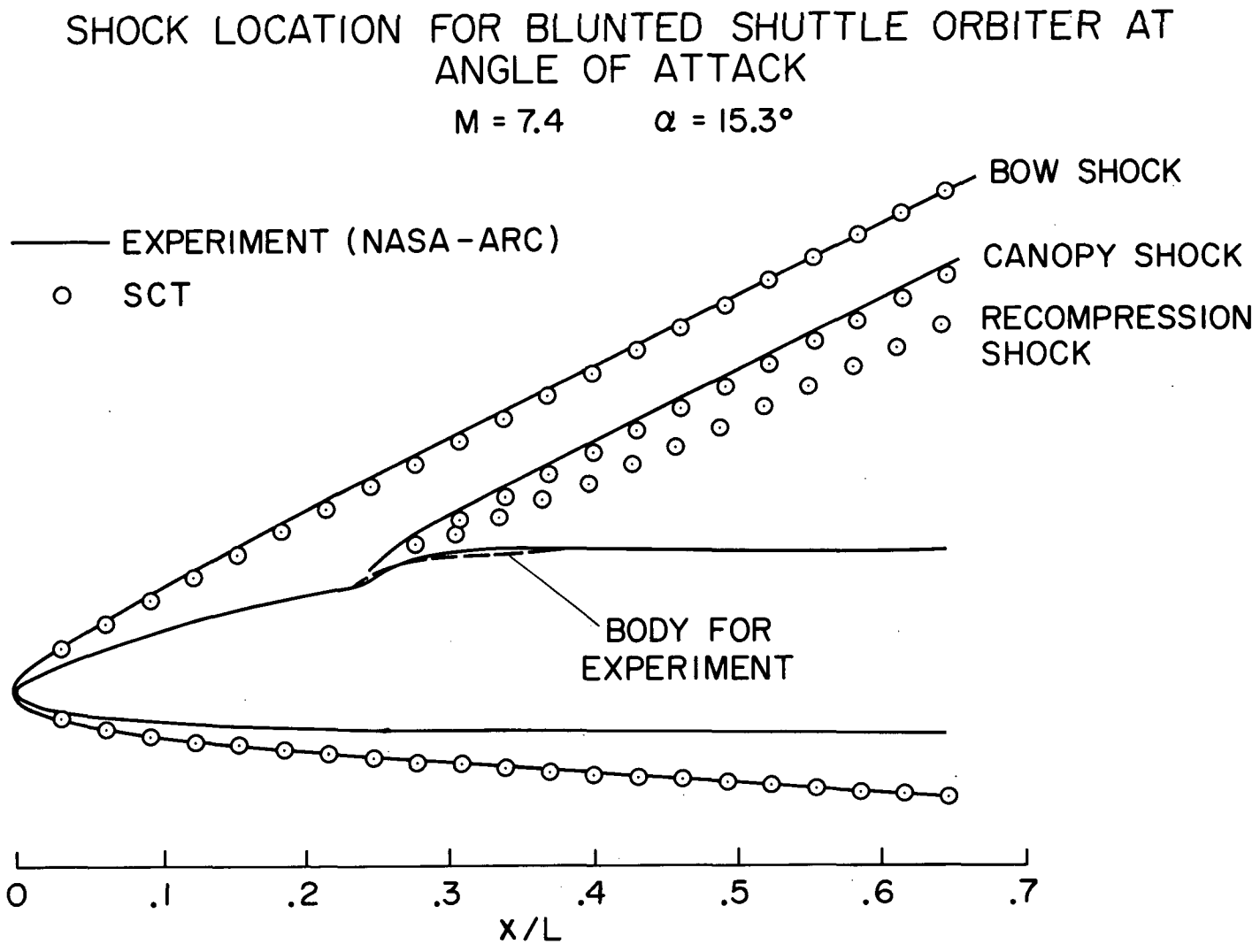
SHOCK LOCATION FOR BLUNTED SHUTTLE ORBITER AT ANGLE OF ATTACK
M = 7.4 α = 15.3°
EXPERIMENT (NASA-ARC)
SCT
BOW SHOCK
CANOPY SHOCK
RECOMPRESSION SHOCK
BODY FOR EXPERIMENT
0
.1
.2
.3
.4
.5
.6
.7
X/L

Figure 4

SHOCK SHAPE FOR NARC SHUTTLE ORBITER

(Figure 5)

The next set of figures shows the effect of equilibrium gas properties on the flow over the North American Rockwell orbiter. The calculations were performed with the MOC code[1] and using the Ames RGAS tables.[3] Equilibrium calculations correspond to a flight velocity of 7.3 km/sec (24,000 fps or M = 26.3) and with ambient conditions corresponding to 76 km (250,000 ft) altitude. Comparisons are made with perfect gas calculations at M = 7.4, for which experimental data are available. It should be noted that there are no ground test facilities that can simulate these flight conditions.

Figure 5 shows the bow shock shapes on the vertical plane of symmetry. The equilibrium shock standoff distance is about half the perfect gas value. Part of the difference is due to the different Mach numbers, but it is believed that most of the difference is due to dissociation of molecular oxygen. The perfect gas results are in reasonably good agreement with the experimental shock shape shown in Figure 4. Thus, while these experimental results are useful for checking the numerical calculations, experimental shock shapes are not easily extrapolated to flight conditions. This has a bearing on the design of a thermal protection system for areas where the bow shock may intersect the wing or control surfaces.

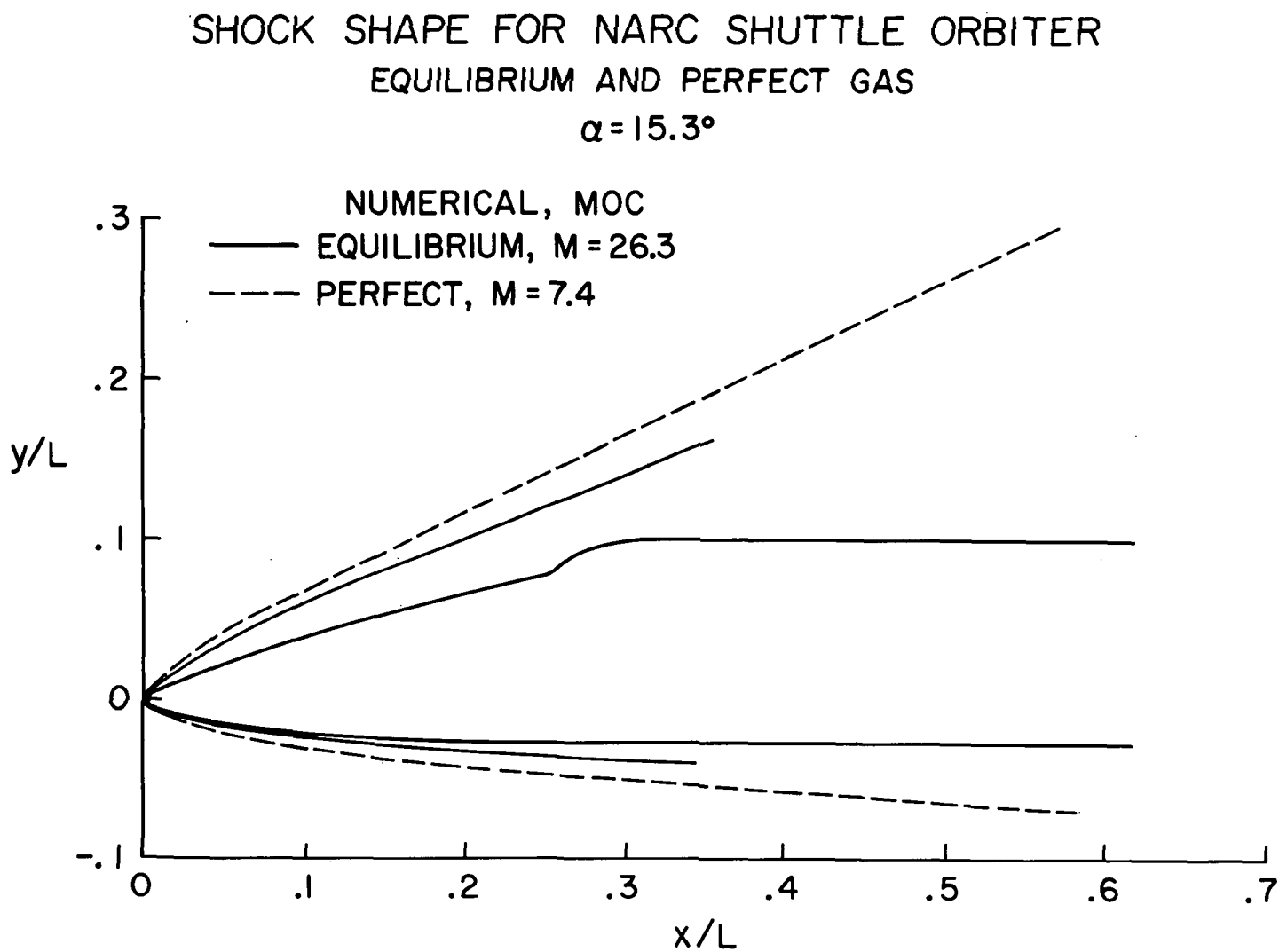
SHOCK SHAPE FOR NARC SHUTTLE ORBITER
EQUILIBRIUM AND PERFECT GAS
α = 15.3°
NUMERICAL, MOC
EQUILIBRIUM, M = 26.3
PERFECT, M = 7.4
y/L
.3
.2
.1
0
-.1
0
.1
.2
.3
.4
.5
.6
.7
x/L

Figure 5

SURFACE PRESSURES FOR NARC SHUTTLE ORBITER

(Figure 6)

A comparison of surface pressures is shown in figure 6. In this case there is only a small difference between the perfect and equilibrium real gas results. The effect of the different Mach numbers is accounted for in the pressure coefficient. Experimental pressures obtained by C. C. Pappas in the Ames 3.5-foot hypersonic wind tunnel are also shown. The small differences between theory and experiment in the vicinity of the nose are attributed to differences between the model and theoretical body shapes.

These calculations with the MOC code employed from 11 to 21 points between the body and shock on each of 19 meridional planes. The real gas calculations take about 60% longer than for the same perfect gas case. For the perfect gas, the unit computation time is about 4×10^{-4} minutes per point on an IBM 360/67 computer; total times to $x/L = .34$ are about 80 min. for a perfect gas and 120 min. for a real gas.

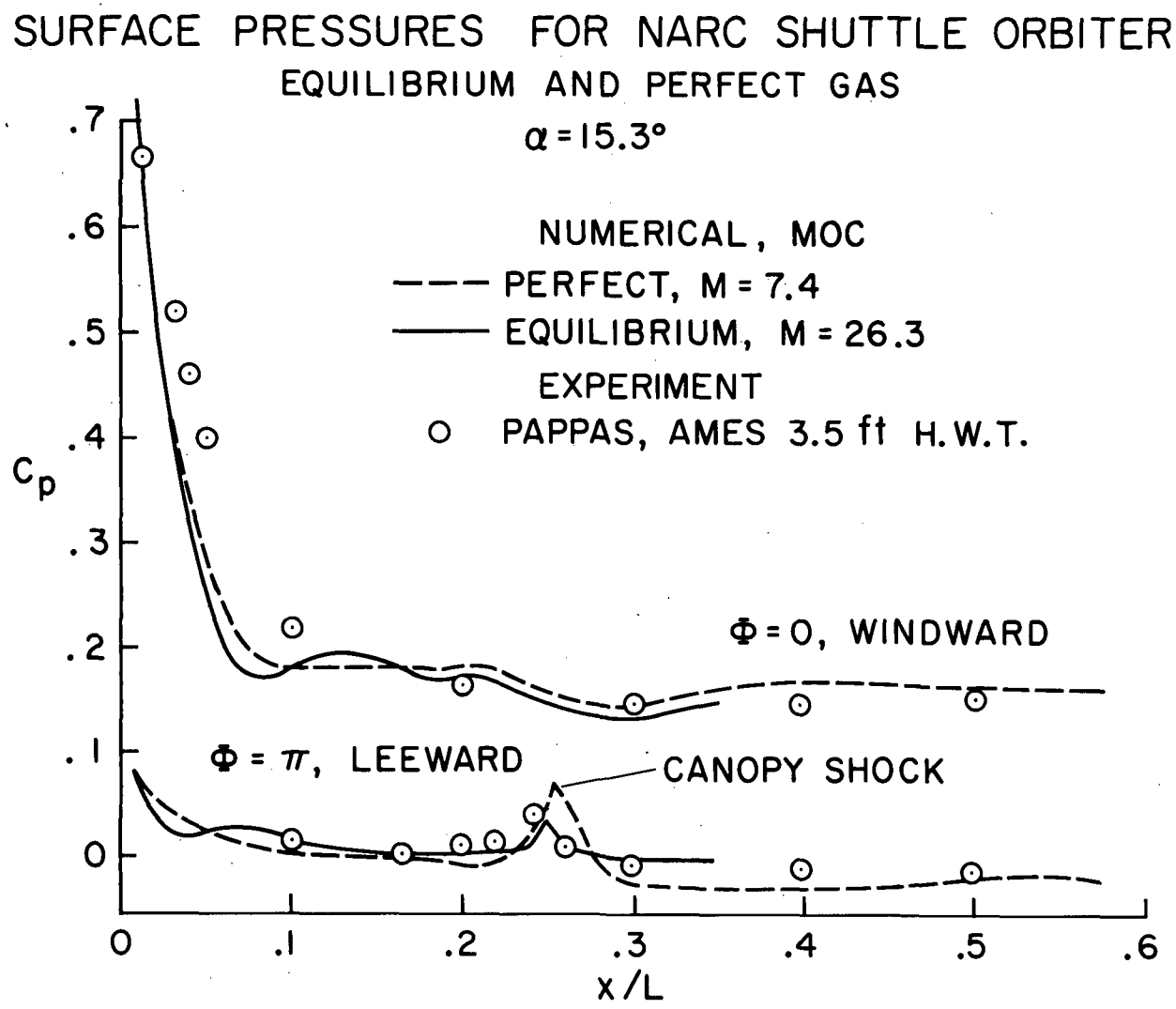
SURFACE PRESSURES FOR NARC SHUTTLE ORBITER
EQUILIBRIUM AND PERFECT GAS
α = 15.3°
NUMERICAL, MOC
PERFECT, M = 7.4
EQUILIBRIUM, M = 26.3
EXPERIMENT
PAPPAS, AMES 3.5 ft H.W.T.
Φ = 0, WINDWARD
Φ = π, LEEWARD
CANOPY SHOCK
Cp
.7
.6
.5
.4
.3
.2
.1
0
0
.1
.2
.3
.4
.5
.6
x/L

Figure 6

SURFACE ENTHALPY AND DENSITY FOR NARC SHUTTLE ORBITER

(Figure 7)

Figure 7 shows two local flow variables, enthalpy, H, and density, ρ, that cannot readily be simulated in ground based tests. These variables, as seen in the figure, are very different for equilibrium and perfect gas flows. The enthalpy ratio is related to velocities by the energy equation as follows:

$$H/H_T = 1 - \frac{V^2}{2H_T}$$

Together with the pressure and viscosity, these quantities affect the aerodynamic heating in a complex way which can only be predicted with a detailed boundary-layer calculation. The present numerical methods provide all of the information needed for such a boundary-layer solution and heat-transfer analysis.

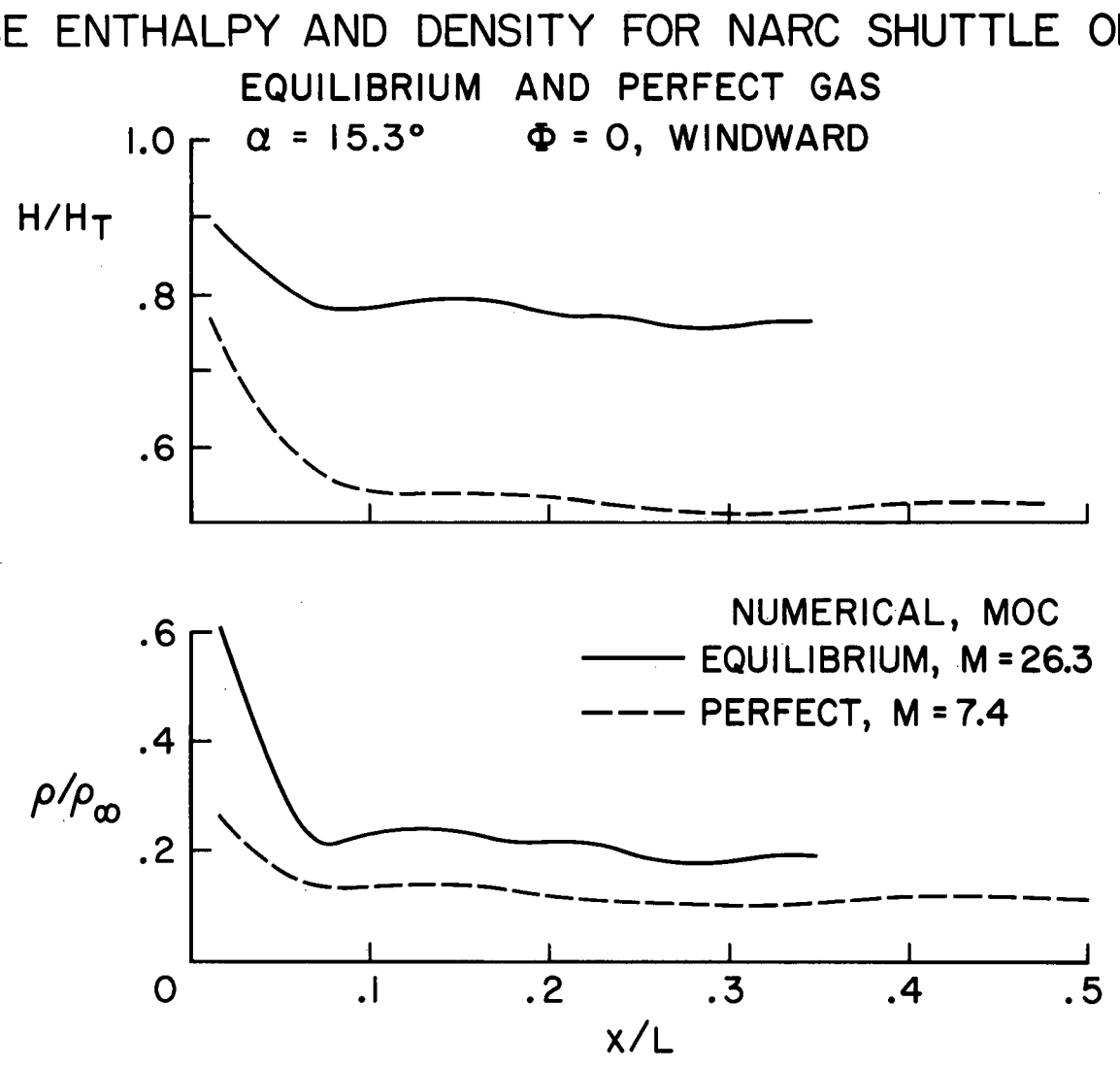
SURFACE ENTHALPY AND DENSITY FOR NARC SHUTTLE ORBITER
EQUILIBRIUM AND PERFECT GAS
α = 15.3°
Φ = 0, WINDWARD
H/H_T
1.0
.8
.6
NUMERICAL, MOC
EQUILIBRIUM, M = 26.3
PERFECT, M = 7.4
ρ/ρ∞
.6
.4
.2
0
.1
.2
.3
.4
.5
x/L

Figure 7

STREAMLINE METRIC FOR NARC SHUTTLE ORBITER

(Figure 8)

For three-dimensional flows such as that over the space shuttle, the boundary layer and heating analysis is complicated by the curved path of the streamlines. Most heating analyses require the metric coefficients for the curvilinear streamline coordinates, which are not known a-priori but can be determined from the inviscid flow field. The metric, h, which determines the distance between streamlines (see sketch in Fig. 8) is most important and is automatically calculated in the present MOC program.

As an example, figure 8 shows the variation of h on the windward plane of symmetry. For this special case the equation governing the change in h with axial distance x has two parts:

$$\frac{r}{h}\left(\frac{\partial h}{\partial x}\right)_{\Phi=0} = \left(\frac{\partial r}{\partial x}\right) + \frac{1}{u}\left(\frac{\partial w}{\partial \Phi}\right) \qquad (1)$$

The first term in Eq. (1) is due to the local body slope, and the second term is due to the crossflow velocity gradient. When the velocity gradient vanishes, then h is the local cylindrical radius, r. When $\partial r/\partial x = 0$, as on a large part of the shuttle, h depends on $\partial w/\partial \Phi$ where w is the <u>cylindrical</u> crossflow velocity. Therefore the crossflow velocity gradient causes h to increase initially as the streamlines are spreading out. The curve flattens out at about $x/L = .35$ due to the adverse crossflow pressure gradient which starts to develop there, and the streamline spreading diminishes.

STREAMLINE METRIC FOR NARC SHUTTLE ORBITER

PERFECT GAS

$M = 7.4$ $\alpha = 15.3°$ $\Phi = 0$, WINDWARD

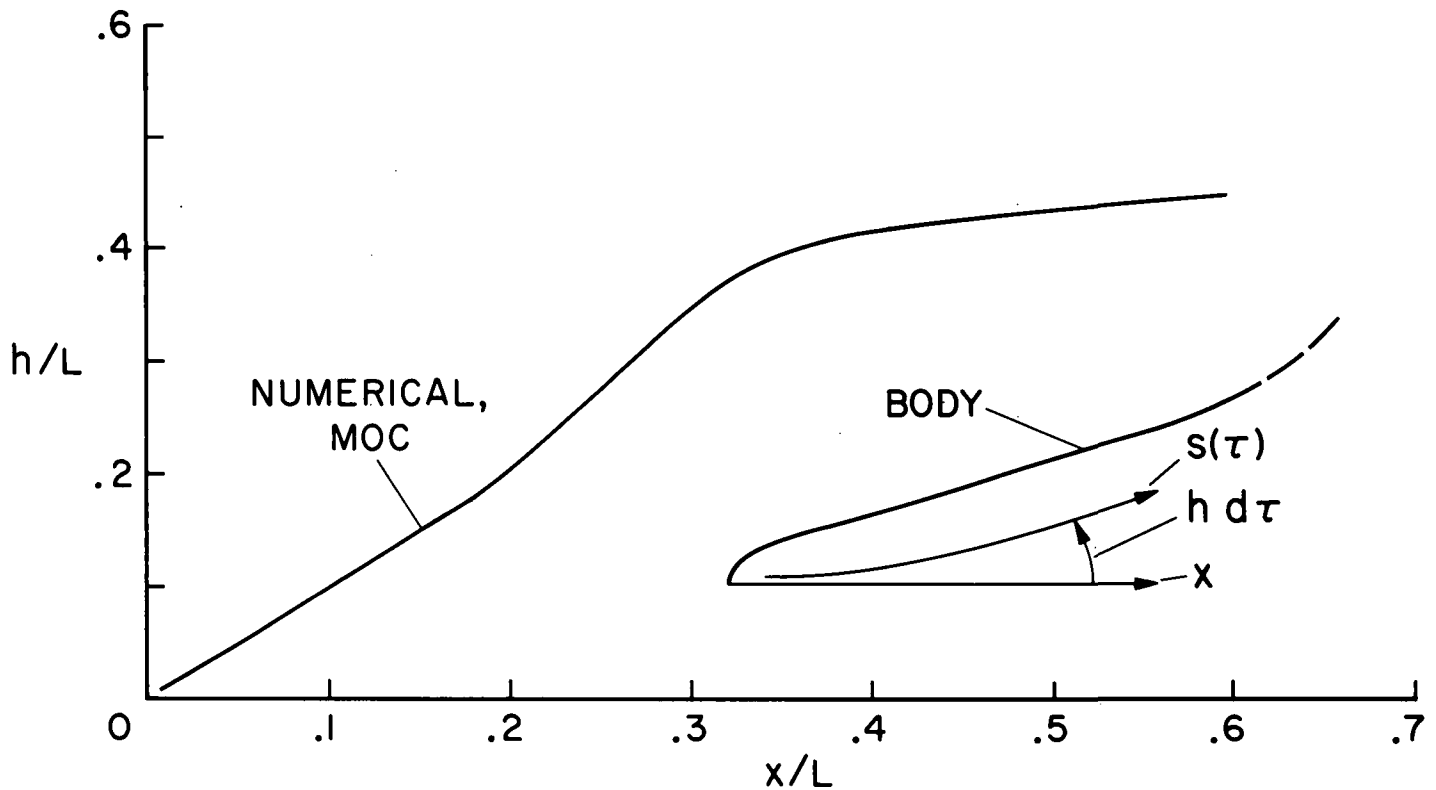

Figure 8

HEAT TRANSFER RATE FOR NARC SHUTTLE ORBITER

(Figure 9)

The axisymmetric or 2-D analog makes use of the fact that for small crossflow the 2-D boundary-layer equations have the same form as for 3-D flow, provided r is replaced by the metric h. Figure 9 shows the heating rate for the windward plane of asymmetry of the NARC shuttle orbiter, normalized by the stagnation heating to a sphere of 0.305 m (1-ft) radius. The metric coefficient from figure 8 was used with the boundary-layer program[6] developed by J. Marvin at NASA-Ames. These numerical predictions agree reasonably well with the data of Lockman and De Rose taken in the Ames 3.5-foot hypersonic wind tunnel.[7]

Also shown in Figure 9 is the predicted heat transfer to a flat plate (h=constant) for the same edge conditions. This comparison of the flat plate and actual heating rates illustrates the importance of knowing the correct streamline metric. The procedure for obtaining the metric and heating is similar to that described by Hamilton and DeJarnette[8]; the main difference is that the present method utilizes exact numerical flow field and boundary layer methods.

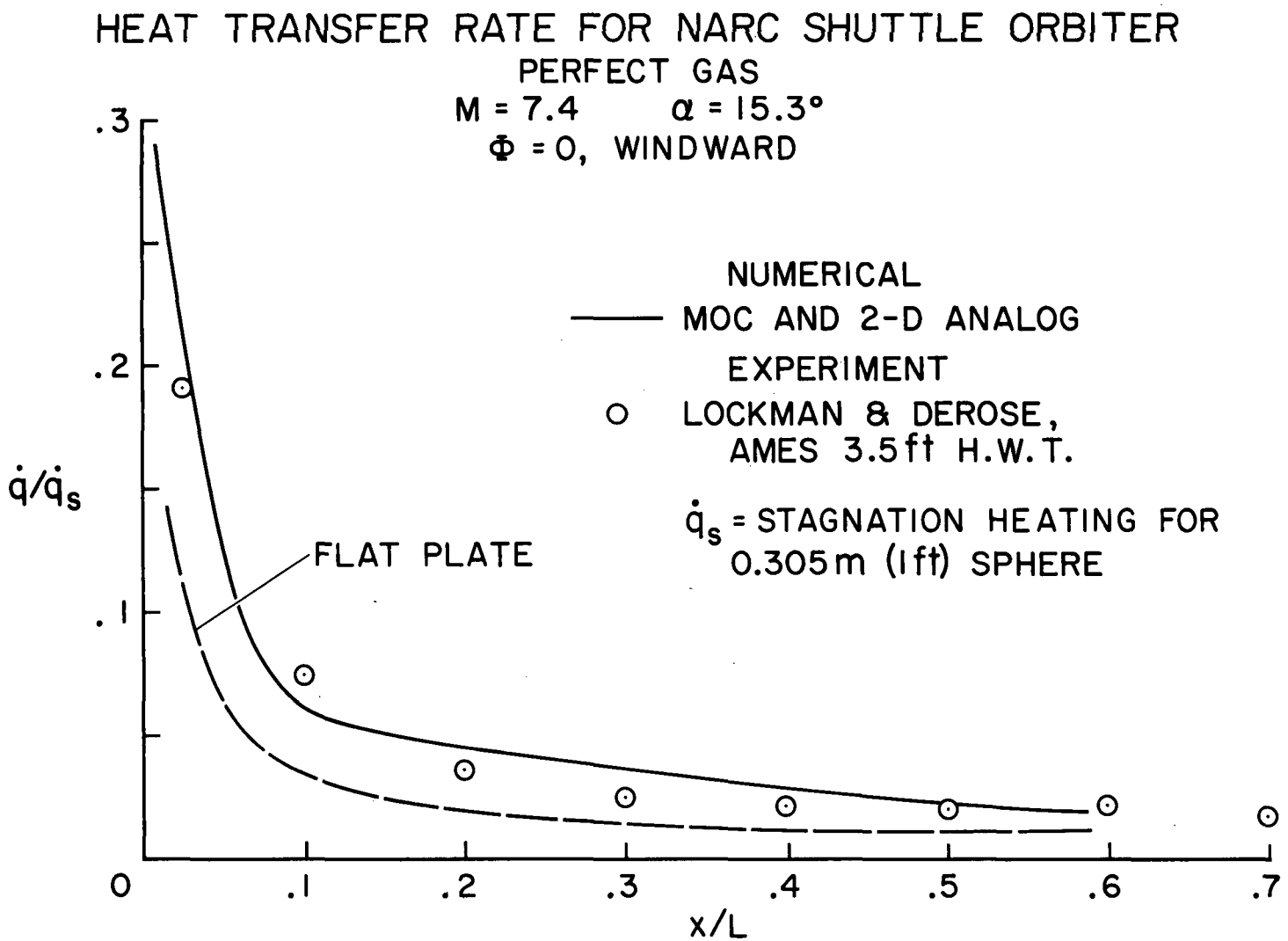
HEAT TRANSFER RATE FOR NARC SHUTTLE ORBITER
PERFECT GAS
M = 7.4 α = 15.3°
Φ = 0, WINDWARD
NUMERICAL
MOC AND 2-D ANALOG
EXPERIMENT
LOCKMAN & DEROSE, AMES 3.5 ft H.W.T.
q̇s = STAGNATION HEATING FOR 0.305 m (1 ft) SPHERE
FLAT PLATE
q̇/q̇s
x/L
.3
.2
.1
0
.1
.2
.3
.4
.5
.6
.7

Figure 9

PROFILE AND PLANFORM SHOCK SHAPES FOR MSC 040A

(Figure 10)

In an attempt to determine the intersection of the bow shock with the wing of NASA's MSC 040A shuttle orbiter, the shock capturing technique[2] was used after obtaining a starting solution from an inverse blunt body code. For this calculation the wing and canopy were left off and a typical body cross section was simulated by two ellipses whose semi-major and semi-minor axes varied as cubic polynomials with longitudinal distance. The shock shape for the fuselage only configuration in Mach 7.4 flow at 15.3° angle of attack is shown in Figure 10 for both the planform and profile views. The shock location plotted in the planform view is the picture that an experimental shadowgraph would depict. Also shown is the intersection between the bow shock and the wing, which occurs well inside the projected shock trace because the body is at angle of attack. This is illustrated in the cross sectional shock shapes shown later.

SHOCK SHAPES FOR MSC 040A SHUTTLE ORBITER FUSELAGE ONLY

$M = 7.4 \qquad \alpha = 15.3°$

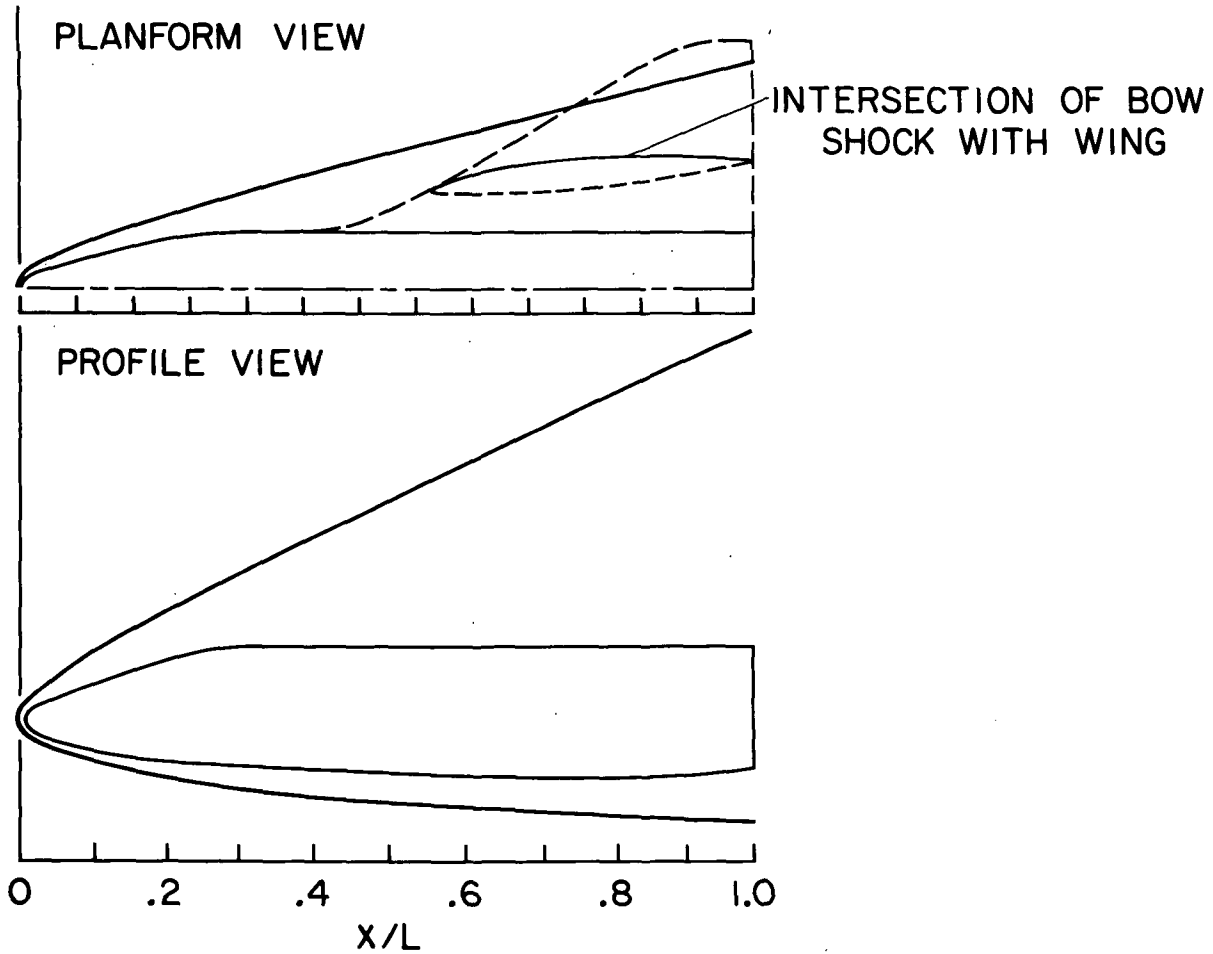

Figure 10

LONGITUDINAL SURFACE PRESSURE DISTRIBUTION FOR MSC 040A

(Figure 11)

The longitudinal variation of the surface pressure coefficient at three meridional locations of the MSC 040A fuselage is shown in Figure 11. Data is plotted beginning at the junction of the spherical nose and the three-dimensional afterbody. Due to numerical difficulties at the surface in the leeward plane the calculation was terminated at an x/L of .65. In approximating the 040A fuselage analytically by the present procedure, no constraint was place on the continuity of the second derivative (curvatures) of the body shape. This, therefore, can result in an unusual behavior of the solution at the matching points of the cubic polynomials. For the 040A the number of matching points was largest near the nose, in an attempt to accurately define it, and this resulted in the peculiar variations (plateaus) of the surface pressure distribution in that region. For this particular calculation the grid size consisted of 30 points in the radial direction and 19 points in the meridional direction. The large number of points was sufficient to clearly define the entropy layer at the surface. These results were obtained using a second-order noncentered, finite difference scheme. To calculate 65 percent of the body in 897 longitudinal steps required 54 minutes on an IBM 360/67 linked with an IBM 2250 cathode ray display tube.

LONGITUDINAL SURFACE PRESSURE DISTRIBUTION FOR MSC 040 A SHUTTLE ORBITER

FUSELAGE ONLY

M = 7.4 α = 15.3°

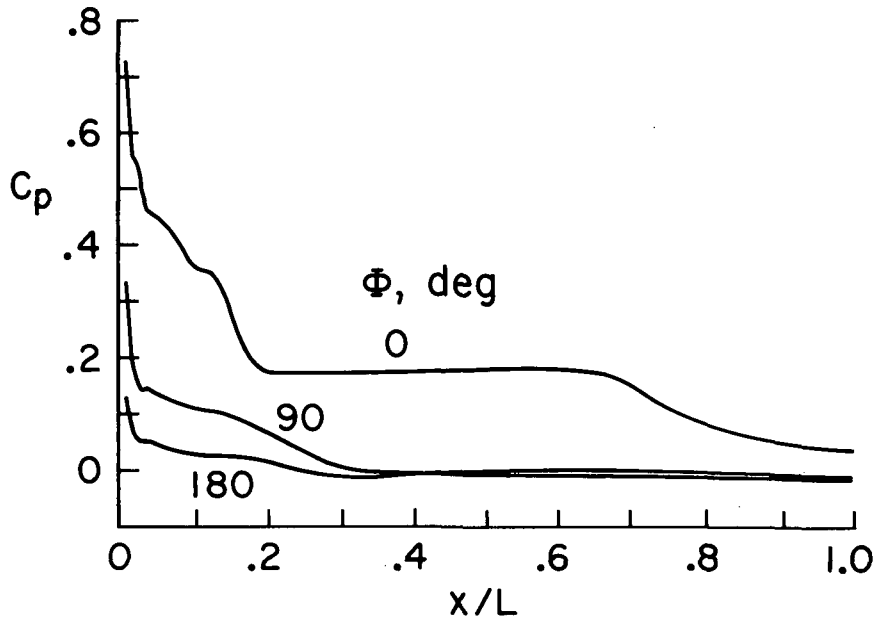

Figure 11

CROSS SECTIONAL SHOCK SHAPES AT VARIOUS LONGITUDINAL STATIONS FOR MSC 040A

(Figure 12)

The cross-sectional shock shapes of various longitudinal stations of the MSC 040A fuselage only configuration are shown in Figure 12. Also shown is a comparison of the actual body cross section with the simulated cross section. It can be seen from this figure that at an x/L of .55 the bow shock intersects the trace of the wing leading edge in the $\Phi = 66°$ meridian ($\Phi = 0°$ is the windward plane). Downstream of this point the wing extends beyond the bow shock and the points of intersection of it on the upper and lower surfaces of the wing can easily be found. The trace of the bow shock on the wing will most definitely be a region of high heat transfer and one important to the thermal protection system design. It is believed that inclusion of the wing in the calculation will not significantly affect the intersection location. However, a more accurate representation of the fuselage at least near the nose could have a slight effect on this intersection location.

CROSS SECTIONAL SHOCK SHAPES FOR MSC 040 A
FUSELAGE ONLY

$M = 7.4 \qquad \alpha = 15.3°$

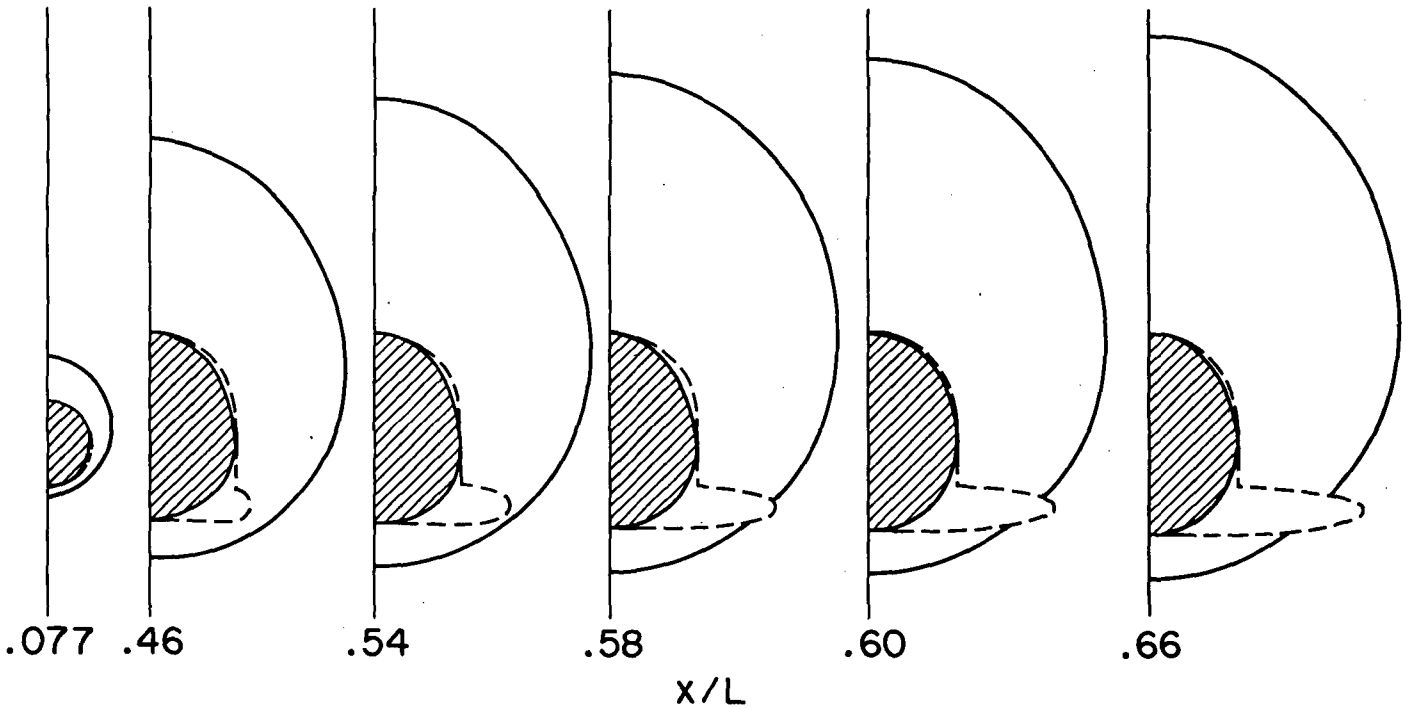

Figure 12

CONCLUDING REMARKS

(Figure 13)

We have presented some typical results obtained with two different computer codes currently in use at NASA-ARC for multidimensional supersonic flow fields. The relative merits of these methods are discussed in greater detail in another paper[4] which showed good agreement between results of the two methods. The shock capturing technique (SCT) is inherently more efficient than the characteristics code (MOC), being about four times faster on a point by point basis. The SCT code usually requires more mesh points than the MOC code when differencing across the bow shock. However, an advantage of using a large number of mesh points to describe the shock layer is that such things as the canopy shock, recompression shock and entropy layer can be accurately predicted. The use of a shock fitting procedure for the main bow shock is an obvious improvement, and work is in progress to develop such a code. This code would still allow the capturing of secondary shocks that form behind the bow shock. Considering its computational efficiency and ease in treating complex shock interaction, the SCT code may have an advantage over the present MOC program.

This paper may be considered a progress report on the efforts at Ames Research Center to develop a computational capability which can contribute, in a significant and timely way, to the design of the Space Shuttle vehicle. Some valuable work has been performed, but much remains to be done. For example, there is a need to include reaction chemistry in the calculations, so that the concentration of atomic species, which may control heat-shield performance, can be estimated. In addition the coupling of the inviscid and boundary-layer programs must be made more automatic. These are tasks that can be accomplished with the present methods and work is progressing in this direction.

SUMMARY

METHOD	ACCOMPLISHMENTS	PROBLEMS AND FUTURE EFFORT
SCT	COMPLEX SHUTTLE SHAPES SECONDARY SHOCKS INTERSECTING SHOCKS	WING LEADING EDGE EQUILIBRIUM GAS REACTING GAS
MOC	COMPLEX SHUTTLE SHAPES EQUILIBRIUM GAS DATA FOR BOUNDARY LAYER ANALYSIS	WING LEADING EDGE REACTING GAS SECONDARY SHOCKS

Figure 13

REFERENCES

1. Rakich, J. V.: Method of Characteristics for Steady Three-Dimensional Supersonic Flow With Application to Inclined Bodies of Revolution. TN D-5341, 1969, NASA.
2. Kutler, P., and Lomax, H.: Shock-Capturing, Finite-Difference Approach to Supersonic Flows. To be published in J. of Spacecraft and Rockets, Nov. or Dec., 1971.
3. Lomax, Harvard, and Inouye, Mamoru: Numerical Analysis of Flow Properties About Blunt Bodies Moving at Supersonic Speeds in an Equilibrium Gas. NASA TR R-204, 1964.
4. Rakich, John V., and Kutler, Paul: Comparison of Characteristics and Shock Capturing Methods With Application to the Space Shuttle Vehicle. Paper presented at the AIAA 10th Aerospace Sciences Meeting, San Diego, January 17-19, 1972.
5. Cleary, J. W.: Hypersonic Shock Wave Phenomena of a Delta-Wing Space Shuttle Orbiter. NASA TM X62,076.
6. Marvin, Joseph G. and Sheaffer, Yvonne S.: A Method for Solving the Nonsimilar Laminar Boundary-Layer Equations Including Foreign Gas Injection. NASA TN D-5516, 1969.
7. Lockman, William K., and DeRose, Charles E.: Aerodynamic Heating of a Space Shuttle Delta Wing Orbiter. TM X62,057, Aug. 1971.
8. Hamilton, H.H., and DeJarnette, F.R.: Inviscid Surface Streamline Program For Use In Predicting Shuttle Heating Rates. Space Shuttle Aerothermodynamics Technology Conference, Ames Research Center, Dec. 15-16, 1971.

FLOW FIELD PREDICTIONS FOR A SLAB DELTA WING AT INCIDENCE

By R. J. Conti, P. D. Thomas, and Y. S. Chou
Lockheed Palo Alto Research Laboratory

SUMMARY

Theoretical results are presented for the structure of the hypersonic flow field of a blunt slab delta wing at moderately high angle of attack. Special attention is devoted to the interaction between the boundary layer and the inviscid entropy layer. The results are compared with experimental data.

The three-dimensional inviscid flow is computed numerically by a "marching" finite-difference method. Attention is concentrated on the windward side of the delta wing, where detailed comparisons are made with the data for shock shape and surface pressure distributions. Surface streamlines are generated, and used in the boundary layer analysis.

The three-dimensional laminar boundary layer is computed numerically using a specially-developed technique based on small cross-flow in streamline coordinates. In the rear sections of the wing the boundary layer decreases drastically in the spanwise direction, so that it is still submerged in the entropy layer at the centerline, but surpasses it near the leading edge. Predicted heat transfer distributions are compared with experimental data.

This work was sponsored by the Lockheed Independent Research Program as part of the analysis of Space Shuttle flow fields.

INTRODUCTION

The main objective of this study was to test a complete three-dimensional flow field prediction, including inviscid flow and boundary layer, by comparison with detailed wind-tunnel measurements. During the development of the computational tools for three-dimensional flow, the computer codes were checked by calculating flow over simple shapes (such as sharp and blunted cones) for which the flow field is well known. The present effort takes a step beyond that by dealing with a more complicated shape. The slab delta wing was chosen for two reasons: good experimental results are available in the work of Whitehead and Dunavant (Ref. 1), and this shape, which is of interest to Space Shuttle applications, poses a more severe test than, say, a typical shuttle fuselage. This is so because the slab delta wing sustains a combination of inboard and outboard transverse pressure gradients, due to the fact that the peak pressure is located at the centerline near the nose, and near the leading edge in downstream sections. As a consequence, both the inviscid and viscous analyses are tested under a combination of effects. The next step, reserved for future work, is to calculate the flow field for a complete shuttle configuration, including fuselage and wings.

There were two secondary objectives in this study. The first was to pursue a complete calculation to its final stage, that is, to an estimate of heat transfer, in order to gain an appreciation for the difficulties involved and of the accuracy needed at the different stages of computation of inviscid and boundary-layer flows. In this respect it was somewhat surprising to find that the calculation of three-dimensional boundary layer demands considerable accuracy in the inviscid calculations. The suspicion that finite-difference calculation of the inviscid flow might constitute "accuracy overkill" did not materialize in this study.

The other secondary objective was to assess the interference of boundary layer and inviscid entropy layer. Unfortunately, it turned out that the model was not long enough to produce an extreme case of interference, but nevertheless the boundary layer did become larger than the

entropy layer in the downstream sections near the leading edge. In this case the conventional first-order boundary layer calculation yielded acceptable values of heat transfer, and, when corrected grossly for edge conditions, the change in heat transfer was small. Nevertheless, this evidence is not sufficient to conclude that the interference between boundary layer and entropy layer is negligible.

MODEL AND STREAM CONDITIONS

(Figure 1)

The inviscid flow was calculated with the method of Thomas, et al. described in Ref. 2. This is a marching finite-difference method for supersonic three-dimensional flows. Some of the main features are a sharp-shock treatment for the bow shock, nonlinear stretching of coordinates in the radial and meridional directions (about the longitudinal axis) to resolve steep gradients in the flow, acceptance of a wide range of body geometries, and perfect-gas or equilibrium-air options. The subsonic and transonic parts of the flow near the nose were calculated, in this case, with the method of Inouye, Rakich and Lomax (Ref. 3). The stream conditions and body shape corresponded exactly to those of the wind-tunnel experiments (Ref. 1). Since real-gas effects were negligible in the experiments, the flow was calculated using the perfect-gas option.

The body was a flat, slab delta wing with spherically-blunted nose and cylindrical leading edges, having a sweep angle of 80 degrees. The angle of attack was 20 degrees. The Mach number was 9.6, ratio of specific heats 1.4, Reynolds number based on thickness 10^5, stagnation pressure 45 atm, and stagnation temperature 920 degrees Kelvin. The wall-temperature ratio was 0.32.

SKETCH OF MODELS. (ALL DIMENSIONS ARE IN CM)

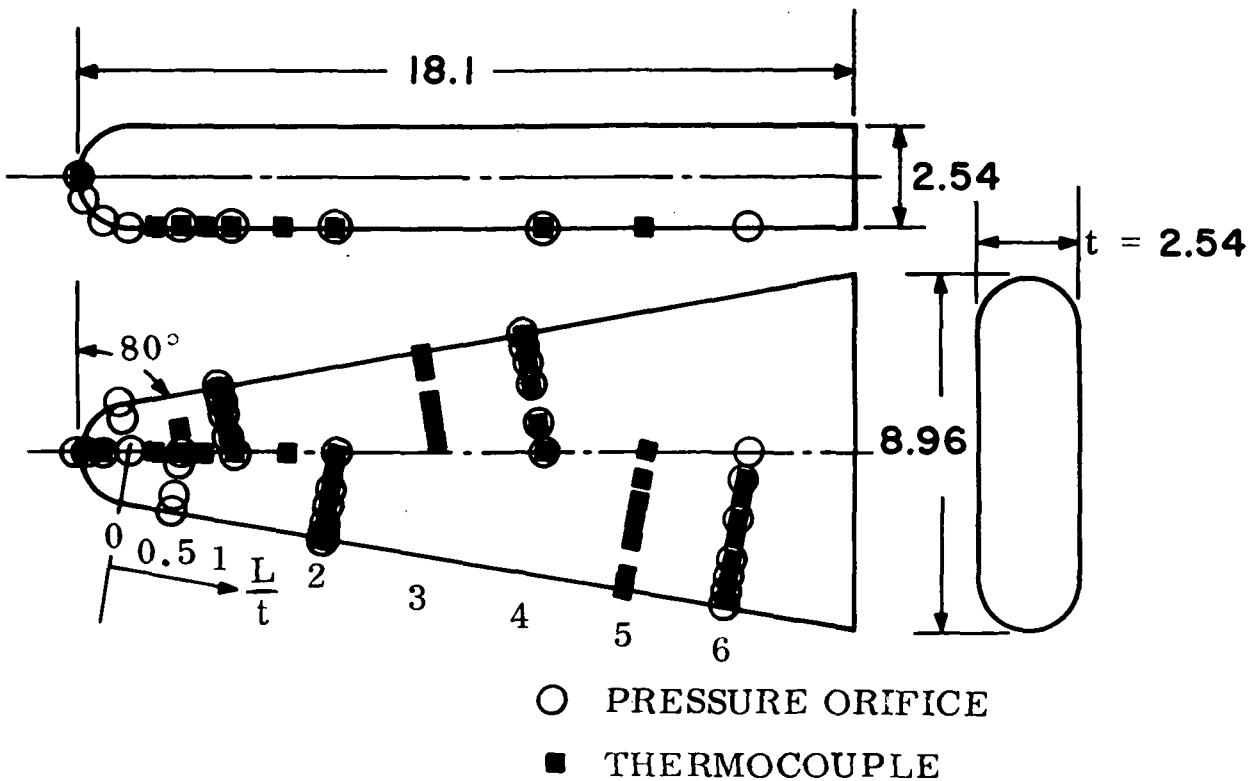

Figure 1

SHOCK SHAPE AND SURFACE STREAMLINE PATTERN

(Figure 2)

The flow field was calculated over the entire cross section (windward and leeward sides) in the forward third of the body. When the cross flow became supersonic the calculation was cut off at the geometric leading edge, and attention was focused on the windward part of the wing. At this angle of attack it is expected that viscous effects in the leeward side are such that the inviscid calculation is irrelevant.

The calculated shock shape agrees well with the measured one, but this is not considered to be a stringent test because shock shape is an insensitive characteristic. The data points were taken from a small photograph, and slight discrepancies with the calculated shock are probably due to reading errors and are unimportant.

The surface streamlines were obtained with a separate calculation, by integrating the inviscid surface velocity. Knowledge of the velocity vector and the unit vector normal to the surface is sufficient to calculate the curvature vector, its projections along and normal to streamlines, and the metric of a streamline-oriented curvilinear coordinate system. In addition, the streamline routine calculates inputs for the boundary layer, such as the transformed longitudinal coordinate (which includes compressibility and edge-property effects) and edge velocity gradient.

The figure shows the effects of transverse pressure gradients on streamline shape. Near the nose, where the peak pressure is at the centerline, all streamlines curve toward the leeward side. Downstream, where there is a pressure ridge near the leading edge, some streamlines are turned leeward and some are turned toward the centerline.

SHOCK SHAPE AND SURFACE STREAMLINE PATTERN
80° SLAB DELTA WING, $\alpha = 20°$, $M_\infty = 9.6$, $\gamma = 1.4$

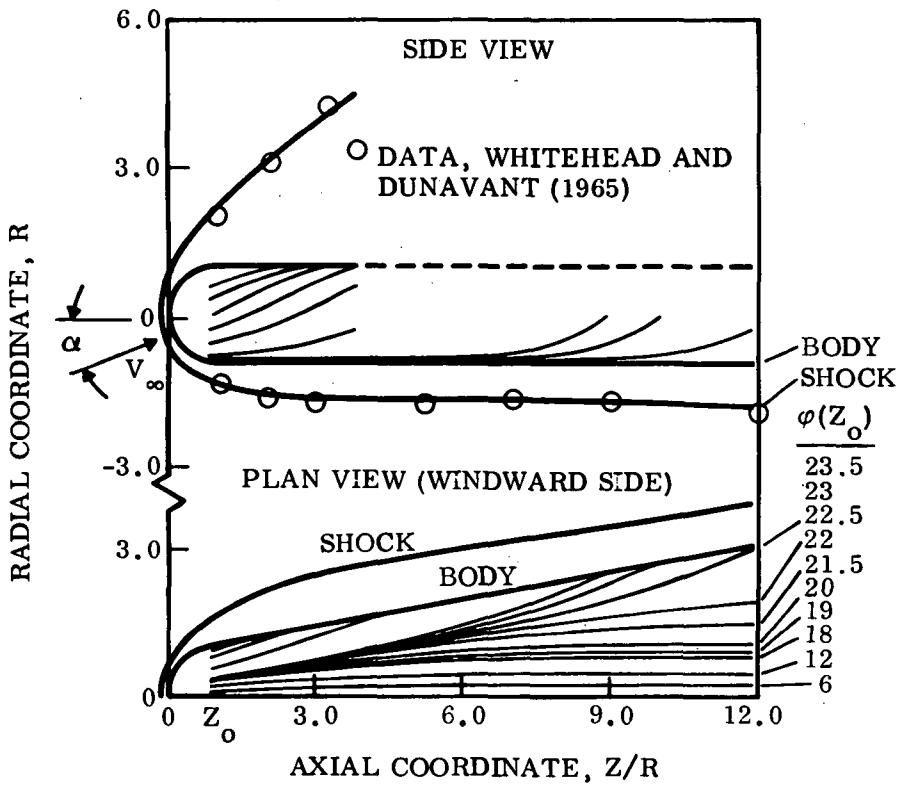

Figure 2

WINDWARD CENTERLINE PRESSURE

(Figure 3)

The surface pressure on the centerline is plotted versus the axial coordinate. The figure shows the rapid expansion around the nose, followed by a slight overexpansion (typical of blunt-nosed bodies) and a subsequent recompression. The agreement between theory and experiment is excellent. The theoretical curve shows a slight oscillation at the juncture between the spherical nose and the flat underside of the wing. This oscillation is induced in the numerical results by the discontinuity in curvature at the juncture.

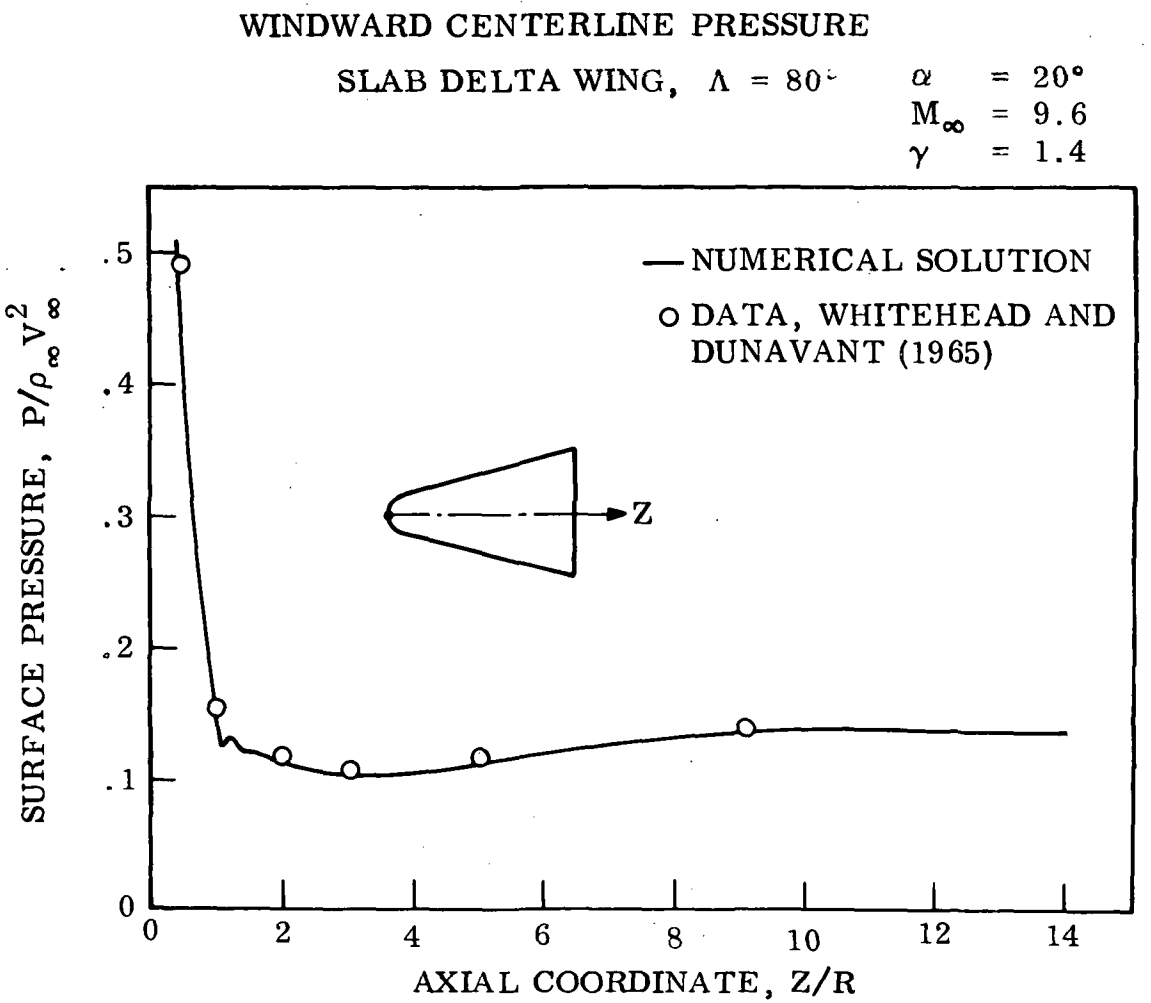
WINDWARD CENTERLINE PRESSURE
SLAB DELTA WING, Λ = 80°
α = 20°
M∞ = 9.6
γ = 1.4
— NUMERICAL SOLUTION
o DATA, WHITEHEAD AND DUNAVANT (1965)
Z
SURFACE PRESSURE, P/ρ∞V∞²
.5
.4
.3
.2
.1
0
0
2
4
6
8
10
12
14
AXIAL COORDINATE, Z/R

Figure 3

SURFACE PRESSURE DISTRIBUTIONS IN PLANES NORMAL TO THE LEADING EDGE

(Figure 4)

Surface pressure distributions are plotted versus distance along the surface, measured from the geometric leading edge, for several downstream locations. Notice that the downstream distance L is measured parallel to the leading edge, rather than to the centerline. Similarly, the surface location S is normal to the leading edge, not the centerline. This change in coordinates was needed to accommodate the experimental data. It has a slight effect on the shape of the curves, notably near the nose where the pressure maximum appears to be off-centerline and the curve appears to be nonsymmetric about the centerline. The agreement between theory and experiment is good, except at isolated points where discrepancies remain unexplained.

SURFACE PRESSURE DISTRIBUTIONS IN PLANES NORMAL TO THE LEADING EDGE

SLAB DELTA WING, $\Lambda = 80^{\circ}$, $\gamma = 1.4$, $\alpha = 20^{\circ}$, $M_{\infty} = 9.6$

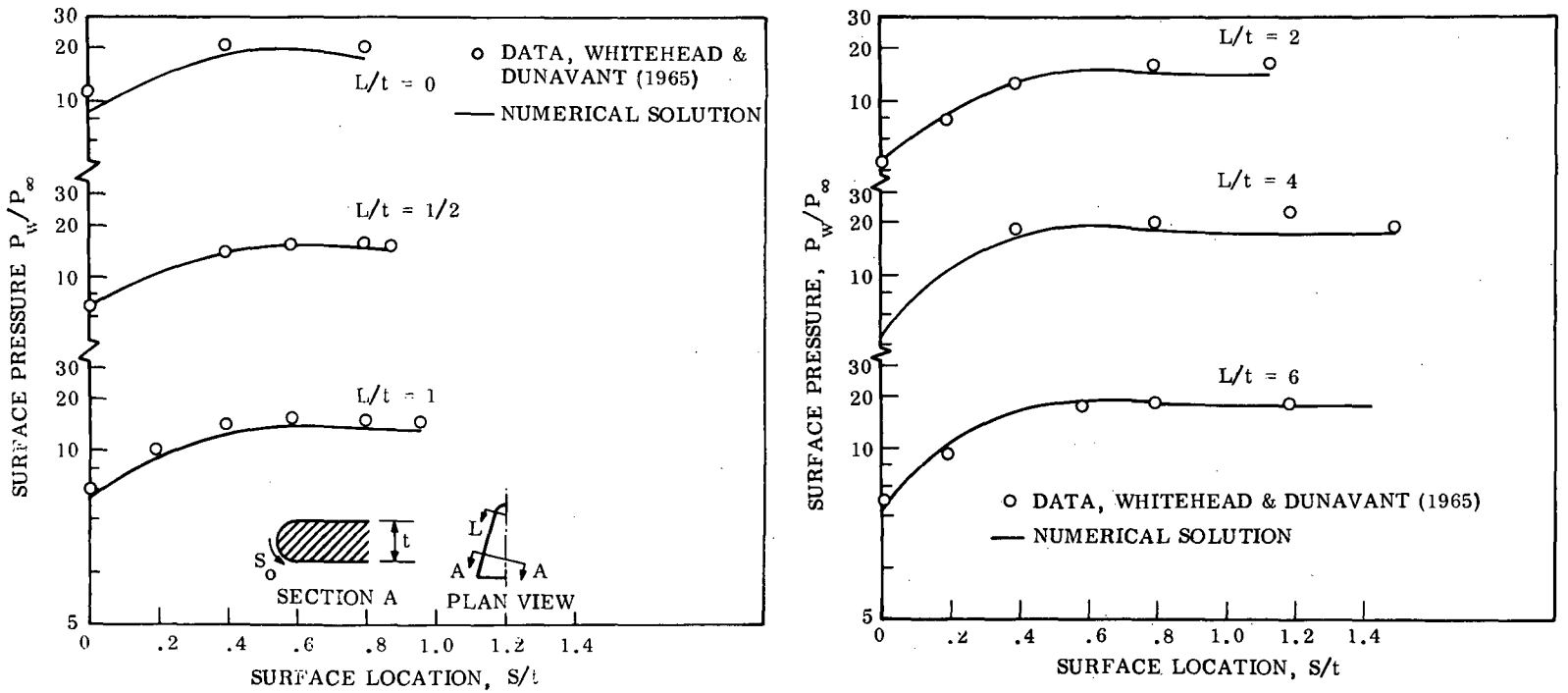

Figure 4

ENTHALPY PROFILE

(Figure 5)

The distribution of enthalpy across the shock layer at about 13 nose radii from the nose is shown for two locations: the centerline and a point near the leading edge. The entropy layer, a region of hot, slow-flowing gas that traversed the bow shock near the nose (where the shock is strongest) is located near the surface. It can be seen that the entropy layer is much thicker at the centerline (about 0.30 nose radii) than near the leading edge (about 0.05 nose radii). This is a feature unknown to axisymmetric flows, where the entropy layer thins out uniformly in the downstream direction.

The presence of the entropy layer extracts a heavy tax from the computational scheme since, in order to resolve the steep gradients in the layer and maintain computational stability, it is necessary to concentrate mesh points near the surface. In the present computational scheme this is done by "stretching" the normal coordinate. Moreover, we have found that a preset stretching (either constant or variable in the downstream direction) is not sufficient to solve the difficulty. We have had to resort to a self-adjusting scheme that will regulate the concentration of mesh points during execution of the calculation. It is emphasized that the difficulty is not just one of losing detail in the entropy layer (which would be affected by viscous effects in any case) but one of losing the integrity of the whole calculation unless every region of the flow is properly resolved. The need to change the stretching factor in the meridional direction is not as critical, in particular in the present scheme where the mesh size is proportional to the shock layer thickness, and therefore the mesh is automatically refined at places (such as leading edges) where the shock layer is thinner.

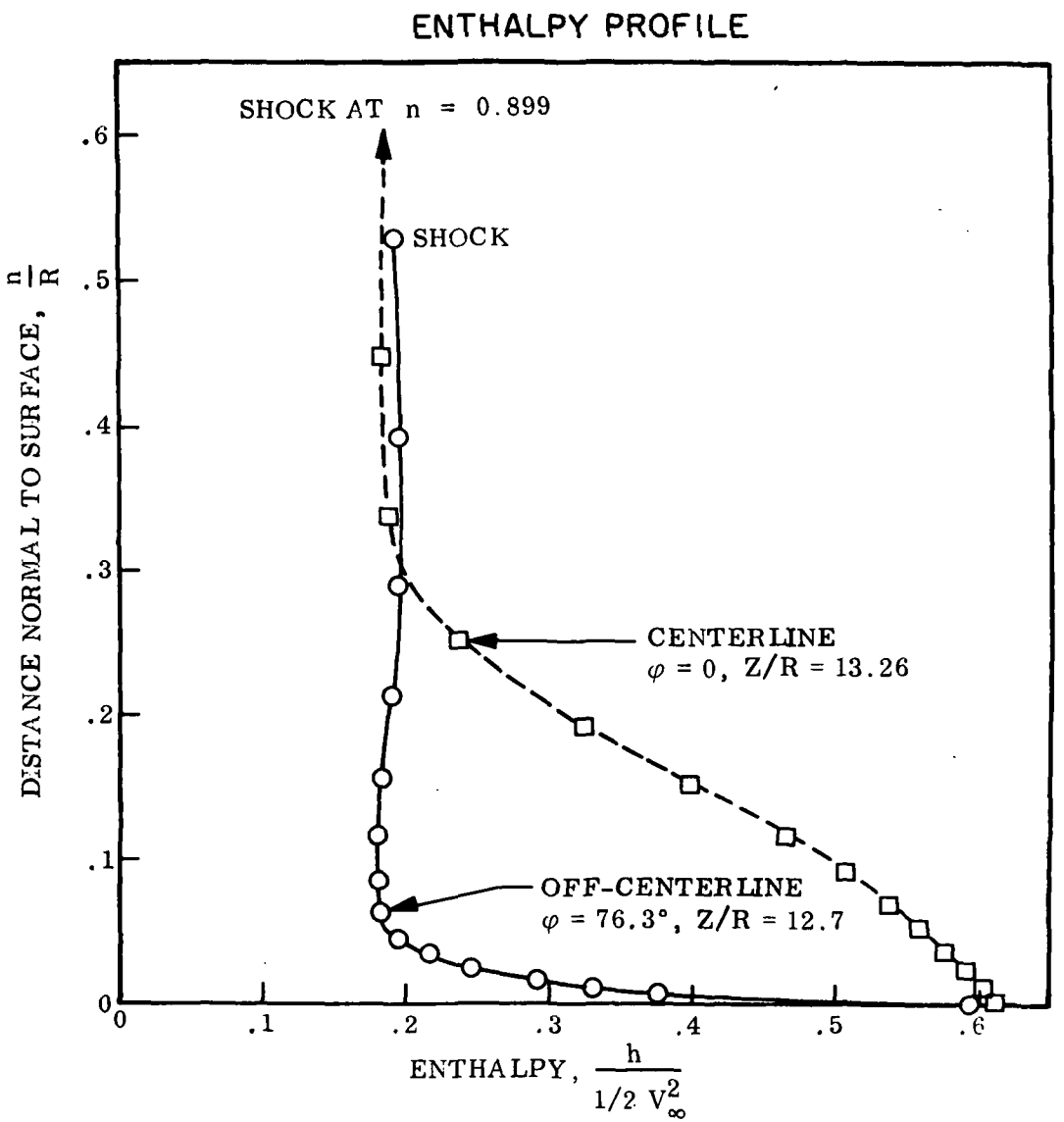
ENTHALPY PROFILE
SHOCK AT n = 0.899
SHOCK
CENTERLINE
φ = 0, Z/R = 13.26
OFF-CENTERLINE
φ = 76.3°, Z/R = 12.7
DISTANCE NORMAL TO SURFACE, n/R
ENTHALPY, h/(1/2 V∞²)
0
.1
.2
.3
.4
.5
.6

Figure 5

BOUNDARY-LAYER CALCULATIONS

Heat Transfer Distribution Along Centerline

(Figure 6)

The three-dimensional laminar boundary layer was calculated with a technique developed by Y. S. Chou for this particular application. The technique is based on small cross flow in streamline coordinates. This places no restriction on the curvature of inviscid streamlines, but assumes that inside the boundary layer the deviation from inviscid streamlines is small, which is a good assumption for hypersonic flow over cold walls. For the sake of simplicity it is assumed that the Prandtl number is constant (not necessarily unity), the product of density and viscosity does not vary across the layer (it is evaluated at the "reference conditions") and the density is inversely proportional to the enthalpy. The theory does not resort to "local flat plate" or self-similarity assumptions. The method has been tested successfully on ellipsoids and blunted cones at incidence.

The centerline distribution of heat transfer coefficient, referred to the stagnation-point value, is shown versus the axial coordinate in nose radii. The striking feature about this distribution is its serpentine character, most of which can be attributed to cross flow effects. This is somewhat surprising in view of the simple geometry of the delta wing but, as stated previously, the cross flow varies and changes sign as one moves downstream. The character of the theoretical curve seems to be supported by the experimental results. The general agreement between theory and experiment is good by heat-transfer standards, the largest discrepancy being about 25 percent. The solid square at the end of the curve indicates the effect of making an entropy-layer correction, to be discussed later.

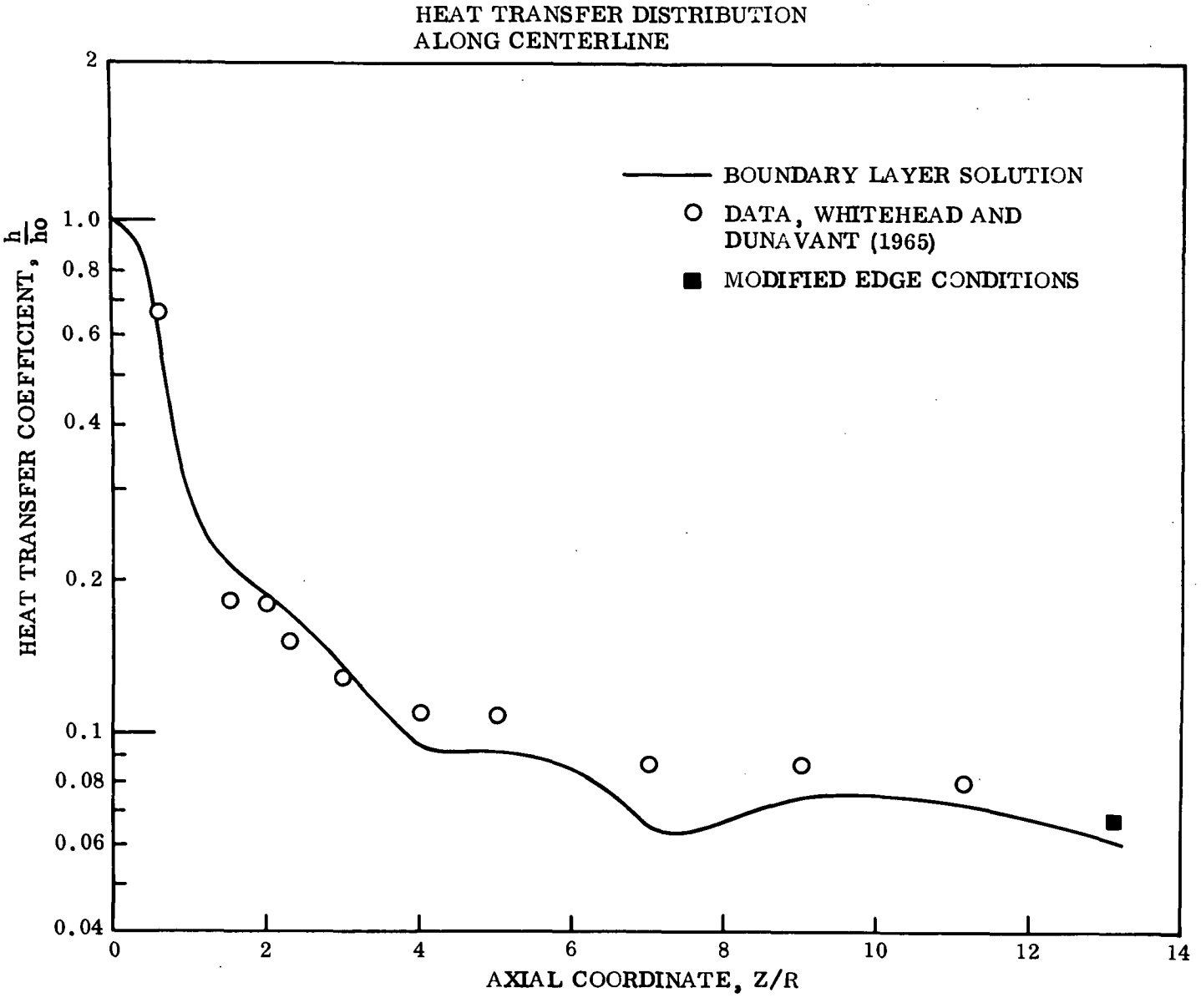
HEAT TRANSFER DISTRIBUTION
ALONG CENTERLINE
BOUNDARY LAYER SOLUTION
DATA, WHITEHEAD AND DUNAVANT (1965)
MODIFIED EDGE CONDITIONS
HEAT TRANSFER COEFFICIENT, h/ho
2
1.0
0.8
0.6
0.4
0.2
0.1
0.08
0.06
0.04
0
2
4
6
8
10
12
14
AXIAL COORDINATE, Z/R

Figure 6

SPANWISE DISTRIBUTION OF BOUNDARY-LAYER THICKNESS

(Figure 7)

The boundary layer varies drastically in the spanwise direction due to three-dimensional effects. At about 12 nose radii from the nose ($L/t = 6$) the physical thickness varies by about a factor of three from the centerline (where it is thicker) to the leading edge. This decrease in thickness towards the leading edge corresponds to an approximately equal increase in heat transfer, in spite of the fact that the pressure is lower at the leading edge. It will be recalled that the entropy layer decreases by a factor of five in the same spanwise region, and therefore the boundary layer thickens with respect to the entropy layer in the outboard direction.

SPANWISE DISTRIBUTION OF BOUNDARY-LAYER THICKNESS AT L/t = 6

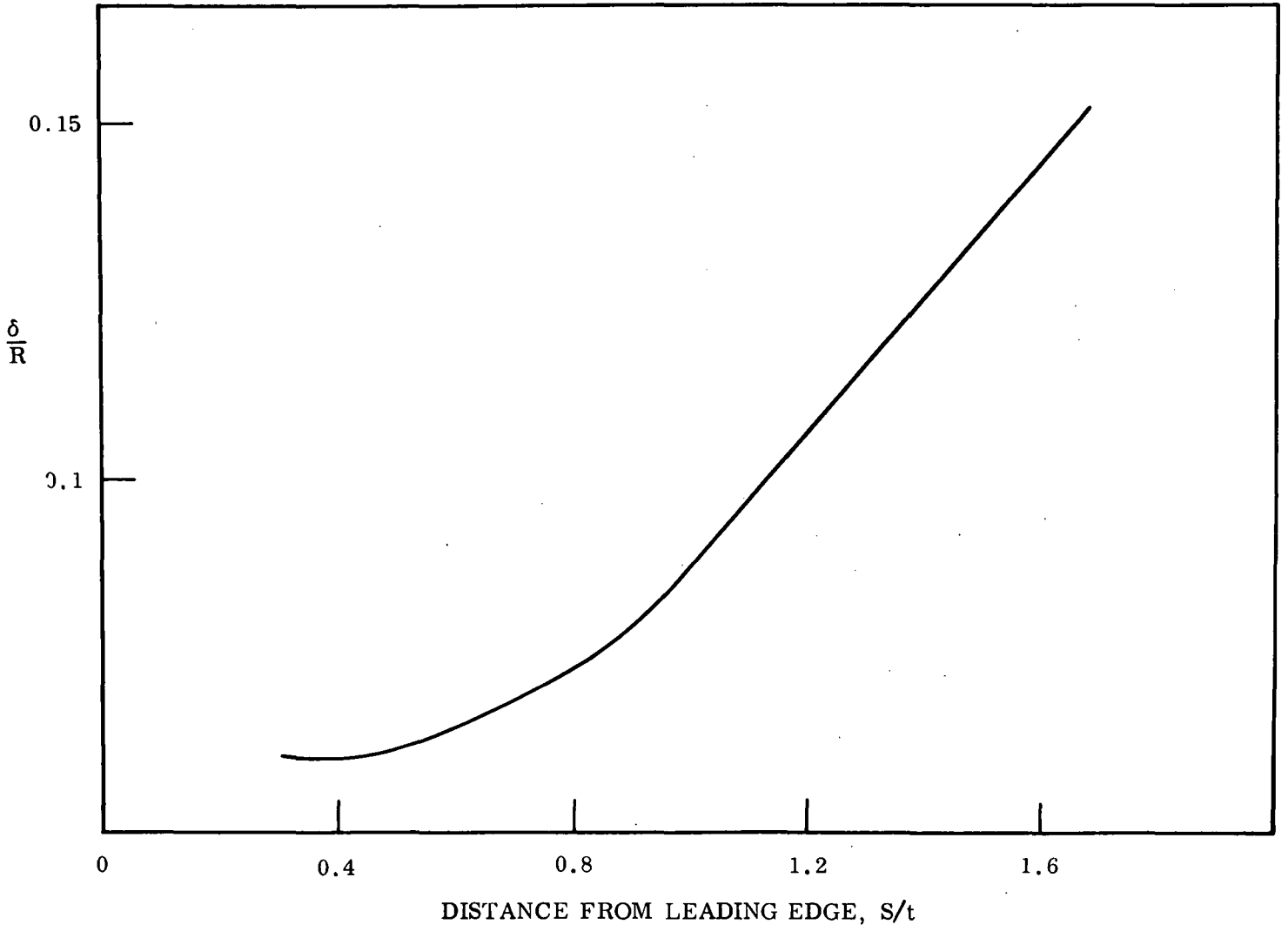

Figure 7

SPANWISE HEAT TRANSFER DISTRIBUTION

(Figure 8)

The absolute heat transfer, represented by the Stanton number, is plotted versus distance from the leading edge at two downstream locations: $L/t = 3$ (about 6 nose radii) and $L/t = 6$ (about 12 nose radii). As indicated previously, the boundary layer thins out in the outboard direction, and the heat transfer follows suit. The general agreement between theory and experiment is good, the largest discrepancy being about 25 percent. This occurs at $L/t = 6$, at one inboard and one outboard point, and remains unexplained. The correction for entropy layer is small, about 10 percent in all cases. It always increases the heat transfer, which seems to be in the direction of the experimental data for the inboard point, but opposite to it for the outboard point.

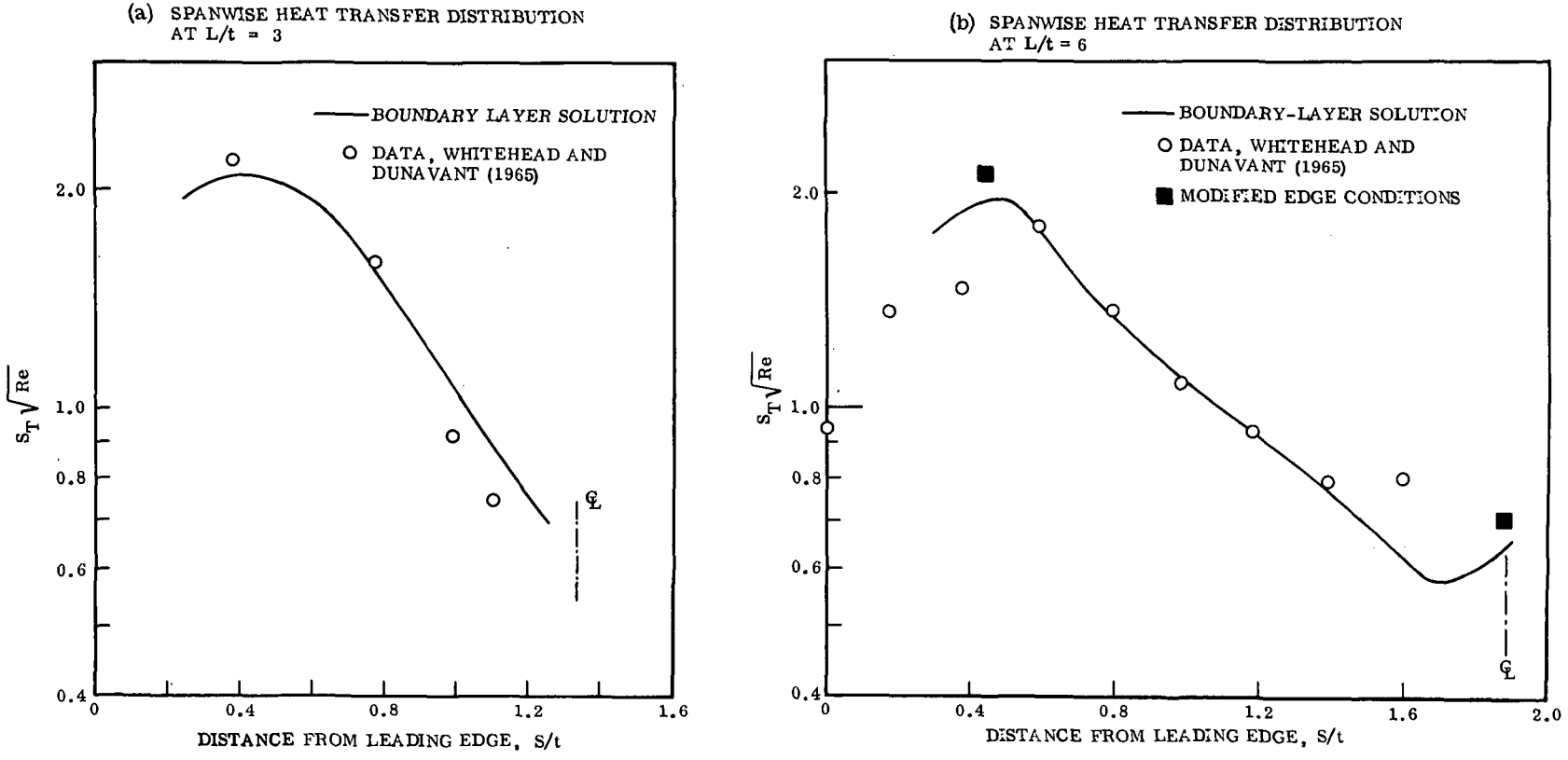
(a) SPANWISE HEAT TRANSFER DISTRIBUTION AT L/t = 3
BOUNDARY LAYER SOLUTION
DATA, WHITEHEAD AND DUNAVANT (1965)
$S_T\sqrt{Re}$
2.0
1.0
0.8
0.6
0.4
0
0.4
0.8
1.2
1.6
℄
DISTANCE FROM LEADING EDGE, S/t
(b) SPANWISE HEAT TRANSFER DISTRIBUTION AT L/t = 6
BOUNDARY-LAYER SOLUTION
DATA, WHITEHEAD AND DUNAVANT (1965)
MODIFIED EDGE CONDITIONS
$S_T\sqrt{Re}$
2.0
1.0
0.8
0.6
0.4
0
0.4
0.8
1.2
1.6
2.0
℄
DISTANCE FROM LEADING EDGE, S/t

Figure 8

ENTHALPY PROFILE IN THE BOUNDARY LAYER

(Figure 9)

It will be recalled that near the base of the model, at about 13 nose radii from the nose, both boundary layer and entropy layer thin out in the outboard direction, the boundary layer by a factor of three, the entropy layer by a factor of five (see figures 5 and 7). The boundary layer, which is about half the thickness of the entropy layer at the centerline, thus becomes somewhat thicker than the entropy layer near the leading edge. In an attempt to estimate the magnitude of the interaction we calculated the boundary layer twice: once in the classical manner, where edge conditions match the inviscid flow at the wall, and once by patching the edge conditions to those in the interior of the inviscid flow, at the point where the physical "edge" of the boundary layer would be. Partial results are shown in figure 9 in the form of enthalpy profiles in the inviscid flow, in the classical boundary layer, and with modified edge conditions.

It can be seen that the enthalpy profile changes substantially, both in magnitude and character. The classical boundary layer has a monotonic profile, the modified one a bulging profile. This is particularly marked at the leading-edge location, where the edge is hotter than the wall in the classical case and colder than the wall in the modified version. Nevertheless, the heat transfer changes by less than 10 percent, as was indicated previously (see figures 6 and 8b). This partial evidence tends to indicate that heat transfer is not very sensitive to entropy layer interaction, but more work is needed before a general conclusion can be reached.

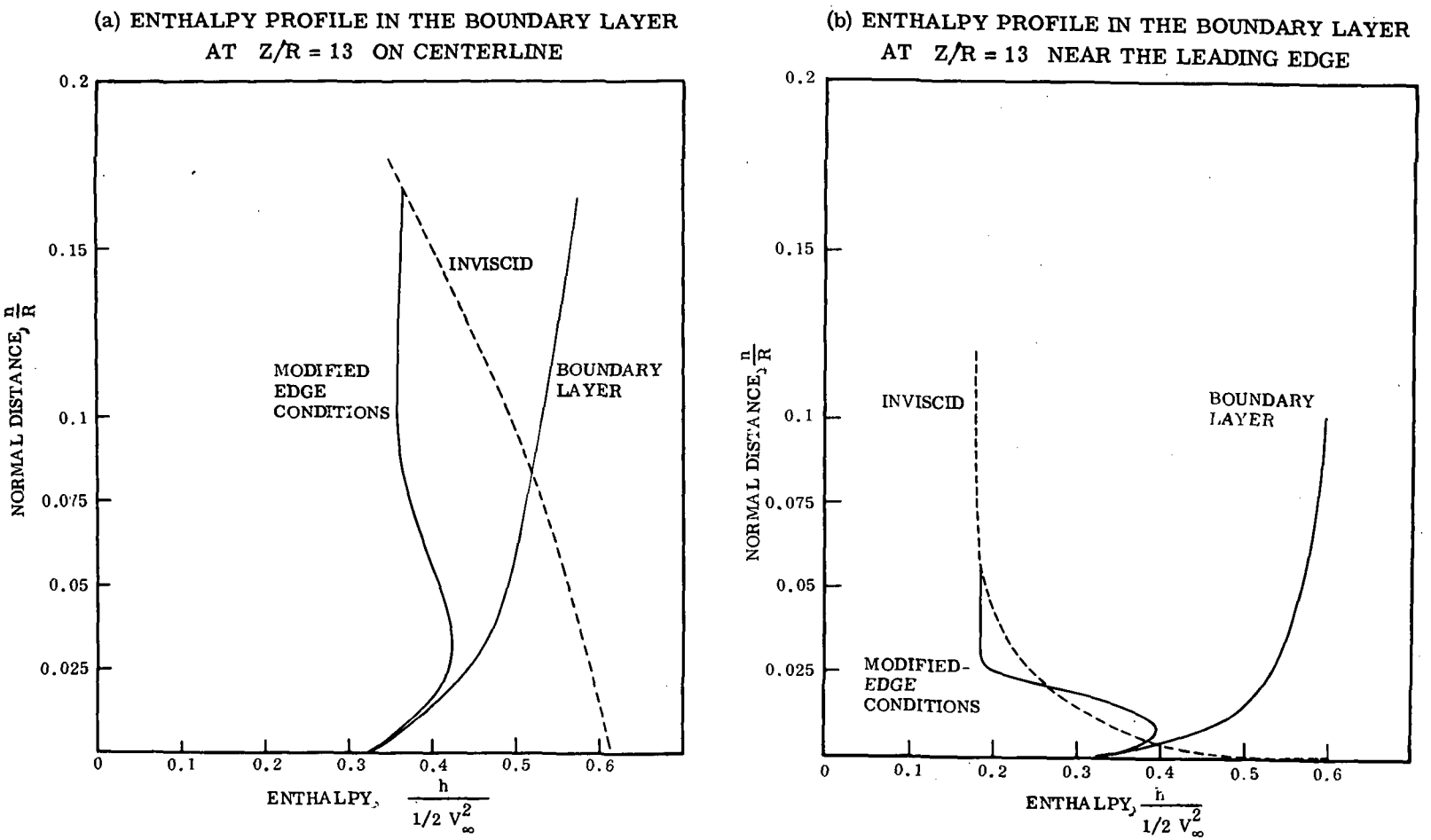
(a) ENTHALPY PROFILE IN THE BOUNDARY LAYER AT Z/R = 13 ON CENTERLINE
NORMAL DISTANCE, n/R
0.2
0.15
0.1
0.075
0.05
0.025
0
0.1
0.2
0.3
0.4
0.5
0.6
ENTHALPY, h / 1/2 V∞²
INVISCID
MODIFIED EDGE CONDITIONS
BOUNDARY LAYER
(b) ENTHALPY PROFILE IN THE BOUNDARY LAYER AT Z/R = 13 NEAR THE LEADING EDGE
NORMAL DISTANCE, n/R
0.2
0.15
0.1
0.075
0.05
0.025
0
0.1
0.2
0.3
0.4
0.5
0.6
ENTHALPY, h / 1/2 V∞²
INVISCID
BOUNDARY LAYER
MODIFIED-EDGE CONDITIONS

Figure 9

REFERENCES

1. Whitehead, A. H. and Dunavant, J. C.: "A Study of Pressure and Heat Transfer over an 80° Swept Slab Delta Wing in Hypersonic Flow." NASA TND-2708, 1965.
2. Thomas, P. D.; Vinokur, M.; Bastianon, R.; and Conti, R.: "Numerical Solution for the Three-Dimensional Hypersonic Flow Field of a Blunt Delta Body." AIAA Paper 71-596, 1971.
3. Inouye, M; Rakich, J. V.; and Lomax, H.: "A Description of Numerical Methods and Computer Programs for Two-Dimensional and Axisymmetric Supersonic Flow over Blunt-Nosed and Flared Bodies." NASA TND-2970, 1965.

SPACE SHUTTLE ORBITER REENTRY FLOW FIELD AND HEATING ANALYSIS

By W. C. Rochelle, TRACOR, Inc., Austin, Tex.,
B. B. Roberts, NASA/MSC, Houston, Tex.,
F. W. Vogenitz, TRW Systems, Redondo Beach, Calif.,
and L. d'Attorre, TRW Systems, Redondo Beach, Calif.

INTRODUCTION

This paper presents the results of a study performed by TRW Systems for NASA/MSC which determined the reentry flow field and thermal environment around the straight wing Shuttle Orbiter vehicle. The objective of the study was to calculate both rarefied and continuum flow fields and associated heating rates on various configurations representative of the Orbiter at high angle of attack. Rarefied flow fields and heating rates were computed by the Monte Carlo Direct Simulation Technique for altitudes above 82.3 Km (Kn > 0.001). Continuum inviscid flow fields were calculated by 2-D unsteady and 3-D steady finite difference/artificial viscosity methods and also by a 2-D shock layer analysis technique. Viscous flow fields and heating rates in the continuum regime were computed by a boundary layer integral matrix method for laminar flow and by an aerodynamic surface heating technique for turbulent flow. Shapes considered in the study included flat plates (representing the underside of the Orbiter fuselage or the wing MAC), Orbiter fuselage cross sections, Orbiter wing airfoils, and 3-D Orbiter configurations, all at high angle of attack (40° - 60°). The theoretical results showed good agreement with pressure and heat transfer data obtained at NASA/MSC, NASA/Ames, NASA/Langley, and Cornell Aeronautical Laboratory (CAL).

(Figure 1)

The first figure shows a table listing all of the cases analyzed in this study by the Monte Carlo direct simulation technique for rarefied flows and by the finite difference/artificial viscosity method for continuum flows. The complete results of this study are given in Ref. 1 and a User's Manual for the Monte Carlo programs is listed as Ref. 2.

The Monte Carlo method was used for 9 cases of a flat plate at high angle of attack simulating the Orbiter wing chord. Three altitudes were considered for the flat plate: 121.8 Km, 102.2 Km, and 88.1 Km. Two cases of rarefied flow around an Orbiter cross section were considered at altitudes of 121.8 Km and 98.1 Km. In addition, a 3-D representation of the Orbiter fuselage and wings at 109.8 Km was analyzed by the Monte Carlo technique. For the cross sections and 3-D shape, a hard sphere molecular model of $\gamma = 1.67$ and $\alpha = 60^{\circ}$ with diffuse reflection at the surface was assumed, while for the flat plates the following parameters were varied: Knudsen No. (altitude and plate length), α, surface reflection, molecular model, and γ.

For the finite difference analysis, 4 flat plate cases at $\alpha = 60^{\circ}$ were considered, two at 59.4 Km (ideal and real gas), one at 81.9 Km, and one at 88.1 Km, all of which simulated the flat underside of the Orbiter. An Orbiter cross section case at 88.1 Km at 60° and a 3-D Orbiter configuration at 76.1 Km at $\alpha = 40^{\circ}$ were also analyzed with the finite difference technique. The flat plate and cross section cases were treated with a 2-D unsteady method based on a modified artificial viscosity technique to dampen out oscillations occurring across shock waves. The 3-D shape was analyzed with a 3-D steady, marching procedure along the axis of the body.

In addition to these methods, a shock layer analysis program (Ref. 3) was used to analyze the flow around 2-D Orbiter airfoils at $\alpha = 40^{\circ}$ and 60° based on the finite difference input. All of the continuum heating analyses were performed with the BLIMP Program (Ref. 4) for laminar flow and either the Aerodynamic Surface Heating Program (Ref. 5) or the BLIMP C Program (Ref. 6) for turbulent flow.

LIST OF FLAT PLATE, ORBITER CROSS SECTION, AND 3-D CASES RUN WITH FINITE DIFFERENCE AND MONTE CARLO PROGRAMS

No.	Type	Altitude (KM)	Altitude (Kft)	Angle of Attack (°)	Mach Number	γ	Knudsen No. (λ_∞ /L)	Remarks
				A. FLAT PLATE CASES				
1	FD	59.4	195	60	13.7	1.4	6.76 E-6	
2	FD	59.4	195	60	13.7	Var.	6.76 E-6	Real Gas
3	FD	88.1	289	60	20	1.4 & Var.	.00556	Compare with CAL Data
4	FD	81.9	269	60	28.3	1.4	.00139	
5	MC	121.8	400	60	28.5	1.67	.994	
6	MC	102.2	335	60	28.5	1.67	.0556	
6a	MC	102.2	335	60	28.5	1.4	.0556	
7	MC	102.2	335	45	28.5	1.67	.0556	
8	MC	88.1	289	60	20	1.67	.00556	Compare with CAL Data
8a	MC	88.1	289	60	20	1.4	.0111	
9	MC	102.2	335	60	28.5	1.67	.0556	30% Specular Reflection
10	MC	102.2	335	60	28.5	1.67	.0556	12th Power Molecular Model
11	MC	88.1	289	60	20	1.4	.00556	Compare with CAL Data
				B. ORBITER CROSS SECTION CASES				
1	FD	81.9	269	60	28.3	1.4	.001	Kn = λ_∞ / D
2	MC	121.8	400	60	28.5	1.67	.721	Kn = λ_∞ / D
3	MC	98.1	322	60	24.0	1.67	.02	Kn = λ_∞ / D
				C. 3-D CASES				
1	FD	76.1	250	40	26.65	1.4	6.41 E-5	26.5° Half Angle Cone for Nose
2	MC	109.8	360	60	28.5	1.67	.0117	Channel Section with Cyl. Top

NOTE: All M.C. calculations performed with hard sphere molecular model with diffuse reflection at walls except as noted.

Figure 1

(Figure 2)

Figure 2 shows the cell structure for flow over a flat plate at 102.2 Km for computation by the Monte Carlo method. Notice that there are three types of layers of cells with the smallest layers near the body where the changes in flow properties are the greatest. In a particular cell, pairs of molecules are selected at random and are retained for collision with probability proportional to their relative velocity raised to an exponent whose value depends upon the molecular model (hard sphere, Maxwell, 1/12 power, energy sink, etc.).

In the total flow field a relatively small number of molecules (of the order of several thousand) compared to the number in an actual gas is set in uniform motion in a field of size sufficient to contain the disturbance caused by the body. The molecules are distributed uniformly in space, and their velocity components are assigned by sampling from a distribution which is Maxwellian about the free stream velocity. The molecular paths between collisions are computed exactly but collisions are treated statistically. The calculation procedure consists of holding all molecules motionless for a time interval while collisions are computed in the field, and then allowing the molecules to move with their new velocities for another time interval. After a time interval has passed sufficient for the mean flow to traverse a distance of a few body lengths the flow is considered to be sufficiently close to the steady state. In this manner a collection of simulated molecules numbering many orders of magnitude less than those in the real gas behaves on the average as does the collection of real molecules, and by continuing the calculation for a sufficiently long time an accurate description of the flow field and surface properties can be obtained.

CELL ARRANGEMENT FOR FLOW OVER FLAT PLATE AT ANGLE OF ATTACK AT 102.2 KM

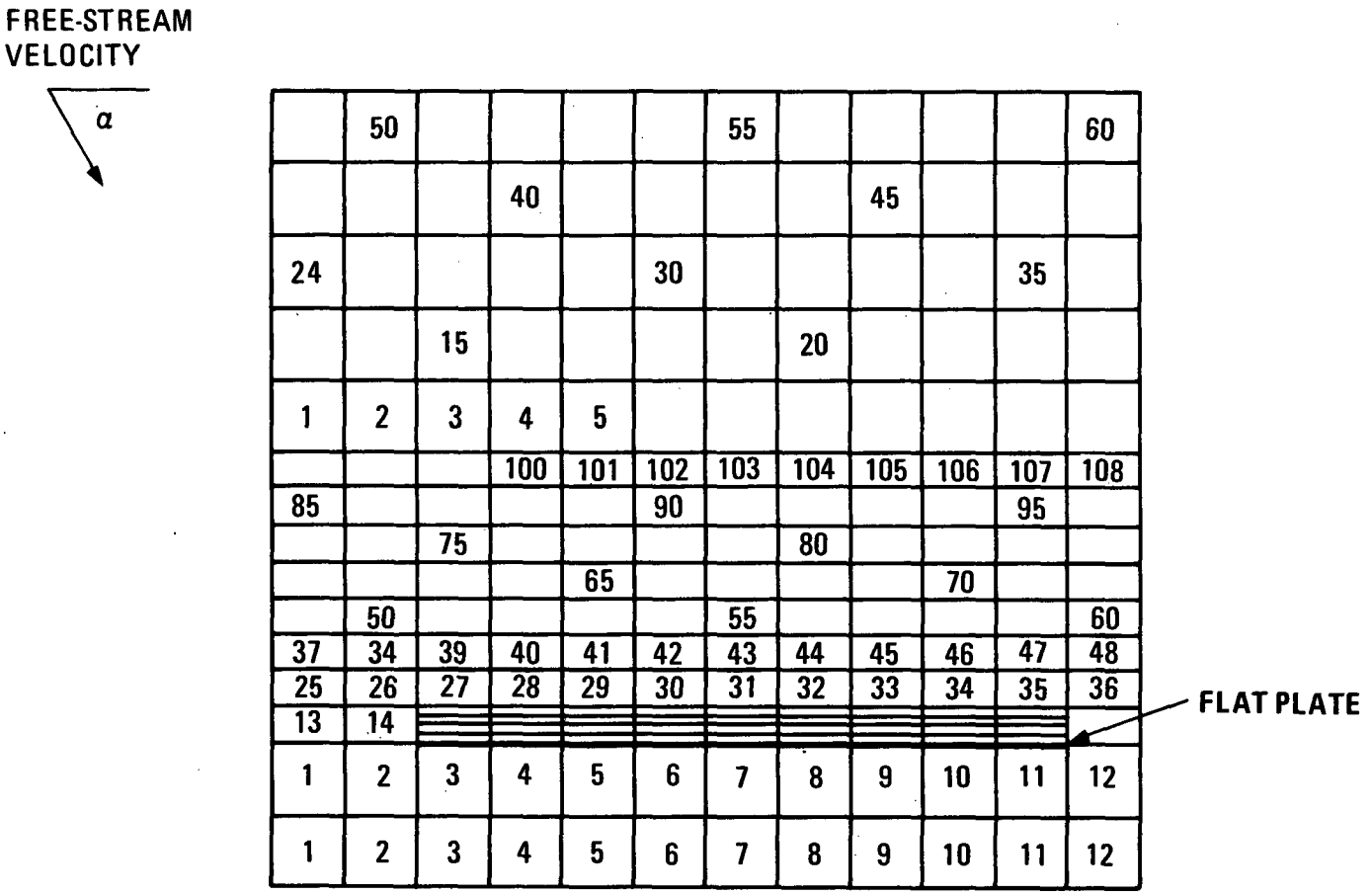

Figure 2

(Figure 3)

This figure shows the results of 5 Monte Carlo calculations of heating rate to a flat plate at 102.2 Km for Kn = 0.0556 which corresponds to an Orbiter wing chord of 4.24 meters. Four parameters have been varied: angle of attack, type of surface reflection at the wall, molecular model, and ratio of specific heats. In all cases the heating rate increases as the leading edge is approached but remains below the free molecular value for each case. The heating rates are lowest for the $\alpha = 45^{\circ}$ case since the free molecular heat transfer coefficient is proportional to the cosine of the angle between the freestream velocity vector and the surface normal. Also, when the wall is 30% specularly reflective, the heat transfer is reduced since the free molecular heat transfer coefficient is proportional to the accomodation coefficient which is 0.7 for this case. The heating rate coefficient is highest for the diatomic hard sphere gas which has an extra component of rotational heat transfer due to the internal energy of the impinging molecules. For the case of the 1/12 power molecules the heating rates are essentially the same as the case of hard spheres for the same α, γ, and surface reflection.

EFFECTS OF α, MOLECULAR MODEL, γ, AND SURFACE REFLECTION ON HEAT TRANSFER TO FLAT PLATE AT 102.2 M (335 KFT) USING MONTE CARLO METHOD

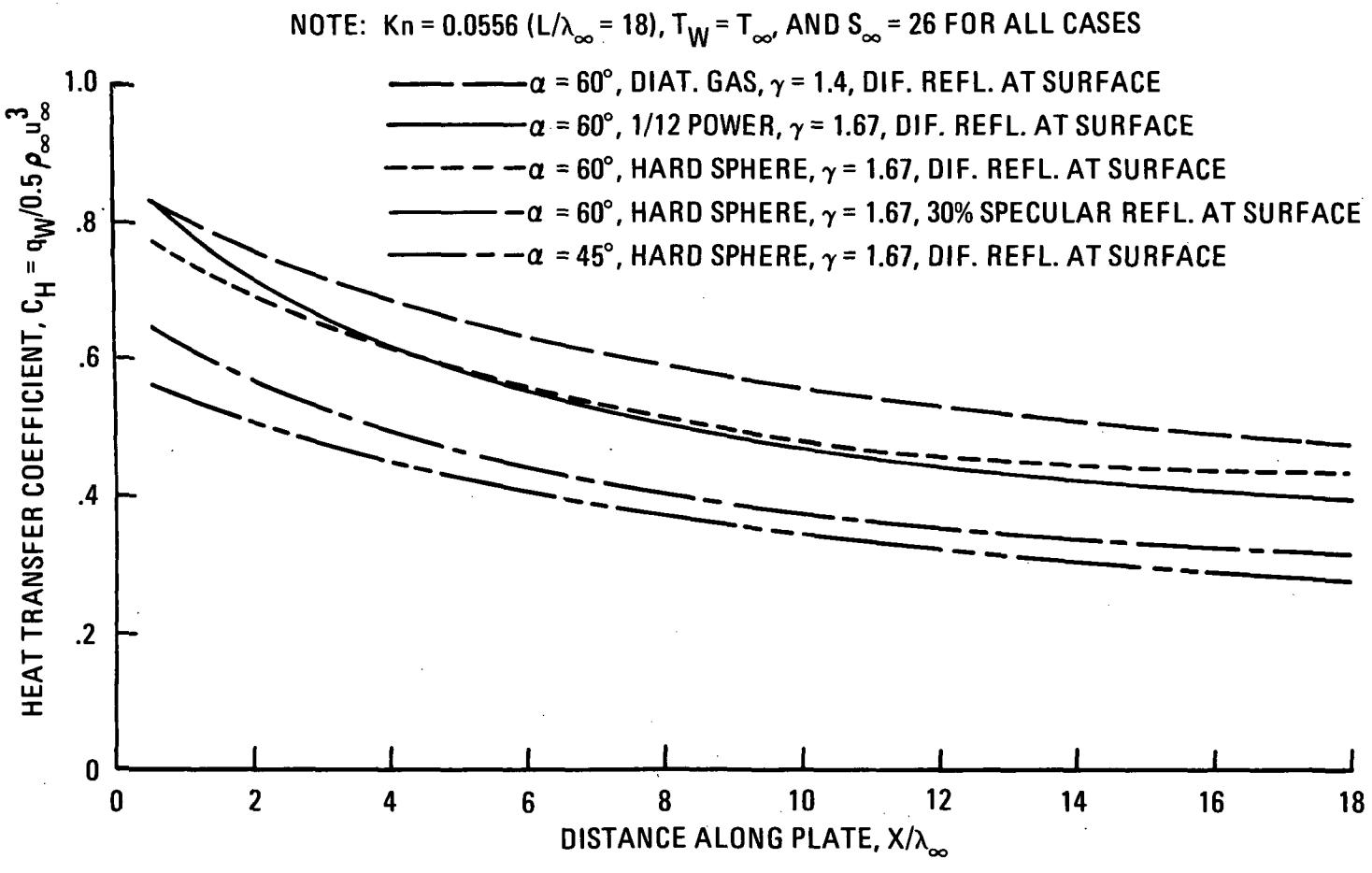

Figure 3

(Figure 4)

In this figure the cell structure around an Orbiter cross section at 121.8 Km is shown as computed by the Monte Carlo Method. For this case the Knudsen No. = λ_w/D = 0.721 with an angle of attack of 60°. A monatomic (γ = 1.67) hard sphere gas was assumed with diffuse reflection at the walls. The large number of small cells are needed in the stagnation region where the density rapidly rises. At this altitude, however, the shock layer was found to be fully merged with no distinct shock wave or boundary layer.

MONTE CARLO CELL CONFIGURATION FOR ORBITER CROSS-SECTION AT ANGLE OF ATTACK AT 121.8 KM, KNUDSEN NUMBER = $\lambda_\infty/D = 0.721$

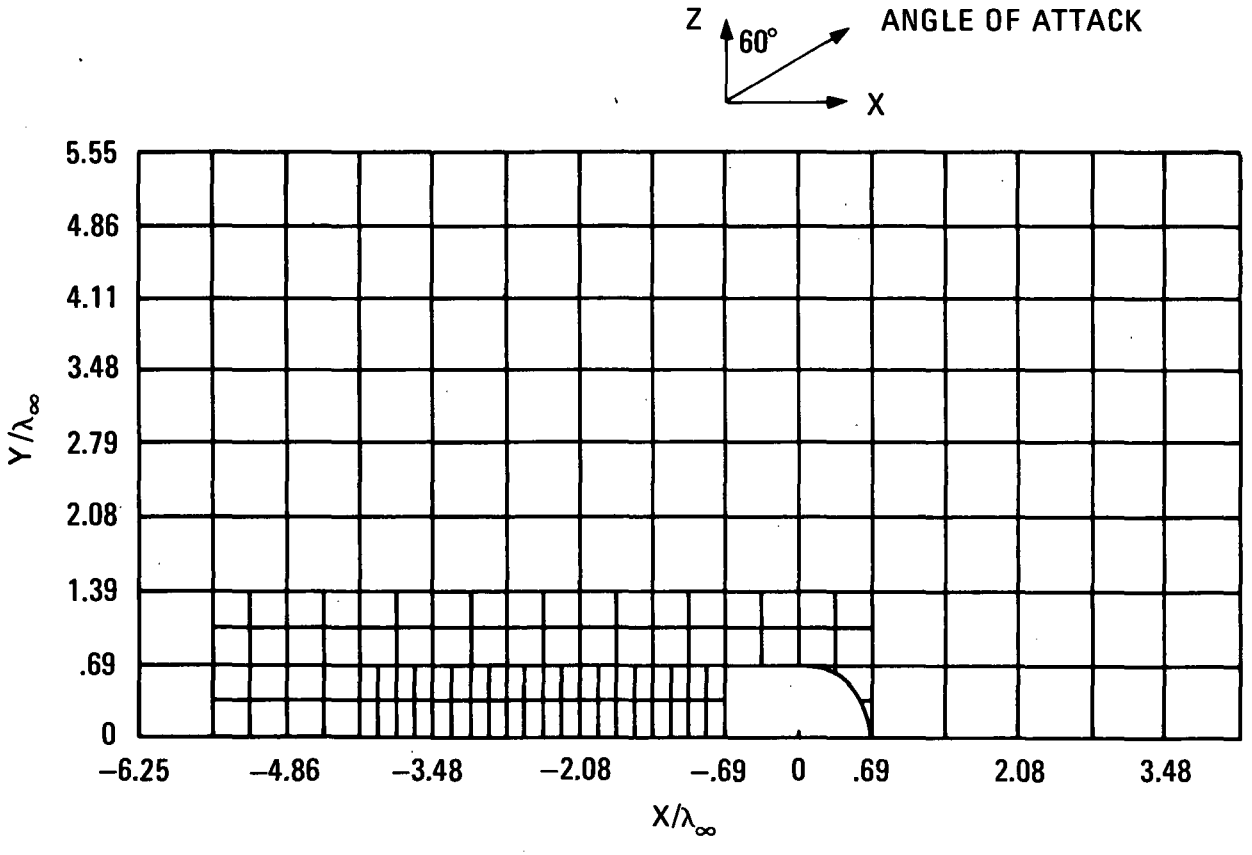

Figure 4

(Figure 5)

The local heat transfer coefficient computed by the Monte Carlo method for the Orbiter cross section is shown in the next figure as a function of the distance measured along the surface from the stagnation line. At an altitude of 121.8 Km the average heat transfer coefficient is about 0.54 while the free molecular value is about 0.87. On the flat side the average heat transfer coefficient is about 0.094 while the value calculated from free-molecular theory is 0.011. At an altitude of 98.1 Km at $\alpha = 60^{\circ}$, the average heat transfer coefficient on the front face is about 0.3 while on the flat side the average value is about 0.05. It is thus seen that heating rates to the flat side are under predicted by free-molecule theory by a factor of about 4 or 5 at 98.1 Km and by a factor of about 9 at 121.8 Km.

LOCAL SURFACE HEAT TRANSFER DISTRIBUTION ON THE ORBITER CROSS-SECTION AT 60° ANGLE OF ATTACK AT 121.8 KM AND 102.2 KM USING MONTE CARLO METHOD

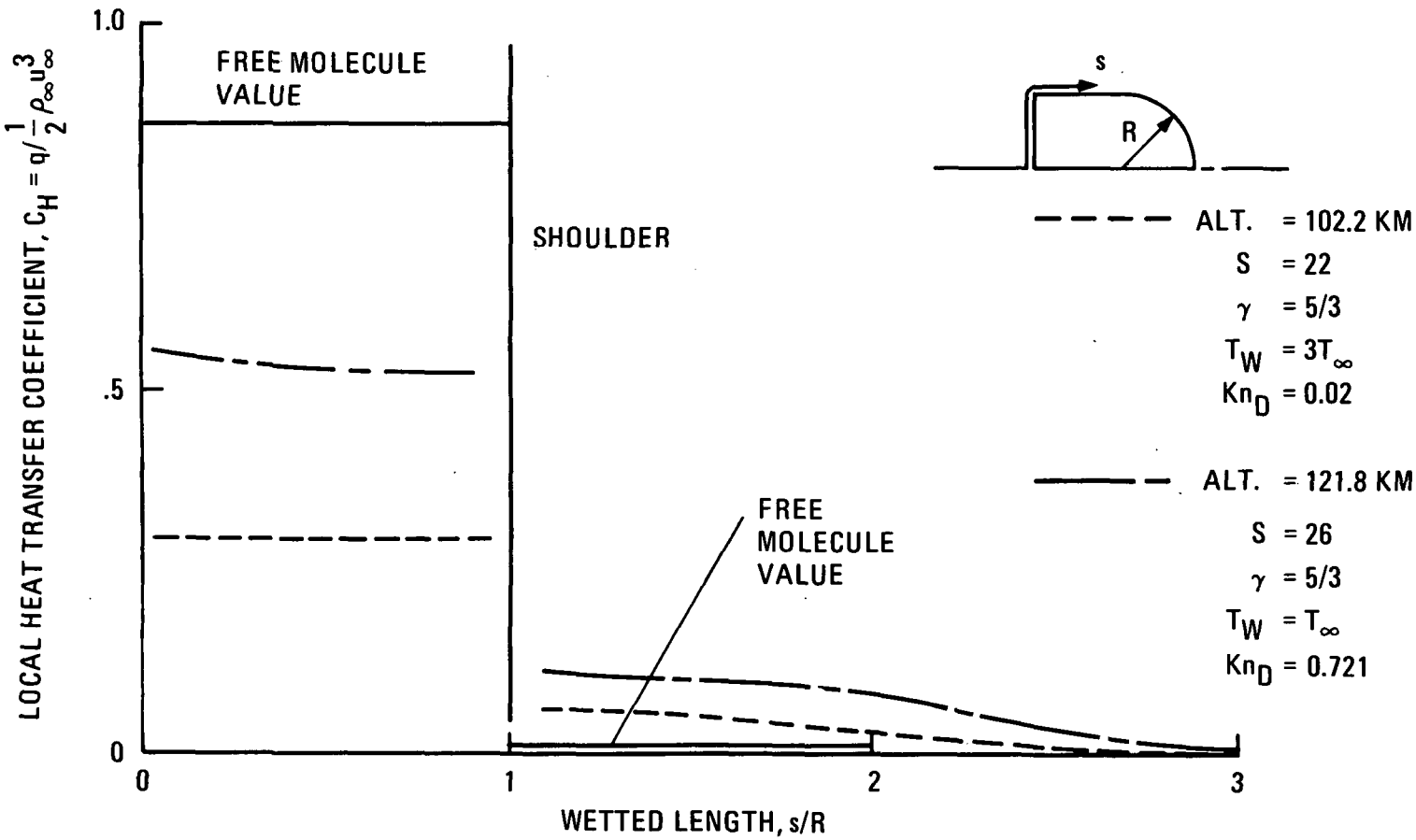

Figure 5

(Figure 6)

The next figure shows a comparison between Monte Carlo and finite difference calculations of pressure coefficient on a flat plate at $\alpha = 60^{\circ}$ corresponding to the test conditions of Vidal and Bartz at CAL (Ref. 7). The pressure data were taken on a flat plate of length $L = 180\lambda_{\infty}$ with the measurements made on the first half of the plate. This data was selected for comparison because at the time this was the only existing flat plate data (as determined by the survey of Ref. 8) at high enough angle of attack to be considered representative of Orbiter reentry conditions.

Monte Carlo calculations were made for a diatomic gas ($\gamma = 1.4$) for a plate length of $L = 90\lambda_{\infty}$ and finite difference calculations were made for $L = 180\lambda_{\infty}$. The fact that the Monte Carlo pressures were somewhat lower than the data is presumably due to the difference in plate length since at 60° angle of attack the "trailing edge effect" would be expected to be significantly large over much of the plate. The finite difference calculations were made for an ideal gas ($\gamma = 1.4$) and for a real gas of variable γ. It is seen that the real gas curve was higher at the stagnation region and oscillated somewhat while the ideal gas distribution was relatively flat in the stagnation region.

PRESSURE COEFFICIENT COMPARISON ON FLAT PLATE AT 60° ANGLE OF ATTACK WITH EXPERIMENTAL DATA OF VIDAL AND BARTZ

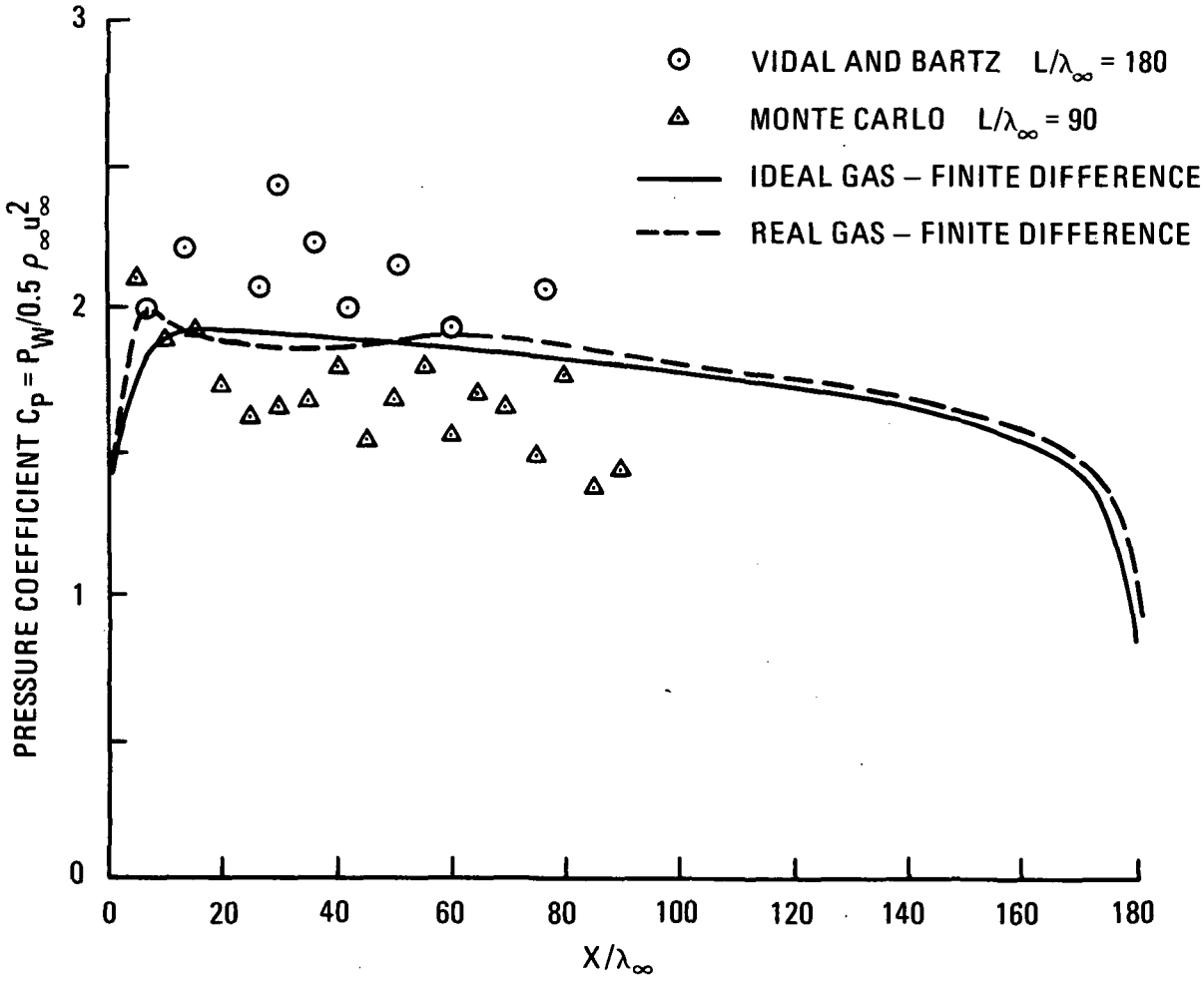

Figure 6

(Figure 7)

This figure shows the heat transfer coefficients computed by the Monte Carlo method for plate lengths of $L = 18\lambda_\infty$ and $90\lambda_\infty$ compared with the CAL data (Ref. 7) for plate lengths of $L = 18\lambda_\infty$ and $180\lambda_\infty$. Also shown are the BLIMP laminar heating rate calculations based on the finite difference ideal and real gas flow fields.

The Monte Carlo results for the shorter plate are in excellent agreement with the experimental data over the entire instrumented plate length. The Monte Carlo calculations for the plate length $L = 90\lambda_\infty$ agree well with the data for about the first 30 mean free paths, but depart from the data on the downstream portion. Again, the most likely source of this difference is a "trailing edge effect" due to the plate length.

The finite difference/BLIMP heating results showed better agreement with the CAL heating rate data near the leading edge using the real gas analysis but better agreement near the trailing edge using the ideal gas analysis. The reason for this can be partly explained by viewing the next figure.

HEAT TRANSFER COMPARISON ON FLAT PLATE AT 60° ANGLE OF ATTACK WITH EXPERIMENTAL DATA OF VIDAL AND BARTZ

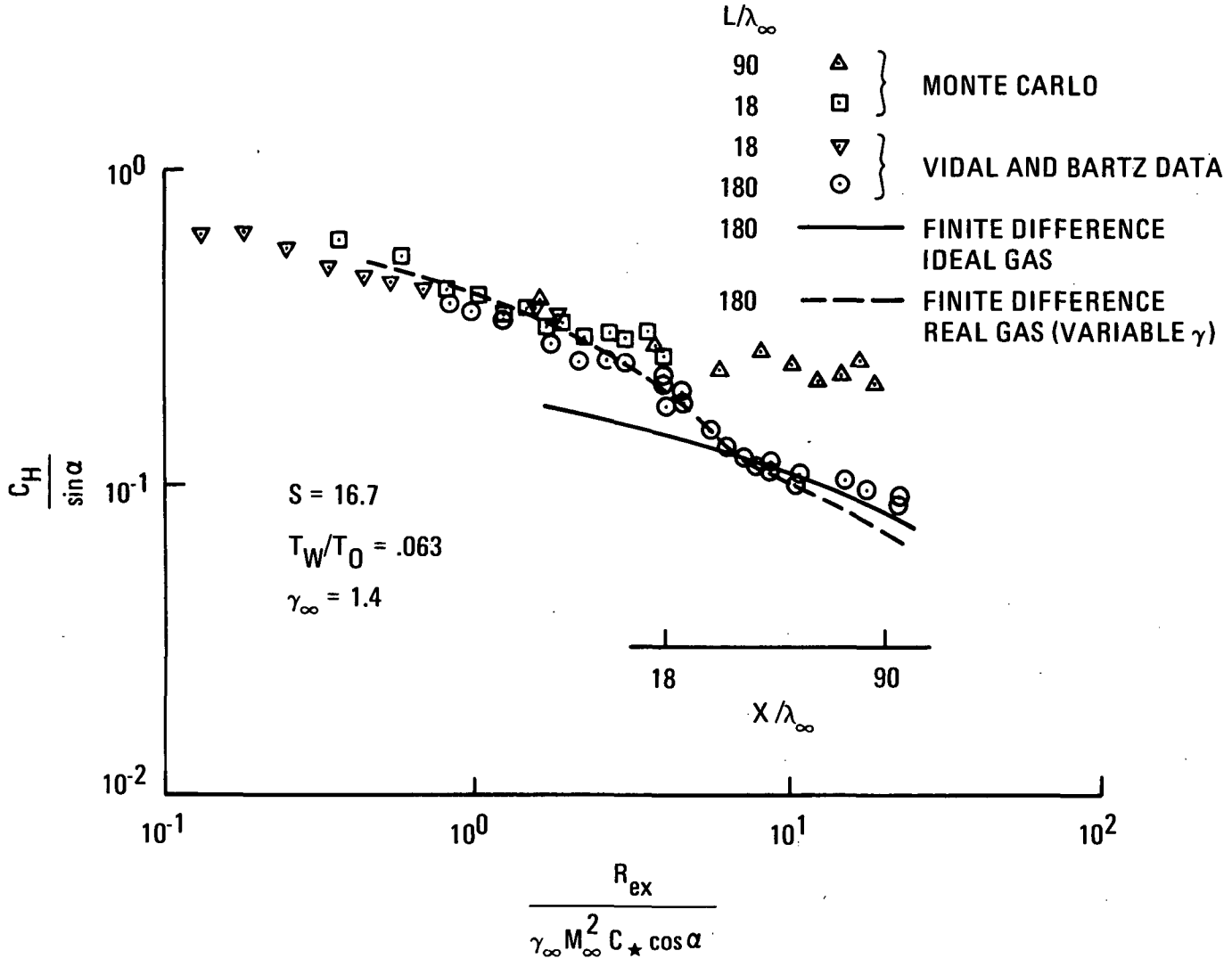

Figure 7

(Figure 8)

This figure shows the sonic lines and shock waves for this flat plate of Vidal and Bartz as computed by both the ideal and real gas finite difference analyses. For the real gas case the stagnation point lies closer to the leading edge than for the ideal gas, resulting in steeper pressure and velocity gradients (and hence higher heating rates in this region). Note that the sonic line and shock wave are closer to the plate for the real gas than for the ideal gas analysis.

FLOW-FIELD MESH, SONIC LINE AND SHOCK WAVE FOR ORBITER CROSS SECTION AT 60° ANGLE OF ATTACK, V_∞ = 7.84 KM/SEC, COMPUTED BY 2-D UNSTEADY FINITE DIFFERENCE METHOD

NOTE: EACH UNIT OF M AND N = 0.00763 METERS (0.025 FT)

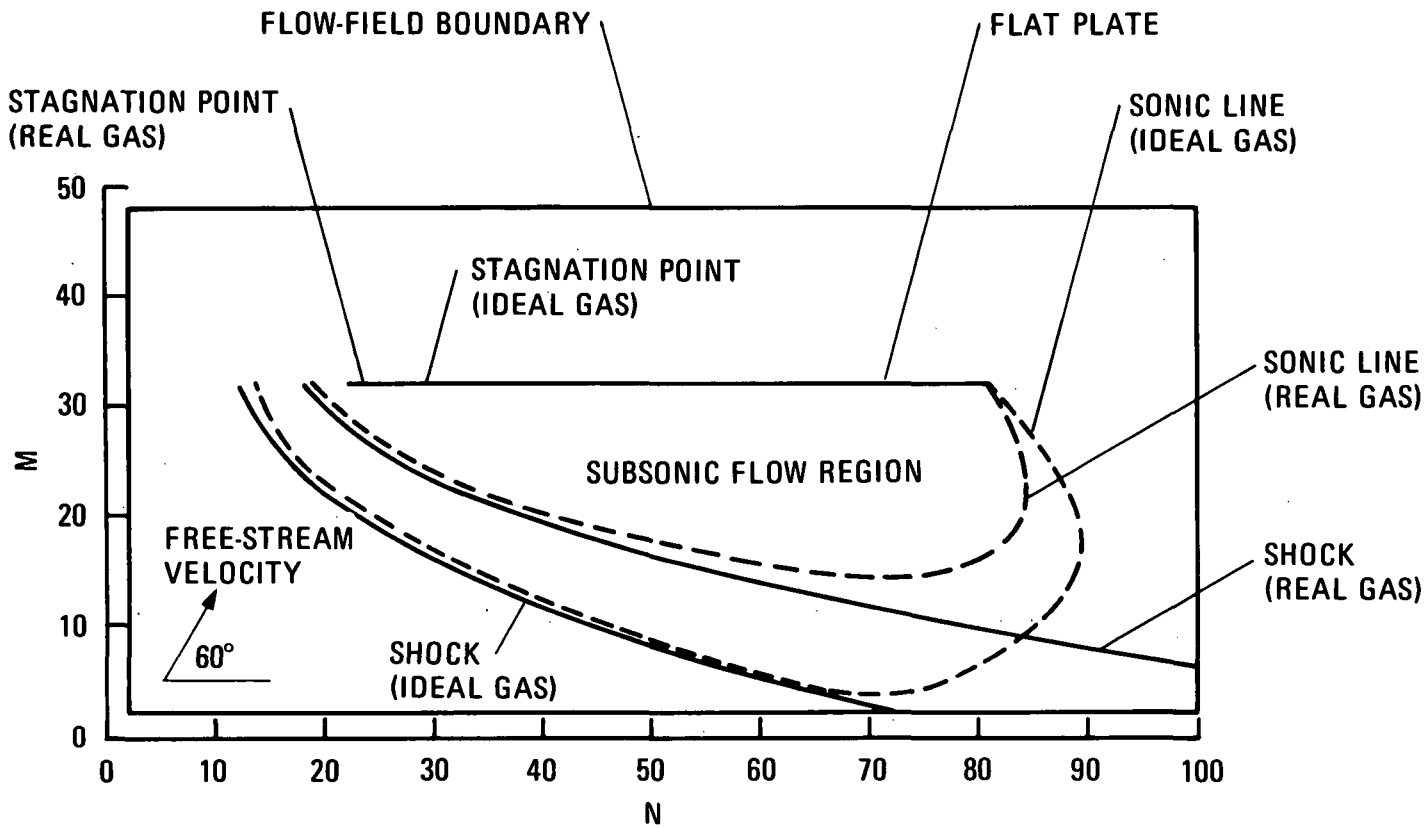

Figure 8

(Figure 9)

In this figure the Mach No. distribution along a flat plate at 60° angle of attack as calculated by the finite difference method is shown. For this particular case the altitude was 59.4 Km, the velocity was 4.45 Km/sec, and the plate length was taken to be 36.6 meters, corresponding to the length of the flat underside of the Orbiter fuselage. Note the large region of subsonic flow along nearly the entire length of the plate (and consequently the Orbiter fuselage).

MACH NO. DISTRIBUTION ALONG FLAT PLATE (M = 32) AT 60° ANGLE OF ATTACK FOR CYCLE 800

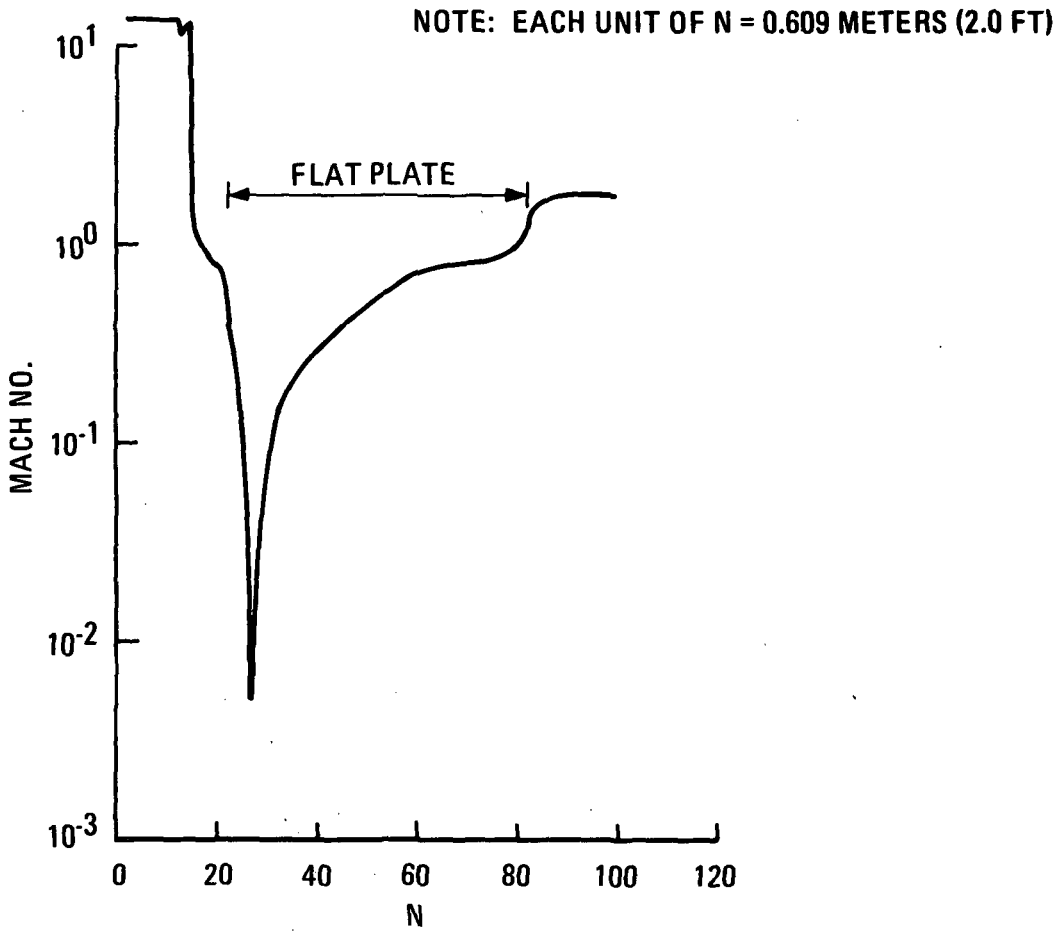

Figure 9

(Figure 10)

Heating rates along the same flat plate discussed in the previous figure are shown in this figure. Also shown for comparison is the fairing of the Orbiter fuselage heating data taken from Langley paint tests (Ref. 9). Reasonably good correlation with the heating rate data occurred when the 2-D laminar heating rates were corrected for 3-D effects. The curve marked turbulent in the figure occurs for the actual 36.6 meter plate at these conditions; however, the flow field for the Langley tests was purely laminar ($Re < 10^5$) along the fuselage so that the data did not exhibit a rise in heating due to turbulent flow.

COMPARISON OF HEATING RATES ALONG FLAT PLATE AT 60° ANGLE OF ATTACK WITH NASA/LANGLEY ORBITER PAINT TEST DATA

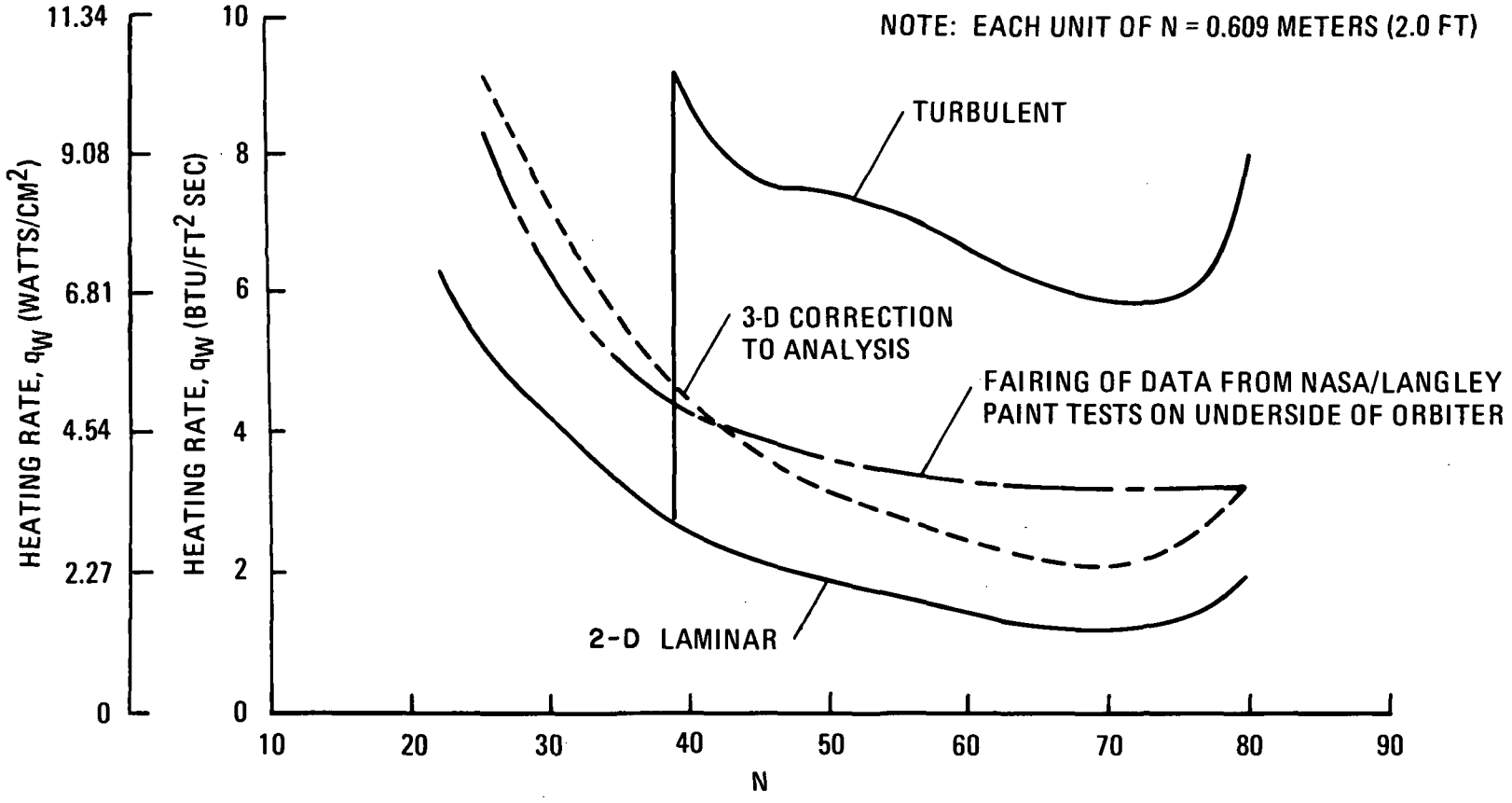

Figure 10

(Figure 11)

The finite difference 2-D unsteady technique was used to predict the flow field and shock structure around an Orbiter cross section as seen in figure 11. This case was for 81.9 Km altitude and free stream Mach No. of 28.3. The shock waves and sonic lines shown are based on ideal gas flow and the calculations were stopped at cycle 980 which was effectively steady state. Notice the large subsonic region in the neighborhood of the stagnation point. There is also a subsonic flow region at the top of the cross section which for the actual Orbiter will be all separated flow. The pressure distribution varied by some three orders of magnitude around this cross section and the heating rates by some two orders of magnitude, as will be seen in a later figure. The results of this analysis were used as input to an analysis of an airfoil at 60° angle of attack and also served to provide basic flow field knowledge for the 3-D finite difference calculations discussed in the next figure.

FLOW-FIELD MESH, SONIC LINE AND SHOCK WAVE FOR FLAT PLATE AT 60° ANGLE OF ATTACK, V = 3.14 KM/SEC, COMPUTED BY 2-D UNSTEADY FINITE DIFFERENCE METHOD

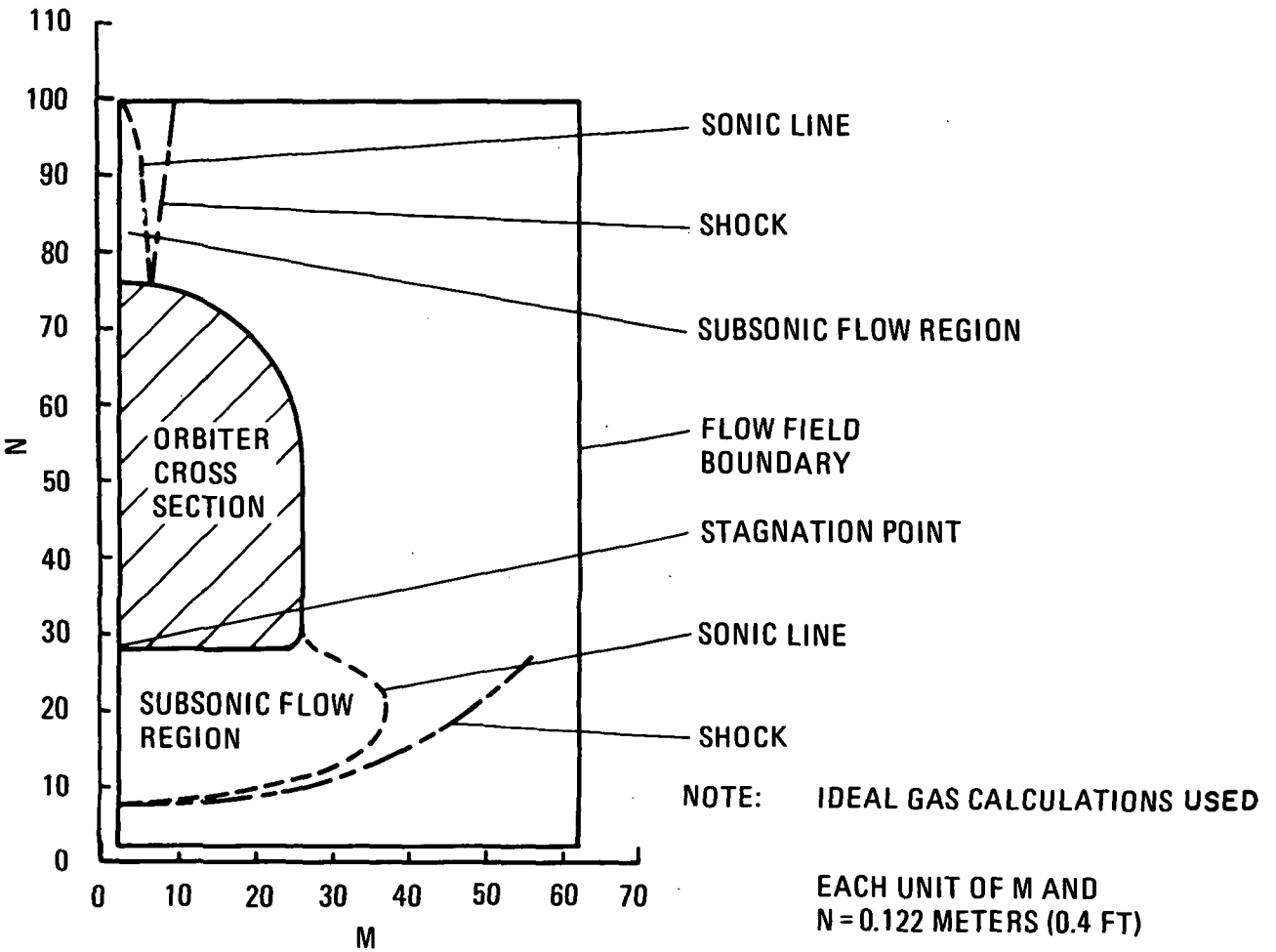

Figure 11

(Figure 12)

This figure shows a 3-D representation of the Orbiter fuselage and wings as analyzed by the 3-D steady finite difference method at an altitude of 76.1 Km. This method was used to calculate the flow field around the 3-D body at an angle of attack which was low enough (i.e., 40°) to maintain supersonic flow all along the body. The nose of the body was pointed such that the shock remained attached to the body and the flow was completely supersonic as compared to the subsonic/supersonic 2-D unsteady flow fields discussed previously.

The 3-D method of analysis was based on the numerical solution of the finite difference analog of the hyperbolic equations that represented the inviscid flow. The numerical scheme of computation was an explicit one where a marching procedure along one of the three space coordinates was used. The flow calculation progresses from an initial surface to the next parallel surface whereupon the flow is calculated and the new flow values are used for computation of the next surface. The procedure is repeated until the entire range of interest is covered, which was for our case about the midpoint of the Orbiter wing or about 1200 cycles beyond a cone calculation of about 200 cycles. The most accurate cone that approximated the front part of the fuselage was a 26.5^{o} half-angle cone with its axis at an angle of 11.5^{o} to the main axis of the fuselage. This conical surface was gradually tapered into the fuselage cross section some distance downstream of the nose as seen in the next figure.

3-D ORBITER FUSELAGE CONTOUR USED IN 3-D STEADY FINITE DIFFERENCE CALCULATIONS

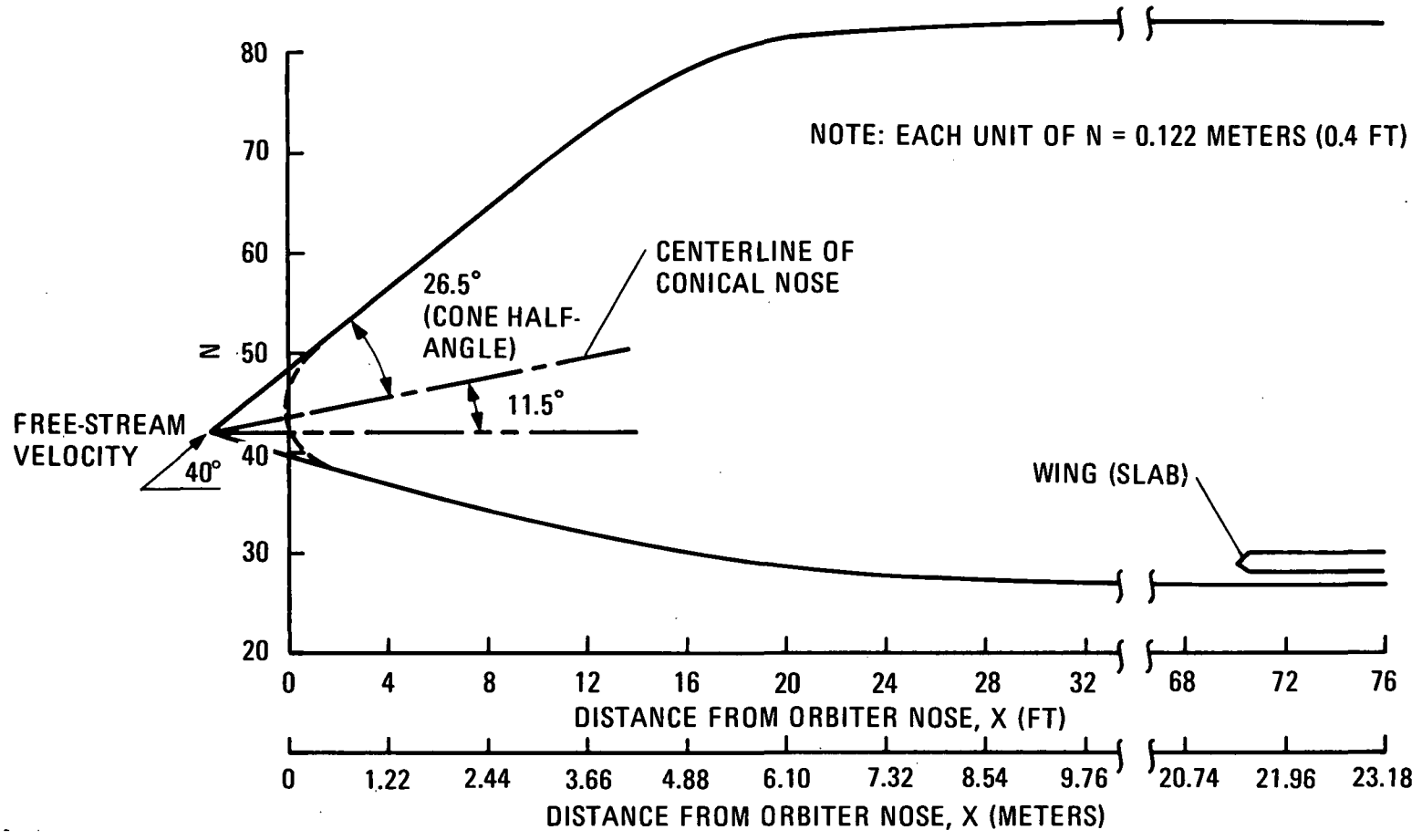

Figure 12

(Figure 13)

Some of the 3-D Orbiter fuselage cross sections and shock waves are shown in this figure. The fuselage bow shocks become increasingly larger until the fuselage changes into its constant contour between cycle 680 and 1020 during which time the shocks do not increase significantly. At roughly cycle 1010 or about 21.6 meters from the nose the wing was reached. The peak in pressure along the span moves outward until it is at about 37% of the span of the wing at about 1 meter back on the chord.

3-D ORBITER FUSELAGE CROSS SECTIONS AND SHOCKS COMPUTED BY FINITE DIFFERENCE METHOD

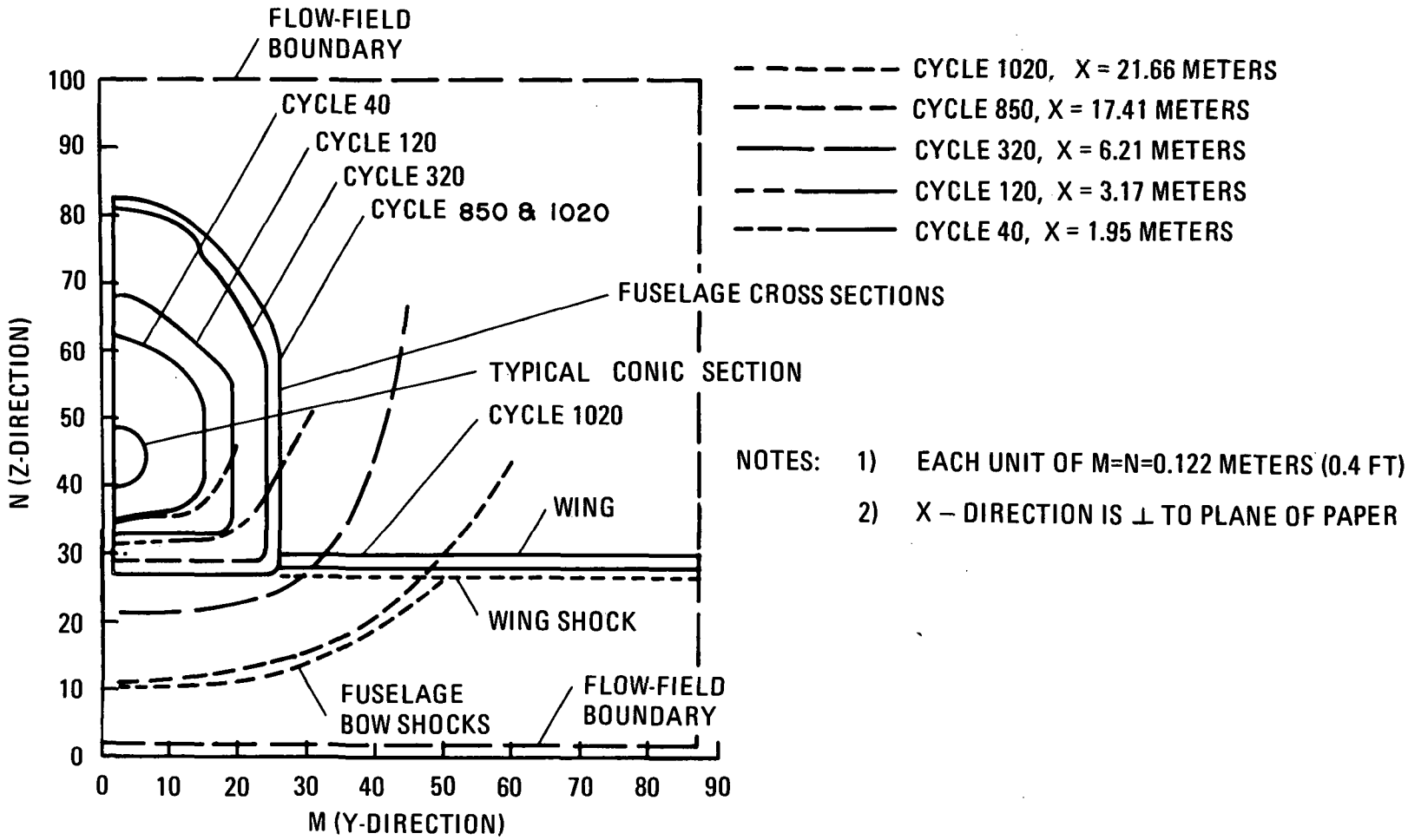

Figure 13

(Figure 14)

The calculated finite difference pressures on the bottom of the fuselage for $\alpha = 40^{o}$ are shown compared with recent NASA/Ames test data (C. Pappas) for a North American Rockwell straight wing Orbiter configuration. The finite difference calculations show remarkedly good correlation with the test data for $\alpha = 45^{o}$. These pressures were used to compute heating rates along the bottom of the fuselage as seen in the next figure.

PRESSURES ON UNDERSIDE OF ORBITER FUSELAGE AT VARIOUS ANGLES OF ATTACK

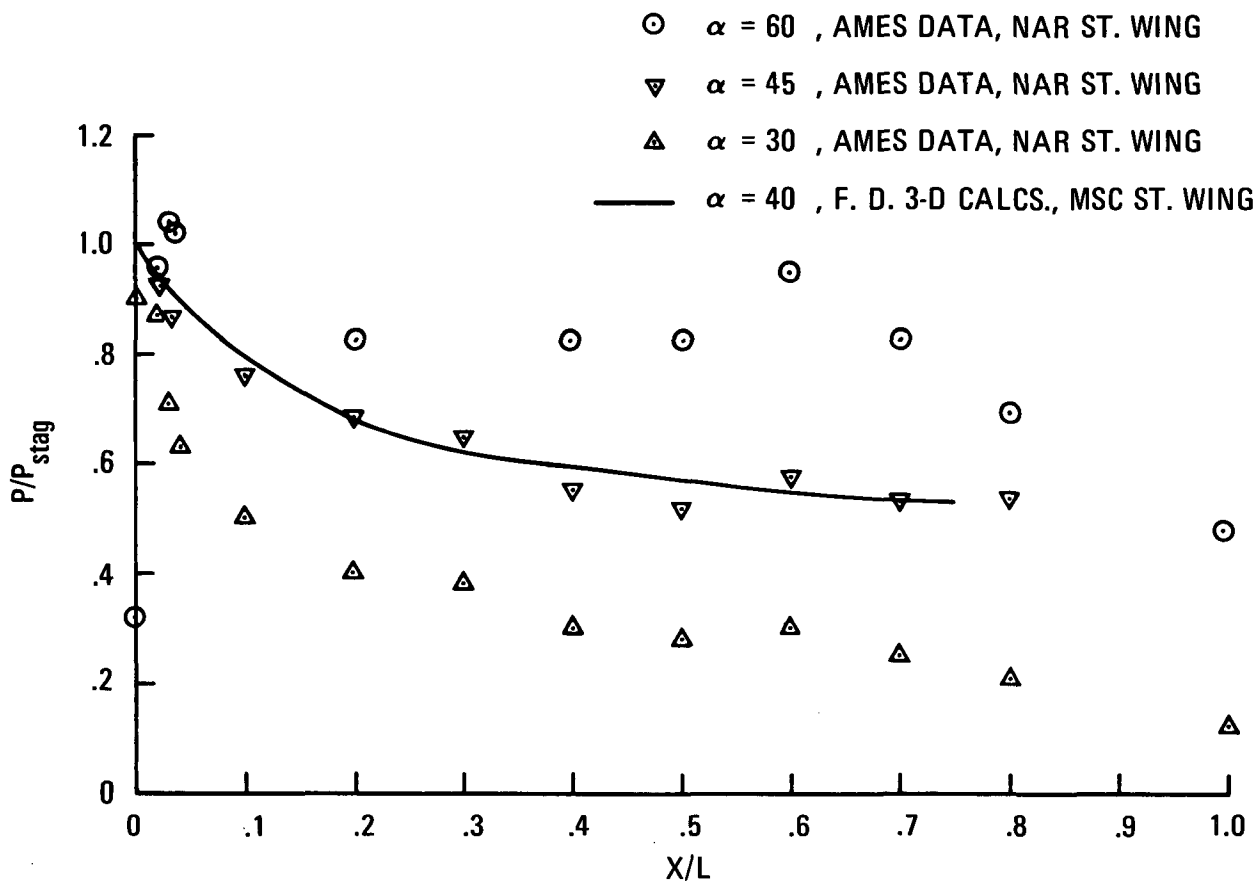

Figure 14

(Figure 15)

Heating rates along the underside of the Orbiter fuselage at $\alpha = 40^{\circ}$ as predicted by the BLIMP laminar and turbulent programs are shown in this figure. These calculations which are based on the previous pressure distributions are compared with Ames test data of Ref. 10 for the MSC straight wing Orbiter. Note the very good correlation for laminar flow using the 3-D axisymmetric option of BLIMP. The turbulent curve shown resulted only when the Ames test conditions were used since for the actual vehicle at this point in a 40° trajectory the transition point would not occur until a value of X/L of about 0.8 was reached.

HEATING RATES ON UNDERSIDE OF ORBITER FUSELAGE AT 40° ANGLE OF ATTACK

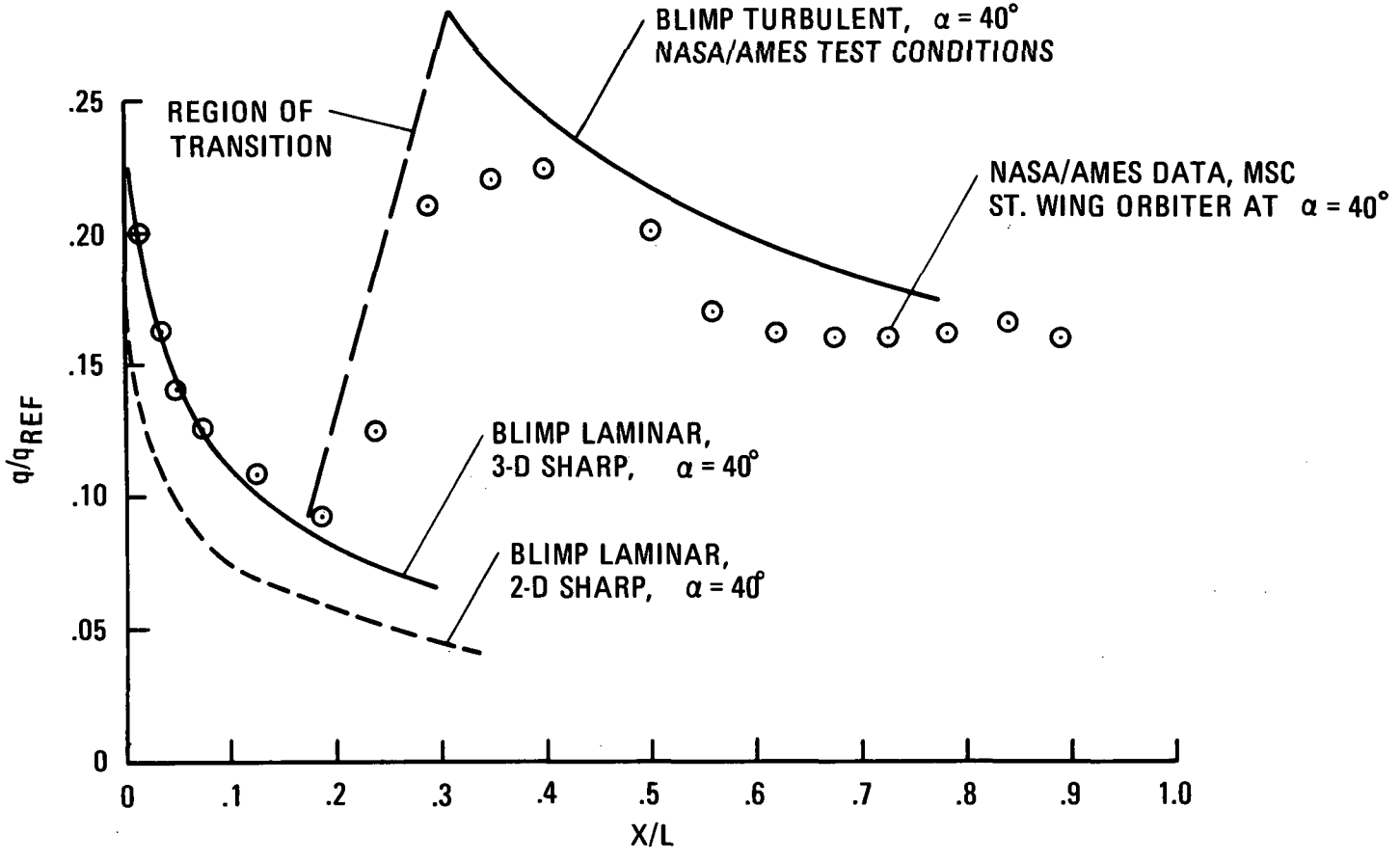

Figure 15

(Figure 16)

Surface pressures predicted by the 3-D steady finite difference program along a cross section at X/L of 0.2 are shown in this figure. Good correlation is seen between the 3-D calculations and Ames test data for the NAR straight wing Orbiter obtained from Ref.10 at this station (and also at several other stations not shown). Pressure distribution calculations at stations such as these were used to input to heating calculations such as seen in the next figure.

PRESSURES ON CROSS SECTION OF ORBITER FUSELAGE AT X/L = 0.2
COMPUTED BY FINITE DIFFERENCE METHOD

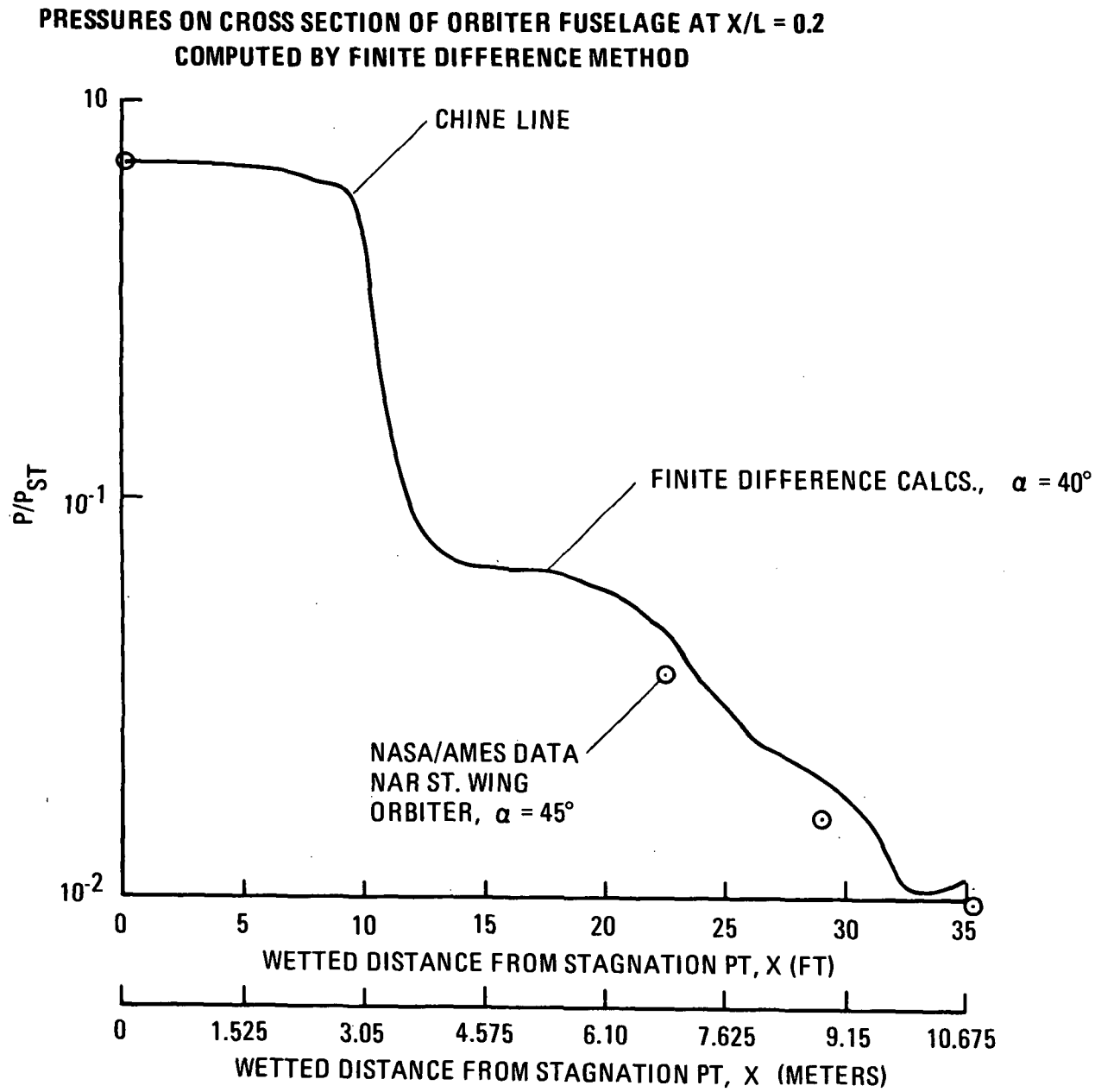

Figure 16

(Figure 17)

This figure shows calculations made along a cross section at X/L = 0.45 based on the 3-D steady finite difference pressures for $\alpha = 40^{\circ}$. Since no heating rate data on the side of the Orbiter fuselage could be found for $\alpha = 40^{\circ}$ a data point for an MSC Arc-Jet Test (by C. Scott) for $\alpha = 60^{\circ}$ was used. The heating rate calculation shown for $\alpha = 40^{\circ}$ represents fairly good correlation with the data as the data is somewhat higher for $\alpha = 60^{\circ}$. Notice the large increase in heating rate at the chine line (a factor of nearly 2) even though there is a drop in pressure at the chine line. This is due to the rapid acceleration of the flow toward the corner and was observed in the MSC tests.

HEATING RATES ON CROSS SECTION OF ORBITER FUSELAGE AT X/L = 0.45

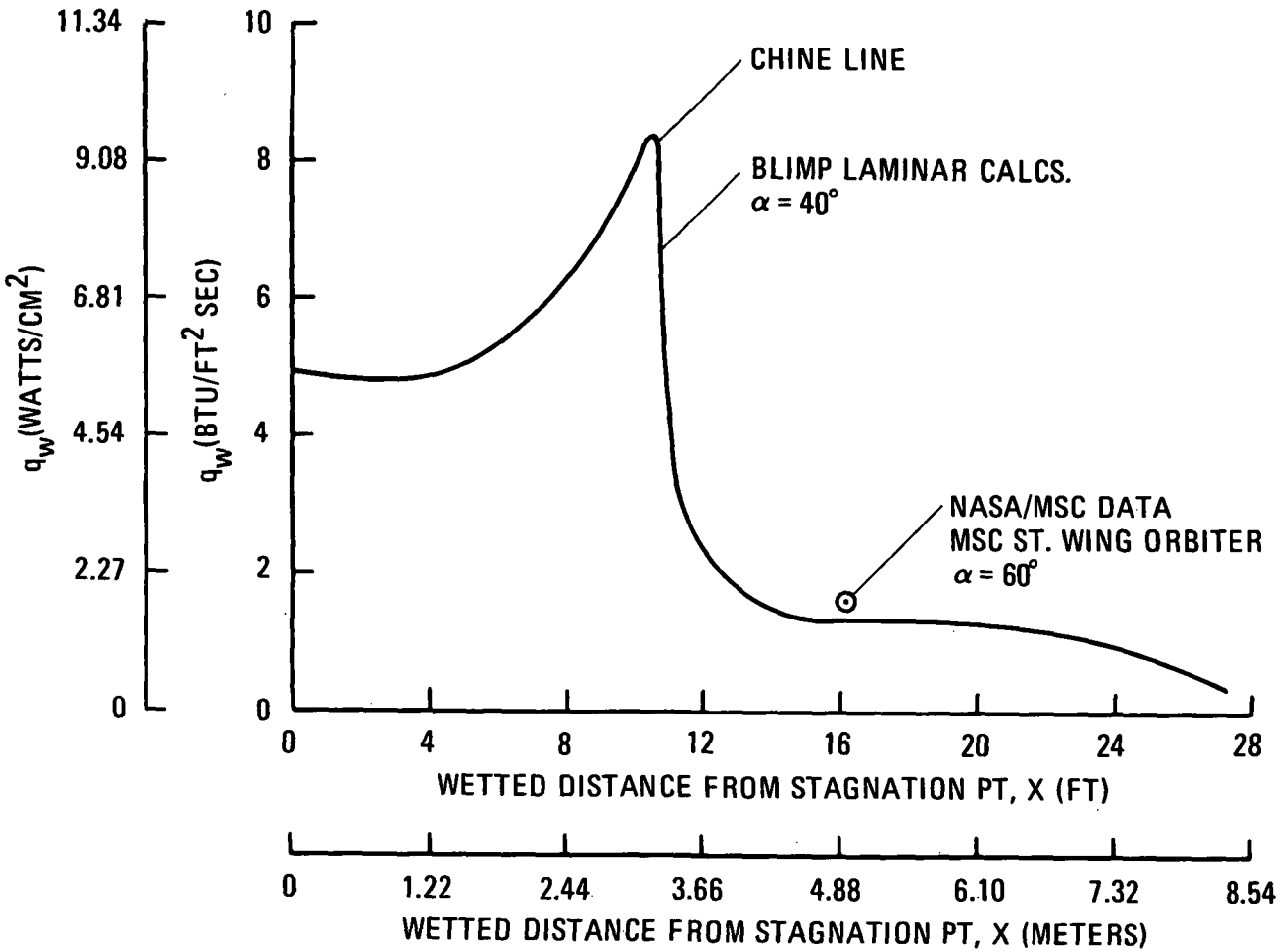

Figure 17

(Figure 18)

The results of the finite difference flow field for the 2-D cross section were used together with the TRW Shock Layer Analysis Program (Ref. 3) and the BLIMP Program to predict the location of the fuselage shock inpingement on the Orbiter wing. A simulated wing was attached to the chine line of the cross section at a dihedral angle of 7°. Four points inboard of the shock intersection point on the wing and one point outboard were used to make calculations. The flow field around 2-D airfoils at these points was calculated by the Shock Layer Program based on input from the finite difference 2-D analysis and neglecting the flow velocity in the spanwise direction of the wing. The resultant heating rates as computed by the BLIMP Program are seen in figure 18 compared with MSC arc jet data (C. Scott) at 60° angle of attack. It may be seen that good agreement exists using either of two correlation expressions relating flat faced cylinder heating rates to hemisphere heating rates as reported by C. Scott. The location of the bow shock impingement on the wing appears to be between 35 and 40% of the exposed span as shown by both experimental data and theoretical analysis.

COMPARISON OF PREDICTED HEATING RATES ON ORBITER WING LEADING EDGE AT 60° ANGLE OF ATTACK WITH MSC ARC JET TEST DATA

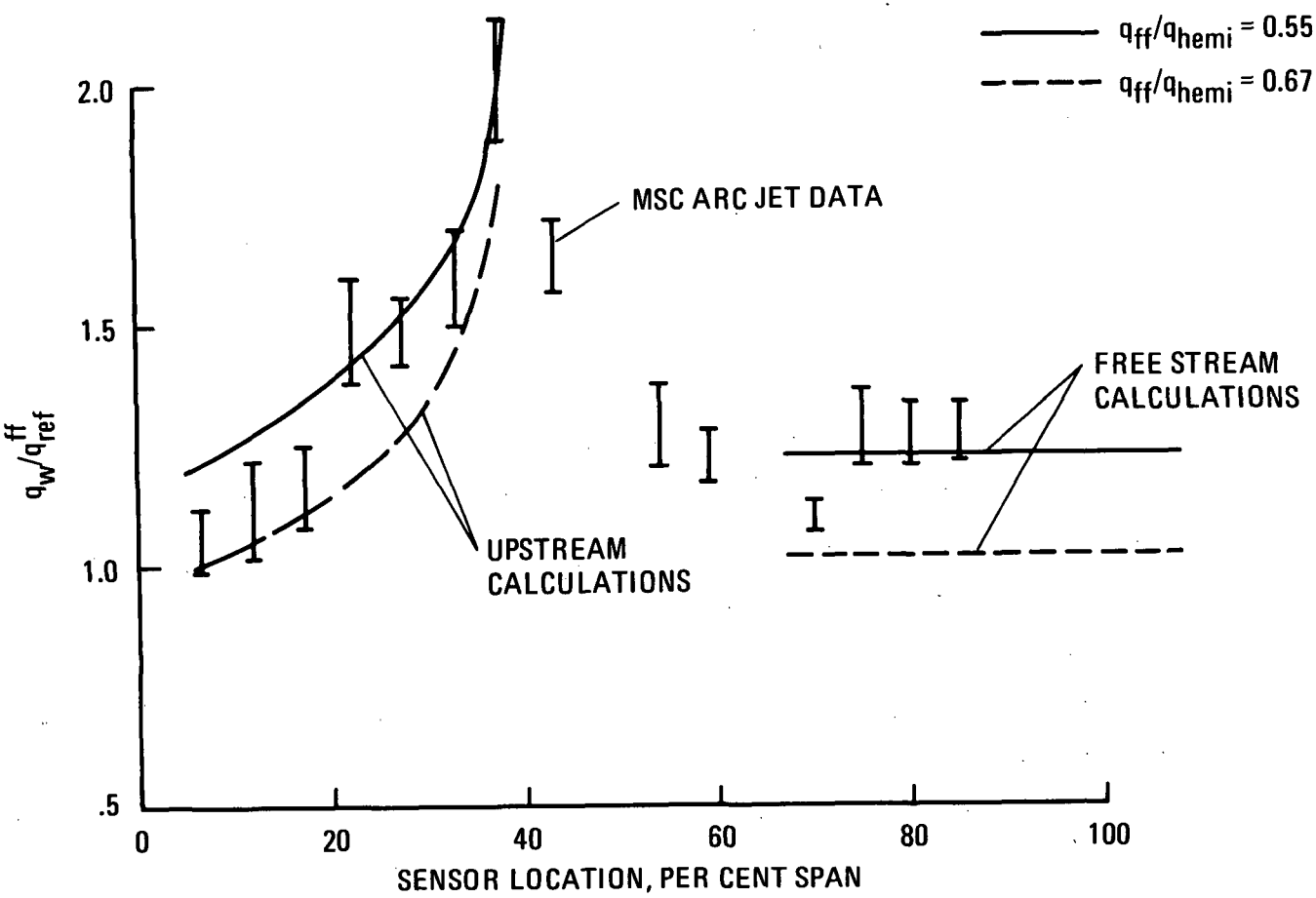

Figure 18

(Figure 19)

A similar procedure for an airfoil at $\alpha = 40^{\circ}$ was performed for the 3-D finite difference flow field by using the property values at cycle 1000 (just upstream of the wing leading edge) as input. In this analysis the velocities along the span as well as along the axis were allowed to vary. Also about 12 points along the span were considered. The predicted heating rates on the airfoil at $\alpha = 40^{\circ}$ which were obtained from BLIMP, based on pressure distributions from the Shock Layer Analysis Program, are shown in this figure. Notice that very good agreement resulted with Ames test data (Ref. 10) for an MSC straight wing Orbiter model at $\alpha = 40^{\circ}$ and that the shock impingement point was about 37-38% of the exposed span.

HEATING RATES ON LEADING EDGE OF ORBITER WING AT 40°

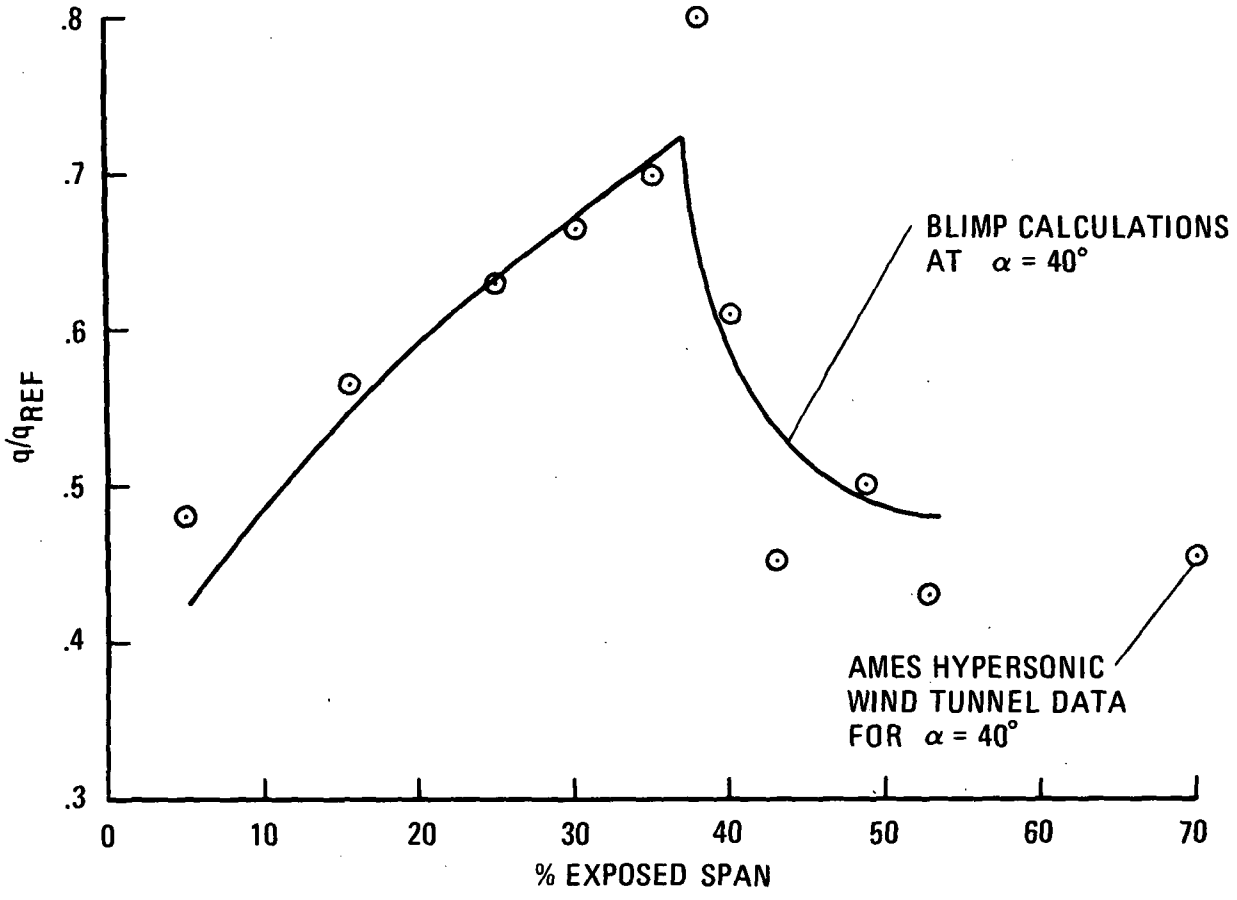

Figure 19

CONCLUSIONS

This paper has presented a summary of a reentry flow field and heating analysis performed for the MSC straight wing Orbiter at high angle of attack. Rarefied flow fields and heating were calculated by the Monte Carlo Direct Simulation Technique at high altitudes. For lower altitudes a 2-D unsteady and 3-D steady finite difference method combined with an artificial viscosity technique was used. Flow fields and associated heating rates were computed for flat plates, Orbiter fuselage cross sections and airfoils, and 3-D representations of the Orbiter for a wide variety of free stream conditions, molecular models, α, γ, surface reflection, etc.

It was felt that this study contributed to the state of the art in flow field computational techniques for both rarefied and continuum flows. The Monte Carlo technique provided a more accurate method for analyzing flows in the transition and merged layer regimes which previously had been treated by a combination of free-molecule and continuum theories. The finite difference methods were able to treat more accurately the continuum flows behind both detached and attached shock waves because of the modified artificial viscosity approach. The finite difference method together with the shock layer and heating analysis for airfoils was able to provide an accurate definition of the Orbiter bow shock/wing shock interaction region. In many cases where experimental data was available, good and in some cases excellent correlation was obtained between these flow field and heating methods and the experimental data, thus verifying that the data was adequate for Space Shuttle Orbiter preliminary design purposes.

REFERENCES

1. Rochelle, W. C., Vogenitz, F. W. and D'Attorre, L., et. al., "Final Report - Space Shuttle Vehicle Reentry Flow Field Analysis", TRW Systems Rpt. No. 16209-H002-R0-00, 19 July 1971
2. Vogenitz, F. W. et. al., "Monte Carlo Direct Simulation Technique - User's Manual", TRW Systems Rpt. No. 16209-001-R0-00, 12 July 1971
3. Gomez, A. V., "Hypersonic-Blunt Body, Shock Layer Analysis Program (AH002A)," TRW Systems Rpt. 70.4352.30-02, 8 May 1970
4. Bartlett, E. P., and Kendall, R. M., "Non-Similar Solution of the Multicomponent Laminar Boundary Layer by an Integral Matrix Method", Aerotherm Corp. Rpt. 66-7, Part III, March 1967
5. Wilkinsen, H. R. and Heimler, G. H., "Aerodynamic Surface Heating Program - Program No. AH005H", TRW Systems Rpt. 3123.22-172, 9 Oct. 1967
6. Bartlett, E. P., et. al., "User's Manual - Boundary Layer Integral Matrix Procedure, Version C (BLIMPC), Aerotherm Rpt. No. UM-70-20, June 22, 1970
7. Vidal, R. J. and Bartz, J. A., "Experimental Studies of Low-Density Effects in Hypersonic Wedge Flows", Rarefied Gas Dynamics, Vol. I, 1965
8. Rochelle, W. C., "A Review of Hypersonic Rarefied Flow Over Sharp and Blunted Flat Plates at Angle-of-Attack", TRW Systems Rpt. No. 70.4352.16-2, 17 March 1970
9. Lee, D. B., "Aerothermodynamic Data on MSC Space Shuttle", NASA/MSC Memo ES5/7-10(0)/163(m), 14 July 1970

REFERENCES (Cont'd)

10. Marvin, J.G., et. al., "Flow Fields and Aerodynamic Heating of Space Shuttle Orbiter", Paper Presented at Space Shuttle Technology Conference, Langley Research Center, 24 March 1971.

A VISCOUS STARTER SOLUTION FOR SHUTTLE FLOW FIELD COMPUTATIONS

By
C. P. Li
Lockheed Electronics Company, Inc.
Houston Aerospace Systems Division
Houston, Texas

and
W. D. Goodrich
NASA Manned Spacecraft Center
Houston, Texas

SUMMARY

A time-dependent numerical procedure that calculates the viscous flow in the shock layer around the shuttle nose has been developed. It has been applied to the free-stream conditions that may be encountered in the shuttle flight trajectory and found to be efficient and in satisfactory agreement with other steady and unsteady techniques. Two features associated with the present formulation are responsible for its successful applications. The first is that the flow field computation is made within the shock layer; the second is that the mapping of the computational region places proportionately more mesh points in the vicinity of the wall than in the remaining computational region. Qualitative agreement is also obtained with experimental heat transfer and skin friction coefficients for $Re_\infty = 5000$, at which point the thin boundary layer concept is no longer valid. This procedure is presently developed for a 2D geometry; however, it can be readily modified to consider an angle-of-attack case if used

Page intentionally left blank

in conjunction with a larger and faster computer than the UNIVAC 1108 system at the Manned Spacecraft Center (MSC). The numerical results may be used for low-altitude flight to determine the edge conditions for a thin boundary layer, to provide initial boundary layer profiles for downstream boundary layer calculations, and to start supersonic computations. For high-altitude flight, it may be used to determine the complete flow field in the nose region and also provide a starter solution for subsequent supersonic flow computations.

STARTER SOLUTION DEVELOPMENT

(Figure 1)

The NASA Manned Spacecraft Center and Lockheed Electronics Company, Inc., at Houston have been active in computational flow field development for the past 2-1/2 years. This effort has been concentrated on using the time-dependent finite-difference technique to compute flow fields based on the continuum theory. Applications of the numerical technique have included the inviscid, ideal gas and equilibrium and chemical nonequilibrium air in the shock layer around the Apollo command module at an angle of attack and both the inviscid and viscous flow calculations for a shuttle orbiter wing and nose. In the viscous formulation the shock layer and the laminar wake were considered in order to analyze the flow-separation problem. Since the computer code that calculates the complete flow field around a blunt body has not been completed, we will stress the shock layer flow field in this discussion. Note that our development of a viscous starter solution could be used in conjunction with the plan now being executed at the NASA Ames Research Center under the category of inviscid solutions.[1]

STARTER SOLUTION DEVELOPMENT

INVISCID FLOW

2D
- CARTESIAN COORDINATES
- IDEAL GAS
- EQUILIBRIUM AIR
- DISSOCIATING DIATOMIC GAS

3D
- SPHERICAL POLAR COORDINATES
- IDEAL GAS
- EQUILIBRIUM AIR
- DISSOCIATING DIATOMIC GAS
- FINITE-RATE AIR

VISCOUS FLOW

2D
- CARTESIAN COORDINATES
- IDEAL GAS
- EQUILIBRIUM AIR

Figure 1

FLOW FIELD DESCRIPTION

(Figure 2)

The interest in the flow field computation at the leeward side of the shuttle vehicle at a high angle of attack stems predominately from the aerodynamic heating problem associated with the vast surface area in the leeward flow region as well as the L/D prediction problem at high attitude. With the recent advance in numerical techniques, it seems possible to compute the complete flow around the vehicle by a unified scheme. The flow field may be divided into the shock layer and the laminar near wake that can be extended downstream until turbulence begins.

The flow field at a low angle of attack is relatively simple since it is predominately supersonic downstream of a small subsonic nose region. The viscous shock layer calculation has primary applications in three areas. It can be used to properly start the inviscid supersonic solution since the boundary layer displacement is included. It can also be used to initiate a boundary layer calculation adjacent to the body and downstream from the subsonic region. This latter application is required to augment the downstream inviscid solution. A third possible application is the prediction of flow properties for high-altitude flight when rarefaction effects become important.

FLOW FIELD DESCRIPTION

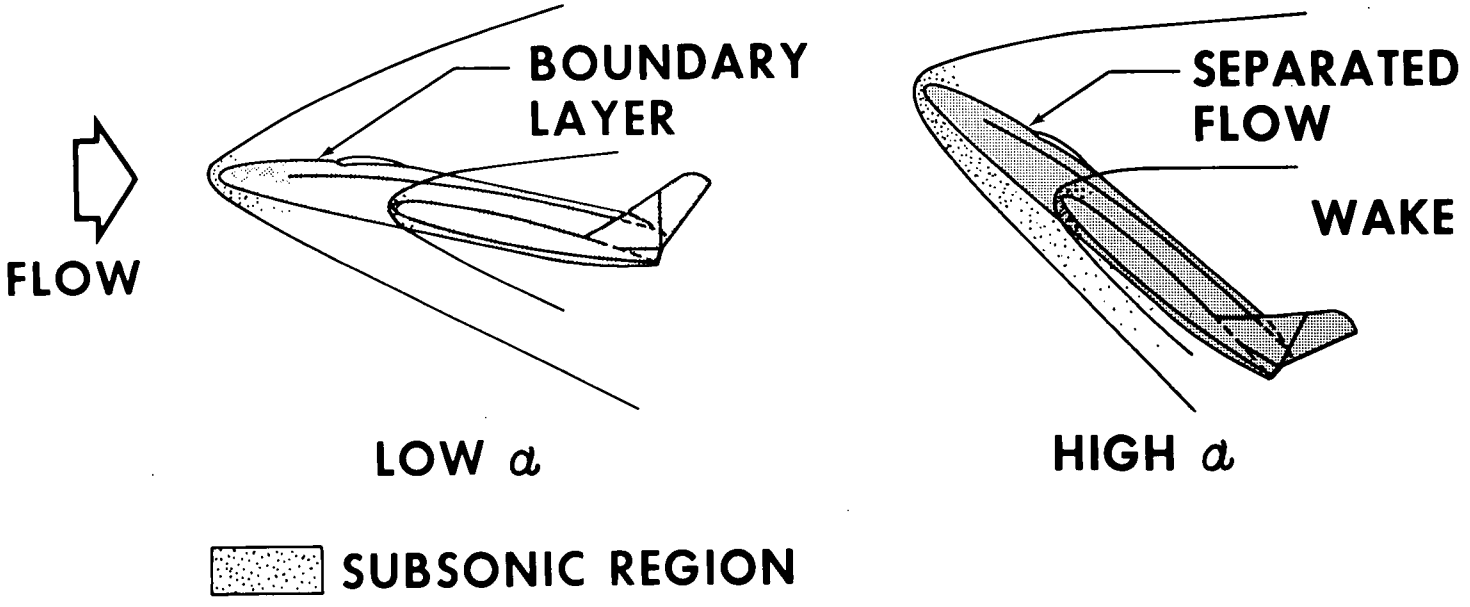

Figure 2

SPACE SHUTTLE TRAJECTORY

(Figure 3)

The importance of analyzing the viscous shock layer can be seen in this figure. It shows the velocity-altitude curves for a typical shuttle trajectory during launch and reentry. Also shown here are boundaries indicating two important flow regions taken from Probstein.[2] These boundaries, however, are relatively arbitrary in nature because of the dependence on the configuration and surface temperature. This figure is therefore intended to indicate the flow dynamics problem that might arise during shuttle flight. The top curve defines the upper boundary in altitude and velocity for which continuum assumption remains valid, while the bottom one denotes the boundary of departure from the classical thin boundary layer concept. It is then seen that all the significant heating and pressure occurs in the boundary layer and viscous layer regimes. The term *viscous layer* refers to the thickening of the boundary layer until the shock layer is fully viscous and the shock wave thickness is about the order of the shock layer.

SPACE SHUTTLE TRAJECTORY
(HIGH HEATING LOAD, LONG CROSS RANGE ORBITER)

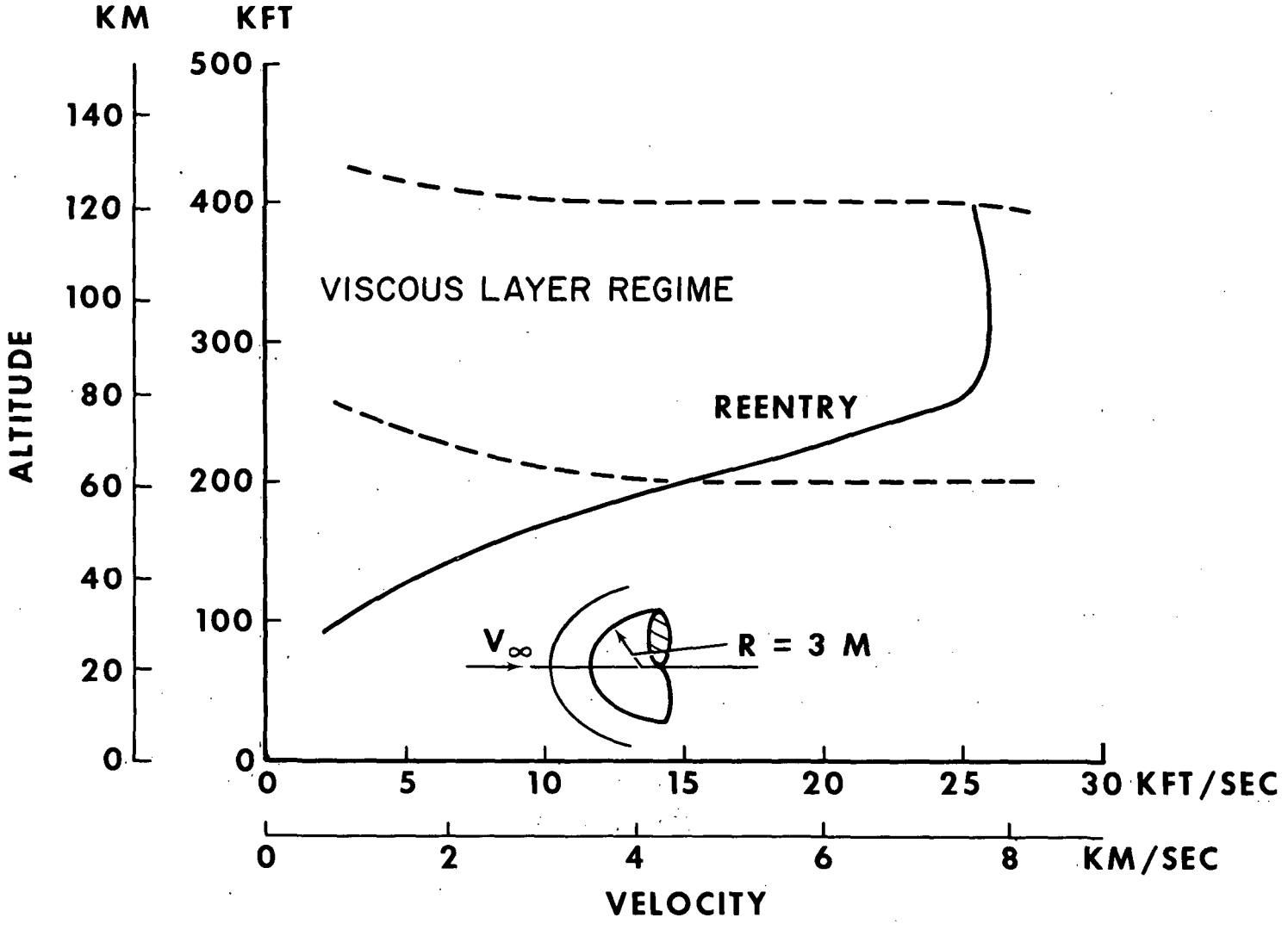

Figure 3

STEADY METHOD

(Figure 4)

This subject has received much attention, and there are many excellent works using various numerical techniques. These formulations are generally valid from low altitudes, where the boundary layer concept is useful, to high altitudes, where they begin to overlap with the kinetic approach. There are at least three methods of solution for the flow along the stagnation streamline: the thin-layer approximation, the higher order boundary layer approximation, and the direct integration through the shock. The first two methods have been applied to the flow downstream of the stagnation point with excellent results. A major assumption used in these two methods is that the shock wave structure does not affect the shock layer solution, or the shock wave is not as thick as the shock layer. The past effort has been reviewed by Cheng.[3]

STEADY METHOD

STAGNATION STREAMLINE

- THIN SHOCK LAYER APPROXIMATION
- HIGHER ORDER BOUNDARY LAYER APPROXIMATION
- DIRECT INTEGRATION THROUGH SHOCK

SHOCK LAYER

- THIN SHOCK LAYER APPROXIMATION
- HIGHER ORDER BOUNDARY LAYER APPROXIMATION

Figure 4

UNSTEADY TECHNIQUE

(Figure 5)

The unsteady or time-dependent technique has been applied in recent years by Scala and Gordon[4] and others to solve the viscous blunt-body problem. This approach has certain advantages over the steady techniques in solving for the flow field not limited to the stagnation point. One is that since the full Navier-Stokes equations are used, the high-order effects on the thin boundary layer are automatically included, and the thin shock layer thickness is not required a priori. In the time-dependent technique a convergent, time-asymptotic solution is obtained if certain stability criteria are met. Most past efforts in solving the unsteady Navier-Stokes equations are similar to the direct integration technique in the steady method, which has been shown to match the free molecular flow limit smoothly at very low Reynolds numbers. Unlike the steady technique that is applicable to the stagnation streamline only, however, these time-dependent techniques are more general and often far more expensive in computing cost because of the nature of the time-marching procedure. To circumvent the prohibitive costs of the large computational domain associated with vehicles at an angle of attack, we decided to follow Moretti's approach[5] in which the flow field within the shock layer was considered. This restricts the technique to flow regimes where the shock wave structure does not influence the shock layer solution.

UNSTEADY TECHNIQUE

- DIRECT PROBLEM
- TWO-LAYER FLOW MODEL
- MODIFIED RANKINE-HUGONIOT RELATIONS
- FINITE-DIFFERENCE MATCHING PROCEDURE FOR SHOCK
- TWO-STEP METHOD IN TIME-MARCHING
- VALID FOR ARBITRARY REYNOLDS NUMBER

Figure 5

BASIC FORMULATION

(Figure 6)

The basic equations of our study are the Navier-Stokes equations plus the nonslip and no-jump conditions for velocity and temperature along the wall. A simple gas model is used to take into account the ideal gas and the equilibrium air properties. In addition, the bulk viscosity is taken to be identically zero, and only plane and axisymmetric flows are considered.

The computational region is enclosed by the inner edge of the shock wave, the body, the axis of symmetry, and the upper boundary. A new set of independent variables is introduced that maps the region into a rectangle with the shock and the body parallel to each other. Further mappings are used to place more mesh points adjacent to the body according to an exponential law. The final mesh consists of uniformly spaced lines in both of the new coordinate axes. The dependent flow variables are chosen as the pressure, the velocity components, and the entropy to suit the Mollier chart for air. More details are given in reference 6.

BASIC FORMULATION

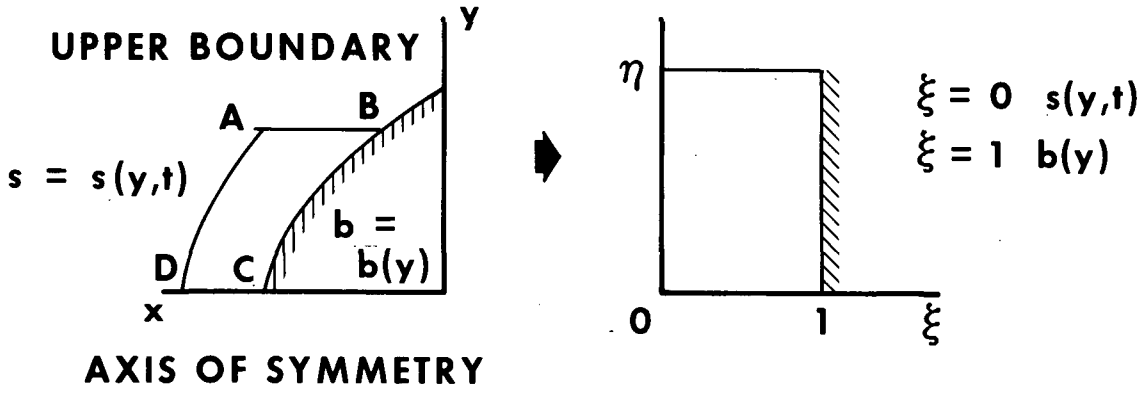

MAPPING 1

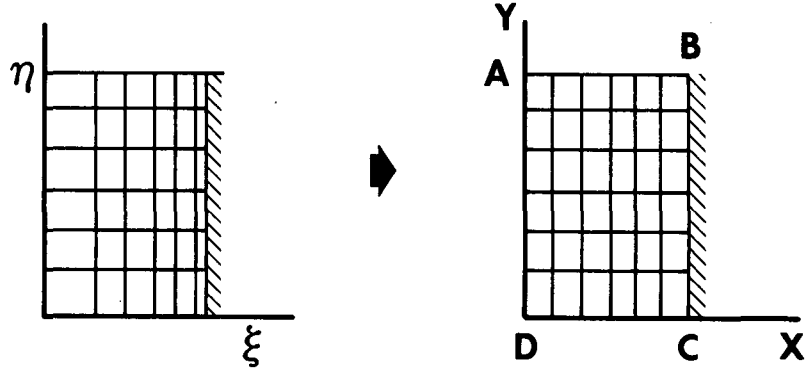

MAPPING 2

Figure 6

EFFECT OF MESH CONSTRUCTION

(Figure 7)

A computer code was written to carry out computations of a viscous flow in the nose region of a hyperboloid with a 10° asymptotic half-angle. The free-stream conditions were given by altitude = 75 km, velocity = 6 km/sec . The wall temperature was assigned to 1,000° K. The effects of mesh on the computational results were investigated under the assumption that the viscosity remained constant in the shock layer. Because of the wall temperature gradient, 20 mesh points were used across the layer and 11 points along the other direction. Convergent or time-asymptotic solutions were found after 500 time steps using 16 minutes on the UNIVAC 1108 system. Oscillations of the temperature profile were observed near the body when the second mapping was not used. The oscillation was damped out for $\beta = 1$ or 2 , where β indicates the degree of squeezing the mesh points toward the cooled body surface. This suggests that the time-dependent technique may provide useful results without resorting to a large number of mesh points in the flow regime close to the thin boundary layer.

EFFECT OF MESH CONSTRUCTION

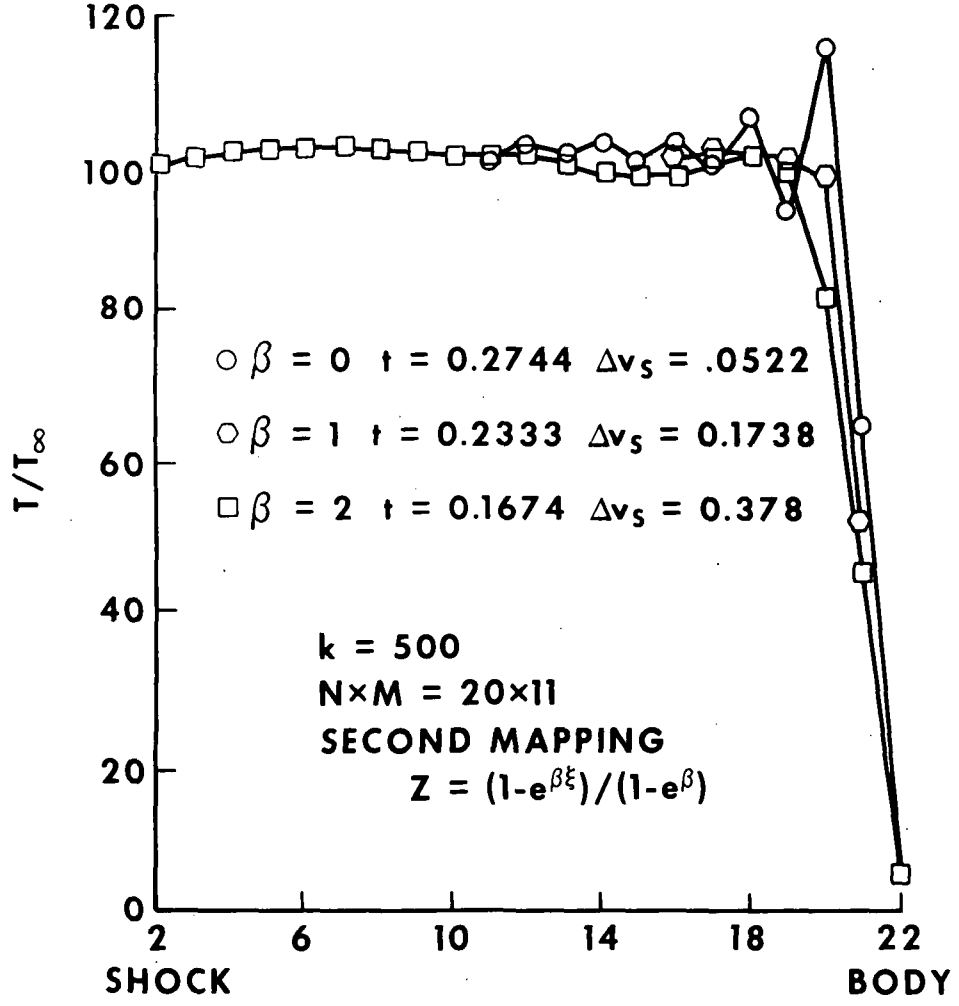

Figure 7

SHOCK SHAPES

(Figure 8)

A series of calculations was made for $Re_\infty = 10^5$, 5000, 500, and 50 to learn the effect of the Reynolds number on the flow field. The results indicated that as the Reynolds number was increased, the shock layer became thinner, and the computation converged to a steady state more rapidly. The steadiness of the solution may be indicated by the value of Δv_s, the range of the shock speed. The noticeably thinner shock layer at the lower Reynolds numbers is because the wall temperature is more strongly diffused upstream, which in turn increases the density inside the layer. Note that the shock shapes in this figure are the inner edges of the shock waves. A separate analysis would be required to obtain the shock wave structure. All calculations except $Re_\infty = 50$ used 500 time steps. The convergence was very slow at lower Reynolds numbers. Solutions generated for $Re_\infty = 50$ required approximately twice the number of time steps to achieve a similar convergent solution for $Re_\infty = 10^5$. Also shown in the same figure is an inviscid solution using velocity slip conditions. The shock wave is very thin and is located closer to the body than the results of $Re_\infty = 5000$ and above. The absence of the boundary layer in the inviscid calculation may have contributed to this result.

SHOCK SHAPES

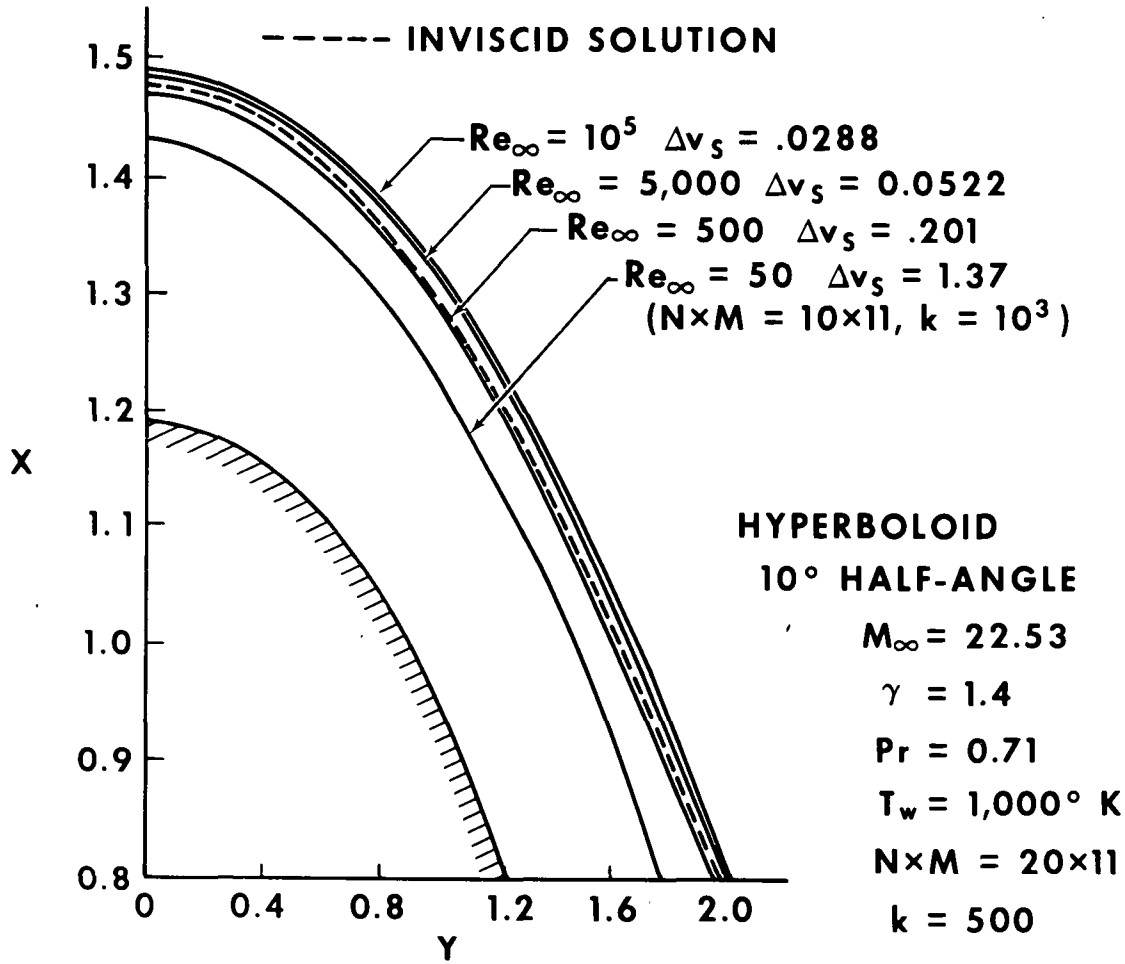

Figure 8

ENTROPY LAYER

(Figures 9(a) and 9(b))

The entropy layer structures are appreciably affected by the Reynolds number. The entropy value is nearly constant along the axis of symmetry for $Re_\infty \geq 500$ but shows an abrupt decrease at the stagnation point and continues decreasing downstream. The nonadiabatic body may be largely responsible for this. The entropy profile at $Re_\infty = 50$ is quite different from the other curves. Its behavior is caused by the merged shock wave and the boundary layer.

The entropy profile obtained for different wall temperatures is also compared with one from an adiabatic condition. The most interesting thing found is that the rate of convergence does not seem to be influenced by the wall temperature.

SURFACE ENTROPY

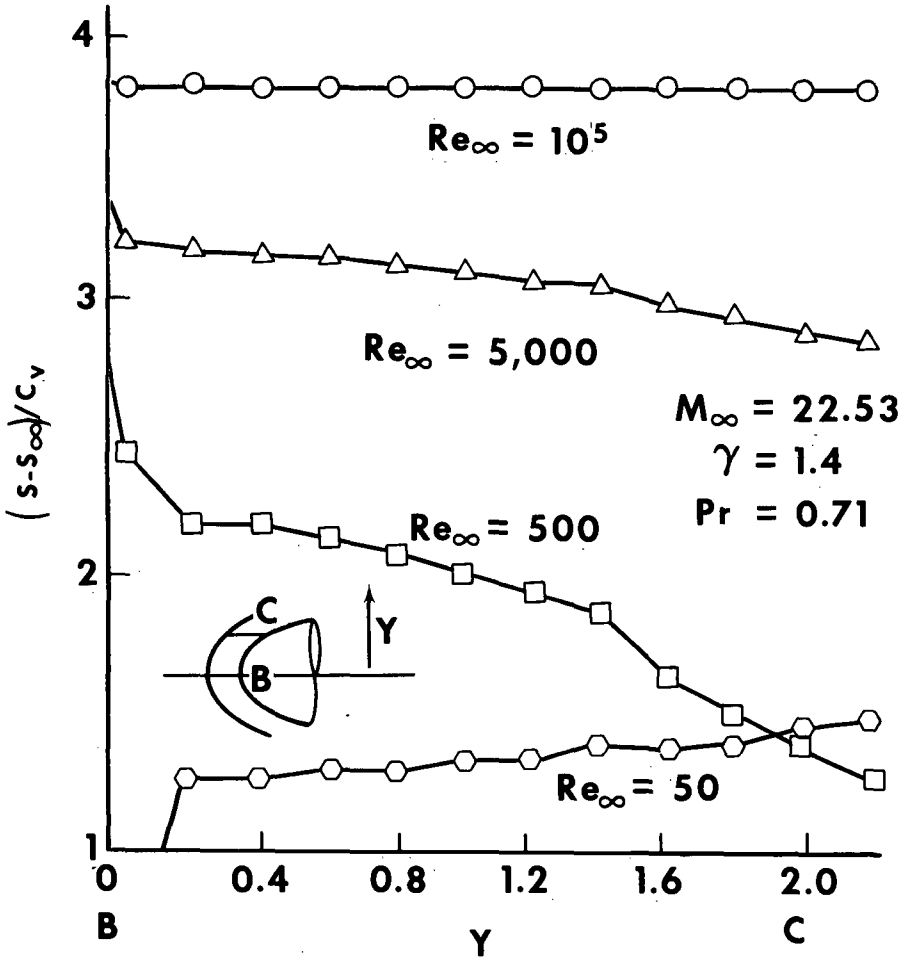

Figure 9(a)

Page intentionally left blank

SURFACE ENTROPY

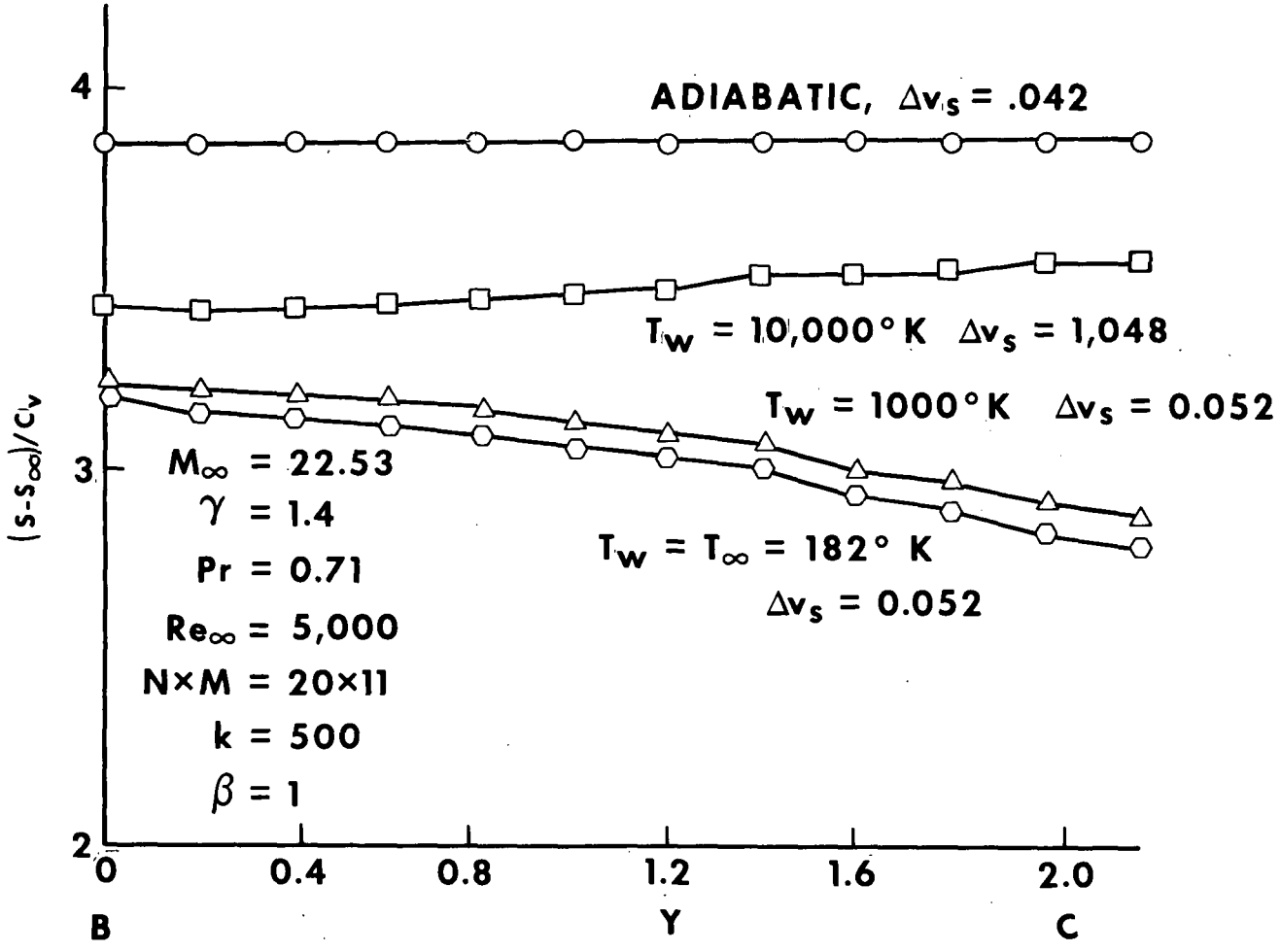

Figure 9(b)

COMPARISON WITH EXPERIMENT AND OTHER THEORIES

(Figure 10)

Experiments to determine heat transfer and skin friction coefficients for blunt-body flows in the regimes other than the thin boundary layer are difficult and scarce. A recent test by Little[7] has raised some question concerning the accuracy of the steady techniques used in predicting the skin friction coefficients C_F close to the stagnation point. Our computed values differ from those of other theories by nearly an order of magnitude; however, they agree very well with the experimental data being extrapolated to the stagnation point. The heat flux coefficient C_H obtained at $Re_\infty = 5000$, however, is quite close to the current theory. Several other results presented in the figure are not compared with either experiments or other theories. Our computed results obtained with 20 mesh points across the shock layer cannot be viewed as highly accurate for flows in the boundary layer regime. Moreover, the results available from other sources have provided too few details in the nose region to warrant a meaningful comparison with our results. The accuracy of the present formulation cannot be judged conclusively at this time.

COMPARISON WITH EXPERIMENT AND OTHER THEORIES

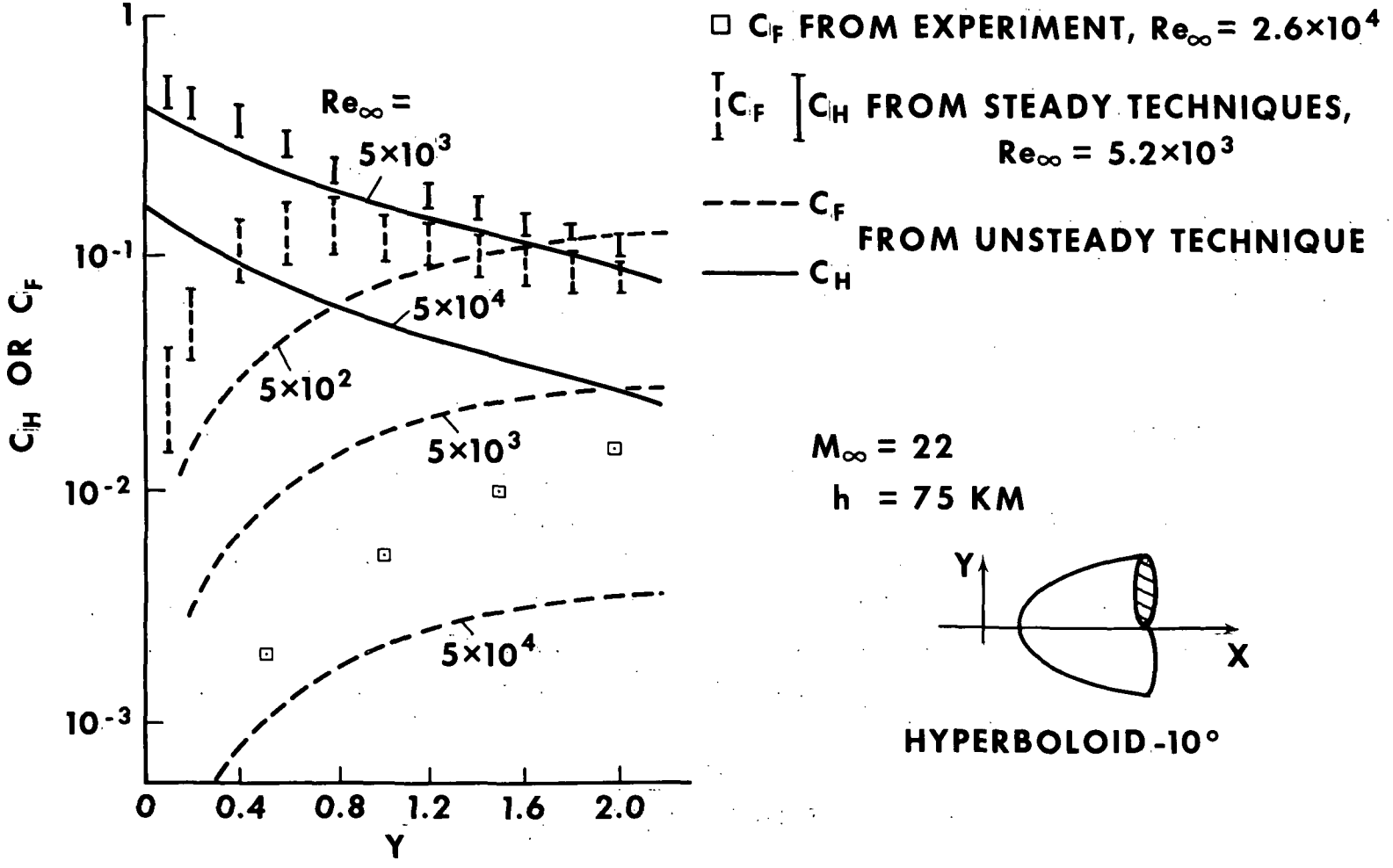

Figure 10

STARTER SOLUTION IN PROGRESS

(Figure 11)

With the encouraging results obtained from this solution of the full Navier-Stokes equation, a more general and sophisticated formulation is being developed that considers the nonequilibrium phenomena neglected in the present viscous flow study. Both finite-rate chemical reactions and a vibrational harmonic-oscillator model for the diatomic species will be included for a real airflow field calculation. The nonequilibrium phenomena could be significant for the reusable shuttle vehicle. This is particularly true for regions where the surface catalycity affects the surface heat fluxes. This formulation uses the conservative form of the flow equations written on a curvilinear coordinate system. It may economically extend the computational domain further downstream from the subsonic nose region than is allowed by the present Cartesian coordinate system and provide more accurate skin friction and heat flux coefficients at the body surface.

STARTER SOLUTION IN PROGRESS

- CONSERVATIVE-TYPE EQUATIONS
- CURVILINEAR COORDINATE SYSTEM
- FINITE-RATE CHEMICAL REACTION
- HARMONIC-OSCILLATOR MODEL
  FOR DIATOMIC SPECIES
- CHAPMAN-COWLING
  1st APPROXIMATION TO THE
  TRANSPORT PROPERTY

Figure 11

REFERENCES

1. Kutler, P.; Rakich, J. V.; and Mateer, G. G.: Application of Shock Capturing and Characteristics Methods to Shuttle Flow Fields. Space Shuttle Aerothermodynamics Technology Conference, Vol. I, 1972, pp. 65-92.

2. Probstein, R. F.: Shock Wave and Flow Field Development in Hypersonic Re-entry. ARS Journal, 31, pp. 185-194, February 1961.

3. Cheng, H. K.: Viscous Hypersonic Blunt-Body Problems and the Newtonian Theory in the "Fundamental Phenomena in Hypersonic Flow." Hall, J. G., ed., Cornell University Press, N. Y., pp. 90-132, 1966.

4. Scala, S. M., and Gordon, P.: Solution of the Time-Dependent Navier-Stokes Equations for the Flow Around a Circular Cylinder. AIAA Journal, 6, pp. 815-822, May 1968.

5. Moretti, G., and Abbett, M.: A Time-Dependent Computational Method for Blunt Body Flows. AIAA Journal, 4, pp. 776-782, December 1966.

6. Li, C. P.: Numerical Solutions of the Navier-Stokes Equations for the Shock Layer. TR 675-44-459, Lockheed Electronics Company, Inc., Houston Aerospace Systems Division, August 1971.

7. Little, H. R.: Surface Conditions on Hyperboloids and Paraboloids in Hypersonic Flow. AIAA paper no. 70-182, January 1970.

CHEMICAL NONEQUILIBRIUM EFFECTS ON THE FLOW IN THE WINDWARD PLANE OF SYMMETRY OF A BLUNTED DELTA ORBITER

by

J. A. Lordi and R. J. Vidal

Cornell Aeronautical Laboratory, Inc., Buffalo, New York

C. B. Johnson

NASA Langley Research Center, Hampton, Virginia

INTRODUCTION

The entry trajectory of the shuttle orbiter is designed for rapid deceleration of the vehicle at high altitude. The resulting combination of low velocity at high altitude leads to significant departures from chemical equilibrium in the flow field for that portion of the flight where real gas effects are important. In this paper, the extent, and some of the consequences, of nonequilibrium effects in the inviscid orbiter flow field are examined. To this end, calculations have been made for the reacting flow along selected streamlines in the windward plane of symmetry of a blunted delta shape representative of a shuttle orbiter.

An approximate model of the pressure field in the windward plane of symmetry of a blunted delta wing was constructed from wind tunnel measurements of the body surface pressure distribution and approximate calculations of the shock shape and streamline locations. Then numerical solutions for the flow along streamlines were obtained for this pressure distribution. Solutions were obtained for both equilibrium and finite-reaction-rate, nonequilibrium chemical reactions. Since the streamtube solutions are much easier to compute than fully three-dimensional, reacting flows, results were obtained for a wide range of conditions. The validity of this approach is based on the assumptions that the pressure field is insensitive to nonequilibrium effects and that the flow along streamlines is quasi-one dimensional. Numerical solutions have been used to verify this approach for other blunted slender shapes such as spherically blunted cones.[1]

The experimental surface pressure distributions were obtained in the NASA Langley Research Center Mach 8 Variable-Density Tunnel.[2] Pressure data were obtained for two shuttle test shapes, a blunted delta and a straight body, at angles of attack of 0, 20°, 40°, and 60°. All of these experimental results are presented even though the reacting flow calculations were confined to angles of attack of 20° and 40°. The streamline flow calculations were obtained with a computer program[3] previously developed at the Cornell Aeronautical Laboratory for the quasi-one-dimensional, reacting flow of a general gas mixture. In the present work,* air was assumed to be composed of a neutral species N_2, O_2, NO, N, O and Ar. Ionization of NO was also included. The thermodynamic and chemical kinetic data employed in the calculations are listed in Ref. 3.

The present paper first presents the data for the body surface pressure distributions. Next the construction of the approximate model of the pressure field in the windward plane of symmetry is described. Then results of both equilibrium and nonequilibrium flow calculations are discussed for three typical shuttle trajectory points in the altitude range of 60.96 to 76.20 km (200,000 to 250,000 ft). Calculations are compared for two angles of attack, 20° and 40°, and two nose radii, 0.305 m (1 ft) and 1.22 m (4 ft). Finally, the implications of the departures from chemical equilibrium to shuttle technology are discussed. The questions of surface heating rates, boundary layer transition, and entropy layer swallowing are treated.

*The nonequilibrium flow studies were supported by the NASA Langley Research Center under Contract No. NAS 1-10710.

PRESSURE TEST MODELS
(Fig. 1)

A series of experiments to measure the windward surface pressure distributions on two shuttle orbiter test shapes were conducted in the NASA Langley Mach 8 variable-density hypersonic tunnel. Surface pressures were obtained for the blunted delta and straight bodies shown below.

DELTA-WING AND STRAIGHT-BODY MODELS FOR WIND TUNNEL PRESSURE MEASUREMENTS

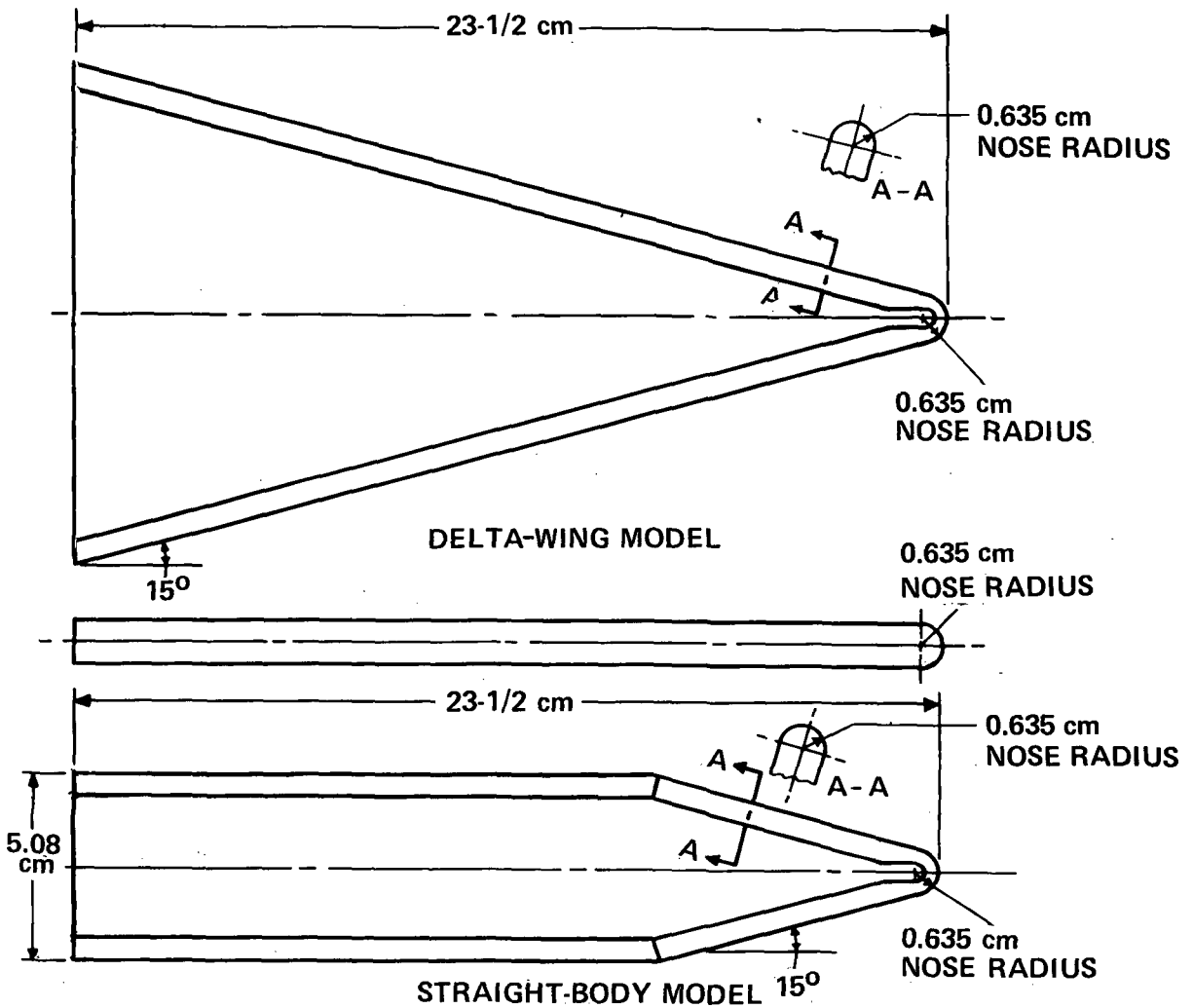

Figure 1

TEST CONDITIONS FOR PRESSURE MEASUREMENTS
(Fig. 2)

The tests were conducted at a nominal test-section Mach number of 8.0, unit Reynolds numbers in the range $8.8 \times 10^6\ m^{-1}$ to $41.5 \times 10^6\ m^{-1}$, and angles of attack of 0°, 20°, 40°, and 60°. The Reynolds numbers given in the figure are based on model length.

EXPERIMENTAL TEST CONDITIONS

RUN NO.	MACH NO.	REYNOLDS NO.	ANGLE OF ATTACK	T_o	p_o
		$\times 10^{-6}$	(deg)	(^oR)	(atm)
3	8.04	4.66	20	1455	102.7
4	7.99	3.37	20	1405	69.0
5	8.04	5.05	40	1405	105.1
6	7.99	3.37	40	1405	69.0
10	8.04	5.04	60	1385	102.4
11	7.99	3.41	60	1395	69.0
12	7.91	2.06	60	1305	36.4
28	8.11	8.46	0	1460	191
29	8.03	5.19	0	1315	96.3
30	8.03	4.53	20	1410	96.3
31	8.11	8.97	20	1410	191
32	8.03	4.64	40	1405	96.3
33	8.00	9.67	40	1380	193
34	7.95	2.32	60	1400	47.6
35	8.04	4.89	60	1385	95.2
36	8.00	9.75	60	1370	192

Figure 2

PRESSURE DATA FOR STRAIGHT BODY
(Fig. 3)

In this figure, the data from the experiments on the straight-wing body are tabulated. The data are given in the form p/p_{T_2} where p_{T_2} is the model stagnation pressure. The streamwise distance, S/R_N, is measured from the model centerline, b is the local span.

CENTERLINE PRESSURE DATA FOR THE STRAIGHT BODY

RUN NO.	28	29	30	31	32	33	34	35	36
S/R_N	p/p_{T_2}	p/p_{T_2}	p/p_{T_2}	p/p_{T_2}	p/p_{T_2}	p/p_{T_2}	p/p_{T_2}	p/p_{T_2}	p/p_{T_2}
1.134	.1918	.1948	.5421	.5480	.8874	.8439	.9525	.9766	.9570
1.571	.0466	.0449	.1969	.2002	.5270	.5104	.8587	.8963	.8802
2.071	.0344	.0337	.1491	.1537	.4870	.4724	.8233	.8635	.8465
2.823	.0302	.0305	.1331	.1357	.5110	.4983	.8187	.8573	.8386
4.114	.0236	.0273	.1275	.1311	.5262	.5218	.8249	.8573	.8374
5.614	.0194	.0225	.1315	.1382	.5230	.5053	.8203	.8589	.8276
7.611	.0152	.0178	.1491	.1546	.5222	.4995	.8295	.8565	.8284
10.61	.0152	.0194	.1602	.1663	.5374	.5143	.8387	.8698	.8296
13.61	.0143	.0202	.1602	.1608	.5350	.5088	.8233	.8526	.8096
16.06	.0152	.0225	.1578	.1562	.5278	.4979	.8157	.8378	.7943
20.61	.0131	.0187	.1501	.1560	.5194	.4892	.7839	.8182	.7727
24.06	.0144	.0211	.1598	.1593	.4749	.4318	.7667	.8009	.7473
28.61	.0118	.0163	.1477	.1458	.4806	.4398	.7527	.7867	.7361
32.61	.0144	.0195	.1412	.1382	.4312	.4034	.7418	.7772	.7298

Figure 3(a)

SPANWISE PRESSURE DATA FOR THE STRAIGHT BODY

	RUN NO.	28	29	30	31	32	33	34	35	36
S/R_N	$2y/b$	p/p_{T_2}	p/p_{T_2}	p/p_{T_2}	p/p_{T_2}	p/p_{T_2}	p/p_{T_2}	p/p_{T_2}	p/p_{T_2}	p/p_{T_2}
7.611	−.451	.0139	.0178	.1514	.1579	.5118	.4908	.8110	.8401	.8127
	−.180	.0139	.0194	.1491	.1529	.5214	.5018	.8249	.8542	.8269
	0	.0152	.0178	.1491	.1546	.5222	.4995	.8295	.8565	.8284
	.180	.0160	.0202	.1498	.1537	.5190	.5002	.8233	.8542	.8261
	.451	.0139	.0194	.1530	.1575	.5086	.4944	.8095	.8386	.8088
13.61	−.625	.0114	.0154	.1706	.1709	.5246	.5018	.7834	.8027	.7618
	−.438	.0118	.0170	.1658	.1663	.5334	.5135	.8064	.8355	.7931
	−.250	.0123	.0178	.1618	.1629	.5358	.5112	.8157	.8409	.8026
	−.125	.0148	.0194	.1594	.1604	.5350	.5092	.8249	.8511	.8088
	0	.0143	.0202	.1602	.1608	.5350	.5088	.8233	.8526	.8096
	.125	.0160	.0217	.1634	.1608	.5318	.5073	.8310	.8518	.8080
	.250	.0135	.0202	.1610	.1613	.5326	.5057	.8203	.8448	.8022
	.438	.0135	.0217	.1682	.1633	.5318	.5061	.8110	.8355	.7916
	.625	.0135	.0225	.1762	.1726	.5286	.5041	.7803	.8019	.7575
20.61	−.625	.0097	.0082	.1429	.1454	.4644	.4327	.7325	.7685	.7326
	−.438	.0135	.0163	.1534	.1551	.4935	.4608	.7714	.8024	.7548
	−.250	.0131	.0171	.1534	.1572	.5065	.4727	.7761	.8127	.7691
	−.125	.0127	.0154	.1517	.1577	.5194	.4826	.7870	.8190	.7723
	0	.0131	.0187	.1501	.1560	.5194	.4842	.7839	.8182	.7727
	.125	.0127	.0203	.1517	.1564	.5186	.4834	.7870	.8182	.7719
	.250	.0135	.0171	.1542	.1572	.5089	.4735	.7792	.8111	.7671
	.438	.0148	.0179	.1566	.1589	.4968	.4600	.7730	.8064	.7604
	.625	.0118	.0187	.1501	.1509	.4612	.4287	.7356	.7724	.7294
32.61	−.625	.0148	.0187	.1299	.1293	.4094	.3903	.6936	.7219	.6798
	−.438	.0157	.0187	.1372	.1348	.4272	.4053	.7232	.7519	.7095
	−.250	.0148	.0203	.1388	.1382	.4320	.4073	.7403	.7709	.7250
	−.125	.0165	.0187	.1396	.1382	.4344	.4065	.7434	.7732	.7290
	0	.0144	.0195	.1412	.1382	.4312	.4034	.7418	.7772	.7298
	.125	.0144	.0195	.1404	.1386	.4288	.4006	.7418	.7748	.7286
	.250	.0152	.0195	.1380	.1365	.4247	.4002	.7403	.7724	.7238
	.438	.0161	.0195	.1380	.1339	.4231	.3974	.7278	.7582	.7087
	.625	.0169	.0171	.1324	.1288	.4053	.3816	.6936	.7203	.6754

Figure 3(b)

PRESSURE DATA FOR THE DELTA BODY
(Fig. 4)

In this figure, the data are tabulated for the experiments on the blunted delta wing. Again the data are normalized by the model stagnation pressure and the streamwise distance is measured from the model centerline.

CENTERLINE PRESSURE DATA FOR THE DELTA BODY

RUN NO.	3	4	5	6	10	11	12
S/R_N	p/p_{T_2}	p/p_{T_2}	p/p_{T_2}	p/p_{T_2}	p/p_{T_2}	p/p_{T_2}	p/p_{T_2}
1.134	.4243	.4558	.7932	.7845	.9745	.9761	.9540
1.571	.1710	.1882	.4849	.4720	.8886	.9367	.8570
2.071	.1355	.1459	.4620	.4438	.8651	.8494	.8314
2.823	.1243	.1347	.4944	.4691	.8593	.8466	.8314
4.114	.1184	.1347	.4963	.4832	.8475	.8466	.8264
5.614	.1262	.1431	.4868	.4889	.8475	.8382	.8161
7.611							
10.61	.1496	.1572	.4924	.4889	.8475	.8579	.8212
13.61	.1516	.1657	.4887	.4973	.8553	.8579	.8264
16.61	.1399	.1572	.4849	.4917	.8690	.8748	.8417
20.61	.1457	.1572	.5020	.5001	.8593	.8720	.8417
24.61	.1574	.1684	.4811	.4944	.8475	.8579	.8314
28.61	.1399	.1684	.5096	.5114	.8358	.8438	.8161
32.61	.1418	.1572	.4754	.4860	.8241	.8298	.8161

Figure 4(a)

SPANWISE PRESSURE DATA FOR THE DELTA BODY

	RUN NO.	3	4	5	6	10	11	12
S/R_N	$2y/b$	p/p_{T_2}	p/p_{T_2}	p/p_{T_2}	p/p_{T_2}	p/p_{T_2}	p/p_{T_2}	p/p_{T_2}
7.611	−.484	.1457	.1618	.4849	.4832	.8339	.8298	.8110
	−.193	.1360	.1516	.4868	.4748	.8514	.8466	.8212
	0	–	–	–	–	–	–	–
	.193	.1360	.1488	.4887	.4748	.8514	.8410	.8212
	.484	.1418	.1572	.4792	.4748	.8299	.8241	.8008
13.61	−.664	–	–	–	–	–	–	–
	−.483	.1554	.1684	.4868	.4944	.8397	.8438	.8161
	−.302	.1477	.1628	.4887	.4944	.8494	.8494	.8212
	−.121	.1516	.1657	.4887	.4973	.8534	.8607	.8264
	0	.1516	.1657	.4887	.4973	.8553	.8579	.8264
	.121	.1558	.1657	.4906	.4973	.8553	.8607	.8264
	.302	.1516	.1657	.4906	.4973	.8494	.8523	.8264
	.483	.1554	.1657	.4906	.4917	.8378	.8410	.8110
	.664	.1593	.1684	.4811	.4860	.8124	.8184	.7854
20.61	−.798	.1574	.1741	.4697	.4804	.7928	.7847	.7651
	−.588	.1516	.1684	.4868	.4860	.8553	.8579	.8212
	−.378	.1477	.1628	.4982	.4944	.8612	.8720	.8366
	−.210	.1477	.1600	.5001	.4973	.8593	.8720	.8366
	−.084	.1457	.1572	.5020	.5001	.8593	.8720	.8366
	0	.1457	.1572	.5020	.5001	.8593	.8720	.8417
	.084	.1457	.1572	.5020	.5001	.8593	.8748	.8417
	.210	.1477	.1600	.4982	.5001	.8612	.8748	.8468
	.378	.1477	.1684	.4924	.4973	.8632	.8748	.8468
	.588	.1535	.1741	.4849	.4973	.8534	.8466	.8314
	.798	.1574	.1769	.4678	.4832	.7811	.7819	.7549
32.61	−.856	.1328	.1741	.4639	.4776	.7440	.7481	.7344
	−.635	.1516	.1657	.4792	.4944	.8045	.8101	.7906
	−.414	.1457	.1628	.4899	.5086	.8202	.8241	.8110
	−.249	.1457	.1628	.4811	.5029	.8221	.8269	.8161
	−.138	.1457	.1628	.4811	.4944	.8241	.8298	.8161
	−.055	.1418	.1572	.4754	.4860	.8241	.8258	.8161
	0	.1418	.1572	.4754	.4860	.8241	.8298	.8161
	.055	.1438	.1572	.4734	.4889	.8241	.8298	.8161
	.138	.1399	.1572	.4716	.4917	.8221	.8269	.8110
	.249	.1438	.1600	.4754	.5001	.8221	.8269	.8110
	.414	.1438	.1600	.4754	.5001	.8182	.8241	.8059
	.635	.1477	.1600	.4716	.4832	.8026	.8101	.7957
	.856	.1554	.1713	.4527	.4720	.7381	.7424	.7344

Figure 4(b)

SCHLIEREN PHOTOGRAPHS OF MODEL FLOW FIELDS
(Fig. 5)

In the series of experiments to measure surface pressure on the shuttle test shapes, Schlieren photographs were also taken. The photographs from two of the test conditions are shown in this figure. The cases illustrated are the blunted-delta and straight body at an angle of attack of 40°.

For the blunted delta wing the shock shapes over the windward surface are quite straight for $\alpha = 20°$ and $\alpha = 40°$. In the nonequilibrium flow calculations described later in the paper the flow downstream of the nose is assumed to be a uniform flow region and this assumption appears to be accurate.

The comparison of the two Schlieren photographs shown here indicates that the difference in the body shapes is reflected in the shock shape for this angle of attack. Both the Schlieren photographs and the pressure data indicate that the cross flow begins to affect the inviscid flow in the windward plane of symmetry at $\alpha = 40°$. At $\alpha = 60°$, the difference in the shock shapes is more pronounced. Also, the windward centerline pressure decays toward the base of the body; the pressure decreases more rapidly for the straight-body. At an angle of attack of 20° the shock shapes and windward centerline pressure distributions are nearly the same for these two body shapes.

SCHLIEREN PHOTOGRAPHS OF MODEL FLOW FIELDS

$M_\infty = 8, \alpha = 40^\circ$

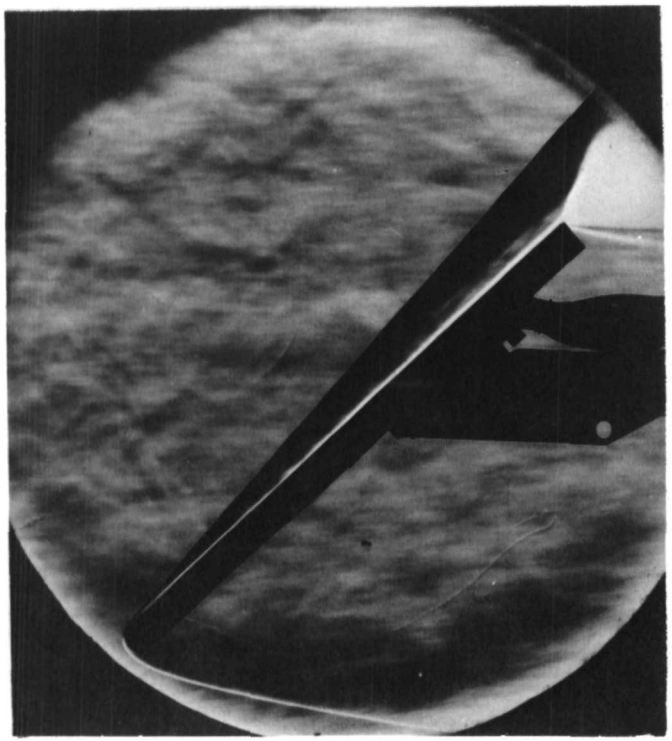

RUN 5

BLUNTED-DELTA BODY

RUN 33

STRAIGHT-BODY

Figure 5

WINDWARD SIDE CENTERLINE PRESSURE DISTRIBUTIONS FOR BLUNTED-DELTA SHAPE (Figs. 6 and 7)

In a previous study[1] of the hypersonic flow over blunted slender cones the surface pressure distribution was found to be insensitive to nonequilibrium effects. Since the flow along the windward plane of symmetry of the blunted-delta wing should be much like a cone flow this result has been used in the present study to scale the measured pressure distributions to flight conditions. The data were normalized by the tunnel-model stagnation pressure and the pressures on the flight vehicle were obtained by using the appropriate value of the stagnation pressure. The initial portion of the pressure distribution, i.e. between the stagnation point and the first data point, was taken from a composite correlation[1] of ideal gas, equilibrium and nonequilibrium flow calculations, and experimental data for the flow over spherically blunted bodies. The stagnation point was assumed to be the point where the body surface is normal to the free stream direction. A full scale body length of 45.6 m (150 ft) was used.

The body surface pressure distributions which were used in the streamtube calculations for $\alpha = 20°$ and $\alpha = 40°$ are shown in the next two figures, together with the experimental data on which they are based. Here and throughout the remainder of the paper S_b denotes distance along the surface streamline, measured from the stagnation point.

PRESSURE DISTRIBUTION ALONG WINDWARD CENTERLINE FOR BLUNTED-DELTA BODY, $\alpha = 20^{o}$

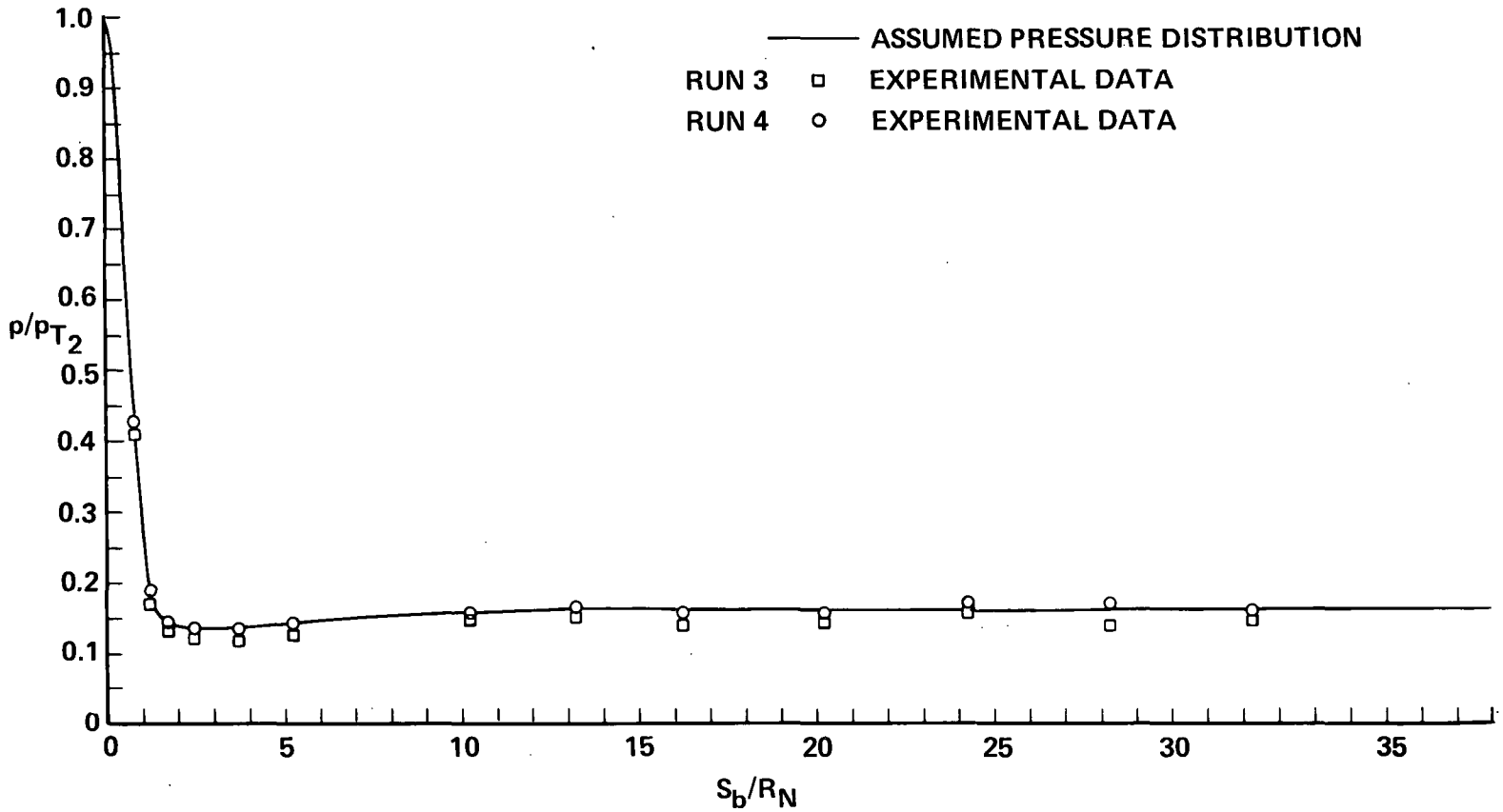

Figure 6

Page intentionally left blank

PRESSURE DISTRIBUTION ALONG WINDWARD CENTERLINE FOR BLUNTED-DELTA BODY, $\alpha = 40^{\circ}$

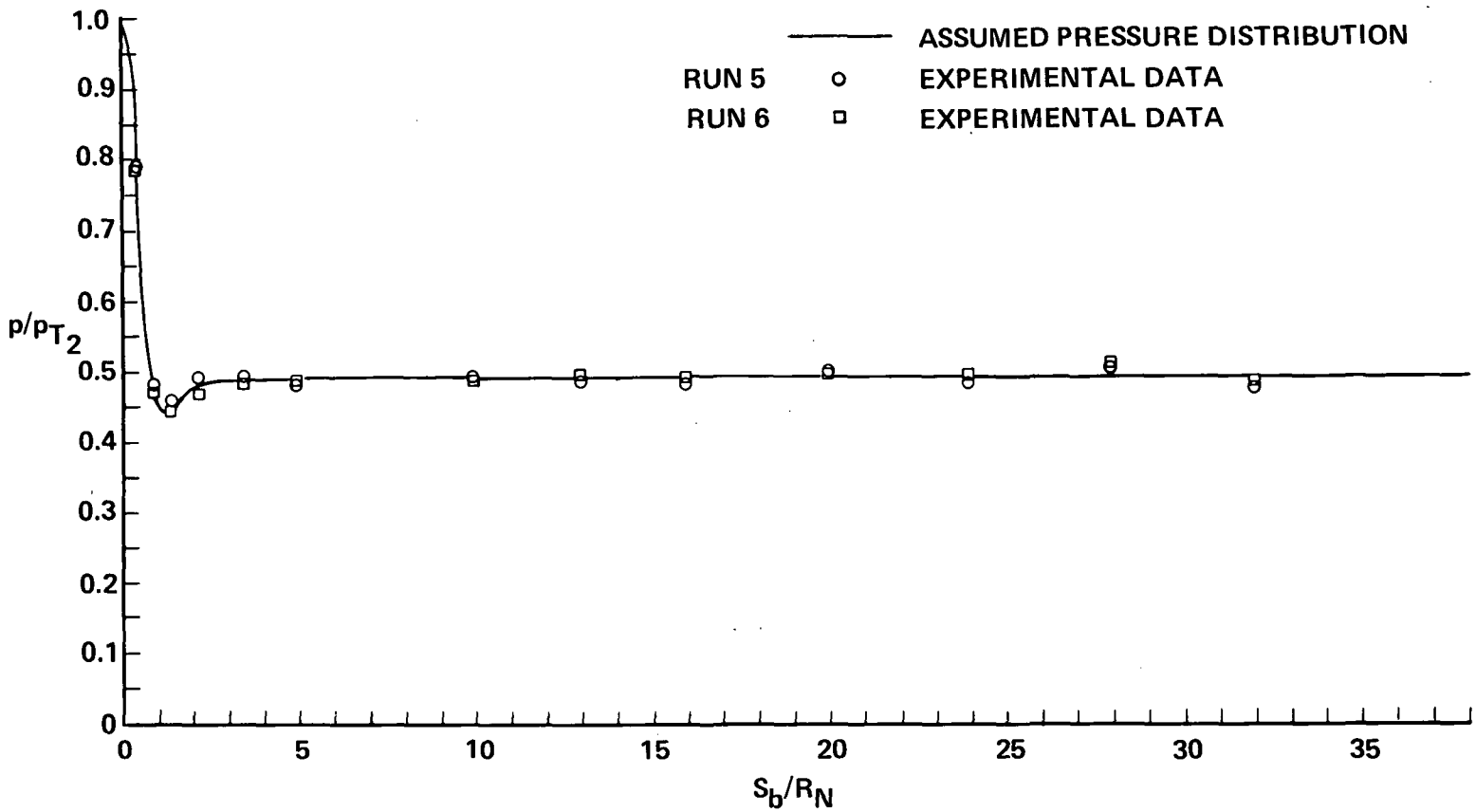

Figure 7

APPROXIMATE CALCULATION FOR SHOCK SHAPES AND STREAMLINE LOCATIONS (Figs. 8 and 9)

In order to obtain the pressure histories along streamlines off the body surface, an approximate model of the pressure field was devised. The shock shapes and streamline locations were obtained for equilibrium flow and again an appeal was made to the results for the flow about blunted cones. These results indicate that the shock shape as well as the surface pressure is insensitive to nonequilibrium effects.

The bow shock wave was assumed to be circular in the nose region and straight on the afterbody. The final shock angle was determined from the asymptotic, experimental surface pressure and oblique shock solutions for equilibrium flow. The circular portion of the shock was not taken to be concentric with the body. Rather, the center and radius of curvature were found by using a correlation for shock standoff distance at the stagnation point[4] and a mass balance to get the shock standoff distance at the body shoulder. The mass balance was done by assuming the flow in the stagnation region of the windward plane of symmetry to be the same as that in the axisymmetric flow over a blunted cone. The circular portion of the shock was joined to the straight portion at the point of tangency. In the nose region, the streamline locations also were found using a mass balance technique. The mass flux was assumed to vary linearly from the shock to the body along normals to the body surface. The solution for the equilibrium flow along the body streamline was computed using the known pressure distribution and an isentropic expansion from the known stagnation conditions. The values at the shock were obtained from the shock angle and shock tables for equilibrium flow.[5] In the afterbody region the streamlines were assumed to be parallel to the body. This assumption of a uniform pressure field on the afterbody appears justified both by Schlieren photographs obtained in this study (see Fig. 5) and three-dimensional flow calculations for equilibrium flow over a blunted delta wing.[6] Having established the streamline locations, the pressure distributions along them were computed assuming a linear variation between the pressure at the body and the shock, along normals to the body.

The shock shapes and streamline locations obtained for $\alpha = 20°$ and $\alpha = 40°$ are illustrated in the accompanying figures. The flow field consists basically of two regions: those streamlines which are processed by the strong curved shock and those which pass through the limiting oblique shock. The streamline which passes through the point where the shock becomes straight is referred to as the outer streamline or oblique-shock streamline. The pressure field between this streamline and the shock is assumed to be uniform. While these streamline locations may not be precise, the important point is that the pressure histories are realistic and the streamline calculations provide an accurate assessment of the nonequilibrium flow effects. Furthermore, for the extreme cases of the body surface streamline and the outer streamline, the calculations are good approximations to the results obtained from more general flow field calculations.

SHOCK SHAPE AND STREAMLINE PATTERN IN NOSE REGION, $\alpha = 20^{o}$

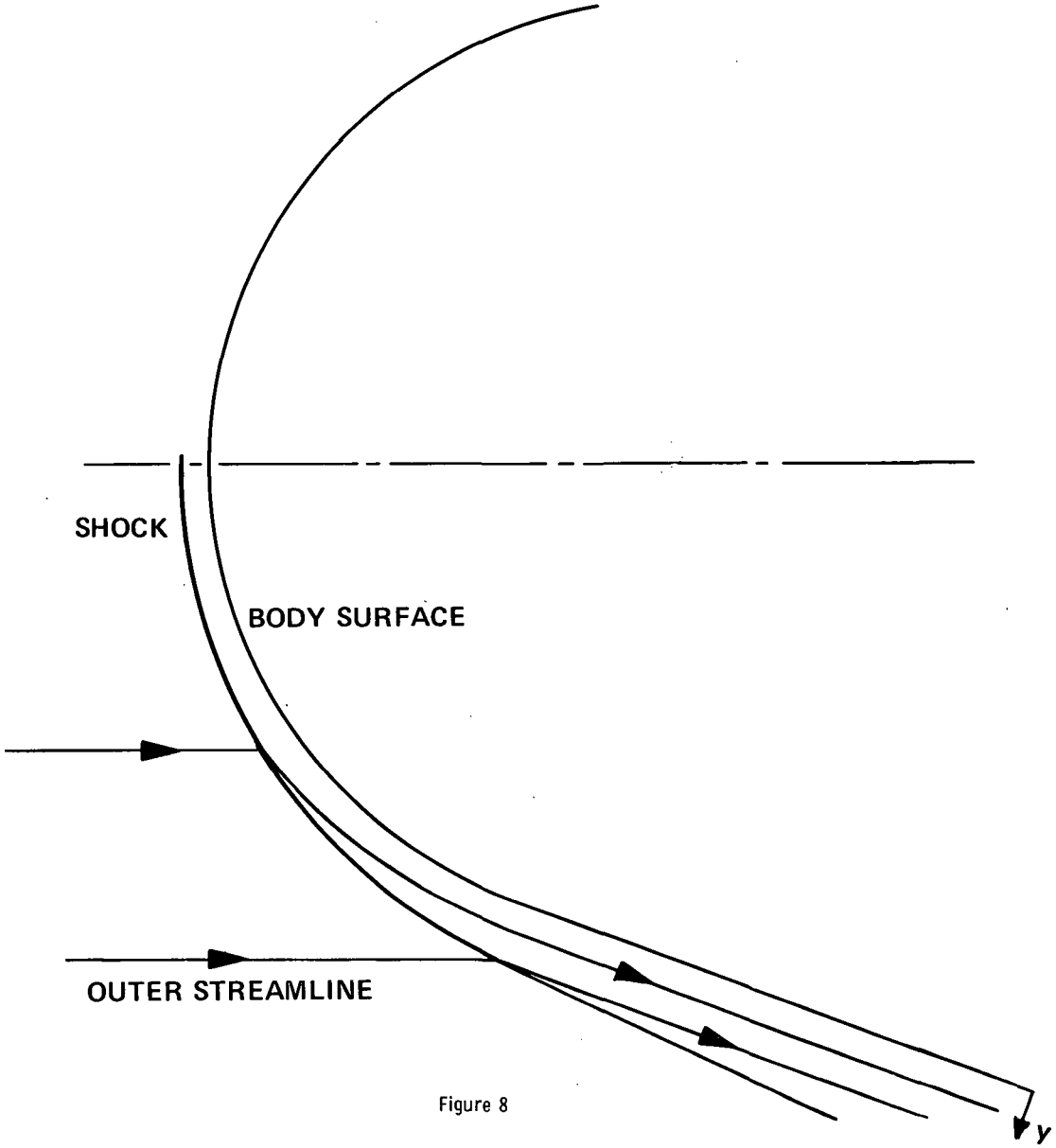

Figure 8

Page intentionally left blank

SHOCK SHAPE AND STREAMLINE PATTERN IN NOSE REGION $\alpha = 40^{o}$

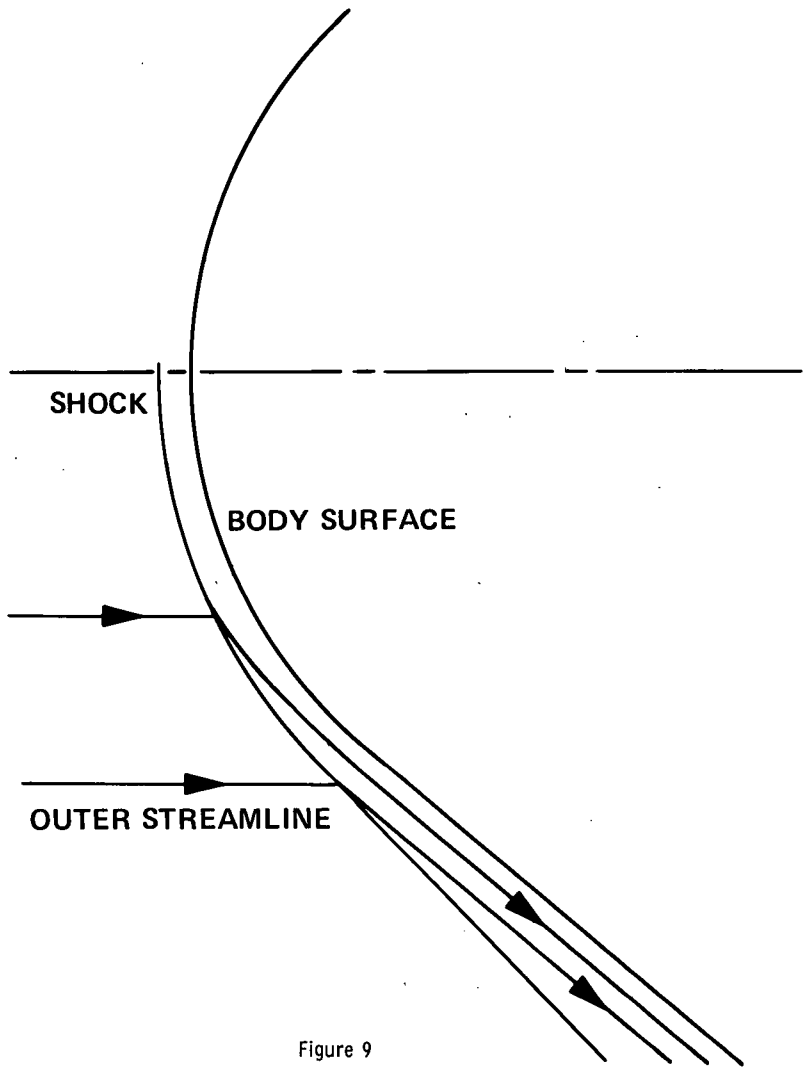

Figure 9

EQUILIBRIUM AND NONEQUILIBRIUM FLOW CALCULATIONS
(Fig. 10)

Calculations of the flow along selected streamlines have been made for both equilibrium and nonequilibrium chemical reactions. The trajectory points at which calculations were done are listed in the table below. Calculations have been made along the body surface streamline, a streamline about in the middle of the entropy layer and the outer streamline, or that which passes through the limiting oblique shock. The influence of changes in angle of attack and nose radius are also demonstrated.

The departure from chemical equilibrium are of a different type for those streamlines near the body than for the outer streamlines. In the entropy layer, that is along those streamlines near the body surface, the flow approaches chemical equilibrium in the stagnation region and then departs from equilibrium in the rapid expansion of the flow around the nose of the body. Along the outer streamlines, the flow is very much like the relaxing flow behind a shock wave. The flow is chemically frozen through the shock wave and then approaches equilibrium over the entire body length. Thus, near the body surface the departure from equilibrium is a lag in the rate of recombination as the flow expands from the stagnation point, while along the outer streamlines there is a lag in the dissociation rate.

TRAJECTORY POINTS USED IN STREAMLINE CALCULATIONS

1. V_∞ = 4.877 km/sec, h = 60.96 km
   (16 kfps) (200 kft)

2. V_∞ = 6.096 km/sec, h = 67.06 km
   (20 kfps) (220 kft)

3. V_∞ = 7.315 km/sec, h = 76.20 km
   (24 kfps) (250 kft)

Figure 10

FLOW ALONG BODY SURFACE STREAMLINES
(Fig. 11)

Several calculations have been made for the flow along the body surface streamline, starting from an equilibrium stagnation point. In the altitude range of 200 to 250 kft, the flow along the body surface streamlines is composed mainly of N_2, N, and O for both equilibrium and nonequilibrium flow. The principal nonequilibrium effect is the lag in the nitrogen atom recombination as the flow expands in the nose region. The oxygen is fully dissociated and remains so. The variation in temperature, density, velocity, and species concentrations along the streamline are illustrated in the figures below for the trajectory point V_∞ = 4.877 km/sec (16,000 fps), h = 60.96 km (200,000 ft), and for R_N = 1.22 m (4 ft), and $\alpha = 20°$.

The temperature distribution is a direct consequence of the nonequilibrium effect on the N-atom recombination rate. The nonequilibrium flow temperature falls much below the equilibrium temperature in the nose region because the nitrogen atom recombination reaction becomes frozen. Then, in the fairly uniform flow on the flat aftersurface, some recombination takes place and the nonequilibrium temperature approaches the equilibrium value toward the base of the body. Notice that this approach is gradual and the flow is almost frozen over the entire body. The nonequilibrium effects on density and velocity are slight and in the direction such that there is very little effect on the mass flow rate.

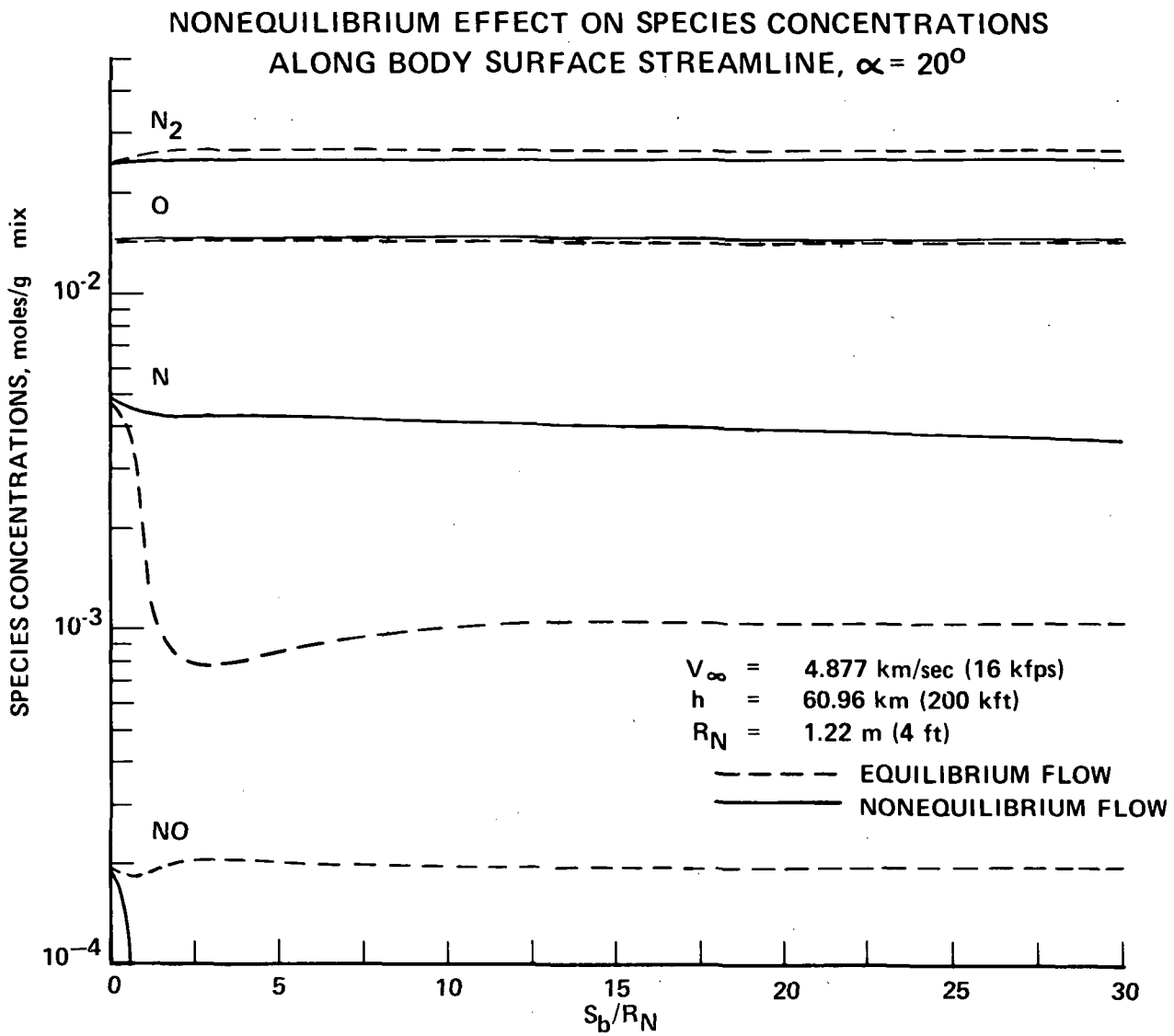
NONEQUILIBRIUM EFFECT ON SPECIES CONCENTRATIONS
ALONG BODY SURFACE STREAMLINE, α = 20°
SPECIES CONCENTRATIONS, moles/g mix
N2
O
N
NO
10-2
10-3
10-4
0
5
10
15
20
25
30
Sb/RN
V∞ = 4.877 km/sec (16 kfps)
h = 60.96 km (200 kft)
RN = 1.22 m (4 ft)
EQUILIBRIUM FLOW
NONEQUILIBRIUM FLOW

Figure 11(a)

NONEQUILIBRIUM EFFECT ON TEMPERATURE ALONG BODY SURFACE STREAMLINE, $\alpha = 20^{o}$

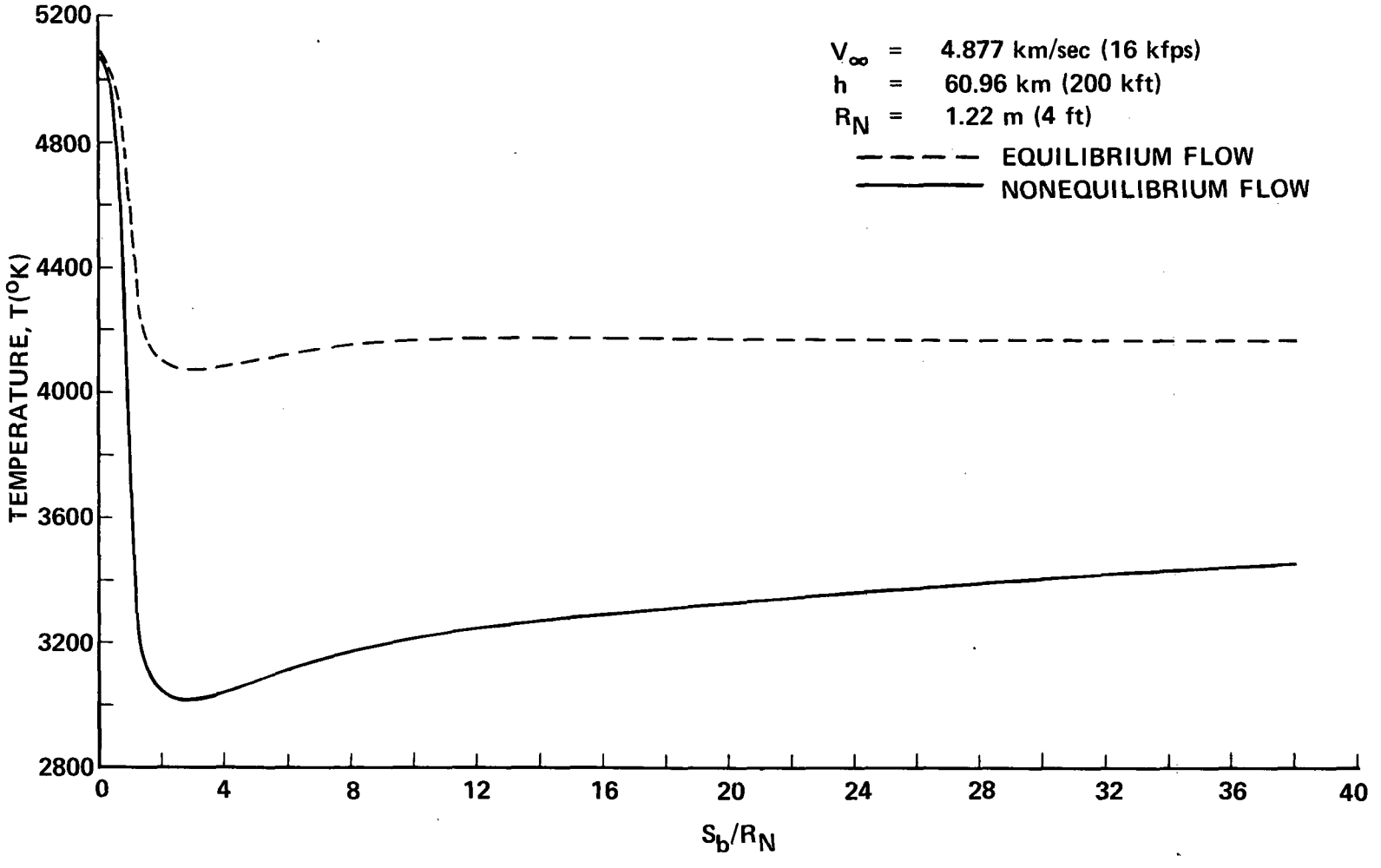

Figure 11(b)

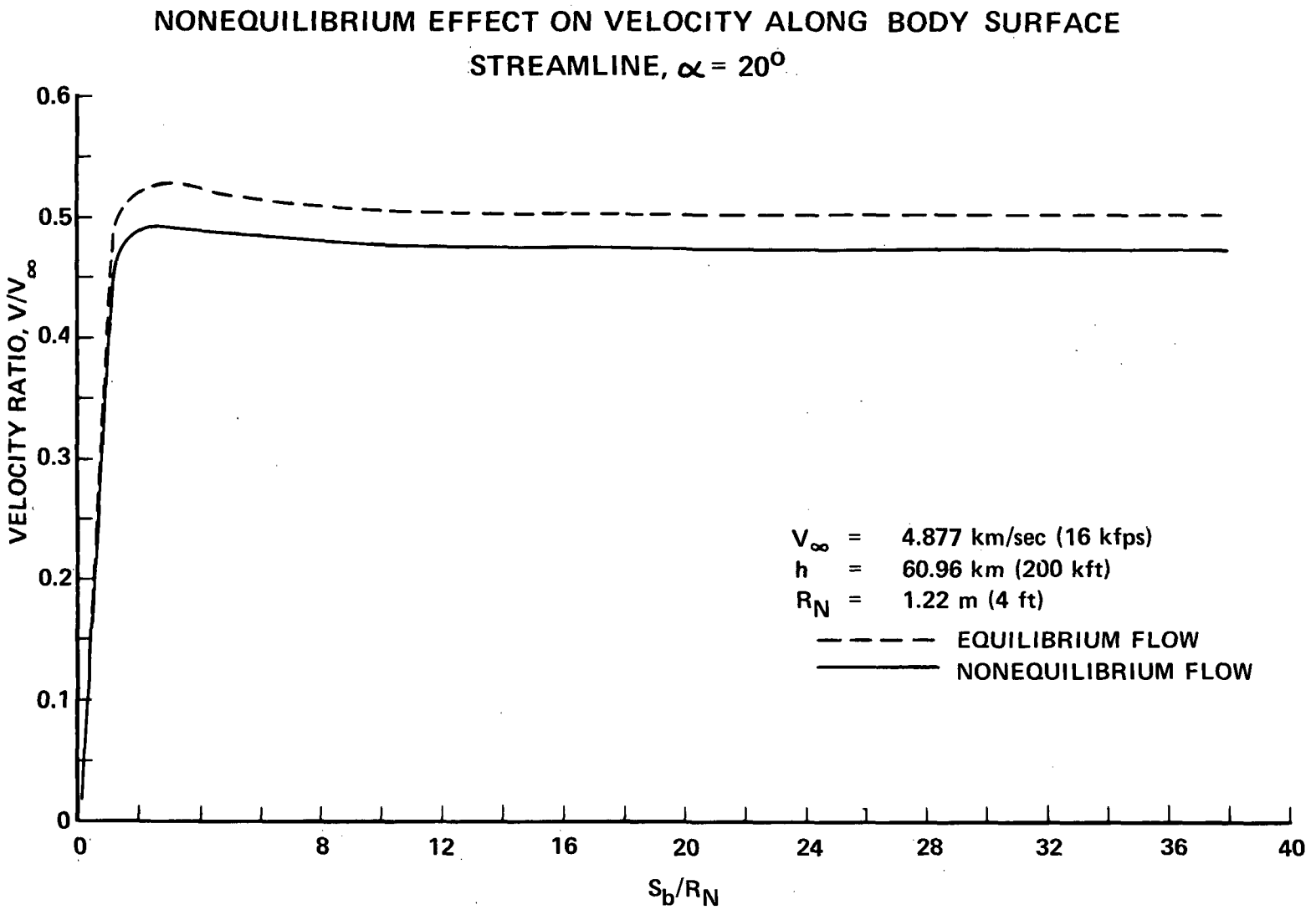
NONEQUILIBRIUM EFFECT ON VELOCITY ALONG BODY SURFACE
STREAMLINE, α = 20°
VELOCITY RATIO, V/V∞
0.6
0.5
0.4
0.3
0.2
0.1
0
0
8
12
16
20
24
28
32
36
40
Sb/RN
V∞ = 4.877 km/sec (16 kfps)
h = 60.96 km (200 kft)
RN = 1.22 m (4 ft)
EQUILIBRIUM FLOW
NONEQUILIBRIUM FLOW

Figure 11(c)

Page intentionally left blank

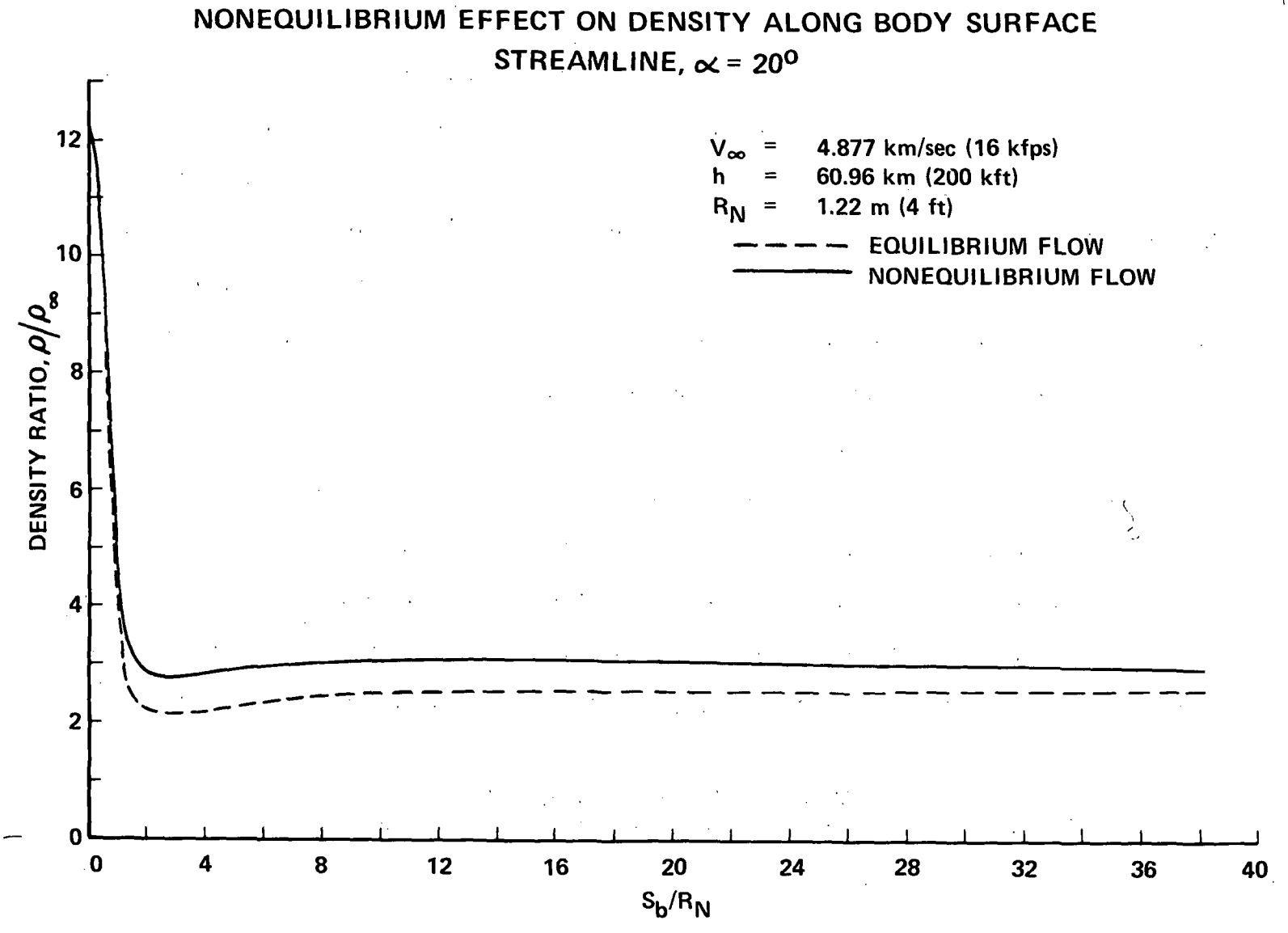
NONEQUILIBRIUM EFFECT ON DENSITY ALONG BODY SURFACE STREAMLINE, $\alpha = 20^{o}$
V_∞ = 4.877 km/sec (16 kfps)
h = 60.96 km (200 kft)
R_N = 1.22 m (4 ft)
EQUILIBRIUM FLOW
NONEQUILIBRIUM FLOW
DENSITY RATIO, ρ/ρ_∞
0
2
4
6
8
10
12
0
4
8
12
16
20
24
28
32
36
40
S_b/R_N

Figure 11(d)

TRAJECTORY VARIATION OF NONEQUILIBRIUM EFFECTS ON THE BODY STREAMLINE FLOW
(Fig. 12)

Numerical solutions were obtained for the equilibrium and nonequilibrium flow along the body streamlines for the three trajectory points given in the table of Fig. 10. These calculations were done for an angle of attack of 20° and a body nose radius of 1.22 m (4 ft). The variation of the nonequilibrium effects from one trajectory point to the next is one of degree rather than kind. In this series of calculations, the temperature distributions are all similar to that shown in Fig. 11 and so the difference between the equilibrium and nonequilibrium flow temperatures at the base of the body is a good representation of the effect of nonequilibrium chemical reaction on the body streamline flow for these conditions. Accordingly, these temperatures are listed in the table for the three trajectory points at which calculations were made. The difference between the equilibrium and nonequilibrium temperatures is greatest at the highest altitude, highest velocity point because the nitrogen dissociation is greatest there and the most energy is frozen in chemical composition for this case.

NONEQUILIBRIUM EFFECTS ON SURFACE STREAMLINE TEMPERATURE

TRAJECTORY POINT	T_{EQ} (^oK)	T_{NEQ}* (^oK)
1. V = 4.877 km/sec (16 kfps) h = 60.96 km (200 kft)	4178	3459
2. V = 6.096 km/sec (20 kfps) h = 67.06 km (220 kft)	4973	3721
3. V = 7.315 km/sec (24 kfps) h = 76.20 km (250 kft)	5198	3372

* AT S_b = 45.6 m (150 ft)

Figure 12

FLOW ALONG OUTER STREAMLINES
(Fig. 13)

The flow along the outer streamlines in the blunted-delta wing flow field is much like the flow behind an oblique shock wave. The reacting flow behind strong shock waves was extensively reviewed in Ref. 7. There several calculations were made to investigate scaling and distances to equilibrium. In addition, the mapping of normal shock wave flows to approximate wedge flows was shown to be quite accurate. The results found here are very much in line with what would be expected in terms of the flow behind such equivalent normal shocks. At the velocities and altitudes of interest the distances to equilibrium can be considerable. For an angle of attack of 20°, the shock angle determined by the limiting pressure ratio is about 25° and varies little from one trajectory point to the next. The flow behind this wave, computed here as a constant pressure streamline flow, is essentially frozen over the length of the orbiter. The temperature at a distance of 45.6 m (150 ft) from the shock wave is shown for three trajectory points in the table below. At the lowest altitude of interest here, it can be seen that the flow is essentially an ideal gas flow. At the highest velocity and highest altitude, the difference between the equilibrium and non-equilibrium flow temperature is significant. Along the outer streamlines this discrepancy is due mainly to a lag in the oxygen dissociation rate and nitric oxide formation while the nitrogen remains virtually undissociated.

NONEQUILIBRIUM EFFECTS ON OUTER STREAMLINE TEMPERATURE

$\alpha = 20^{o}$ $R_N = 1.22$ m (4 ft)

TRAJECTORY POINT	T_{EQ} (^{o}K)	T_{NEQ}* (^{o}K)
1. V = 4.877 km/sec (16 kfps) h = 60.96 km (200 kft)	2053	2120
2. V = 6.096 km/sec (20 kfps) h = 67.06 km (220 kft)	2486	2997
3. V = 7.315 km/sec (24 kfps) h = 76.20 km (250 kft)	2707	3720

* AT S_b = 45.6 m (150 ft)

Figure 13

NONEQUILIBRIUM EFFECTS ON THE TEMPERATURE DISTRIBUTION THROUGH THE SHOCK LAYER (Fig. 14)

The manner in which chemical nonequilibrium effects change as attention is focused in turn on streamlines near the body surface and then on streamlines further out in the shock layer was briefly described in Fig. 10. Along the body streamline the static temperature of the nonequilibrium flow falls significantly below the equilibrium flow value as the flow expands around the nose. Along the outer streamlines, the temperature in the nonequilibrium flow increases toward the equilibrium value as the flow approaches chemical equilibrium. For one of the trajectory points, V_∞ = 4.877 km/sec (16,000 fps), h = 60.96 km (200,000 ft), α = 20°, the flow along several streamlines in the shock layer has been computed. The results for the variation of the temperature normal to the body surface are shown in this figure for S_b/R_N = 30, where S_b is the distance along the body from the stagnation point. The relative values for equilibrium and nonequilibrium flow reflect the behavior of the flow chemistry, as described above. For this case the flow along the streamlines outside the entropy layer is essentially an ideal gas flow.

NONEQUILIBRIUM EFFECT ON TEMPERATURE DISTRIBUTION THROUGH THE SHOCK LAYER

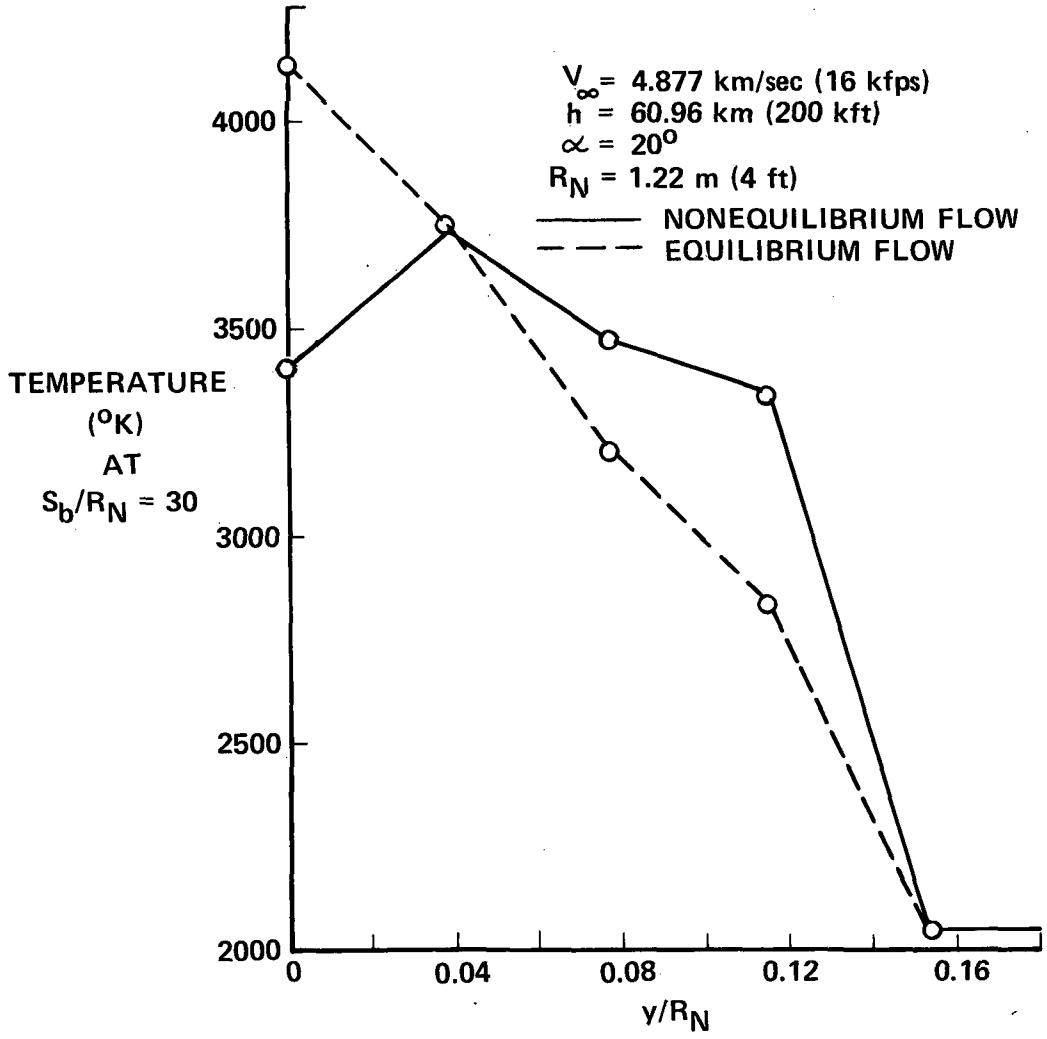

Figure 14

EFFECT OF ANGLE OF ATTACK
(Fig. 15 and 16)

Streamline calculations have also been made at $\alpha = 40°$. At this angle of attack the flow expansion around the nose of the body is weaker. Hence there is less of a lag in the recombination rate for nitrogen atoms. On the afterbody the density level is higher and the flow approaches equilibrium much more rapidly than for $\alpha = 20°$, both along the body streamlines and the outer streamlines. The temperature distribution along the body streamline and along the outermost streamline are illustrated below for the case $V_\infty = 4.877$ km/sec (16,000 fps), $h = 60.96$ km (200,000 ft), and $R_N = 1.22$ m (4 ft). Again these figures are typical of the results at the other trajectory points considered in this study.

NONEQUILIBRIUM EFFECT ON TEMPERATURE ALONG BODY SURFACE STREAMLINE, $\alpha = 40^{o}$

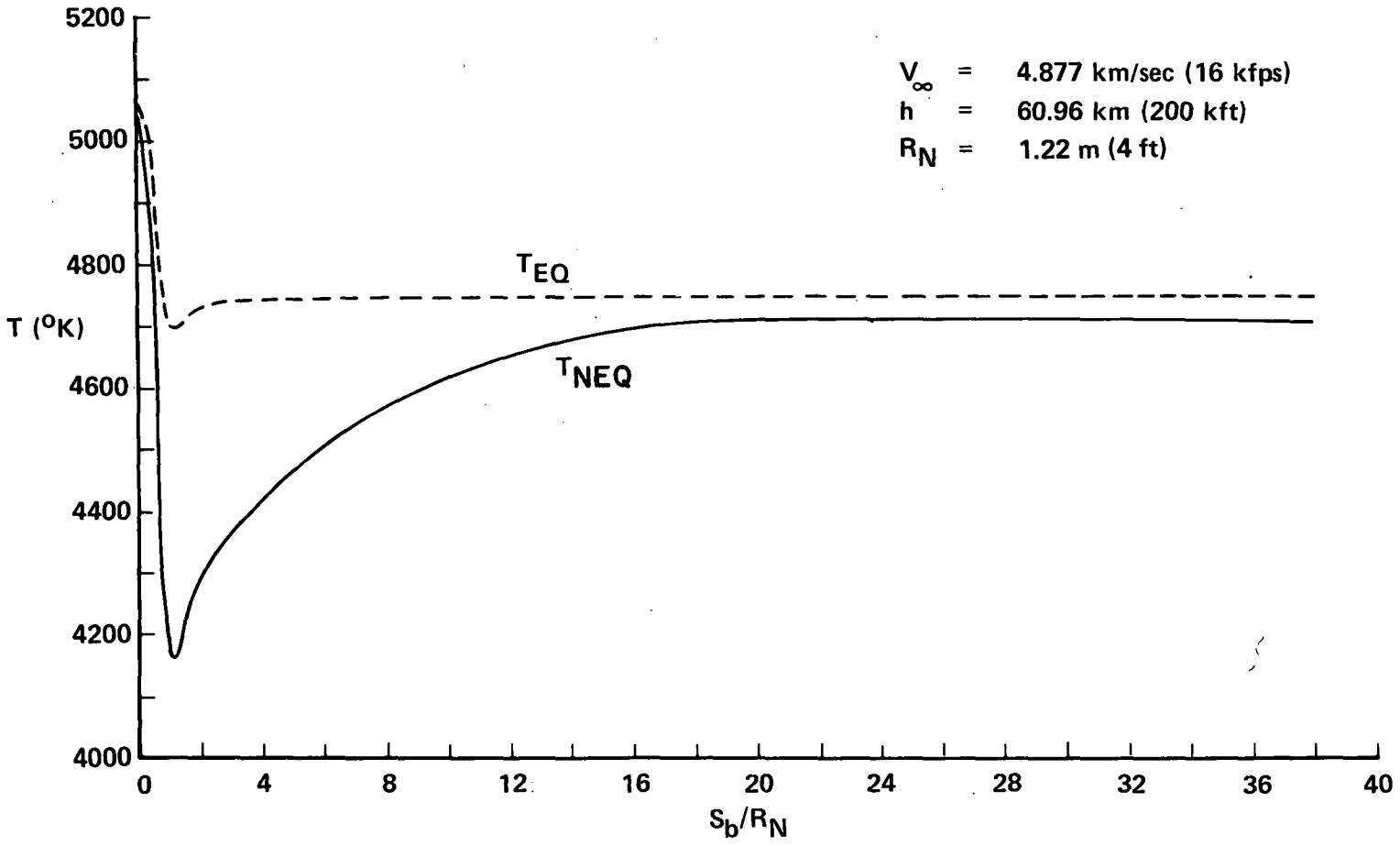

Figure 15

Page intentionally left blank

NONEQUILIBRIUM EFFECT ON TEMPERATURE ALONG OUTER STREAMLINE, $\alpha = 40^{o}$

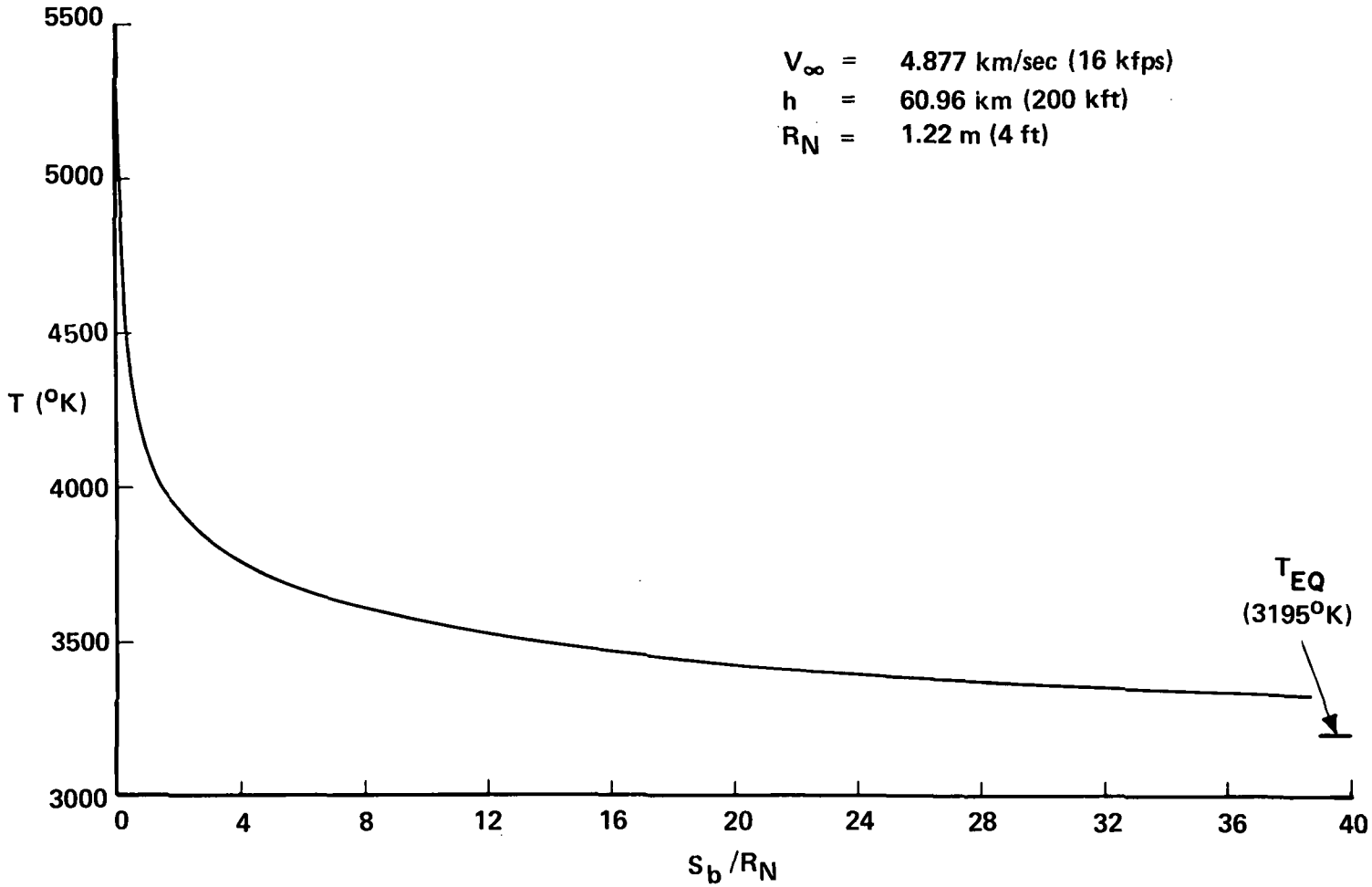

Figure 16

EFFECT OF NOSE RADIUS
(Fig. 17)

The flow along the outer streamlines is, of course, dependent only on the distance from the bow wave and is not influenced by the body nose radius. On the other hand, the flow along the streamlines in the entropy layer are affected by changes in body scale or nose bluntness. In the present framework, a change in body nose radius changes the rate at which the pressure drops in the expansion around the blunt nose. The rate of this pressure drop determines the departure from equilibrium. In order to investigate the effect of nose radius, the body streamline calculations for $\alpha = 20°$ were repeated for a body nose radius of .305 m (1 ft). Again the temperature variation along the streamline has been used to characterize the nonequilibrium effects. The equilibrium solution and the nonequilibrium solutions for $R_N = 0.305$ m (1 ft) and $R_N = 1.22$ m (4 ft) are compared in the accompanying figure. As indicated by these results very little more energy is frozen in the expansion around the smaller nose. In addition, the rate of increase toward equilibrium is about the same in terms of absolute distance, the temperatures being virtually identical at a distance of 45.7 m along the streamline. These results are typical for the range of trajectory points considered and nose radii in the .305 m to 1.22 m range. The flow along the body streamline becomes frozen in the expansion around the blunt nose and recombines only a slight amount over the body lengths of interest.

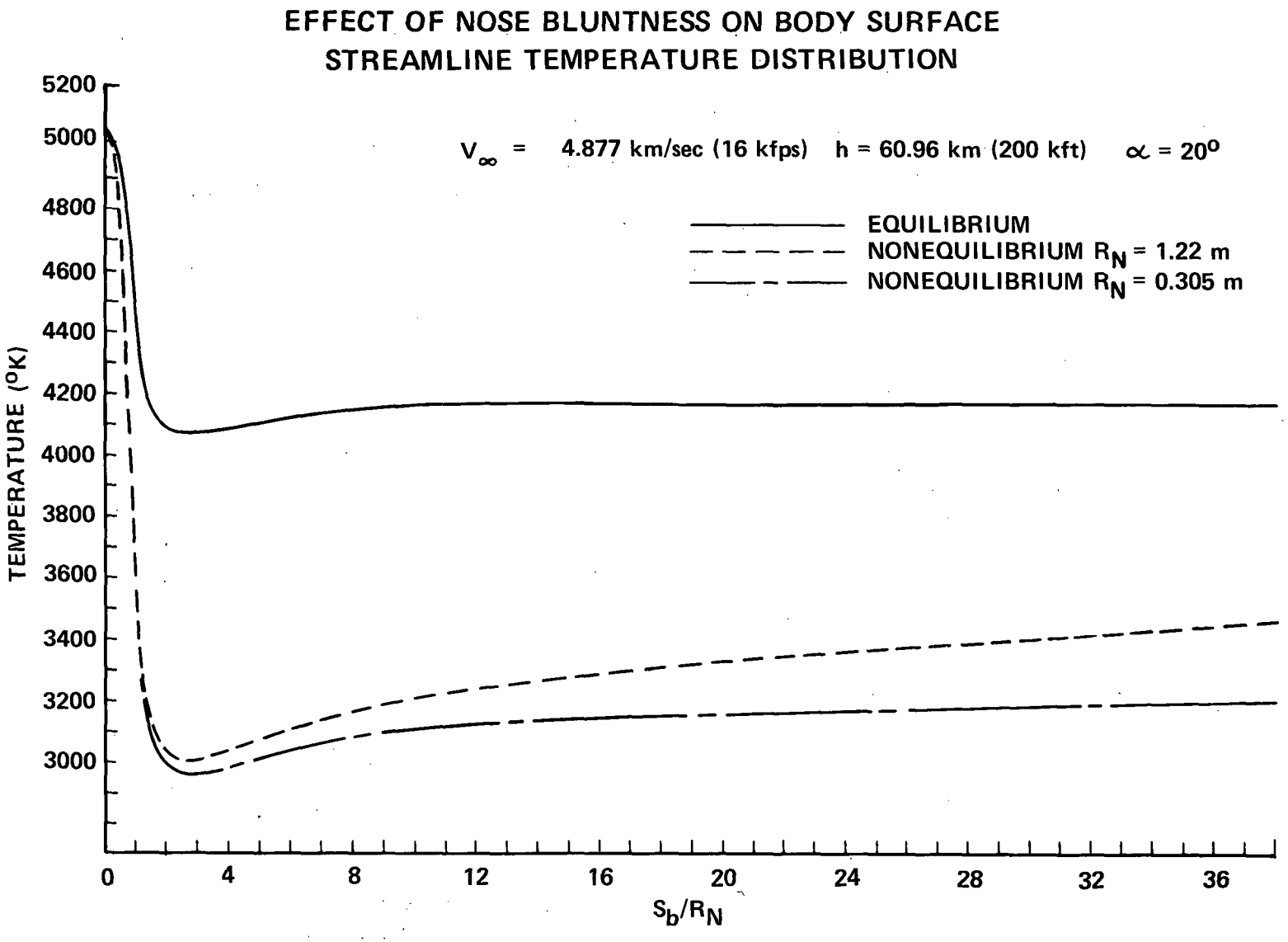
EFFECT OF NOSE BLUNTNESS ON BODY SURFACE
STREAMLINE TEMPERATURE DISTRIBUTION
V_∞ = 4.877 km/sec (16 kfps) h = 60.96 km (200 kft) α = 20°
EQUILIBRIUM
NONEQUILIBRIUM R_N = 1.22 m
NONEQUILIBRIUM R_N = 0.305 m
TEMPERATURE (°K)
5200
5000
4800
4600
4400
4200
4000
3800
3600
3400
3200
3000
0
4
8
12
16
20
24
28
32
36
S_b/R_N

Figure 17

INFLUENCE OF CHEMICAL NONEQUILIBRIUM IN THE INVISCID FLOW FIELD ON SURFACE HEATING RATES
(Fig. 18)

The calculation of the inviscid flow on the shuttle orbiter influences estimates of the surface heating rates through the edge conditions used in the boundary layer calculations. For example, consider the laminar heat transfer rate in the nose region. For a chemically frozen boundary layer on a noncatalytic surface, a local similarity calculation gives the heat transfer rate proportional to $(H_{T_f} - h_w)$ where H_{T_f} is the total "frozen" enthalpy. Assuming that the body surface streamline is the edge streamline, the laminar heating rates for equilibrium and nonequilibrium flow in the body streamline are compared in the figure below. The results are shown for the case V_∞ = 7.32 km/sec (24,000 fps), h = 76.2 km (250,000 ft), α = 20°, R_N = 1.22 m (4 ft).

The assumption of frozen boundary layer flow was chosen as a point of comparison because the inviscid flow becomes frozen in the corner expansion and that indicates that the chemical state of the boundary layer will be far from equilibrium. It should also be noted that if the surface is completely catalytic the surface heat transfer rate depends very little on the chemical state of the boundary layer. Furthermore, the only way that nonequilibrium effects would then be important is through the transport properties.

In order to calculate accurately the influence of the inviscid flow on the surface heating rate the "swallowing" of the inviscid flow by the boundary layer should be accounted for. While this was not done in the above calculation, it is noted that calculations of the boundary layer thickness indicate that the boundary layer is thin compared to the shock layer. Thus, in the nose region the streamlines in the entropy layer, where nonequilibrium effects are most severe, determine the boundary layer edge conditions.

The entropy layer will be swallowed at some point along the body and the boundary layer edge conditions near the base of the body are determined by the outer streamlines of the inviscid flow. The ratio of $H_{T_f} - h_w$ for nonequilibrium flow to that for equilibrium flow along the outer streamlines is about 1.07 for the highest altitude, highest velocity case considered here. While the static temperatures are considerably different for the equilibrium and nonequilibrium flow along this streamline the frozen total enthalpy is not appreciably affected because the flow is a high Mach number flow and the static enthalpy is small compared to the total. Hence the nonequilibrium effects on the flow in the outer streamlines do not appear to have much of an effect on the surface heat transfer rate, at low angles of attack.

INFLUENCE OF NONEQUILIBRIUM INVISCID FLOWS ON THE LAMINAR HEATING RATE OF A FROZEN BOUNDARY LAYER ON A NONCATALYTIC SURFACE

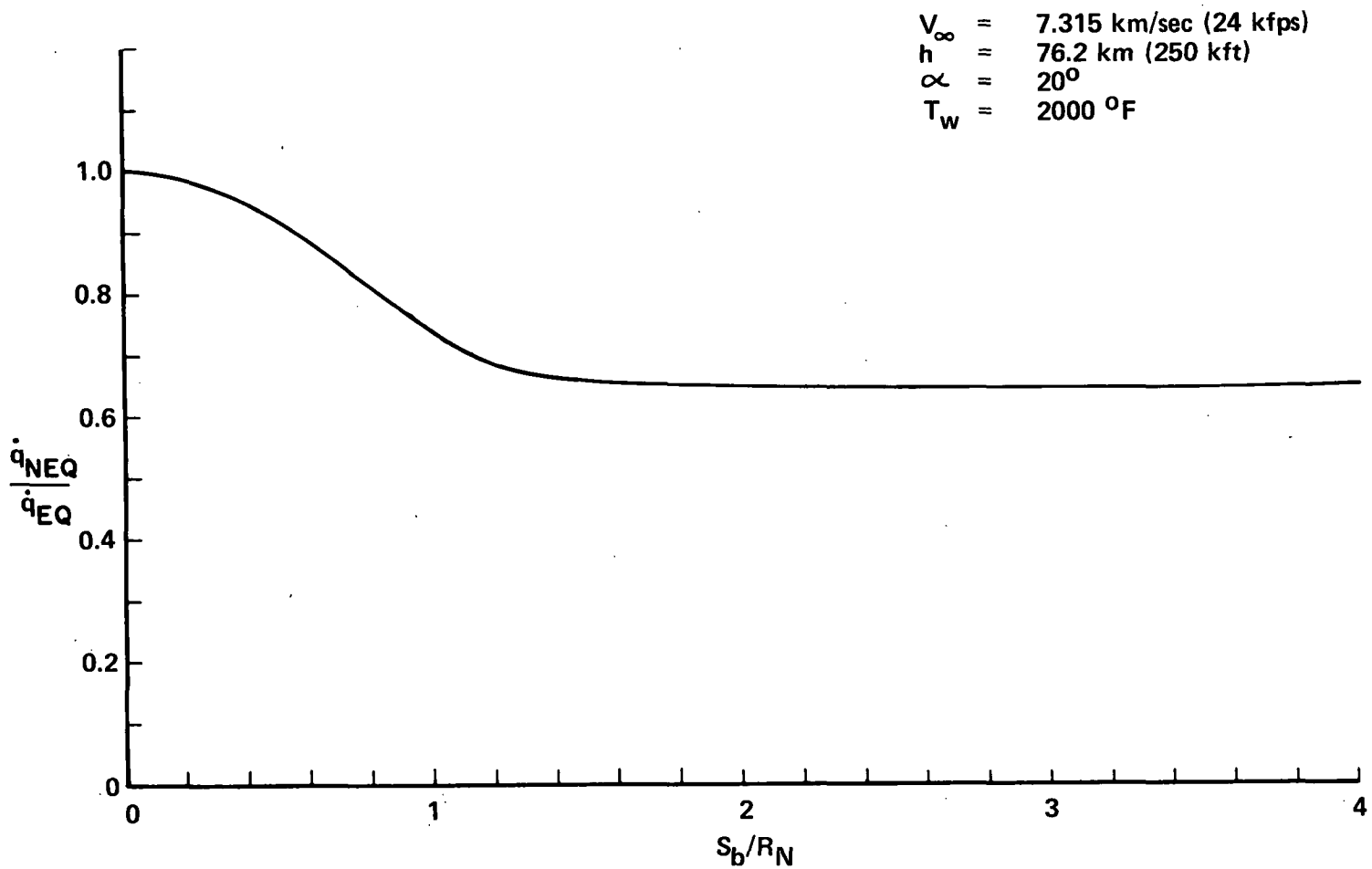

Figure 18

BOUNDARY LAYER THICKNESSES, TRANSITION, AND SWALLOWING OF THE ENTROPY LAYER
(Fig. 19)

The results of the inviscid streamtube computations have been applied to estimate boundary layer transition, the thicknesses of the laminar and turbulent boundary layers, and the location in the flow field where the entropy layer will be fully consumed by the boundary layer, i.e. entropy layer swallowing. Transition estimated were based on the NASA interim transition criterion. For $\alpha = 20°$, this criterion requires $R_{e_\theta}/M_e/Re/\ell)^{1/5} \approx 10$, where all parameters are evaluated for conditions at the boundary layer edge. The laminar boundary layer thicknesses were estimated by using Cheng's two-dimensional local similarity solution,[8] generalized to relax the hypersonic approximations and to obtain a solution based on boundary layer edge conditions. For the present purposes, it was assumed that the boundary layer was fully turbulent immediately following transition, and the thickness estimates were based on the Spaulding-Chi theory[9] and on procedures given by Johnson.[10] The Spaulding-Chi theory was approximated by a logarithmic law, $F_c C_f \approx .039 \left[F_{R_x} \; Re_x\right]^{-1/6}$, with errors of less than 10%, and this was applied in the usual momentum integral relation for boundary layer thickness. The exponent in the power law velocity profile was determined from Johnson's relations, with an effective starting length defined to yield an approximate Blasius profile at transition. Transition and the boundary layer thicknesses were determined by using the various nonequilibrium streamlines in the entropy layer for edge conditions, and by using an equilibrium streamline processed by the oblique shock wave. The latter is often used in calculating boundary layer characteristics, and the present comparison provides a check on the accuracy of this procedure.

The results of these calculations are shown in Fig. 19 for the three trajectory points considered here and for an angle of attack of 20°. At an altitude of 61 km (200kft), Fig. 19(a), the calculations show that the laminar boundary layer thickness is insensitive to the edge conditions, but transition is strongly influenced. The streamlines are labeled according to their distance from the body surface. The transition location varies by a factor of 2 1/2, depending on whether the nonequilibrium body streamline or the equilibrium oblique shock streamline is used. For these flight conditions, the latter corresponds to an ideal gas streamline, and there are essentially no nonequilibrium effects in that portion of the flow field. The thickness of the entropy layer is indicated in the figure, and it shows that the laminar boundary layer and transition are governed by conditions in the nonequilibrium entropy layer. The predominate nonequilibrium effect in this region is in the static temperature, and it differs from the equilibrium value by about 30%. This enters directly into the criterion for transition length through the square of the Mach number.

It can be seen in Fig. 19(a) that following transition, the boundary layer thickens rapidly, and it is thicker by a factor of 2 where the nonequilibrium entropy layer governs the flow. These boundary layer estimates indicate that the nonequilibrium entropy layer is fully consumed in the boundary layer at a distance of about 20 nose radii from the leading edge, i.e. the boundary layer development on the forward half of the body is governed by the nonequilibrium entropy layer and the boundary layer on only the aft can be estimated using conditions based on the oblique shock wave.

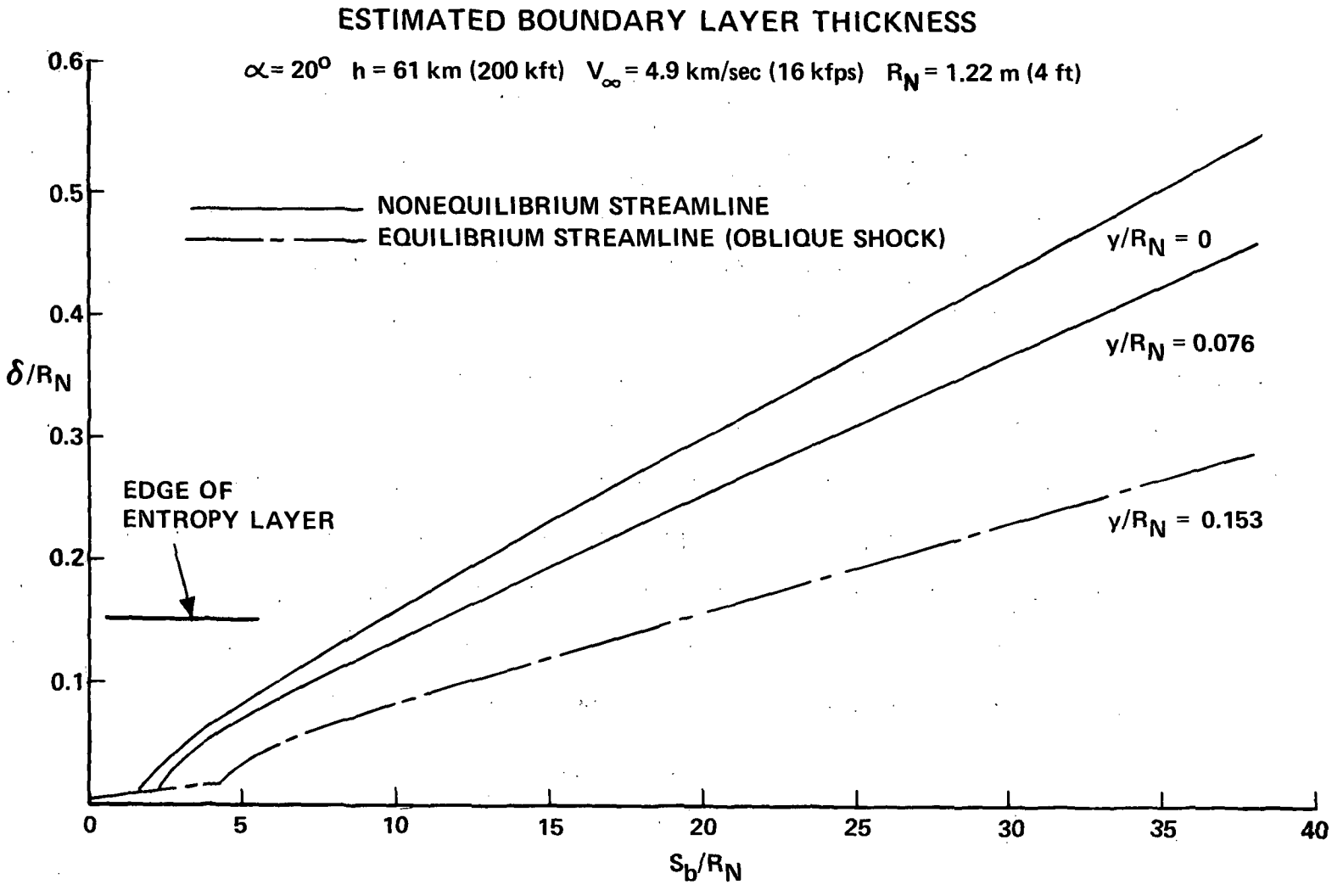
ESTIMATED BOUNDARY LAYER THICKNESS
α = 20° h = 61 km (200 kft) V∞ = 4.9 km/sec (16 kfps) RN = 1.22 m (4 ft)
NONEQUILIBRIUM STREAMLINE
EQUILIBRIUM STREAMLINE (OBLIQUE SHOCK)
y/RN = 0
y/RN = 0.076
y/RN = 0.153
EDGE OF
ENTROPY LAYER
δ/RN
Sb/RN
0.6
0.5
0.4
0.3
0.2
0.1
0
5
10
15
20
25
30
35
40

Figure 19(a)

(Fig. 19(b))

The calculated boundary layer characteristics at an altitude of 67 km (220 kft) are shown in Fig. 19b. These show that the thickness of the laminar layer is influenced by the edge conditions, and that the laminar layer develops under conditions corresponding approximately to the nonequilibrium body streamline. Again these results show that the transition length is a factor of four shorter than that predicted using equilibrium oblique shock conditions. The thickness of the nonequilibrium entropy layer is shown in Fig. 19b, and it can be seen that much of the boundary layer develops under the influence of the entropy layer. For this flight condition, the nonequilibrium entropy layer is fully consumed by the boundary layer about sixteen nose radii from the leading edge. Consequently, nominally the forward half of the boundary layer is governed by nonequilibrium conditions in the entropy layer while the aft half is governed by equilibrium, or in this case, ideal gas conditions behind the oblique shock wave.

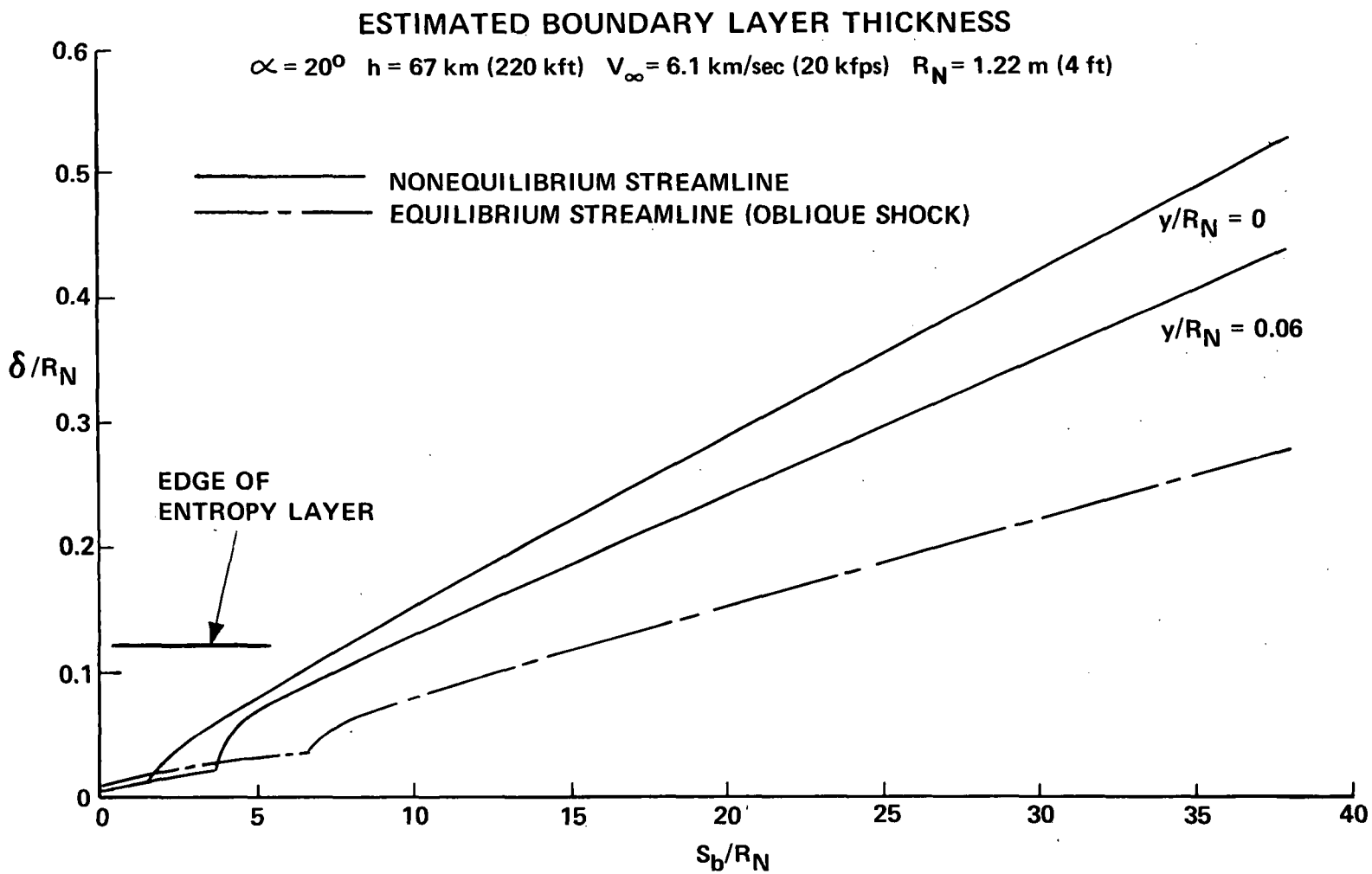
ESTIMATED BOUNDARY LAYER THICKNESS
α = 20° h = 67 km (220 kft) V∞ = 6.1 km/sec (20 kfps) RN = 1.22 m (4 ft)
NONEQUILIBRIUM STREAMLINE
EQUILIBRIUM STREAMLINE (OBLIQUE SHOCK)
y/RN = 0
y/RN = 0.06
EDGE OF
ENTROPY LAYER
δ/RN
0.6
0.5
0.4
0.3
0.2
0.1
0
0
5
10
15
20
25
30
35
40
Sb/RN

Figure 19(b)

(Fig. 19(c))

The calculated boundary layer characteristics at an altitude of 76 km (250 kft) are shown in Fig. 19c. These show that the thickness of the laminar layer is influenced appreciably by the assumed edge conditions, differing by a factor of two for the streamlines considered. Again, transition is strongly and adversely effected by the nonequilibrium entropy layer and is predicted to occur at $S_b / R_N = 5$ as compared with the prediction based on the equilibrium oblique shock conditions at $S_b / R_N = 17$. For this flight condition, the entire inviscid flow field is affected by thermochemical nonequilibrium and it is not appropriate to calculate streamline conditions based on equilibrium flow behind the oblique shock. The streamline at $y / R_N = 0.1$ is processed by the oblique wave, and the nonequilibrium effects on boundary layer thickness can be seen by comparing the results for that streamline with those for the equilibrium oblique shock streamline. The entropy layer is thinner that at the lower altitudes and the indications are that it will be consumed by the boundary layer at about 12 to 14 nose radii from the leading edge. For this case, about 1/3 of the body length is dominated by the nonequilibrium entropy layer, and the entire inviscid flow field is influenced by nonequilibrium effects.

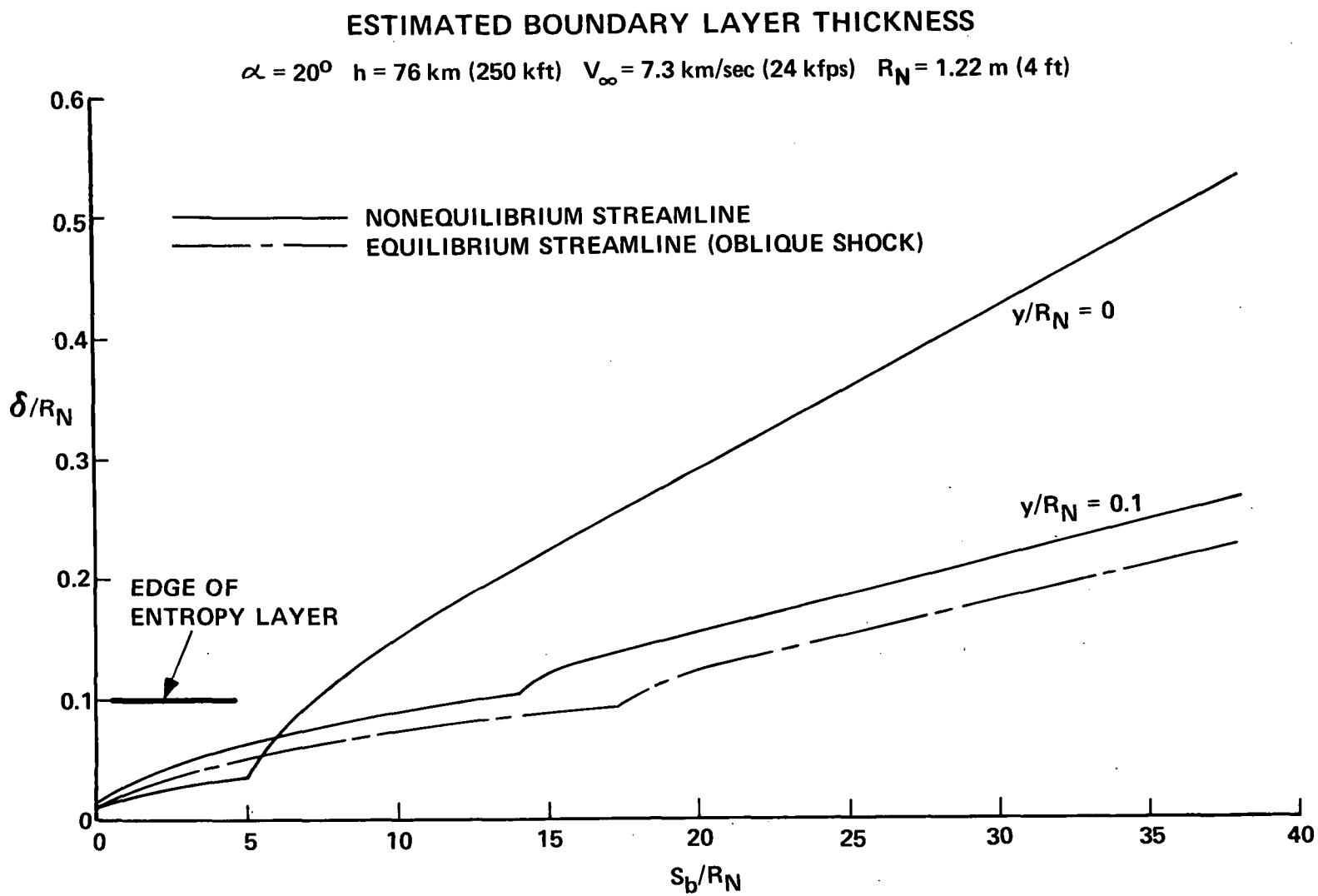
ESTIMATED BOUNDARY LAYER THICKNESS
α = 20° h = 76 km (250 kft) V∞ = 7.3 km/sec (24 kfps) RN = 1.22 m (4 ft)
NONEQUILIBRIUM STREAMLINE
EQUILIBRIUM STREAMLINE (OBLIQUE SHOCK)
y/RN = 0
y/RN = 0.1
EDGE OF
ENTROPY LAYER
δ/RN
Sb/RN
0.6
0.5
0.4
0.3
0.2
0.1
0
0
5
10
15
20
25
30
35
40

Figure 19(c)

SUMMARY

The degree of chemical nonequilibrium in the inviscid flow field of a blunted delta body typical of a shuttle orbiter was examined. This investigation was carried out within the framework of numerical calculations of the reacting flow along selected streamlines in the windward plane of symmetry. An approximate model of the pressure field was devised and the reacting streamline flows were computed for specified pressure histories.

Pressure data obtained on two test shapes, a blunted delta wing and a straight-wing body were presented. Experimental results were presented at angles of attack of 0, 20°, 40°, and 60°. Streamline calculations were performed at three typical trajectory points in the altitude range of 60.96 to 76.2 km (200 to 250 kft). Results were obtained for two angles of attack, 20° and 40°, and for two nose radii, 0.305 m and 1.22 m (1 ft and 4 ft).

Most of the calculations were done for the 20° angle of attack and the 1.22 m nose radius. The results for these cases were very similar over the range of trajectory points considered. On the streamlines close to the body the flow approaches chemical equilibrium in the stagnation region and then freezes in the expansion around the spherical nose. Along the inner streamlines the flow is composed of essentially N_2, N, and O for the conditions treated. Along the outer streamlines, the flow was essentially frozen for the 20° angle of attack. The difference between the equilibrium and nonequilibrium solutions became appreciable at the highest trajectory point considered.

The effect of angle of attack was investigated by computing streamline flows for $\alpha = 40°$ and comparing them with the $\alpha = 20°$ results. The increase in density level on the windward surface was sufficient to promote an approach to chemical equilibrium along both the inner and outer streamlines in the shock layer. The calculations carried out for $R_N = 0.305$ m (1 ft) indicated very little effect of nose radius or scale on the degree of nonequilibrium. This is because the flow along the body streamline freezes even for larger values of the nose radius. The streamline outside the entropy layer are independent of nose bluntness effects.

The edge conditions of the laminar boundary layer in the nose region are determined by streamlines which pass through the nearly normal portion of the bow shock. On the other hand the streamlines which pass through the limiting oblique shock determine the edge conditions of the boundary layer toward the base of the body. The calculations done here for an angle of attack of 20° show a fairly large fraction of the total enthalpy, e.g. about 30%, can be frozen in the chemistry along the body streamlines. On the other hand, in the flow along the outer streamlines the chemistry is nearly frozen but accounts for less than 10% of the total enthalpy. As the angle of attack increases the fraction of the total enthalpy accounted for by dissociation increases, but so does the rate of dissociation. At an angle of attack of 40°, the flow in the outer streamlines is near equilibrium over most of the length of the vehicle.

The influence of nonequilibrium effects on the boundary layer has been estimated using approximate boundary layer calculations. These show that for all three trajectory points, the laminar boundary layer development is governed by the nonequilibrium entropy layer. In each case, transition is determined by conditions in the nonequilibrium entropy layer and not by conditions behind the oblique wave. In each case the effect was detrimental in that transition occurred substantially earlier than predicted on the basis of equilibrium flow behind the oblique shock. In all cases covered, the nonequilibrium entropy layer governs the boundary layer development on the forward 1/3 to 1/2 of the body. The boundary layer development on the aft portions is governed by equilibrium flow behind the oblique shock at the two lower altitudes, and by nonequilibrium flow behind the oblique shock wave at the highest altitude.

There are several features of the nonequilibrium flow over a shuttle orbiter which deserve mention before concluding. First, it should be noted that the flow in the windward plane of symmetry does not necessarily represent the extreme so far as chemical nonequilibrium effects are concerned. Along streamlines which enter the nearly normal portion of the bow shock on the windward side but are then swept around the edge of the body to the leeward side, the flow undergoes a much greater expansion than in the plane of symmetry. Consequently, the difference between the equilibrium and nonequilibrium flow

properties and composition along such streamlines could be greater than along those treated in this study.

Although the presence of ionization was allowed for in the calculations the results for the electron concentration have not been presented in detail. However, the effect of nonequilibrium in the ionization and deionization reactions is even more pronounced than on the neutral chemistry. For the range of conditions considered here the electron number densities were between 10^{13} cc^{-1} and 10^{14} cc^{-1} in the nose region and between 10^{11} cc^{-1} and 10^{12} cc^{-1} at the base of the body.

The results of the present study indicate that nonequilibrium effects will persist at altitudes below 60.96 km (200,000 ft) for those streamlines near the body surface. Also nonequilibrium effects along the outer streamlines could be important at higher angles of attack at altitudes above 76.2 km (250,000 ft).

For the range of trajectory points considered here the nonequilibrium effects on a blunted delta shape at an angle of attack of 20° are much like those in the flow on blunted slender cones. Nonequilibrium effects are most important in the entropy layer. However, significant effects on the temperature and composition exist throughout the flow field in portions of the orbiter entry trajectory. The influence of the nonequilibrium effects on the boundary-layer edge conditions have been discussed. However, the nonequilibrium effects on the viscous portions of the flow field have not been treated beyond this. Furthermore the results of the present work indicate that the flow in the boundary layer will be far from equilibrium in the altitude range above 60.96 km (200,000 ft).

REFERENCES

1. Wittliff, C.E.; and Sundaram, T.R.: A Study of Real-Gas Effects on Blunted Cone Flows. AEDC-TR-69-36, 1969.

2. Schaefer, W.T. Jr.: Characteristics of Major Active Wind Tunnels at the Langley Research Center. NASA TMX-1130, 1965.

3. Lordi, J.A.; Mates, R.E.; and Moselle, J.R.: Computer Program for the Numerical Solution of Nonequilibrium Expansions of Reacting Gas Mixtures. NASA CR-472, 1966.

4. Inouye, M.: Shock Standoff Distance for Equilibrium Flow Around Hemispheres Obtained from Numerical Calculations. AIAA J. Vol. 3, No. 1, Jan. 1965, p. 172.

5. Wittliff, C.E.; and Curtis, J.T.: Normal Shock Wave Parameters in Equilibrium Air. Cornell Aeronautical Laboratory Report No. CAL-111, 1961.

6. Thomas, P.D.; Vinokur, M.; Bastianon, R.; and Conti, R.J.: Numerical Solutions for the Three Dimensional Hypersonic Flow Field of a Blunt Delta Body. AIAA Paper 71-596, AIAA 4th Fluid and Plasma Dynamics Conference, Palo Alto, Calif. June 21-23, 1971.

7. Wittliff, C.E.; Sundaram, T.R.; Rae, W.J.; and Lordi, J.A.: A Study of High-Density Hypervelocity Flows and Similitudes. AEDC-TR-67-72, 1967.

8. Cheng, H.K.; Hall, J.G.; Golian, T.C.; and Hertzberg, A.: Boundary Layer Displacement and Leading-Edge Bluntness Effects in High Temperature Hypersonic Flow. JAS, Vol. 28, No. 5, May 1961, p. 353.

9. Spaulding, D.B. and Chi, S.W.: The Drag of Compressible Turbulent Boundary Layer on a Smooth Flat Plate With and Without Heat Transfer. J.F.M., Vol. 18, Pt. 1, Jan. 1964, p. 117.

10. Johnson, C.B. and Boney, L.R.: A Simple Method for the Calculation of Real-Gas Turbulent Boundary Layers with Variable Edge Entropy. NASA TN D-6217, June 1971.

INVISCID-SURFACE-STREAMLINE PROGRAM FOR USE IN PREDICTING SHUTTLE HEATING RATES

By

H. Harris Hamilton
NASA Langley Research Center
Hampton, Virginia

and

Fred R. DeJarnette
North Carolina State University
Raleigh, North Carolina

10

INVISCID-SURFACE-STREAMLINE PROGRAM FOR USE IN PREDICTING SHUTTLE HEATING RATES

By H. Harris Hamilton and Fred R. DeJarnette*

INTRODUCTION

The previous papers in this session have indicated that a number of methods are currently under development for computing the "exact" three-dimensional flow field about real configurations. However, even when these methods are available, they will require large computational times on present-generation computers. Thus, there is still a need to develop approximate methods to solve three-dimensional flow problems. This paper describes an inviscid-surface-streamline program (for predicting shuttle heating rates) which uses approximate methods to obtain a solution. The basic method used herein is described in detail in reference 1.

---

*The work was done jointly by H. Harris Hamilton of NASA Langley Research Center and Fred R. DeJarnette of North Carolina State University (under Contract No. NAS1-10277).

SYMBOLS

H	scale factor in β-direction
L	length of delta-wing orbiter model, 0.323 meter
M_∞	free-stream Mach number
p	static pressure
q_{REF}	heat-transfer rate at stagnation point of a scaled 0.3048-meter-radius sphere
q_w	heat-transfer rate at wall
$q_{w,s}$	heat-transfer rate at stagnation point
r_N	nose radius of blunt cone, 0.925 cm
$R_{\infty,N}$	free-stream Reynolds number based on nose radius
u,v	velocity components in boundary layer in ξ- and β-directions, respectively
V_∞	free-stream velocity
x	axial distance from nose
α	angle of attack
β	coordinate normal to streamline on surface
η	coordinate normal to surface
ξ	coordinate along a surface streamline
φ	circumferential angle measured from lower surface plane of symmetry

BOUNDARY-LAYER SOLUTION

(Figure 1)

If the boundary-layer equations are written in a surface-oriented, streamline coordinate system where the ξ-coordinate is in the direction of an inviscid surface streamline, the typical velocity profile in the boundary layer will be as depicted in this figure. If it is assumed that the crossflow in the boundary layer (i.e., flow in the β-direction) is small and can be neglected, the three-dimensional (3-D) boundary-layer equations reduce to an equivalent form for axisymmetric flow about a body at zero incidence (see refs. 2 and 3). The distance along an inviscid surface streamline is interpreted as the distance along an equivalent axisymmetric body, and the scale factor for the β-coordinate (which is a measure of the streamline divergence) is interpreted as the radius of an equivalent axisymmetric body. The small crossflow approximation has been shown to be valid when the ratio of wall to stagnation enthalpy is small (ref. 4) as is the case in most space-shuttle applications.

This approximation makes a significant simplification to the boundary-layer problem and allows computations to proceed along inviscid surface streamlines using any boundary-layer solution available for axisymmetric flow. To be applicable to space shuttle the boundary-layer solution must be capable of handling laminar, transitional, and turbulent flow. Techniques that involve numerical solution of the nonsimilar boundary-layer equations (e.g., ref. 5) could be used. However, since this would destroy some of the simplicity desired in the present method, the local similarity method of Beckwith and Cohen (ref. 6) is used to predict laminar heating rates and a modification of the integral method of Reshotko and Tucker (ref. 7) is used to predict the turbulent heating rates. In the transitional region a weighted average of laminar and turbulent values is used. The present analysis includes both ideal-gas and equilibrium-air thermodynamic properties. The results that will be presented in this paper are for laminar flow of an ideal gas.

BOUNDARY-LAYER SOLUTION

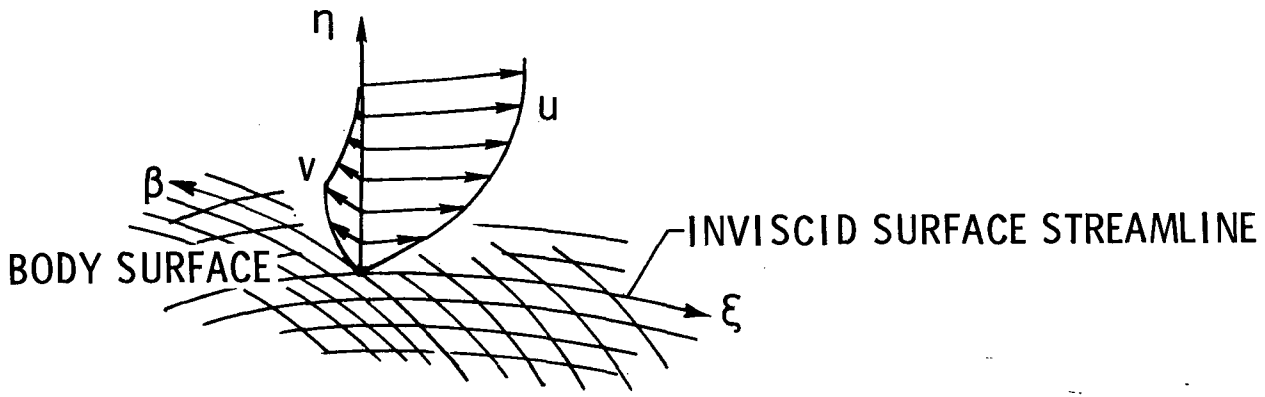

1. ASSUME SMALL CROSSFLOW IN BOUNDARY LAYER

2. REDUCE 3-D BOUNDARY-LAYER EQUATIONS TO EQUIVALENT FORM FOR AXISYMMETRIC FLOW AT $\alpha = 0°$

3. APPLY COMPUTATIONS ALONG INVISCID SURFACE STREAMLINES USING ANY METHOD APPLICABLE TO AXISYMMETRIC FLOW

4. INCLUDE LAMINAR, TRANSITIONAL, AND TURBULENT FLOW

5. INCLUDE IDEAL-GAS AND EQUILIBRIUM-AIR THERMODYNAMIC PROPERTIES

Figure 1

INVISCID-SURFACE-STREAMLINE SOLUTION

(Figure 2)

If the entropy and pressure distribution on the surface are known, ordinary differential equations can be obtained for the streamline path and for the scale factor H from Euler's equations and the equations of the surface geometry. In Phase I of the present development, the flow in the vicinity of the surface is assumed to have passed through a normal shock (typical blunt-body assumption). This is not a valid approach for space-shuttle applications at high flight velocities; thus the method is being extended in Phase II to account for variable entropy at the boundary-layer edge. The results that will be presented in this paper are for a Phase I approach.

Thus, starting at the stagnation point, the streamline path, the scale factor H, and the heat-transfer rate are computed along a selected streamline independent of other streamlines. Solutions are then computed along other streamlines until an adequate surface heating distribution is obtained.

The surface pressure distribution must be known to start the calculation and must be obtained independently. Experimental pressures can be used, if they are available in sufficient detail. However, they must be very accurate since second derivatives of the pressure are required. Approximate methods such as Newtonian theory appear to be the most promising source for surface pressure distributions at this time, but as more exact methods become available they can be used.

Another critical problem area is the description of the surface geometry. Two approaches have been used. First, a two-dimensional (2-D) cubic spline function has been used to "surface fit" body coordinates. The application of this method is easy and it has proven useful in describing certain simple geometric shapes, but it has not yielded the mathematical consistency necessary for describing complex configurations. The second method used to describe the surface geometry is analytic equations.

INVISCID-SURFACE-STREAMLINE SOLUTION

1. ASSUME ENTROPY AND PRESSURE DISTRIBUTION ON SURFACE

2. OBTAIN ORDINARY DIFFERENTIAL EQS. FOR STREAMLINE PATH AND SCALE FACTOR (H) FROM EQS. OF MOTION AND GEOMETRY

3. STARTING AT STAGNATION POINT, CALCULATE STREAMLINE PATH, SCALE FACTOR (H), AND BOUNDARY-LAYER SOLUTION FOR A SELECTED STREAMLINE

4. OBTAIN SURFACE PRESSURE DISTRIBUTION FROM
   - A. EXPERIMENTAL DATA
   - B. APPROXIMATE METHOD

5. DESCRIBE SURFACE GEOMETRY
   - A. 2-D CUBIC SPLINE
   - B. ANALYTICAL EQS.

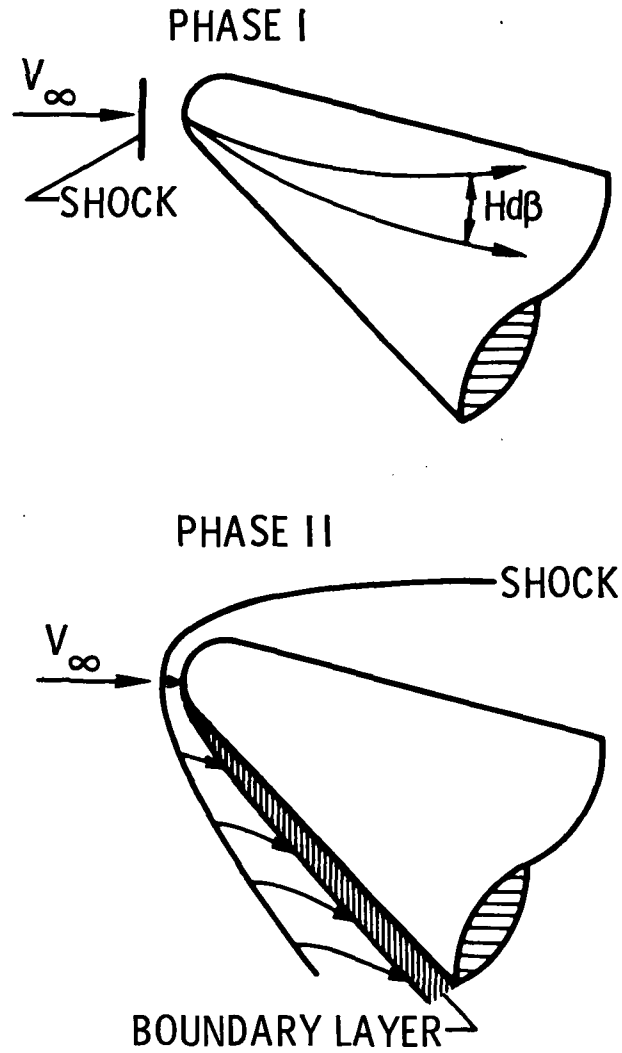

Figure 2

RESULTS FOR BLUNT 15° HALF-ANGLE CONE

(Figure 3)

This figure shows heating rates for a blunt 15° half-angle cone at $\alpha = 20^\circ$ and $M_\infty = 10.6$. The data, taken from reference 8, are presented as a ratio of local heating rate to that at the stagnation point $q_w/q_{w,s}$. The left-hand side of this figure shows axial distributions of $q_w/q_{w,s}$ for two rays on the cone, the most windward ray $(\varphi = 0^\circ)$ and the side ray $(\varphi = 90^\circ)$. In both cases, the agreement between the heating rates computed by the present theory and the experimental data is excellent.

The right-hand side of this figure shows a circumferential distribution of heating at $x/r_N = 26.5$. Again, the agreement between theory and experiment is excellent.

In computing the heating rates for this case, Newtonian theory was used to calculate the pressure distribution and a two-dimensional cubic spline function was used to describe the surface geometry.

Although other approximate methods have been developed that are applicable to simple axisymmetric bodies such as blunt cones (e.g., ref. 9), they cannot be applied to general three-dimensional bodies. The present method is not restricted to simple body shapes.

RESULTS FOR BLUNT 15° HALF-ANGLE CONE

$\alpha = 20°$

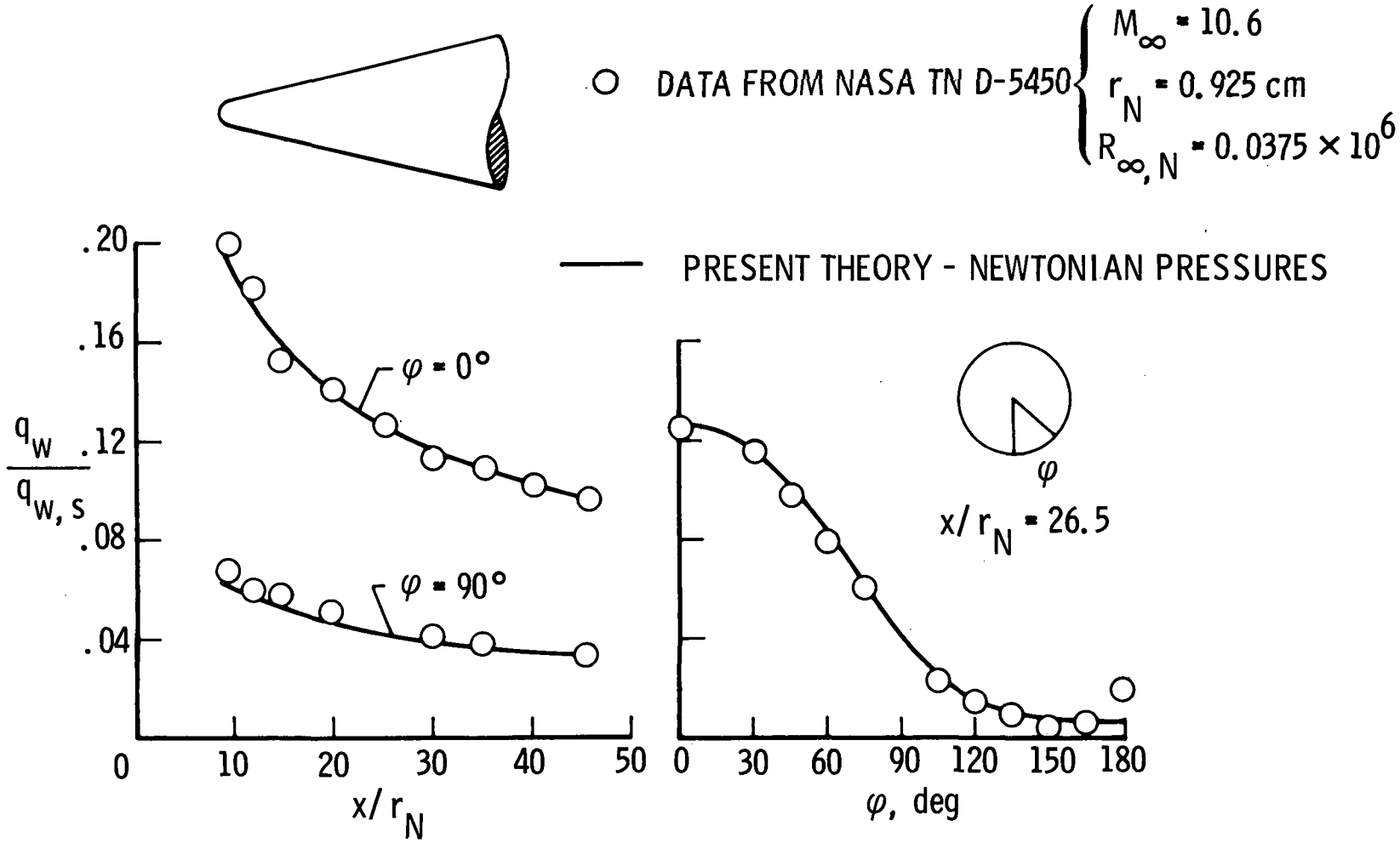

Figure 3

NAR 134B DELTA-WING ORBITER
(Figure 4)

This figure shows the NAR 134B delta-wing orbiter on which computations have been performed. This configuration was selected because of the availability of thermocouple heat-transfer data that were obtained at Ames Research Center (ARC) at $M_\infty = 7.4$ (ref. 10). The dimensions shown on the figure are for the ARC thermocouple test model. The surface geometry was described by analytical equations, with the use of a method suggested by J. V. Rakich of ARC and discussed in paper no. 5 by P. Kutler, J. V. Rakich, and G. G. Mateer. Basically, the method consisted of fitting the planform and plane-of-symmetry profile with polynomial functions of x and then using different elliptical segments to fit the upper- and lower-half cross sections.

NAR 134B DELTA-WING ORBITER

ARC THERMOCOUPLE TEST MODEL

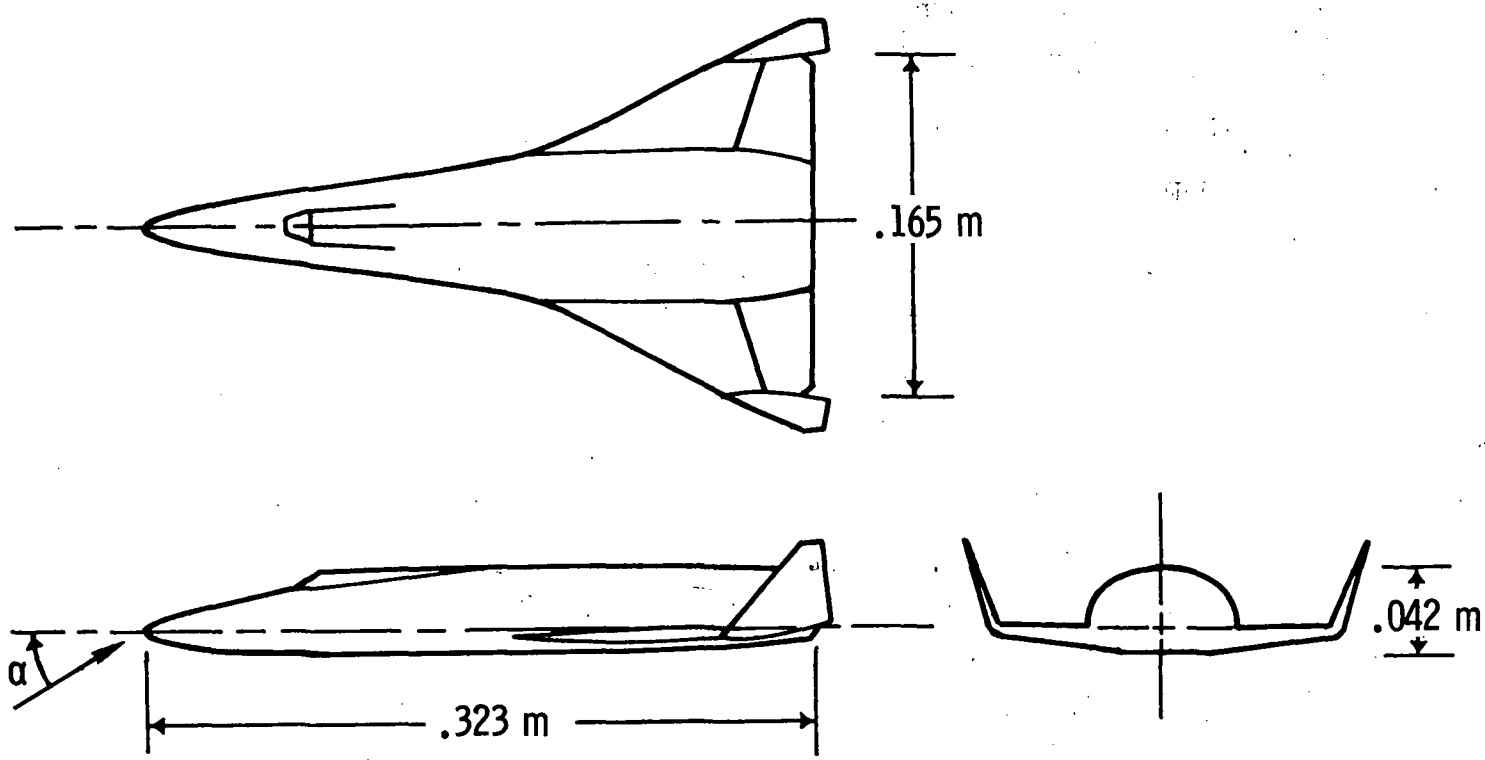

Figure 4

RESULTS FOR NAR 134B DELTA-WING ORBITER

(Figure 5)

This figure shows a comparison of heating rates computed by the present theory, using a Newtonian pressure distribution, with experimental data at $\alpha = 30^{\circ}$ for the NAR 134B delta-wing orbiter shown in figure 4. The heat-transfer data are presented as a ratio of local heating rate to a reference value q_w/q_{REF}, where the reference value is at the stagnation point of a scaled 0.3048-meter-radius sphere. Axial distributions of q_w/q_{REF} are presented in the upper part of the figure for the windward plane of symmetry ($\varphi = 0^{\circ}$). The theory and data are in good agreement over the forward portion of the model (i.e., $x/L < 0.5$), but the theory falls below the data over the aft portion (i.e., $x/L > 0.5$). Newtonian theory predicts a maximum pressure occurring on the windward plane of symmetry for $x/L \lesssim 0.4$; thus $(\partial^2 p/\partial\varphi^2)_{\varphi=0} < 0$ in this region and the surface streamlines tend to diverge. (Note that $(\partial p/\partial\varphi)_{\varphi=0} = (\partial^2 p/\partial x\, \partial\varphi)_{\varphi=0} = 0$ due to symmetry.) For $x/L \gtrsim 0.4$, Newtonian theory predicts a maximum pressure occurring off the windward plane of symmetry; thus $(\partial^2 p/\partial\varphi^2)_{\varphi=0} > 0$ in this region, the surface streamlines tend to converge, and the heating rates are reduced. Examining unpublished experimental pressure data obtained on this same configuration at ARC, one finds that the data (although sparse) tend to indicate that as far back as $x/L = 0.6$, $(\partial^2 p/\partial\varphi^2)_{\varphi=0} \leqq 0$. Thus, the previous calculation was repeated with the condition $(\partial^2 p/\partial\varphi^2)_{\varphi=0} = 0$ for $x/L > 0.4$ and resulted in the heat-transfer rates shown by the dashed line. This result is in better agreement with the experimental data and suggests that the previous computation (solid line) underpredicted the data over the rearward portion of the model because of the unrealistic lateral pressure distribution obtained from Newtonian theory.

The circumferential distribution of heating is shown in the lower left-hand part of the figure. The thermocouple data were supplemented by paint-test data obtained at Langley Research Center (LaRC) at $M_\infty = 8$. The theory and data are in reasonably good agreement. In the lower right-hand part of the figure, the computed inviscid surface streamlines are shown over the forward portion of the lower surface. The streamline divergence increases as the leading edge is approached. This fact accounts for the increase in heating in the vicinity of the leading edge.

RESULTS FOR NAR 134B DELTA-WING ORBITER

$\alpha = 30°$

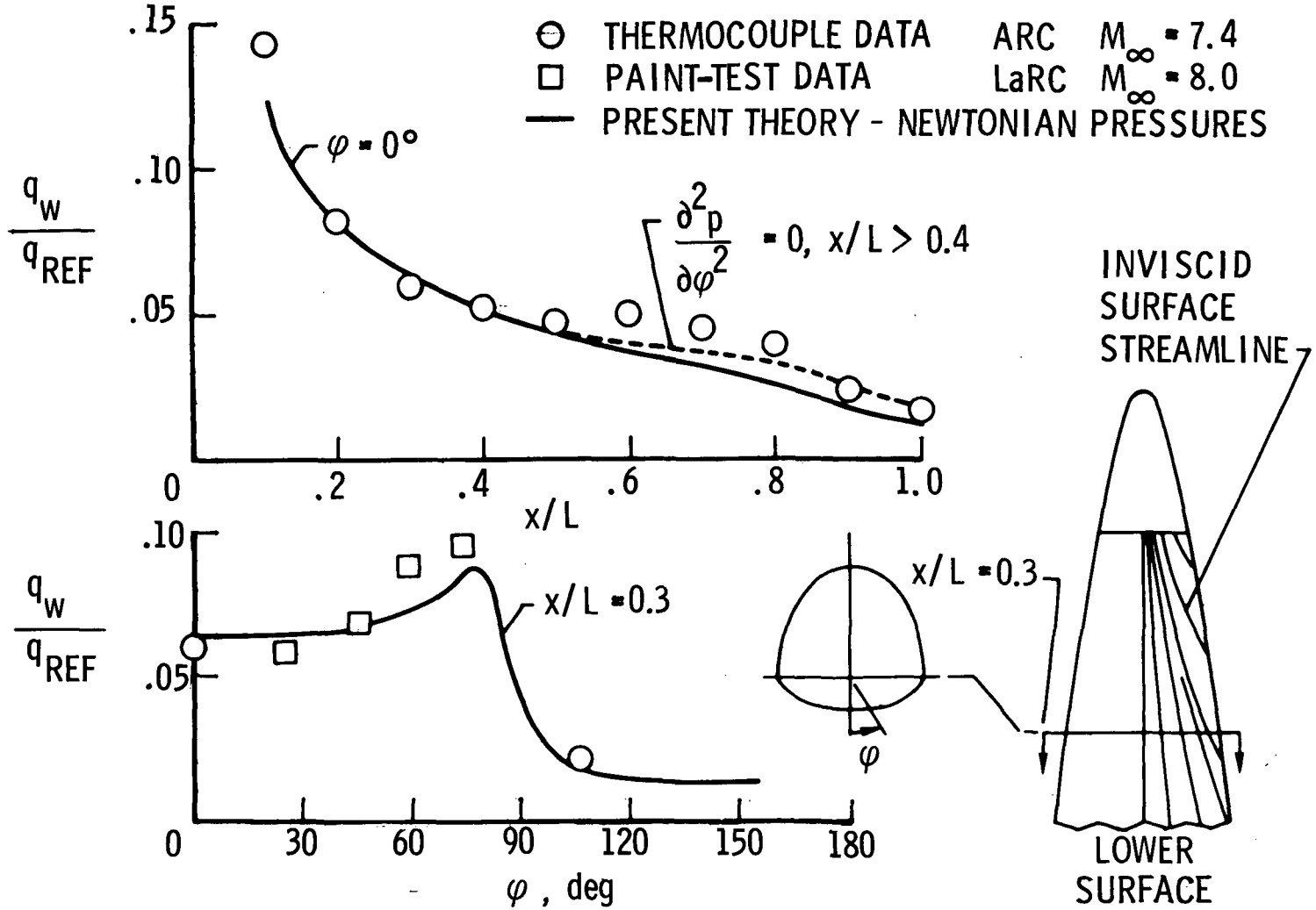

Figure 5

SUMMARY REMARKS
(Figure 6)

A simple method has been developed for computing the three-dimensional heating on shuttle-type configurations. The method is very fast; for example, typical results presented in this paper for a single streamline required only a few seconds of computing time on the CDC 6600 computer. In general, it requires that the surface pressure distribution be obtained independently, although Newtonian theory is a self-contained option in the basic computer program. For cases where the surface pressure distribution can be approximated with reasonable accuracy, the heating rates computed by the present method have been shown to compare favorably with experimental data. As more exact methods become available for computing the surface pressure distribution, these methods can be used to obtain the surface pressure distributions needed in the present theory.

The basic computer program for Phase I (normal-shock entropy) with a cubic-spline geometry routine is available. Further work is in progress to include variable boundary-layer-edge entropy in the program and to improve the mathematical representation of complex geometries.

SUMMARY REMARKS

1. A SIMPLE METHOD HAS BEEN DEVELOPED FOR COMPUTING 3-D HEATING ON SHUTTLE-TYPE CONFIGURATIONS

2. HEAT TRANSFER RATES COMPUTED BY THIS METHOD HAVE BEEN SHOWN TO COMPARE FAVORABLY WITH EXPERIMENTAL DATA

3. THE BASIC COMPUTER PROGRAM FOR PHASE I (NORMAL-SHOCK ENTROPY) WITH A CUBIC-SPLINE GEOMETRY ROUTINE IS AVAILABLE

4. WORK IS IN PROGRESS TO:

   A. INCLUDE VARIABLE BOUNDARY-LAYER-EDGE ENTROPY IN THE PROGRAM
   B. IMPROVE THE MATHEMATICAL REPRESENTATION OF COMPLEX GEOMETRIES

Figure 6

REFERENCES

1. DeJarnette, Fred R.: Calculation of Inviscid Surface Streamlines and Heat Transfer on Shuttle Type Configurations. Pt. I.- Description of Basic Method. Contract No. NAS1-10277, North Carolina State Univ., 1971. (Available as NASA CR-111921.)
2. Beckwith, Ivan E.: Similarity Solutions for Small Cross Flows in Laminar Compressible Boundary Layers. NASA TR R-107, 1961.
3. Cooke, J. C.; and Hall, M. G.: Boundary Layers in Three Dimensions. Rep. No. Aero. 2635, British R.A.E., Feb. 1960.
4. Vaglio-Laurin, Roberto: Laminar Heat Transfer on Three-Dimensional Blunt Nosed Bodies in Hypersonic Flow. ARS J., vol. 29, no. 2, Feb. 1959, pp. 123-129.
5. Harris, Julius E.: Numerical Solution of the Equations for Compressible Laminar, Transitional, and Turbulent Boundary Layers and Comparisons With Experimental Data. NASA TR R-368, 1971.
6. Beckwith, Ivan E.; and Cohen, Nathaniel B.: Application of Similar Solutions to Calculation of Laminar Heat Transfer on Bodies With Yaw and Large Pressure Gradient in High-Speed Flow. NASA TN D-625, 1961.
7. Reshotko, Eli; and Tucker, Maurice: Approximate Calculation of the Compressible Turbulent Boundary Layer With Heat Transfer and Arbitrary Pressure Gradient. NACA TN 4154, 1957.
8. Cleary, Joseph W.: Effects of Angle of Attack and Bluntness on Laminar Heating-Rate Distributions of a 15° Cone at a Mach Number of 10.6. NASA TN D-5450, 1969.
9. DeJarnette, Fred R.; and Davis, Ruby M.: A Simplified Method for Calculating Laminar Heat Transfer Over Bodies at an Angle of Attack. NASA TN D-4720, 1968.
10. Lockman, William K.; and DeRose, Charles E.: Aerodynamic Heating of a Space Shuttle Delta-Wing Orbiter. NASA TM X-62057, 1971.

FLOW FIELDS SESSION

SUMMARY

by

Joseph G. Marvin
NASA Ames Research Center

The preceding papers provide material from which to form a judgement regarding the status and future needs of exact flow field calculations, as summarized in figure 1.

Exact methods are available to provide the starting data for the three-dimensional inviscid calculations used when the flow field is predominately supersonic. At the high altitudes where viscous effects in the shock layer are important a two-dimensional method for generating starting data is available which has the promise of extension to three dimensions. Methods for calculating inviscid flows for realistic shuttle geometries at angles of attack where the flow is predominately supersonic (i.e. α to 30°) are available. At high angles of attack where the flow field is predominately subsonic two-dimensional methods have been applied to calculate shuttle flow fields in an approximate way. In each of the aforementioned inviscid flows, thin boundary-layer methods have been applied with reasonable success, but extension to three dimensions should be undertaken.

While the present status indicates good progress toward the ultimate objective of calculating the complete flow over shuttle vehicles, much work remains. In particular, the need for a three-dimensional method applicable at high angles of attack is clear, as is the need for including the viscous-dominated regions over the leeside of the vehicles. Furthermore, each of the methods needs to include real gas chemistry as part of its development. To accomplish this work large storage, high speed computers such as Illiac IV, to be operating in the Fall of 1972, must play a major role. Such machines should make possible economical calculations of complete flow fields on a timely schedule for shuttle development.

EXTERNAL FLOW FIELD CALCULATIONS

- PRESENT STATUS
  - STARTING FLOWS

    3-D INVISCID
    2-D VISCOUS
  - INVISCID FLOWS

    3-D LOW α
    2-D HIGH α
  - VISCOUS

    THIN BOUNDARY LAYER (SMALL CROSS FLOW)
- FUTURE NEEDS
  - 3-D VISCOUS STARTING SOLUTION
  - 3-D INVISCID, HIGH α
  - 3-D VISCOUS
  - REACTING CHEMISTRY
  - LARGE STORAGE, HIGH SPEED COMPUTERS

Figure 1

NASA-Langley, 1971 — 31 L-8136

Page Intentionally Left Blank

NATIONAL AERONAUTICS AND SPACE ADMINISTRATION
WASHINGTON, D.C. 20546

OFFICIAL BUSINESS
PENALTY FOR PRIVATE USE $300

FIRST CLASS MAIL

POSTAGE AND FEES PAID
NATIONAL AERONAUTICS AND
SPACE ADMINISTRATION

U.S.MA

POSTMASTER: If Undeliverable (Sec
Postal Manual) Do N

"The aeronautical and space activities of the United States shall be conducted so as to contribute . . . to the expansion of human knowledge of phenomena in the atmosphere and space. The Administration shall provide for the widest practicable and appropriate dissemination of information concerning its activities and the results thereof."

—NATIONAL AERONAUTICS AND SPACE ACT OF 1958

NASA SCIENTIFIC AND TECHNICAL PUBLICATIONS

TECHNICAL REPORTS: Scientific and technical information considered important, complete, and a lasting contribution to existing knowledge.

TECHNICAL NOTES: Information less broad in scope but nevertheless of importance as a contribution to existing knowledge.

TECHNICAL MEMORANDUMS: Information receiving limited distribution because of preliminary data, security classification, or other reasons.

CONTRACTOR REPORTS: Scientific and technical information generated under a NASA contract or grant and considered an important contribution to existing knowledge.

TECHNICAL TRANSLATIONS: Information published in a foreign language considered to merit NASA distribution in English.

SPECIAL PUBLICATIONS: Information derived from or of value to NASA activities. Publications include conference proceedings, monographs, data compilations, handbooks, sourcebooks, and special bibliographies.

TECHNOLOGY UTILIZATION PUBLICATIONS: Information on technology used by NASA that may be of particular interest in commercial and other non-aerospace applications. Publications include Tech Briefs, Technology Utilization Reports and Technology Surveys.

Details on the availability of these publications may be obtained from:

SCIENTIFIC AND TECHNICAL INFORMATION OFFICE

NATIONAL AERONAUTICS AND SPACE ADMINISTRATION

Washington, D.C. 20546